Outils numériques avancés pour le dimensionnement de rotors sustentateurs d'hélicoptère

Debbie Leusink

2013-ENAM-0010

École doctorale n° 432 : Science des Métiers de l'Ingénieur

Doctorat ParisTech

T H È S E

pour obtenir le grade de docteur délivré par

l'École Nationale Supérieure d'Arts et Métiers

Spécialité " Mécanique "

présentée et soutenue publiquement par

Debbie LEUSINK

5 avril 2013

Advanced numerical tools for aerodynamic optimization of helicopter rotor blades

Outils numériques avancés pour l'optimisation aérodynamique des rotors d'hélicoptères

Directeur de thèse : **Paola CINNELLA**
Co-encadrement de la thèse : **Jean-Christophe ROBINET**
Co-encadrement de la thèse : **David ALFANO**

CONFIDENTIEL JUSQU'AU 5 AVRIL 2023

Jury

M. Serge HUBERSON, Professeur des Universités, Université de Poitiers	Président
M. Michel COSTES, Dr., Ingénieur de recherche ONERA, Meudon	Rapporteur
M. Christophe CORRE, Professeur des Universités, Université de Grenoble	Rapporteur
M. Klausdieter PAHLKE, Dr.-Ing., Research Manager Helicopters, DLR, Braunschweig, Allemagne	Examinateur
Mme. Paola CINNELLA, Professeur des Universités, DynFluid, Arts & Métiers ParisTech	Examinateur
M. Jean-Christophe ROBINET, Professeur des Universités, DynFluid, Arts & Métiers ParisTech	Examinateur
M. David ALFANO, Dr., Ingénieur d'études EUROCOPTER, Marignane	Examinateur

T H È S E

Arts et Métiers ParisTech - Centre de Paris
Laboratoire DynFluid

Remerciements

Etant quelque part de multiples nationalités, ces mots sont un reflet de moi-même...

D'abord, je souhaite remercier mes encadrants Parisiens Paola Cinnella et Jean-Christophe Robinet pour le suivi de ma thèse. Malrgé la distance, les échanges se sont très bien passés, avec un suivi régulier, mais toujours la liberté dans mon propre développement. La combinaison a bien marché !

Je remercie mes rapporteurs, Michel Costes et Christophe Corre, pour la relecture de ce mémoire et leurs remarques pertinentes, qui ont contribué à l'amélioration de ce rapport de thèse.

Merci également à Serge Huberson d'avoir présidé mon jury de thèse. And thanks to Klaus-dieter Pahlke for being a member of my jury and for his precise remarks in the PhD report.

Une pensée à mes collègues que je tiens à remercier pour le travail effectué ensemble, pour les discussions, les relectures et l'ambiance général très agréable. Raphael, Guillaume, Guillaume, Damien, Mathieu, Antoine, Françoise, Sebastien, Fred, Bernard et tous les collègues d'ETGA/L, merci pour ces trois années passées ensemble. J'espère prolonger ça avec vous encore un bon petit bout de temps ! Et aux collègues d'ETGP où j'ai passé les derniers mois de thèse : j'ai beaucoup aimé mon passage chez vous en fin de thèse ; merci pour l'ambiance si agréable.

Une pensée aux collègues doctorants du DynFluid, en particulier Karim et Pierre-Yves, courage pour la fin de vos thèses.

Je tiens par ailleurs à remercier mes amies pour leur soutien long et indéfectible, surtout les derniers mois de thèse qui n'ont pas toujours été facile, tant sur le plan professionnel que personnel. Sylvie, Roland, Pascale, Setareh, Emilie et tous les autres dont je peux donner les noms car la liste serait trop longue, je pense à vous chaleureusement. Je suis heureuse de vous avoir comme amis !

Ik wil mijn familie bedanken voor hun steun in de afelopen 3 jaar en in het bijzonder voor de afgelopen maanden. Wat mooi om voor jullie mijn eindpresentatie te mogen doen. Bedankt dat jullie er waren, dat we samen deze dag hebben gedeeld om deze periode, soms moeilijk maar vooral ontzettend waardevol, op een prachtige manier af te ronden, en daarmee een nieuwe start in te luiden.

Enfin, je tiens à sincèrement remercier mon encadrant industriel David Alfano. Merci pour ton encadrement, pour tes conseils de toutes sortes, pour la liberté de recherche que tu m'as laissé tout en me guidant vers les sujets les plus intéressants, pour toutes les discussions, pour ... Tout ! Je suis heureuse de continuer de travailler dans ton équipe !

Debbie Leusink
April 2013

Table of Contents

List of Figures

List of Tables

Nomenclature

Latin letters

A	rotor disk surface	$[m^2]$
a	speed of sound	$[m\,s^{-1}]$
b	number of blades	[-]
$\bar{C}$	torque coefficient	[-]
C_l	sectional lift coefficient	[-]
C_d	sectional drag coefficient	[-]
C_p	pressure coefficient	[-]
c	chord	$[m]$
$\bar{c}$	mean aerodynamic chord	$[m]$
c_p	heat capacity at constant pressure	$[J\,K^{-1}]$
c_v	heat capacity at constant volume	$[J\,K^{-1}]$
E	total energy	$[J]$
e	internal energy	$[J]$
$\mathbf{Fc}$	convective flux vector	
$\mathbf{Fd}$	diffusive flux vector	
g	gravity constant	$[kg\,m^2\,s^{-2}]$
H	total enthalpy	$[J]$
h	specific enthalpy	$[J\,kg^{-1}]$
k	turbulence kinetic energy	$[kg\,m^2\,s^{-2}]$
M	Mach number	[-]
M_{dd}	drag divergence Mach number	[-]
M_{crit}	critical Mach number	[-]
$\dot{m}$	mass flow	$[kg\,s^{-1}]$
P	power	$[kW]$
Pr	Prandtl number	[-]
Pr_t	turbulent Prandtl number	[-]
p	pressure	$[kg\,m^{-2}]$
Q	rotor torque	$[N\,m]$
q_i	components of heat flux vector $\mathbf{q}$	$[W\,m^2]$
R	blade radius	$[m]$
R	specific gas constant	$[J\,kg^{-1}\,K^{-1}]$
r	radial position	$[m]$

r/R	relative radial position along blade radius	[-]
S_t	Sutherland temperature	$[K]$
S_{ij}	deformation rate tensor	$[rad\,s^{-1}]$
T	temperature	$[K]$
T	rotor thrust	$[N]$
t	time	$[s]$
U_R	local contribution of rotational velocity	$[m\,s^{-1}]$
u_i	components of velocity vector $\mathbf{u} = (u, v, w)^T$	$[m\,s^{-1}]$
V	volume of hexahedron mesh cell	$[m^3]$
V_H	forward flight velocity	$[km\,h^{-1}]$
v_i	induced velocity	$[m\,s^{-1}]$
W	weight	$[kg]$
x_i	components of Cartesian coordinate vector $\mathbf{x} = (x, y, z)^T$	$[m]$
$\bar{Z}$	rotor load coefficient	[-]

Greek letters

α	angle-of-attack	$[°]$
β	flap angle	$[°]$
γ	intermittency function for transition modelling	[-]
δ	lead-lag angle	$[°]$
δ_{ij}	kronecker delta symbol	[-]
ϵ	dissipation rate of turbulence kinetic energy	$[m^2 s^{-3}]$
κ	thermal conduction coefficient	[-]
λ	inflow angle	$[°]$
λ_d	second viscosity coefficient	[-]
λ_i	induced velocity coefficient	[-]
Λ	sweep angle	$[°]$
μ	advance parameter $\mu = V_H/\Omega R$	[-]
μ_d	dynamic viscosity	$[kg\,m^{-1}\,s^{-1}]$
μ_t	dynamic turbulent viscosity (eddy viscosity)	$[kg\,m^{-1}\,s^{-1}]$
Π_{ij}	pressure-strain correlation term of SSG turbulence model	
ρ	density	$[kgm^{-3}]$
τ_{ij}	components of viscous stress tensor τ	$[kg\,m^{-1}\,s^{-2}]$
τ_c, τ_s	cosine and sine terms of generalized pressure coefficients (FiSUW)	
τ_w	wall friction	$[kg\,m^{-1}\,s^{-2}]$
θ	pitch angle	$[°]$
χ_2, χ_4	artificial dissipation coefficients (Jameson scheme)	[-]
ψ	azimuth angle	$[°]$
Ω	rotational velocity	$[rad/s]$
ω	specific dissipation rate of turbulence kinetic energy	$[s^{-1}]$

Abbreviations

ANN	Artificial Neural Network
AUSM	Advection Upstream Splitting Method
BET	Blade Element Theory
BVI	Blade Vortex Interaction
CFD	Computational Fluid Dynamics
CPU	Central Processing Unit

DNS	Direct Numerical Simulation
DLR	German Aerospace Centre
	in German: Deutsches Zentrum für Luft- und Raumfahrt
elsA	CFD software developed by ONERA
	in French: ensemble logiciel pour la simulation en Aérodynamique
ERATO	ONERA/DLR rotor optimization project for aeroacoustics
	in French: Etude d'un Rotor Aéroacoustique Technologiquement Optimisé
FiSUW	Finite State Unsteady Wake, induced velocity model
F.M.	Figure of Merit, measure for hover efficiency
HOST	Helicopter Overall Simulation Tool
GA	Genetic Algorithm
LES	Large Eddy Simulation
NACA	National Aeronautics and Space Administration
NASA	National Advisory Committee for Aeronautics
ONERA	French Aerospace Laboratory
	in French: Office National d'Etudes et Recherches Aérospatiales
ORPHEE	French-German blade design project
	in French: Optimisation d'un Rotor Principal d'Hélicoptère par l'Etude et l'Expérimentation
L/D	Lift-to-Drag ratio, measure for forward flight performance
MAC	Mean Aerodynamic Chord
Metar	Rigid-wake induced velocity model
	in French: Modèle d'Etude de l'Aérodynamique Rotor
RANS	Reynolds Averaged Navier-Stokes
RSM	Reynolds Stress Modelling (turbulence model)
	Response Surface Method (optimization technique)
SBO	Surrogate Based Optimization
SSG	Speziale, Sarkar and Gatski turbulence model
SST	Shear Stress Transport model
TPP	Tip Path Plane

Introduction

Helicopters have the specific ability to operate in two distinct flight conditions: hover and forward flight. From an aerodynamic point of view, these two flight conditions are entirely different. In hover, the flow is axi-symmetric about the rotor hub. This means that the relative velocity encountered by main rotor blade sections increases linearly with their radial position but does not vary for different azimuthal positions. However, in forward flight, the local velocity as seen by airfoils is a function of radial and azimuthal position: the local velocity on the advancing blade side is the sum of forward flight and rotational velocities and thus locally higher than in hover flight. Yet, on the retreating blade, the local velocity is lower and equals the rotational contribution minus forward flight speed. On this part of the rotor even a reversed flow zone exists, in which flow locally comes from the trailing edge of the airfoil. Due to these local velocity differences, blade motions over a rotor revolution are required to find equilibrium of forces and moments over the rotor. As a consequence of these evolving flow conditions, complex aerodynamic phenomena occur over the rotor disk. These include transonic flow over the tip of the advancing blade, dynamic stall over the retreating blade and a complex wake structure that may interact with the blades and other helicopter parts. The wake structure influences the blade over its entire span, but especially tip vortices may be strong and persist for multiple rotor revolutions, thereby affecting local flow characteristics of succeeding blades. To improve rotor performance by design of rotor blades, lift generation is to be increased and drag should be reduced.

As hover flow is easier to understand and theoretically optimal design solutions are known, historically rotor blades were principally designed for this flight condition. Also, typical forward flight speeds of helicopters designed until the '70's were significantly lower than today. Forward flight performance was mainly incorporated as a constraint, rather than as a design objective. Until some 20 years ago, blade designs were systematically verified by wind tunnel testing. This implies that only a very limited number of tests could be performed and studying relations between blade geometry and rotor performance was not possible. Simulation tool development in the '90's allowed for rotor blade computation, even if these simulations did not yet consider certain physical phenomena. Parametric studies resulted in better understanding of the relations between rotor blade geometry parameters and aerodynamic performance. Nevertheless, these studies were time consuming as they were performed in a non-automated way and only selected geometries and design objectives could be considered. At that time, forward flight performance became a design objective. In recent years, automation of simulation tools and increased computational resources allow for testing large quantities of blade geometries. Additionally, simulation accuracy has increased, in particular thanks to the extensive use of Computational Fluid Dynamics (CFD) methods that naturally incorporate most physical phenomena. These advances resulted in better understanding of relations between geometry and rotor performance. However, as rotor blades need to be designed for hover and forward flight simultaneously, no evident compromise solution for both flight conditions can be found.

A way to come up with blade designs with optimized performance in hover and forward flight simultaneously is a multi-objective design optimization. This optimization loop is constructed from automated simulation tools for rotor performance prediction, coupled with optimization methods that simultaneously consider both flight conditions. Today, all building blocks for this optimization loop exist, but various difficulties remain to be resolved in preparation of industrial use of this rotor blade design optimization loop.

A first problem in automated rotor blade optimization is that simulation tools need to predict relations between rotor blade geometry and aerodynamic performance correctly. Without this simulation accuracy, optimizations would have no meaning as resulting blades would not provide the expected performance increase in real flight. While interesting for helicopter design, prediction of the exact rotor performance in absolute value is not required for optimization purposes. Instead, accurate capturing of relative performance trends as a function of geometry parameters is of utmost importance. Today, two simulation tools for aerodynamic performance prediction of rotor blades are available at Eurocopter: comprehensive rotorcraft code HOST and Computational Fluid Dynamics (CFD) software *elsA*. HOST is based on coupling of models of all relevant parts of the helicopter to compute loads and accelerations. Rotor aerodynamics is based on 2D blade element theory and uses look-up tables with lift, drag and moment coefficients that originate from wind tunnel tests. This essentially 2D view of aerodynamics is extended to more complex situations through empirical corrections for some physical phenomena. The *elsA* code solves discrete Reynolds Averaged Navier-Stokes equations on computational meshes. This 3D simulation naturally accounts for most physical phenomena occurring over a helicopter rotor, such as airfoil stall, tip vortices and other viscous effects. Before starting any optimization, HOST and *elsA* need to be validated for their correct computation of performance trends as a function of geometry. Advantages and limitations of both tools are to be investigated, to make best use of these tools at appropriate moments in the design process.

A second difficulty to be considered is the simultaneous design for the two significantly different flight conditions. Optimizing a blade for hover flight only will lead to poor forward flight performance, and vice versa. While interesting for understanding geometry influences on rotor performance, these single-objective designs are not useful for industrial employment. Instead, a compromise solution is to be found for this multi-point design problem. In addition, industrial rotor blade design objectives and constraints may be related to acoustics, vibrations or production. Even if these non-aerodynamic performance design goals are not taken into account in today's optimization loop, their future use needs to be planned from today. Taking this all together, an optimization loop and strategy is to be developed for this particular design problem.

A third obstacle for industrial application of automated optimization is the design turn-around time. Even if considerable computational resources are available (access to EADS High Performance Computing cluster; 18 Tflops, 15 000 CPU, 24/36 Gb memory, Nehalem/Westmere; Eurocopter access since 2012), sequential search for optimal solutions quickly leads to significant optimization turn-around times. In fact, HOST simulations have a relatively short turn-around time and low computational cost (1 CPU on PC), as seen in Table **1**. CFD computations, however, require some hours for hover flight simulation and even 2 to 3 days for forward flight simulation. The cost of a single computation is multiplied by several cycles required for optimization convergence. In the end, the total optimization time quickly exceeds industrially acceptable response times. Precisely, industrially acceptable turn-around time is in the order of hours in a preliminary design phase and several days, up to a week, for detailed design. Typically, 3 serial forward flight CFD simulations can be performed within this period of time, so that advanced optimization techniques are required to take full use of this limited number of simulations. In conclusion, a third difficulty to be tackled concerns the intelligent use of simplified (HOST) and advanced (CFD) simulation tools and advanced optimization techniques to make the optimization industrially viable.

Table 1: Typical computational time and cost of rotor performance simulations

	Hover	Forward flight
HOST	1 min	2 min
elsA	3 hours 12 CPU	60 hours 24 CPU

The present PhD Dissertation provides a contribution towards the automated aerodynamic optimization of helicopter main rotor blades in industry. Each of the mentioned difficulties is studied and recommendations are given.

Correct numerical prediction of relative performance differences as a function of geometrical changes is of high importance within the optimization loop. To acquire knowledge on advantages and limitations of simulation tools HOST and *elsA*, these are assessed by various studies. Precisely, for both tools, several computational parameters are tested for their influence on simulation results. Besides these influence studies, four blades of different geometry [28] are computed to determine the ability of HOST and *elsA* to predict their performance hierarchy. The effect of various computational parameters on this hierarchy is examined as well. This study allows to select the most appropriate simulation tool at each moment in the blade design process. This suitability is not only a function of simulation accuracy, but also of turn-around time, which is especially important in the optimization framework.

A second axis of the present thesis is the development of optimization strategies that fulfil requirements of industrial rotor blade optimization: find globally optimal compromise solutions for the multi-objective design problem within an industrially acceptable turn-around time. A first requirement is thus related to the two distinct flight conditions in hover and forward flight. Simultaneous design for both objectives is a major advance for industrial design. In addition, globally optimal and robust solutions in the form of a Pareto Optimal Front allow the design engineer to incorporate non-aerodynamic objectives and constraints in the final selection of one blade geometry. This topic thus concerns the choice of an optimization method that complies with the here stated requirements.

This axis also considers the optimization turn-around time. The optimization loop would only be useful for industrial purposes if design solutions can be achieved within an acceptable period of time. To accomplish this, advanced optimization techniques will be incorporated. Precisely, Design of Experiments (DoE) allow for exploring the design space more efficiently than a random initialization. More information is thus gathered with the same number of cost function evaluations. To further reduce the number of required simulations, Surrogate Based Optimization (SBO) will be employed. In SBO, relations between objectives and parameters are described by analytical functions. The actual optimization is then performed on this low-cost response surface, rather than on full simulations. In surrogate model update steps, accuracy of these analytical functions is improved in interesting zones by additional rotor simulations. Employment of SBO is assessed and compared to a complete optimization. Two surrogate models will be evaluated and their practical implementation in terms of required number of simulations is assessed as well. Another way to reduce total optimization time is the intelligent use of both simulation tools into a hierarchical optimization. A multi-fidelity optimization strategy is then proposed and evaluated.

This Dissertation follows the main subjects discussed above: Chapter 1 describes aerodynamic features of helicopter rotors and explains differences in local flow characteristics between hover and forward flight. Furthermore, relations between blade geometry parameters and rotor performance are presented, allowing for understanding optimization results later on. Examples of rotor blades are given to illustrate these relations. In particular the four ORPHEE blades are described, as they are used in the simulation validation study. A state of the art of rotor blade design and optimization is presented and finally hypotheses and goals of this work are given.

Chapter 2 discusses the various validation studies of simulation tools HOST and *elsA*. Both tools are described as are the experimental data used in these comparative studies. HOST's representation capability of induced velocity models is compared to NASA measurements. For *elsA*, the influence of various numerical parameters on simulation of a wingtip vortex is assessed. Again, experimental data from the NASA is used for evaluation of *elsA*'s ability to foresee wrap-up, shedding and decay of the wingtip vortex. Rotor performance prediction in hover and forward flight is assessed by comparison to measured performance data of the ORPHEE blades. Again, several model parameters are tested and recommendations for best computational settings are given.

Chapter 3 elaborates on the requirements for an optimization method suited for this particular design problem. These criteria are discussed for optimization methods typically used in similar design problems, allowing for selecting one method. Then, optimization techniques that allow for reducing the number of cost function evaluations are discussed. The optimization strategy proposed here to take best use of both simulation tools is elaborated as well.

At last, Chapter 4 combines choices of previous studies to perform rotor blade optimizations. The created optimization loop is described and various validation tests are performed. These include studies on the influence of parameters and objectives, comparison of simulation-based optimization to surrogate model-based optimization and settings of surrogate models. Finally, the multi-fidelity optimization strategy defined earlier is employed and results are analyzed.

Conclusions and perspectives finalize the Dissertation.

Introduction en Français

L'hélicoptère a la capacité spécifique d'opérer suivent deux conditions de vol : en vol stationnaire ou en vol d'avancement. Ces conditions de vol présentent des caractéristiques aérodynamiques complètement différentes. En vol stationnaire, l'écoulement est axisymétrique autour du mât rotor. Ceci implique que la vitesse du vent incident augmente linéairement le long de la pale avec la position radiale mais ne diffère pas avec la position azimuthale. Au contraire, en vol d'avancement, la vitesse locale incidente est à la fois une fonction de la position radiale et azimuthale : côté pale avançante, la vitesse du vent incident est égale à la vitesse d'avancement et de la contribution dû à la rotation résultant en une vitesse totale plus élevée qu'en vol; stationnaire. A contrario, côé pale reculante, la vitesse locale est plus faible et égale à la contribution rotationelle diminuée de la vitesse d'avancement. Sur ce côté du rotor, une région d'écoulement inversé existe, où l'écoulement vient localement du bord de fuite du profil. Ces différences de vitesses locales font que des mouvements des pales sur un tour rotor sont nécessaires pour trouver l'équilibre des efforts et moments sur le rotor. En conséquence des variations des vitesses de l'écoulement, des phenomènes aérodynamiques complexes apparaissent sur le rotor, incluant un ecoulement transonique sur le saumon de la pale avançante, le décrochage dynamique sur la pale reculante et des sillages complexes pouvant interagir avec les pales et les autres éléments de l'hélicoptère. Les sillages sont générés sur toute l'envergure de la pale, en particulier les tourbillons de saumon qui peuvent être intenses et persister durant plusieurs tours rotor, influant sur l'écoulement local du voisinage des pales suivantes. Ces phénomènes peuvent être en partie traité par des modifications géométriques des pales, avec pour conséquence une amélioration des performances du rotor, par une augmentation de la portance résultante, ou un diminution globale de la traînée qu'il induit.

L'écoulement autour du rotor en vol stationnaire est plus facile à appréhender et des solutions donnant théoriquement des performances optimales sont connues. De plus les pales sont historiquement conçu principalement pour ce cas de vol. Jusqu'aux années 70, les vitesses d'avancement usuelles des hélicoptères étaient significativement plus faibles qu'aujourd'hui. La performance en vol d'avancement était principalement pris en compte comme une contrainte, plutôt qu'un objectif de conception. Des pales étaient le plus souvent conçues à partir d'un nombre d'essais limité en soufflerie, rendant impossible une étude détaillée des performances rotor en fonction de la forme des pales. Le développement d'outils de simulation dans les années 90s a permis d'estimer les performances rotor, même si ces calculs ne prenaient pas encore en compte certains phenomènes physiques. Des études numériques paramétriques ont nettement contribué a une meilleure compréhension de l'impact du desgin des pales sur les performances globales du rotor. Néanmoins, le déploiment de ces études paramétriques étaient effectué manuellement, si bien qu'un nombre restreint de géométries pouvaient être considerés. Il devenait toutefois possible d'intégrer l'optimistion des performances rotor en vol d'avancement dans les objectifs de conception. Ces dernières années, l'automatisation des outils de simulation et l'augmentation des ressources de calcul disponibles ont permis d'explorer de grandes quantités de géométries de pale. En outre, la précision de calcul a augmenté, en particulier grâce à l'utilisation intensive des calculs de Mécanique des Fluides Numérique (MFN) qui prennent en compte la plupart des phénomènes physiques. Ces améliorations ont résulté en une meilleure compréhension des relations entre la géométrie des pales et les performances rotor. Cependant, l'optimisation simultanée de pale à la fois pour le vol stationnaire et le vol d'avancement reste délicate, notamment en ce qui concerne le choix d'un compromis parmi toutes les solutions optimales.

Une manière de trouver des géométries de pale offrant des performances optimisées en vol stationnaire et en vol d'avancement est d'avoir recours à l'optimisation multi-objectif. Cette boucle d'optimisation est constituée d'outils de simulation automatisés pour la prédiction des performances rotor, couplée à des méthodes d'optimisation prennant en compte simultanément les deux cas de vol. Aujourd'hui, tous les éléments constituant cette boucle existent, mais divers difficultés de mise en oeuvre persistent en vue du déploiment industriel pour la conception des pales.

Une première difficulté est de disposer d'estimations numériques correctes des performances aérodynamiques en fonction de la géométrie des pales. Bien qu'intéressant d'un point de vue théorique et académique, la prédiction exacte des performances rotor en valeur absolu n'est pas nécessaire pour l'optimisation. On se satisfait le plus souvent de prévisions précises des tendances et des écarts rélatifs, en fonction des paramètres géométriques des pales. Aujourd'hui, deux outils de simulation pour la prédiction des performances aérodynamiques sont disponibles à Eurocopter : le code dédié à la mécanique de vol des hélicoptères HOST et le code de mécanique des fluides numérique *elsA*. HOST repose sur le couplage de différents modèles régissant le comportement des parties de l'hélicoptère pour le calcul des efforts. L'aérodynamique du rotor est basé sur la théorie 2D des éléments de pale et utilise des polaires tabulées des profils pour les coefficients de portance, traînée et moment obtenues par essais en soufflerie. Cette modélisation principalement 2D de l'écoulement est étendu aux situations plux complexes à travers des corrections empiriques pour certains phénomènes physiques. Le code *elsA* résout les équations discrétisés de Navier-Stokes moyennées au sens de Reynolds sur des maillages numériques. Cet outil permet de capturer la plupart des phénomènes survenant sur une pale de rotor d'hélicoptère, comme le décrochage de profil, les tourbillons de saumon et autres effets visqueux.

Les capacités d'estimation des performances aérodynamiques de HOST et *elsA* sont prálablement évaluées. Les avantages et limitations des deux outils sont étudiés, en vue de les lors du processus de conception.

Une deuxième difficulté est la conception simultanée pour les deux conditions de vol qui sont fondamentalement différentes. L'optimisation d'une pale pour le vol stationnaire exclusivement résultera en une pale présentant de mauvaises performances en vol d'avancement, et vice versa. Bien qu'intéressant pour la compréhension des influences des paramètres géométriques sur les performances rotor, ces solutions mono-objectifs ne sont pas utiles pour une application industrielle. Au contraire, une solution de compromis est à trouver pour le problème multi-objectif. De plus, il est tout à fait envisagable d'inclure d'autres objectifs et contraintes industriels dans la boucle d'optimisation, telle que la réduction de bruit rayonné ou les vibrations de la structure. Même si ces points ne sont pas pris en compte dans la boucle d'optimisation actuellement développée, leur insertion est planifié pour des versions futures.

Un troisième obstacle pour l'application industrielle des optimisations automatisées est le temps de réstitution de l'optimisation. Même si des ressources de calcul conséquentes sont disponibles (accès au cluster de calcul d'EADS ; 18 Tflops, 15 000 CPU, 24/36 Go mémoire, Nehalem/Westmere ; accès Eurocopter depuis 2012), la recherche séquentielle de solutions optimales aboutit rapidement à un délai de réponse considérable de l'optimisation. En fait, des calculs HOST ont un temps de réstitution relativement court et un faible coût de calcul (1 CPU sur un ordinateur personnel), comme montré dans le Tableau **1**. Des calculs avec *elsA*, au contraire, nécessitent quelques heures pour une simulation en vol stationnaire, et jusqu'à 2 à 3 jours pour le vol d'avancement. Le coût d'un simple calcul est multiplié par plusieurs cycles pour la convergence de l'optimisation. A terme, le temps d'optimisation total dépasse largement les délais de réponse admissible dans un context industriel. Précisement, un délai industriel acceptable est de l'ordre de quelques heures pendant la phase de conception préliminaire et quelques jours, voire une semaine, pour la conception détaillée. Typiquement, 3 calculs CFD en vol d'avancement peuvent être effectué en séries en ce délai, ce qui implique que des techniques d'optimisation avancées sont nécessaires pour pleinement profiter de ce nombre de simulation limité. En conclusion, un troisième problème à résoudre concerne l'utilisation intelligente des outils de simulation simplifié (HOST) et avancé (*elsA*) et des techniques d'optimisation pour rendre l'optimisation viable en industrie.

Tab. 1: Temps de réponse typique pour une simulation de performances rotor

	Vol stationnaire	Vol d'avancement
HOST	1 min	2 min
elsA	3 heures 12 CPU	60 heures 24 CPU

Cette thèse apporte une contribution à l'optimisation aérodynamique et automatisée des pales du rotor principal des hélicoptères en industrie. Chacun des problèmes précédemment mentionnés est étudié et des recommandations sont présentées.

La prédiction numérique des différences relatives de performance rotor en fonction des changements géométriques est un point crucial pour la qualité de le boucle d'optimisation. Afin de connaître les avantages et les limitations des outils de simulation HOST et *elsA*, ceux-ci sont évalués à travers plusieurs études. Précisement, pour chacun des outils, l'influence de divers paramètres numériques est testée. Conjointement à ces études d'influence, quatre pales de géométrie différente sont calculées afin de déterminer la capacité d'HOST et *elsA* à prédire leur hiérarchie de performance. Cette étude permet de sélectionner l'outil de simulation le plus adapté pour chaque phase de conception de pale. Ce choix n'est pas seulement fonction de la précision de simulation, mais également du délai de réponse, ce qui est particulièrement important en vue de l'optimisation.

Un deuxième axe est le développement d'une stratégie d'optimisation qui remplit les critères d'optimisation des pales en industrie : trouver des solutions de compromis qui sont globalement optimales pour le problème d'optimisation multi-objectif dans un délai de réstitution acceptable en industrie. La conception simultanée pour les deux objectifs est une avancée majeure pour la conception industrielle. D'autre part, trouver des solutions globalement optimales et robustes en la forme d'un Front de Pareto permet à l'ingénieur d'incorporer des objectifs et contraintes non-aérodynamique pour la sélection finale d'une géométrie de pale. Ce thème concerne le choix d'une méthode d'optimisation qui répond aux critères discutés.

Cet axe considère également le temps de restitution de l'optimisation. La boucle d'optimisation n'est exploitable en industrie que si les solutions peuvent être restituée en un délai de temps acceptable. Afin d'y parvenir, des techniques d'optimisation avancées sont intégré. Précisement, un plan d'expérience permet l'exploration de l'espace des paramètres d'une manière plus efficace qu'une initialisation aléatoire. Plus d'information est donc obtenue pour le même nombre d'évaluations de la fonction coût. Afin de réduire encore plus le nombre de simulations, des optimisations sur surface de réponse sont employées. Une surface de réponse décrit les rélations entre objectifs et paramètres par des fonctions analytiques. La vraie optimisation est executée sur cette surface de réponse qui a un faible temps de restitution, plutôt que sur des calculs complets. La surface de réponse est mise à jour par des simulations supplémentaires afin d'améliorer sa précision dans les zones d'intérêt. L'emploi d'optimisation sur surfaces de réponse est évalué est comparé à une optimisation complète. Deux modèles de surfaces de réponse sont évalué et leur implémentation pratique en terme de nombre de simulations est examiné.

Une autre manière de réduire le temps total d'optimisation est d'utiliser intelligement les deux outils de simulation en une optimisation hiérarchique. Une stratégie d'optimisation multi-fidelité est proposée et évaluée.

Le mémoire suit les sujets principaux discutés ci-dessus : le chapitre 1 décrit les caractéristiques aérodynamiques des pales du rotor principal d'un hélicoptère. Cette partie explore les différences d'écoulement local entre le vol stationnaire et le vol d'avancement. De plus, les relations entre les paramètres décrivant la géométrie de pale et les performances rotor sont présentées, ce qui permet ensuite d'analyser les résultats des optimisations. Des exemples des géométries de pale sont données afin d'illustrer ces relations. En particulier les quatre pales ORPHEE sont décrites, puisqu'elles sont utilisées pour l'étude de validation des outils de simulation. Un état de l'art de la conception et optimisation des pales du rotor est présenté et finalement les hypothèses et objectifs de cette thèse sont donnés.

Le chapitre 2 présente les diverses études de validation des outils de simulation HOST et *elsA*. Les deux outils sont décrits, tout comme les données expérimentales utilisées pour ces études comparatives. La capacité des modèles de vitesse induite dans HOST à représenter le champ de vitesse induite est étudiée à l'aide de comparaisons à des données expérimentales publiées par a NASA. Pour *elsA*, l'influence des divers paramètres numériques pour la simulation d'un tourbillon de saumon d'aile est étudié. À nouveau, les données expérimentales de la NASA sont utilisées pour l'évaluation de la capacité d'*elsA* à prédire l'évolution du tourbillon de saumon d'aile. La prédiction des performances rotor en vol stationnaire et vol d'avancement est évaluée par la comparaison aux données de performance mesuré des pales ORPHEE. De nouveau, des paramètres des modèles sont testés et recommandations pour les meilleurs paramètres sont donnés.

Le chapitre 3 détaille les critères pour la méthode d'optimisation adaptée pour ce problème d'optimisation. Ces critères sont discutés pour les méthodes d'optimisation typiquement utilisées pour des problèmes d'optimisation similaires, permettant de sélectionner une méthode. Ensuite, des techniques d'optimisation qui permettent de réduire le nombre d'évaluations de la fonction coût sont décrites. La stratégie d'optimisation proposée ici afin d'utiliser au mieux les deux outils de simulation est également détaillée.

Enfin, le chapitre 4 réunit les choix des études préliminaires afin d'exécuter des optimisations des pales du rotor. La boucle d'optimisation developée est décrite et divers tests de validation sont réalisés. Ceux-ci incluent des études concernant l'influence des paramètres et objectifs, une comparaison des optimisations reposant sur simulation et sur surface de réponse, et paramètres des surface de réponse. Finalement, la stratégie d'optimisation multi-fidelité définie plus tôt est utilisée et les résultats sont analysés.

Des conclusions et perspectives clôsent le mémoire.

Chapter 1

Aerodynamic design of helicopter rotor blades

The present chapter illustrates the aerodynamic flow conditions that are encountered by rotor blades and their impact on blade design. Rotor blade geometry parameters are detailed, and their influence on rotor performance is discussed. Rotor blade design applications are illustrated by published examples. In a third section, the state of the art in rotor blade design and optimization is presented, with focus on recent efforts of industry to integrate automated optimization in the design process. Finally, objectives of the present work and underlying assumptions are specified.

1.1 A brief review of rotor aerodynamics

Helicopters have, besides flying in forward flight as airplanes, the specific ability to maintain in flight at its three-dimensional position in the so-called hover condition. The hover ability allows a helicopter to perform manoeuvres a fixed-wing aircraft could not do and land and take-off in zones where an airplane could not be used.

Lift required to transport the payload in the fuselage is entirely generated by rotation of rotor blades, introducing a relative velocity on the aerodynamic surfaces of the main rotor. Blade rotation is driven by the engine(s), and gear boxes maintain the rotors at their correct rotational speed. Rotation of the main rotor would provoke the fuselage to turn in its opposite direction, unless a lateral force comes to counteract this rotation. This force is in general provided by the tail rotor, which is alleviated by a vertical stabilizer in forward flight. A horizontal stabilizer is added at the rear of the tail boom for longitudinal stability. All these elements are illustrated in Figure 1.1. In the present work, only conventional configurations using a single main rotor and a tail rotor will be studied; other configurations, such as tandem rotors, co-axial rotors or tilt rotor helicopters will not be considered here.

The helicopter rotor fulfils three main functions [83]:

1. It generates the required lift force to sustain the helicopter in air;
2. It generates a horizontal force (thrust) to overcome the drag force created in forward flight;
3. It provides a means of controlling the position and attitude of the helicopter.

All three functions are directly related to the position of the rotor thrust vector. Commanding the rotor, in terms of attitude and rotational velocity, is a vital element of helicopter flight and allows the helicopter to perform manoeuvres.

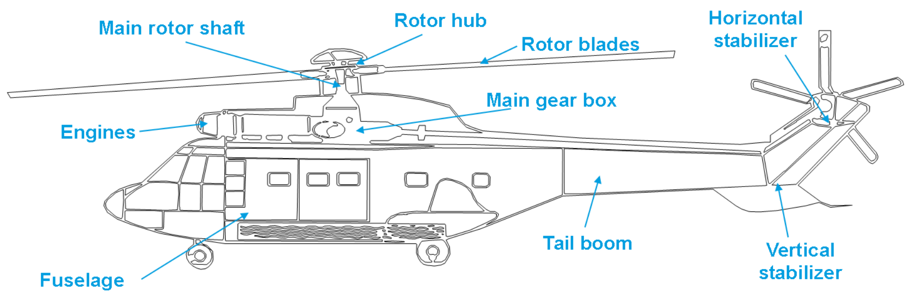

Figure 1.1: Structure and elements of a helicopter

Typical cruise speeds of a helicopter range between 100 to 150 kts (180 to 280 km/h). The forward flight speed is often expressed in terms of the advance parameter μ, defined as:

$$\mu = \frac{V_H}{\Omega R} \tag{1.1}$$

This parameter represents the ratio of forward flight speed V_H to the tip speed of the rotor blades, as expressed in terms of the rotational velocity Ω and blade radius R. Typically, the advance parameter μ is about 0.3 in cruise flight conditions; this corresponds to a forward flight speed of 240 km/h for a 7m-radius rotor rotating at 300 rpm.

The local velocity encountered by blade sections depends on three contributions: local rotation speed, forward flight velocity and induced velocity. In hover, the local velocity due to rotation increases linearly with increasing radial position. The induced velocity, which combines with the rotational velocity, depends on the generated lift force and is therefore a function of the radial position as well. The flow in hover is thus axi-symmetric about the rotor hub.

In forward flight, the local velocity over the rotor disk is a function of both radial and azimuthal position. It combines the rotational contribution with forward flight speed in such a way that a local velocity difference appears over advancing and retreating blade sides. On the advancing blade side the rotational velocity adds up to the forward flight velocity, whereas on retreating blades the forward flight velocity subtracts from the rotational velocity. The induced velocity field becomes a complex field related to the lift distribution of the rotor.

In the following, we first describe main features of rotor aerodynamics both in hover and in forward flight and introduce parameters commonly used to express rotor performance and specifically its efficiency. For the sake of clarity, we consider an idealized isolated rotor, so that no interactions with the fuselage or other parts of the helicopter are considered. This assumption will be retained throughout the manuscript.

1.1.1 Rotor aerodynamics in hover

The hover condition is characterized by a purely helical flow from upstream to downstream of the rotor. This flow is axi-symmetric with respect to the rotor hub so that all blades encounter identical flow conditions. The local velocity over the rotor blades is the sum of rotational and induced velocities. The contribution of rotational velocity gives a linear increase of local velocity along the blade from root to tip. Induced velocity depends on the generated lift force and may be approximated by Froude's theory.

Froude's momentum theory

Induced velocity generated in hover may be evaluated by applying the conservation laws to a well-chosen control volume around the rotor. The flow is assumed to be one-dimensional, quasi-steady and incompressible, inviscid fluid [62, 83]. Rotor inflow can be represented as in Figure 1.2, showing a rotor with a disk area A where the velocity equals the induced velocity $V_A = V_i$. The rotor is represented as an actuator disk across which a pressure difference exists.

Far upstream of the disk, in a section denoted as 0, the velocity is negligibly small, so that we can set: $V_0 = 0$. Sections 1 and 2 are located respectively slightly above and below the rotor disk, so that $A_1 = A_2 = A$. Finally, far downstream, at ∞, the velocity is $V_\infty = w$.

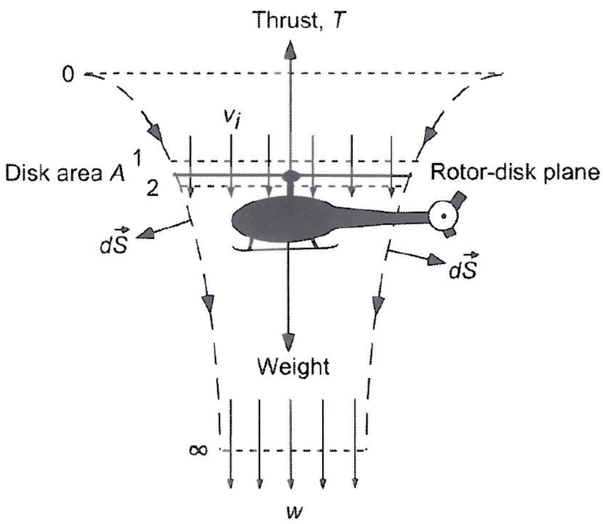

Figure 1.2: Momentum theory in hover, from [83]

Mass conservation applied to sections 2 and ∞ of Figure 1.2 gives:

$$\dot{m} = \iint_2 \rho \vec{V} \cdot d\vec{S} = \iint_\infty \rho \vec{V} \cdot d\vec{S} \tag{1.2}$$

For incompressible flow, the mass conservation equation becomes:

$$\dot{m} = \rho A_\infty w = \rho A_2 v_i = \rho A v_i \tag{1.3}$$

Momentum conservation between inlet and outlet sections provides rotor thrust T:

$$T = \iint_\infty \rho(\vec{V} \cdot d\vec{S})\vec{V} - \iint_0 \rho(\vec{V} \cdot d\vec{S})\vec{V} \tag{1.4}$$

Since the velocity at the far upstream position is 0 in hover, rotor thrust may be expressed by the acceleration given to the mass of the fluid:

$$T = \iint_\infty \rho(\vec{V} \cdot d\vec{S})\vec{V} = \dot{m}w \tag{1.5}$$

Finally, energy conservation allows for computing the power consumed by the rotor, being equal to the change in kinetic energy per unit time:

$$Tv_i = \iint_\infty \frac{1}{2}\rho(\vec{V} \cdot d\vec{S})\vec{V}^2 - \iint_0 \frac{1}{2}\rho(\vec{V} \cdot d\vec{S})\vec{V}^2 \tag{1.6}$$

Since the flow velocity is 0 at the far upstream position, this reduces to:

$$Tv_i = \iint_{\infty} \frac{1}{2}\rho(\vec{V}\cdot d\vec{S})\vec{V}^2 = \frac{1}{2}\dot{m}w^2 \tag{1.7}$$

Now combining 1.5 and 1.7 gives:

$$w = 2v_i \tag{1.8}$$

This derivation may be used to compute the theoretical wake contraction ratio from the mass conservation law 1.3.

$$\dot{m} = \rho A v_i = \rho A_\infty w = 2\rho A_\infty v_i \longrightarrow \frac{A_\infty}{A} = \frac{1}{2} \longrightarrow r_\infty = \frac{R}{\sqrt{2}} \tag{1.9}$$

Experimental results demonstrate that the theoretical wake contraction factor of 0.707 is in practice close to 0.78 [83]. This deviation is mainly due to viscous effects which were excluded in this derivation by the hypothesis for an inviscid fluid.

Rotor power is related to the induced velocity on the rotor disk by:

$$T = \dot{m}w = 2\dot{m}v_i = 2(\rho A v_i)v_i = 2\rho A v_i^2 \tag{1.10}$$

Therefore the induced velocity may be expressed as a function of disk loading T/A by:

$$v_i = \sqrt{\frac{T}{2\rho A}} = \sqrt{\left(\frac{T}{A}\right)\frac{1}{2\rho}} \tag{1.11}$$

The power required to hover may be expressed in two ways:

$$P = Tv_i = T\sqrt{\frac{T}{2\rho A}} = \frac{T^{\frac{3}{2}}}{\sqrt{2\rho A}} \tag{1.12}$$

$$= Tv_i = 2\dot{m}v_i^2 = 2(\rho A v_i)v_i^2 = 2\rho A v_i^3 \tag{1.13}$$

It is equal to the power needed to overcome losses due to the induced velocity and is also called induced power. Note that viscous effects were neglected in the preceding formulation. For a real rotor, the total consumed power is the sum of induced power and profile power that incorporates all non-ideal physical effects related to viscosity.

Induced power is minimized when induced velocity is minimized, or when increasing the mass flow through the disk at constant thrust. Therefore, the rotor disk area should be as large as possible for reducing induced power in hover.

Measures for rotor efficiency in hover

To compare hover performance of rotors, various parameters may be included: for example disk area, blade aspect ratio, airfoil section characteristics and rotor tip speed. As comparison by normalization is not possible due to the various dimensions of these parameters, the so-called Figure of Merit (F.M.) is often used as a non-dimensional measure for hover performance. It is defined as an efficiency ratio of ideal to actual power required to hover:

$$F.M. = \frac{P_{\text{ideal}}}{P_{\text{actual}}} = \frac{C_{T_{\text{actual}}}^{3/2}}{\sqrt{2}C_{P_{\text{actual}}}} \tag{1.14}$$

With rotor thrust coefficient C_T defined as:

$$C_T = \frac{T}{\rho A V_{\mathrm{tip}}^2} = \frac{T}{\rho A \Omega^2 R^2} \tag{1.15}$$

And rotor power coefficient C_P consisting of induced and profile power expressed as:

$$C_P = \frac{P}{\rho A V_{\mathrm{tip}}^3} = \frac{P}{\rho A \Omega^3 R^3} \tag{1.16}$$

In ideal power, only induced power losses are accounted. In practice, profile power losses reduce the F.M. to a typical maximum value ranging between 0.7 and 0.8. At low rotor thrust, profile power is relatively large compared to induced power and the F.M. is low. Increasing the rotor thrust coefficient C_T makes that the induced power increases faster than profile power, and F.M. increases. Maximum F.M. is attained when profile power rises faster than induced power with increasing thrust, which is generally the case when blade stall starts to occur. The relation between thrust and F.M. makes that F.M. can be compared only for rotors having a similar disk loading T/A.

Another measure for comparing rotor hover performance is the power consumed by the rotor at a fixed rotor lift force. This criterion is specifically useful for industrial application since it represents the required power to maintain a certain mass in hover flight. The goal of rotor blade design is to minimize power required to maintain a given weight in hover, i.e. the power required for a given lift. Lift is usually denoted by coefficient $\bar{Z}$ and is defined as:

$$\bar{Z} = \frac{100 F_z}{\frac{1}{2}\rho b \bar{c} R V_{\mathrm{tip}}^2} \tag{1.17}$$

where F_z is the rotor lift, b the number of blades, $\bar{c}$ the mean aerodynamic chord and V_{tip} the velocity at the blade tip due to rotation. $\bar{Z}$ should be kept constant when comparing the consumed power of different rotors.

While not being based on the same formulation, the F.M. and power consumption at a fixed rotor lift may both be used as measures for hover performance. In both cases, comparisons of rotor performance are made for a fixed amount of lift.

1.1.2 Rotor aerodynamics in forward flight

Whereas in hover the only function of the rotor is lift generation, in forward flight it also has to provide a propulsive force. To this end, the rotor is slightly tilted forward, so that the flow enters the rotor disk at a certain angle-of-attack. The flow is no longer axi-symmetric, since the local relative velocity over a blade section now equals to the sum of rotational velocity, induced velocity and forward flight velocity. Induced velocity is in the order of 0 to 8 m/s in forward flight, while forward flight speed is typically 80 m/s and tip speed due to rotation is about 200 m/s, so that the induced velocity can be neglected to a first approximation. Depending on the radial and azimuthal position over the rotor disk, the local velocity follows the distribution of Figure 1.3. The image shows that the local velocity increases on the advancing blade side, as the rotational velocity and forward flight velocity are summed up. The local velocity on the advancing blade thus equals $U + V$. On the retreating side, however, the local velocity as encountered by the leading edge of the blade equals the rotational velocity subtracted by the forward flight component, so that the local velocity equals $U - V$. This means that a reversed flow region exists at the inboard part of the retreating blade over the zone where the contribution of the rotational velocity is larger than the forward flight speed. Figure 1.4 shows the local velocity encountered by blade sections over the rotor disk.

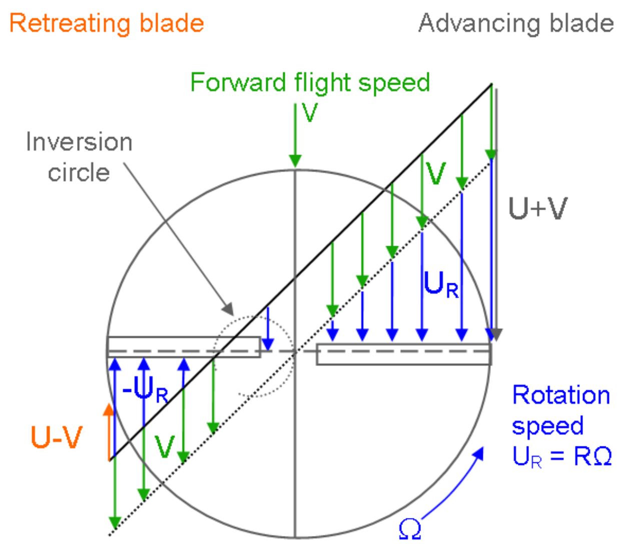

Figure 1.3: Contributions of forward flight and rotational velocity over the rotor disk in forward flight

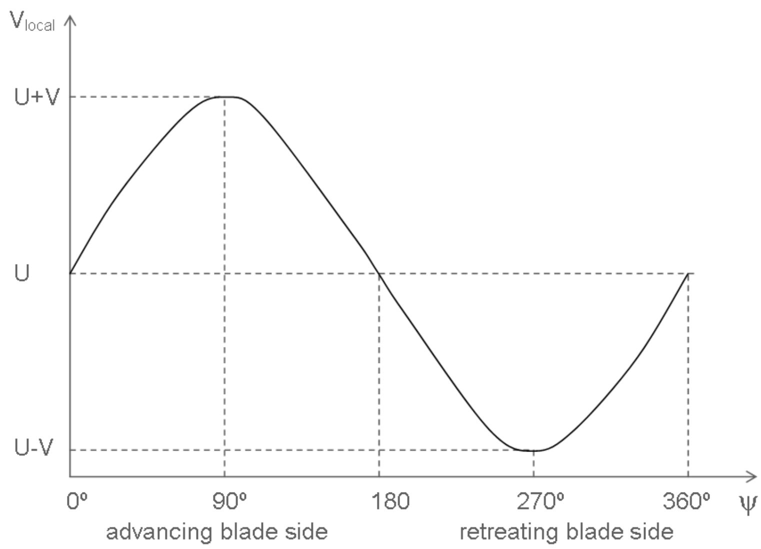

Figure 1.4: Local velocity variation of a blade section in forward flight

Rotor motions

Variations in local velocity over the rotor disk, illustrated by Figure 1.3, lead to faster flow on the advancing blade side than on the retreating blade side. The local velocity difference over one rotor revolution, as seen in Figure 1.4, leads to a lift difference between advancing and retreating blade sides. This lateral lift asymmetry induces a rolling moment on the helicopter. To balance lift and avoid a rolling moment, the pitch angle θ of the blades changes periodically along a rotor revolution. This motion is called feathering.

Lift created over the blade generates a bending moment at the blade root. To avoid huge loads at blade roots, a second axis is released: flapping hinge β. This allows the blade to move up and down within one rotor revolution under the effect of rotor lift and centrifugal forces. The lever of the bending moment passes close to or through the blade attachment, thereby reducing the bending moment at the blade root.

Due to gyroscopic effects, the flapping motion has a nearly 90° delay with respect to lift variation. The combination of flapping and pitching motions of the rotor blade are illustrated in Figure 1.5.

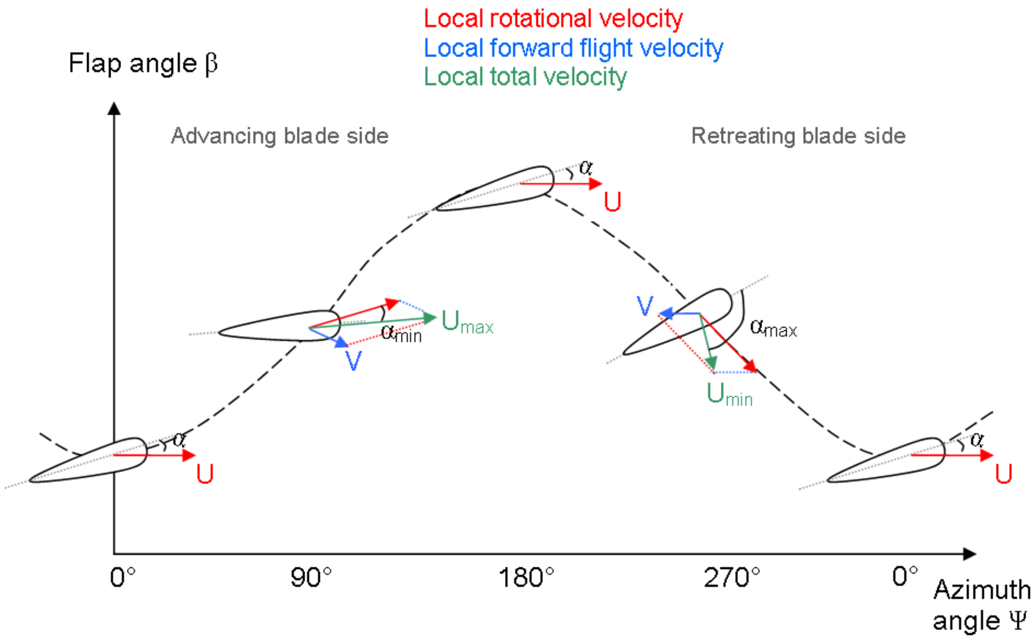

Figure 1.5: Flapping and pichting motions of a blade section in forward flight

Flapping of the rotor blade makes that the local radius of the blade sections changes over a rotor revolution, as may be seen in Figure 1.6. Flapping motion combined with blade rotation induces Coriolis forces that periodically accelerate and decelerate the blade. This phenomenon is called lead-lag motion. To alleviate the blade root from the in-plane stresses, a lead-lag axis δ is introduced. As the lead-lag motion may be unstable, a damper is added on this axis.

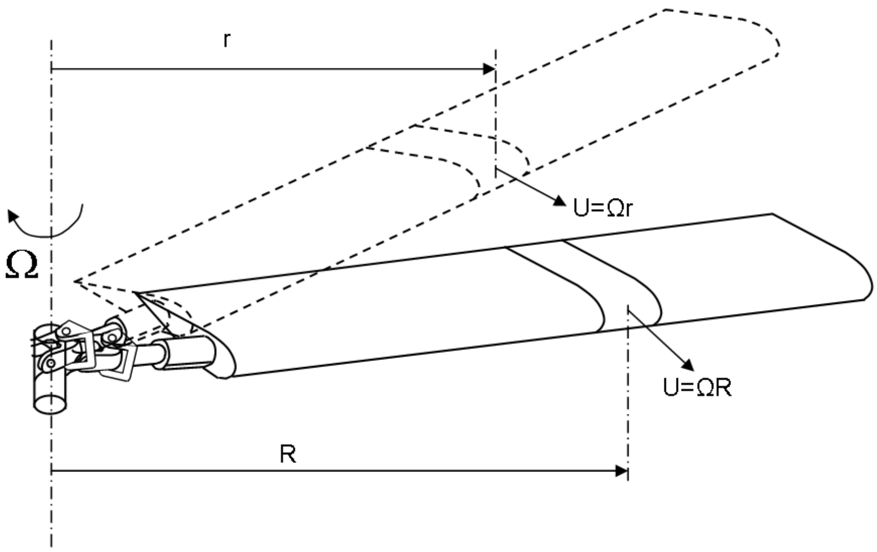

Figure 1.6: Local radius change due to blade flapping (exaggerated angles)

Required pitch, flap and lead-lag motions are set free by the three axes that are illustrated in Figure 1.7. In steady forward flight, blades now can pitch, flap and lag as required for the equilibrium position of the rotor. This equilibrium position is also called a rotor trim. Cyclic variations of pitch, flapping and lead-lag angles may be expressed in harmonics. Table 1.1 gives an example of the amplitude of the 0^{th} (collective value) and 1^{st} rotor harmonics (cosine and sine terms, respectively longitudinal and lateral variations). These values correspond to a EC155 helicopter at 280 km/h forward flight speed.

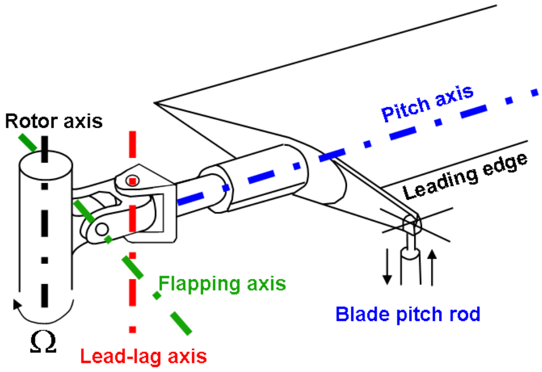

Figure 1.7: Pitch, flap and lead-lag axes

Table 1.1: Example of rotor harmonics at blade root for a EC155 rotor at 280 km/h (150 kts) in steady forward flight, as computed by HOST

	collective	lateral	longitudinal
pitch	6.5°	5.5°	−11.5°
flapping	−2.5°	−2.5°	−0.5°
lead-lag	−3.0°	0.5°	−0.1°

Measures for rotor efficiency in forward flight

As was the case for measuring hover performance, power required by the rotor may be used as a measure for comparing drag created by the rotor. As in the hover case, this comparison is only valid for rotors that generate the same amount of lift and at similar flight conditions.

A way to measure rotor lift and drag simultaneously is the Lift-to-Drag ratio L/D that is defined as [83]:

$$\frac{L}{D} = \frac{T\cos\alpha_{\text{TPP}}}{(P_i + P_p)/V_\infty} \approx \frac{WV_\infty}{P_i + P_p} \tag{1.18}$$

where TPP is the Tip Path Plane: the plane formed by the blade tips. As typically the inclination of the tip path plane is small, the $T\cos\alpha_{\text{TPP}}$ term may be replaced by the helicopter weight W in stabilized forward flight.

The drag term of the rotor is expressed in terms of required rotor power, which equals the sum of induced power P_i and profile power P_p. The power consumed by the rotor decreases when accelerating out of hover thanks to the reduction of induced power, which is a function of induced velocity. Minimum power consumption is achieved at approximately 120 to 150 km/h ($\mu \approx$ 0.1-0.2), then profile power starts to increase. From $\mu > 0.3$ on, power losses due to the reversed flow region on the root of the retreating blade and compressibility effects on the tip of the advancing blade increase required power. These aerodynamic phenomena that occur more specifically in forward flight will be detailed in the next section.

Another way to express rotor performance in forward flight is the power consumed by the rotor to overcome rotor torque. This measure is well adapted for industrial application, as rotor performance can be compared to available power.

1.1.3 Description of relevant flow phenomena

The flow field around a helicopter exhibits very complex features: in hover, the wake structure and tip vortex released by a blade remain close to the rotor and interact with other blades, leading to flow inhomogeneity and unsteadiness. In forward flight, besides blade-wake interactions, flow inhomogeneities are introduced by periodic changes of relative velocity, as explained in the previous section. The main aerodynamic phenomena characterizing helicopter rotors in forward flight are illustrated in Figure 1.8. In the following of this section, we focus on some of the most important flow features impacting on rotor performance.

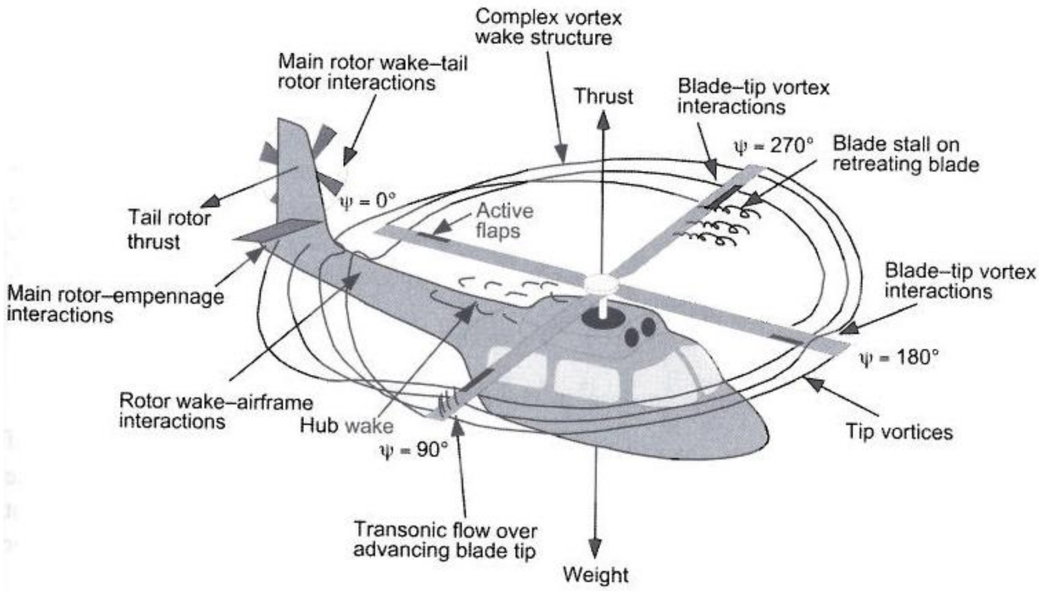

Figure 1.8: Typical flow structure and aerodynamic problems of a helicopter in forward flight, from [83]

Wake structure

Both in hover and in forward flight, local aerodynamic characteristics of each blade are affected by the wake structure created by preceding rotor blades. This lift induced wake is modified by each blade passing by, creating a complex structure, as illustrated in Figure 1.9 for the relatively simple case of a rotor in hover.

In hover, the induced velocity creates a downwards velocity in the order of 10 to 15 m/s. As the wake structure is shed away from the rotor by this induced velocity only, it affects the rotor flow for multiple blade passages. In forward flight, the vertical component of the induced velocity is in the order-magnitude of about 0 to 8 m/s and has a lower influence in the way the wake is shed away from the rotor plane. But, the wake is deviated from the rotor by the forward flight velocity. This forward flight velocity having a higher value than the induced velocity in hover, the wake is shed away more quickly with increasing forward flight speed.

Besides the wake structure over the complete rotor, tip vortices have a particular impact on rotor aerodynamics. Their intensity is directly related to blade loading of which approximate analytical relations are given, obtained from test measurements [30]. However, strong mutual effects between blade loading and tip vortex circulation make prediction of tip vortex strength

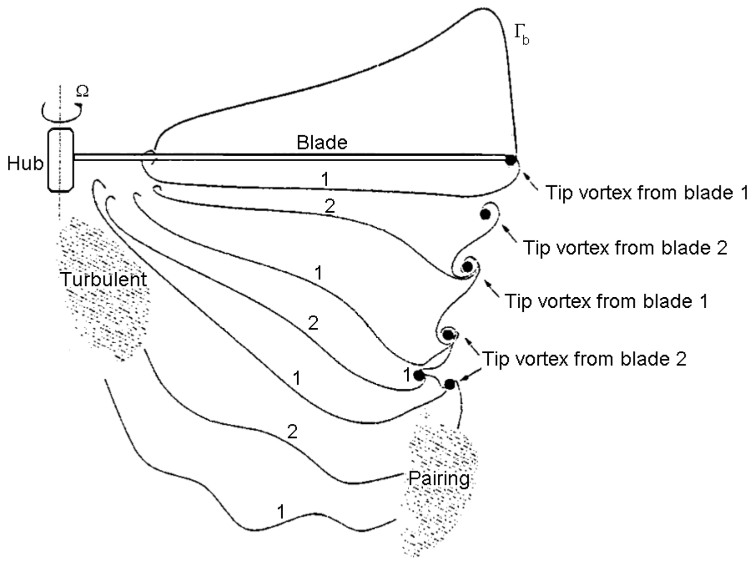

Figure 1.9: Schematic wake structure beneath a 2-bladed rotor in hover, from [90]

and size difficult, even in hover. Tip vortex formation mechanisms are not yet completely understood. Additional difficulties are due to the turbulent diffusion of the vortex [65]. Recent experimental efforts to quantify turbulence of the tip vortex core and its surroundings will help in improving general understanding of formation and decay of the tip vortex [113]. Finally, roll-up and decay of the vortex need to be predicted. The vortex will dissipate and diffuse, but even if analytical prediction of tip vortex decay in hover exist [30], these will not hold in forward flight. Moreover, even if the decay could be predicted accurately, as long as the initial state of decay is not computed correctly, decay will be erroneous as well.

Tip vortices stay close to the rotor during several blade passages. Thereby, they influence the flow field in the tip zone in hover, and may interact all along the span with all other rotor blades at various positions in forward flight. Blade-vortex interaction is highly three-dimensional and time-varying [30].

The wake structure and tip vortices may interact with various other components of the helicopter such as the fuselage and rear parts. These interactions may, amongst others, cause vibrations and modification of control of the helicopter. For this reason, quick dissipation of the wake structure is desirable.

Boundary layer transition

Typical Reynolds numbers over helicopter rotors based on blade chord are about $5 \cdot 10^6$ to $1 \cdot 10^7$. At these Reynolds numbers, the boundary layer transitions from laminar to turbulent flow somewhere over the airfoil. The state of the boundary layer affects skin friction drag, but also stall characteristics and flow separation [83, 93].

On helicopter rotors, various mechanisms of transition may occur, as described in [20, 51]. These may be quite different from 2D mechanisms mainly due to centrifugal forces, hysteresis effects of dynamic stall and turbulence of incoming flow. Also note that surface roughness of blades is not known and may change during flight.

Measurements of transition position [37, 93, 116] allow studying the effect of several parameters, such as rotational velocity and rotor thrust. A general conclusion is that many factors interfere, making transition prediction difficult. Due to the complexity of the problem, fully turbulent flow will be assumed in the following of this work.

Advancing blade in forward flight

In forward flight, rotational and forward flight velocity are summed up over the advancing blade. At the blade tip, where the contribution of the rotational velocity is highest, transonic flow may appear from typically a μ of 0.3 on, in the region illustrated in Figure 1.10.

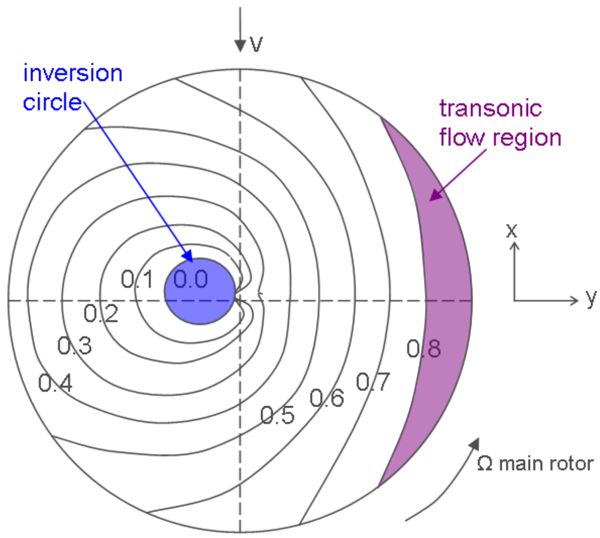

Figure 1.10: Iso-Mach lines over the rotor, as a function of rotational and forward flight velocity

The transonic region is defined as the zone where critical Mach number M_{crit} is attained, meaning supersonic flow occurs locally over the airfoil section. The shock that terminates the supersonic region will lead to wave drag and increased skin friction drag due to interaction between the shock wave and boundary layer [83]. A strong shock implies a high adverse pressure gradient that may cause shock induced stall, which is another reason for drag increase.

Rapid increase of drag for a small Mach number increase occurs from drag divergence Mach number M_{dd} on. It is often defined as the Mach number for which $dC_d/dM_\infty > 0.1$ [83]. As M_{dd} is a function of angle-of-attack and relative thickness of the airfoil, power losses may be limited by using thin airfoils that have a higher M_{dd} over the blade tip. Also, blade sweep may be applied to reduce the local effective Mach number, given by: $M_{\text{eff}} = M \cdot \cos\Lambda$ with Λ the sweep angle.

Retreating blade in forward flight

On the retreating blade in forward flight, the local velocity seen by the blade equals rotational velocity subtracted from forward flight velocity. In the region where forward flight velocity is larger than the local contribution of rotational velocity, reversed flow occurs. This region is called the inversion circle, as shown in Figure 1.10. The size of this circle $r_{\text{inversion circle}}$ increases with advance parameter μ and is related to the azimuth position over the rotor disk ψ as given by [83]:

$$r_{\text{inversion cicle}} = -\mu \sin\psi \tag{1.19}$$

As seen in Figure 1.10, maximum radius of the inversion circle is attained at the retreating blade, at $\psi = 270°$ so that the circle has a radius equal to μR. Thus, for $\mu = 0.3$, 30% of the retreating blade has reversed flow. The airfoil may not be adapted for this specific flow configuration of airflow coming from the trailing edge. A solution may be the use of airfoils that have acceptable characteristics in reversed flow, for example such as patented in [38].

Over the retreating blade, the local velocity is lower than over the advancing blade. Yet, the same amount of lift needs to be created over the two halves of the rotor disk. As detailed in 1.1.2, the lift difference over advancing and retreating blade sides is balanced by a pitch motion of the blade over a blade revolution. Since the local velocity over the retreating blade is low, the angle-of-attack is here increased to create sufficient lift. The relatively quick increase to a high angle-of-attack may, however, lead to dynamic stall over the outer part of the blade. The effect of dynamic stall is twofold: the lift coefficient increases to a value beyond the static $C_{l_{\max}}$, but reduces during the backstroke to a lower value by a hysteris-effect, as illustrated by the lift coefficient curve in Figure 1.11. In addition, a large nose-down pitching moment is created during dynamic stall, see Figure 1.11. These loads and vibrations may lead to fatigue and may exceed the limits of the rotor or control system [83].

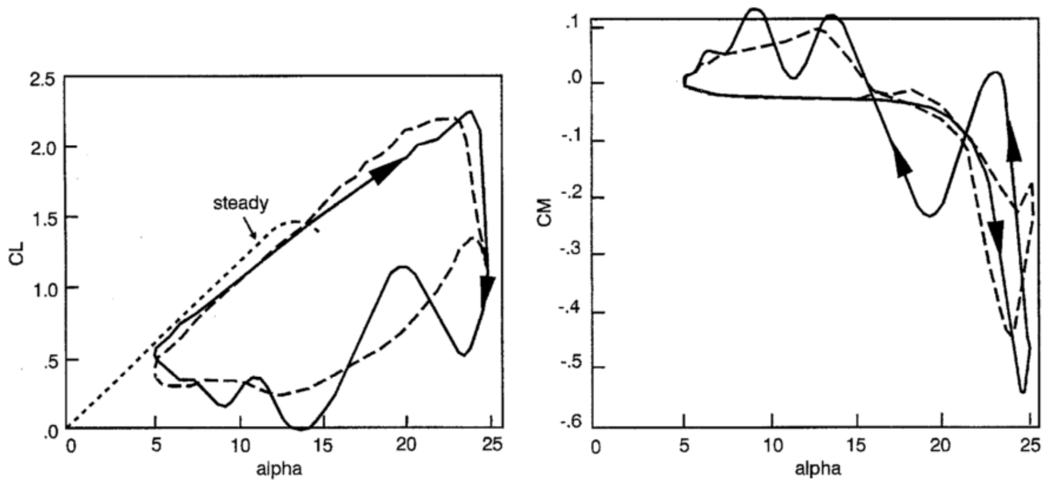

Figure 1.11: Lift and moment coefficients as a function of angle-of-attack for dynamic stall of a NACA0012 airfoil, — calculations, - - - measurements, from [149]

Blade vortex interaction

In low-speed, slightly descending flight, the wake field remains close to the rotor. In this flight attitude, tip vortices have a higher probability to interact with a succeeding blade in a phenomenon called Blade Vortex Interaction (BVI). This phenomenon is related to the impulsive change of angle-of-attack and blade loading when a tip vortex hits a succeeding blade over a larger portion of the blade at the same moment. The sudden change of incoming flow leads to a highly directional, typical BVI-noise [83]. Its noise level is a function of vortex strength, distance between blade and vortex as well as the length of the blade that is involved instantly. BVI may occur at any position over the rotor disk, as illustrated in Figure 1.12.

BVI noise is particularly problematic since it occurs mainly for flight conditions that coincide with those of the approach phase, so that it has a high impact on helicopter acceptance near landing sites. In addition, these flight conditions are part of the noise certification spectrum so that BVI reduction is a blade design goal. Nonetheless, limiting the noise level by changing the strength of tip vortices is difficult as this is directly related to blade loading and thus to rotor lift. The distance between vortex and blade depends on the forward flight speed and descent rate and alternative flight procedures may help in reducing the probability of blade-vortex interaction. Creating variations of the lift force by active control techniques may help in reducing the probability of interaction [63]. The last available parameter, the blade length involved in the interaction, may be reduced by using a sweep law, as will be demonstrated in section 1.2.4.

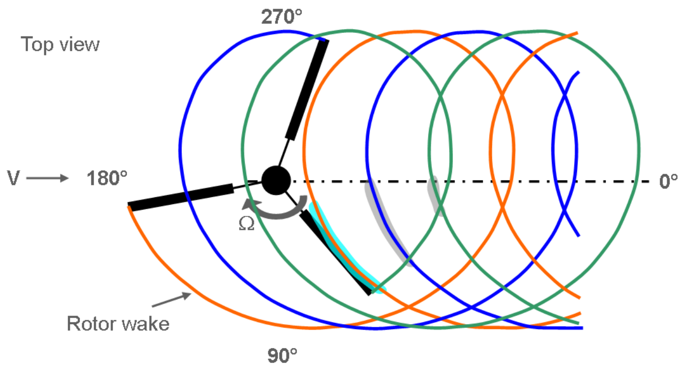

Figure 1.12: Blade Vortex Interaction

1.2 Rotor blade geometry

A typical helicopter rotor blade is a straight, high aspect ratio wing with one or multiple airfoils and a twist variation along the blade. An example of a blade and the coordinate system typically used is given in Figure 1.13. The design of the blade root is not considered in the present work for two reasons:

1. Blade root design is not limited to aerodynamic requirements since for structural reasons a thick section is needed for supporting blade loads at the blade attachment. In particular this part of the blade needs to be designed in cooperation with structure engineers.

2. Interaction of the rotor head wake with the rear rotor and stabilizers, and the possible reingestion of the engine exhaust, make that the blade root section needs to be designed while accounting for integration onto the helicopter. This physically and computationally complex problem is not yet sufficiently mature for automatic optimization.

The outer 5 to 10% of the other blade end, the blade tip, is not considered either in the optimization process:

1. The tip section encounters largely varying flow conditions over one rotor rotation in forward flight so that design robustness is of great importance.

2. Complex aerodynamic phenomena such as dynamic stall and transonic flow separation may occur in highly three-dimensional flow conditions. As for the blade root, physically and computationally complexity does not yet allow for automatic design.

In the following description of geometrical shape of a rotor blade, the main portion of the blade is explored. Influence on rotor performance of each of the geometrical parameters, being airfoil placement, chord, twist, sweep and dihedral, will be described. Then, two sections are devoted to examples of rotor blade geometries. The first will illustrate practical examples of geometry laws. These examples are mainly based on patents as industrially sensitive information of blade geometries is rarely given in other publications. The second part is a presentation of the ORPHEE blade optimization project carried out at Eurocopter.

1.2.1 Influence of airfoil placement

As the flow around the wing of a fixed-wing aircraft is nearly constant for the largest part of a typical flight, design conditions for airfoils used along the wing may be relatively easy to establish. On the contrary, flight conditions encountered by a rotor blade vary largely between

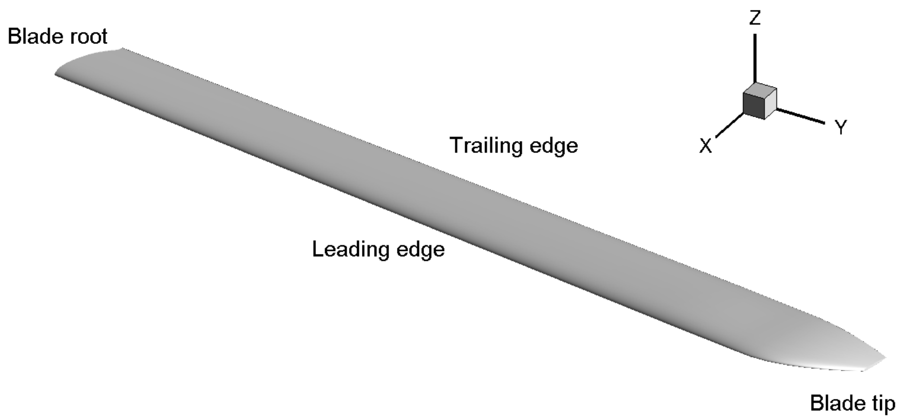

Figure 1.13: Typical shape of a rotor blade

hover and forward flight as well as along a rotor revolution in forward flight. Variations of operating conditions are illustrated by Figure 1.14, showing a typical fluctuation of the local Mach number and lift coefficient as seen by a blade section over one rotor rotation. Boundaries indicate typical rotor limits in forward flight: dynamic stall on the retreating blade and shock induced stall on the advancing blade side.

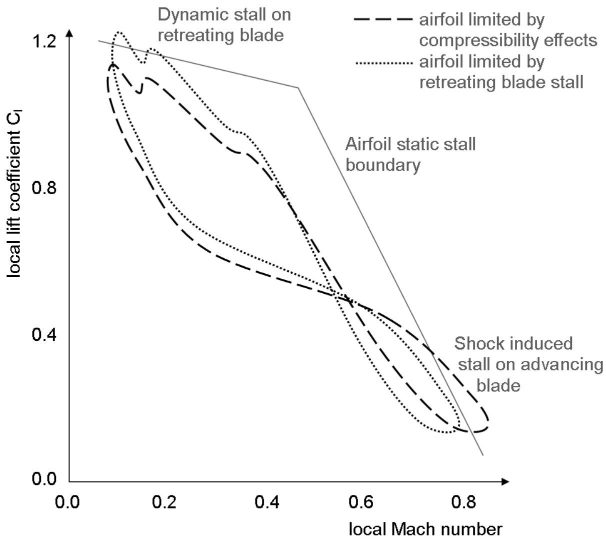

Figure 1.14: Operating conditions of an airfoil in terms of Mach number and angle-of-attack, from [83]

Variations in operating conditions met by airfoil sections over one rotor rotation may be summarized by the following typical values:

- Reynolds number: $5 \cdot 10^6 < Re < 1 \cdot 10^7$
- Mach number: $-0.2 < M < 0.9$
- Angle-of-attack $-5° < \alpha < 15°$

Due to these fluctuations, robustness represents a crucial issue for rotor design and airfoils used on helicopter rotors have characteristics that vary from those designed for fixed-wing aircraft. Typical design requirements for helicopter rotor airfoils are [83]:

1. High maximum lift coefficient $C_{l_{\max}}$ to provide sufficient lift, even in demanding flight conditions (high load factor, high rotor thrust)

2. High drag divergence Mach number M_{dd}, allowing for high speed forward flight without excessive power and noise increase

3. Good lift-to-drag ratio L/D over a large range of Mach numbers to assure good performance for typical flight conditions

4. Low pitching moment C_{m0} to minimize blade torsion moments and pitch link loads

Airfoils used at Eurocopter generally belong to the so-called OA-airfoil family resulting from collaboration between ONERA and Aerospatiale (former name of Eurocopter France). The OA2 airfoil family dates back to the '80's and include the 13% thickness OA213 airfoil as well as the OA209 and OA207 of 9 and 7% relative thickness, respectively. Newer airfoils include the OA3 and OA4 families that were conceived in the '90's.

Lift, drag and moment coefficients of the OA213 airfoil are given in Figure 1.15.

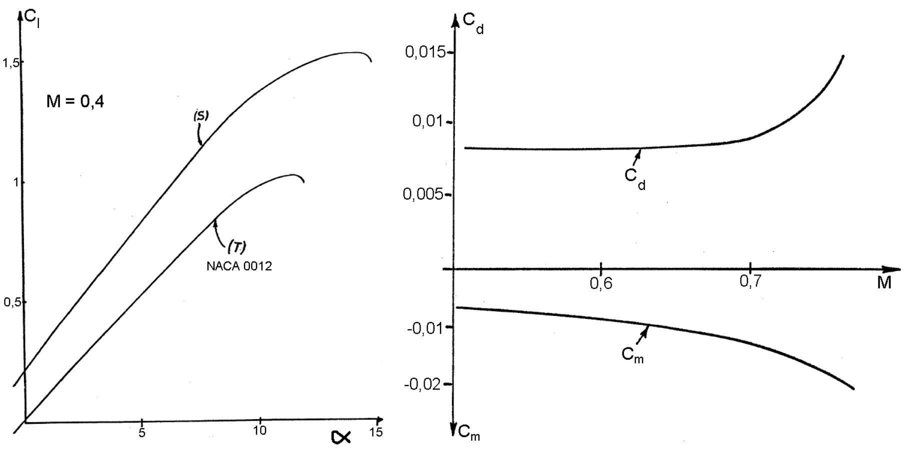

Figure 1.15: Lift, drag and moment coefficients as a function of angle-of-attack of the OA213 airfoil [133]

The effect of airfoil performance on rotor performance in hover and forward flight is often expressed by airfoil equivalent performance metrics: the airfoil Figure of Merit $F.M._{\text{airfoil}}$ and airfoil Lift-to-Drag ratio L/D_{airfoil}. These are defined by:

$$F.M._{\text{airfoil}} = \sqrt{\frac{C_l^3}{C_d^2}} \tag{1.20}$$

$$L/D_{\text{airfoil}} = \frac{C_l}{C_d} \tag{1.21}$$

Typical values of $F.M._{\text{airfoil}}$ for a helicopter rotor airfoil are between 0 and 120. An example of a distribution of L/D_{airfoil} as a function of Mach number and angle-of-attack α is presented in Figure 1.16, showing its large variations according to flight conditions.

It may be demonstrated by derivation of $F.M._{\text{rotor}}$ to $\bar{Z}$ that theoretically $F.M._{\text{rotor}}$ is maximized if for each blade section $F.M._{\text{airfoil}}$ is maximal. However, a helicopter rotor is designed for both hover and forward flight; since L/D_{airfoil} changes over a rotor revolution, it is difficult to establish a unique optimal distribution of airfoil sections maximizing performance for all conditions.

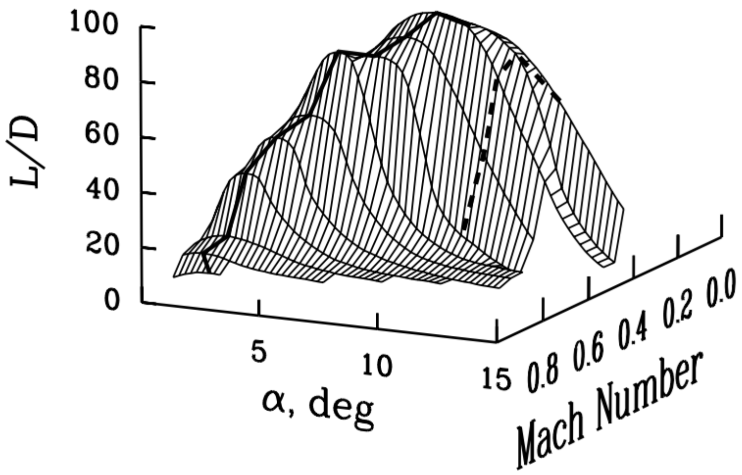

Figure 1.16: L/D of the SC1095 airfoil as measured for typical flight conditions as a function of Mach number and angle-of-attack [33]

The only general criterion of airfoil placement is that the thickness distribution along the blade is related to the local velocity seen by blade sections. For example, the inboard part is characterized by low local velocity, both in hover and in forward flight. As a consequence, thick airfoils (typically 12 or 13%) are preferred to create lift without too high drag. On the outboard part, typically from 0.7 to 0.8R, the 12-13% thick airfoil transitions towards a 7-9% airfoil on the blade tip. Low blade thickness reduces wave drag for high speed conditions encountered on the advancing side in forward flight. In addition, so-called thickness noise, which is a function of absolute sectional thickness and local velocity, is reduced by limiting the relative airfoil thickness near the blade tip. Airfoil placement along the blade is thus a compromise between sectional performances and potential aerodynamic problems that may occur.

1.2.2 Influence of twist law

Momentum theory shows that induced power in hover is minimum when the induced velocity distribution is constant along the blade [121]. Since local velocity depends on the radial position by a quadratic function, a constant lift distribution and thus constant induced velocity is obtained by a hyperbolic twist law.

Unfortunately, this hyperbolic ideal twist law for hover does not work well in high-speed forward flight as high twist angles are not favourable for the high local velocity on the advancing blade side. A high twist angle would especially be problematic at the blade tip of the advancing blade, where the drag coefficient is very sensitive to local angle-of-attack. A small increase of the angle-of-attack may lead to a strong increase of drag as the airfoil drag bucket is much reduced at high velocity. Therefore, the twist angle at the blade tip that is optimized for forward flight is often directly related to flight conditions on the advancing side.

Even more, in forward flight, the main part of the blade encounters different flight conditions and an optimized twist law is a compromise of all these positions.

So, even if an ideal twist law may be determined for hover flight conditions, this hover solution needs to be adapted to avoid typical aerodynamic problems in forward flight, especially on the advancing blade side. A compromise solution respecting as much as possible the hyperbolic law, while avoiding high drag in forward flight, needs to be found. In practise, often linear twist laws are used for simplicity of production, while approaching the hyperbolic law over a large part of the blade.

1.2.3 Influence of chord law

According to momentum theory, optimum rotor hover performance is obtained with a constant induced velocity distribution. Following the same reasoning as for the ideal twist law, the theoretically optimum chord distribution along a non-twisted blade in hover is a hyperbolic taper law, as illustrated in Figure 1.17.

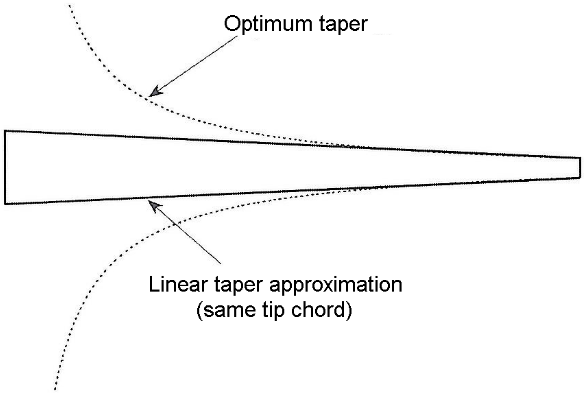

Figure 1.17: Optimum taper distribution, from [83]

As was discussed in section 1.1.3, in forward flight, both blade ends are limited in their aerodynamic performance by typical rotor phenomena. The main blade part is less affected by these phenomena so that it is most efficient for improving rotor performance.

This lift force may be expressed in terms of locally attained lift coefficient and Mach number $C_l M^2$ while drag, or power losses, may be given as $C_d M^3$, based on the local airfoil drag coefficient. Regions over the rotor disk where lift is created efficiently and where power is lost are illustrated in Figure 1.18. It shows a HOST computation (see section 2.1) of created lift and required power over the rotor disk of an EC1 rotor blade (see section 1.2.6) at a forward flight speed of 315 km/h.

It may be seen that the lift is created over the main part of the blade, excluding the blade root and tip from efficient lift creation. Additionally, these outer sections require a large part of rotor power as illustrated by $C_d M^3$. In conclusion, to optimize overall rotor performance at high speed forward flight, the chord of both blade ends should be reduced as much as possible. The importance of this requirement increases with the advance parameter, as power required increases with M^3 on the advancing blade tip and the size of the inversed flow circle on the retreating blade increases.

This theoretical explication is confirmed by numerical simulations as performed in [148] in which a rectangular blade is compared to blades with 6:1, 4:1 and 3:1 taper ratios with different initial taper positions. These blades are illustrated in 1.19. The study shows that lowest required power to hover is found for highest taper (blade iv).

While taper at the blade tip is beneficial for both flight conditions, this is not the case for the blade root where hover and forward flight demands are contrary. A compromise solution needs to be found to augment hover performance while meeting acceptable aerodynamic properties in forward flight.

1.2.4 Additional effects: dihedral and sweep angles

As discussed in Section 1.1.3, the tip section encounters different flow conditions according to its azimuthal position and to the specific flight case. The importance of tip vortices has been illustrated in the discussion of BVI noise but their influence on rotor performance is not limited to noise: the wake structure affects the whole flow field.

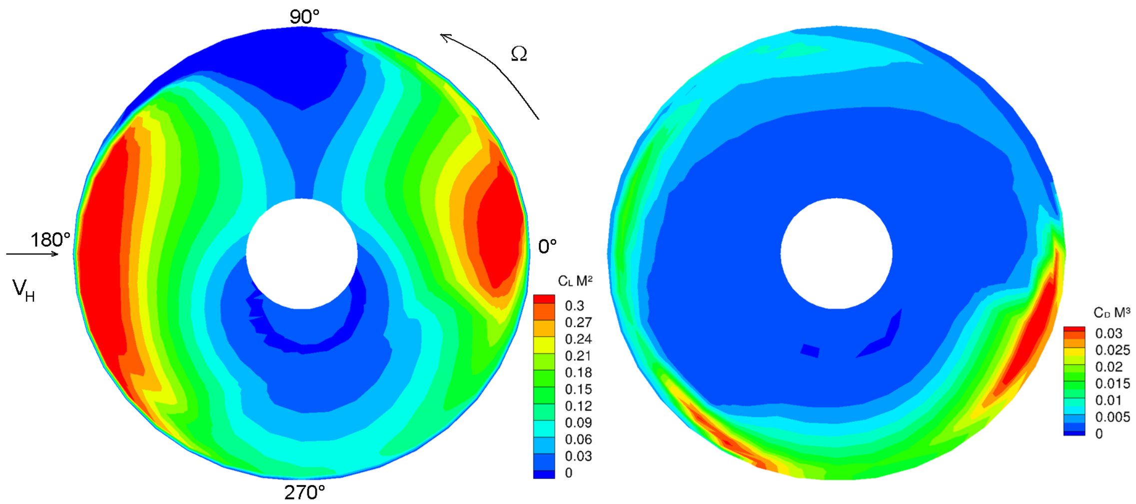

Figure 1.18: Representation of the lift force (left) and power required (right) over the rotor disk for an EC1 rotor at $\mu = 0.417$, $V_H = 315$ km/h, $\bar{Z} = 20$ as computed with HOST

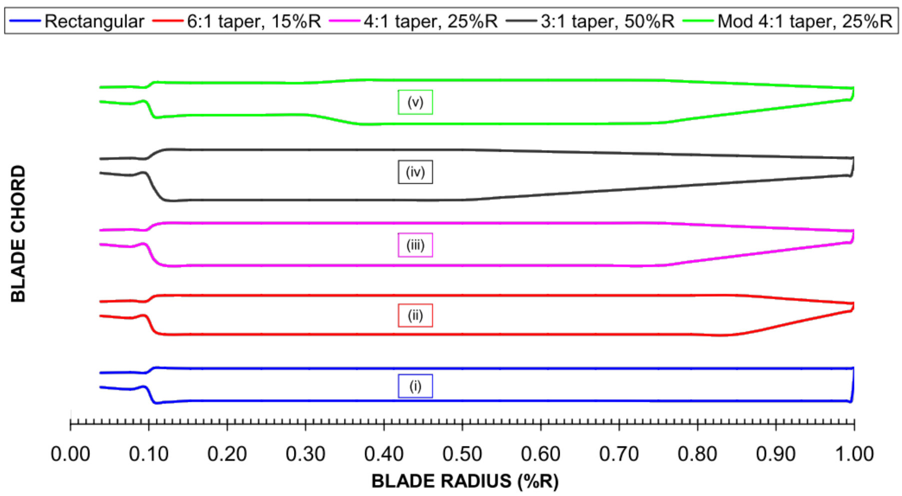

Figure 1.19: Chord laws as used for assessing the effect of taper in [148]

Requirements on blade tip design are numerous because of large variations of local aerodynamic properties such as velocity and angle-of-attack. As seen in previous Sections, the choice of twist angle at the blade tip mainly depends on local flow characteristics on the advancing blade side in forward flight. Blade tapering is beneficial both in hover and in forward flight. In addition to these geometrical parameters, the tip may have dihedral and sweep angles.

For fixed-wing aircraft, dihedral may be increased at the wing tip to reduce local recirculation. This device is called a winglet. For rotorcraft, a winglet would lead to prohibitive drag since the blade also passes in front and aft positions, where the wing tip has a frontal exposition with respect to the incoming airflow. On helicopter blades, a small dihedral angle is applied at rotor tips to deflect the tip vortex downwards. Thanks to this dihedral angle, the tip vortex has a smaller impact on performance of following blades.

Sweep is applied on the blade tip to reduce the effective Mach number encountered on the advancing blade side in forward flight to delay onset of compressibility effects. However, rotor performance is not necessarily improved by applying tip sweep, as this may also reduce the angle-of-attack at which stall occurs on the retreating blade side [83]. This illustrates how delicate the design of a rotor blade tip is.

The design of a rotor blade tip is difficult due to the high impact of small geometrical changes. In addition, this impact might be the contrary of that expected theoretically, as the sweep example showed. Besides today's limited comprehension in blade tip design, simulation of this zone is particularly delicate: comprehensive rotor codes do not account for local three-dimensional effects and are immediately rejected. Simulation by Computational Fluid Dynamics (CFD) requires fine meshes in the tip region, accurate evaluation of the blade loading all over the blade for correct estimation of the tip vortex size and strength, a rotating frame for the transverse flow components, dynamic stall simulation, etcetera. This extremely accurate simulation is time-consuming and not yet suitable for optimization purposes. Therefore, the design optimization blade tip section will not be considered in the present study.

1.2.5 Examples of rotor blade designs

A large number of patents concerning the aerodynamic design of rotor blades exists. The present section is not meant to list all of them but rather to highlight a few recent patents that illustrate previously described design principles.

Twist law

The twist law should have an as high as possible gradient for hover performance, yet this configuration might lead to aerodynamic problems on the advancing side in forward flight.

The patent [144] concerns a twist law optimized for a tiltrotor aircraft that can be compared to one designed for a helicopter rotor in hover: a tiltrotor nearly always operates in flow conditions that can be compared to the hover state of a conventional helicopter rotor. In vertical or hover flight, the tiltrotor is in hover, and once in forward flight, the tiltrotor is completely tilted forward, so that the flow still flows from upstream of the rotor to the downstream position. Only side flow makes the rotor work in a flow condition that deviates from a hover-like state.

The tiltrotor patent shows a twist law that is claimed to lead to a nearly constant lift circulation. Indeed, the twist law has a high gradient of about -25°$/R$ (see Figure 1.20). This approximates the theoretical solution of a hyperbolic twist law that was described in 1.2.2.

Even if this patent is interesting for rotors that operate uniquely in hover-like flow conditions, the design is not suitable for helicopters due to aerodynamic problems that may be expected in forward flight conditions.

Chord law

As stressed in section 1.2.3, a double taper law would be beneficial for rotor performance. This is demonstrated by two patents: Eurocopter's patent [135] of 1996 and the Sikorsky patent [21] of 2005. Both patents, with a slightly different definition, propose a double taper law. The Eurocopter patent fixes the position of maximum chord in the region between 0.65 and 0.85R. The maximum chord is about 1.1 to 1.2 times the mean aerodynamic chord (MAC). The chord is reduced to 0.7 times the MAC at the blade root, and to 0.35 at the blade tip. This is shown in Figure 1.21.

The Sikorsky patent, particularly but not exclusively designed for a co-axial rotor, prescribes a maximum chord region between 0.3-0.4R and 0.75-0.8R. The ratio of root chord to maximum chord ranges between 0.2 and 1.0. This patented definition is illustrated in Figure 1.22.

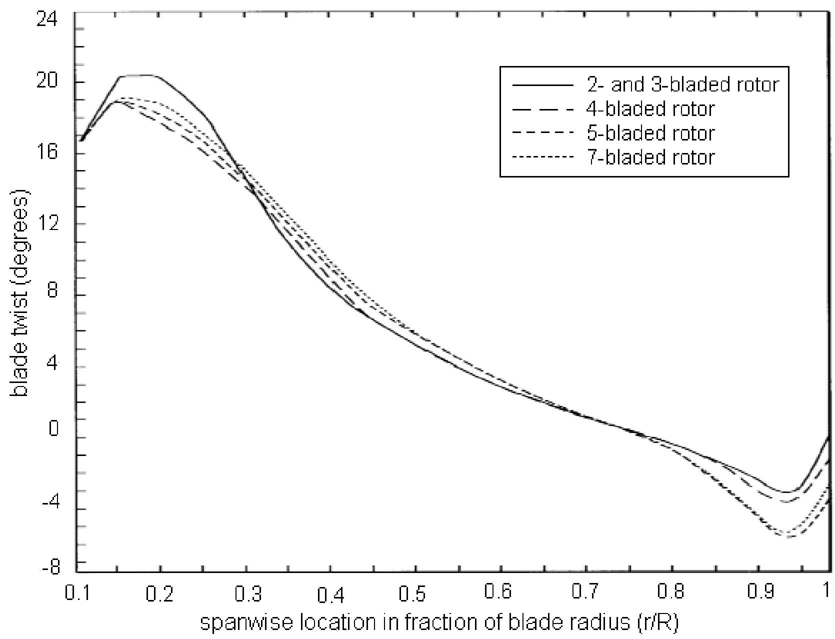

Figure 1.20: Illustration of twist law as patented by [144]

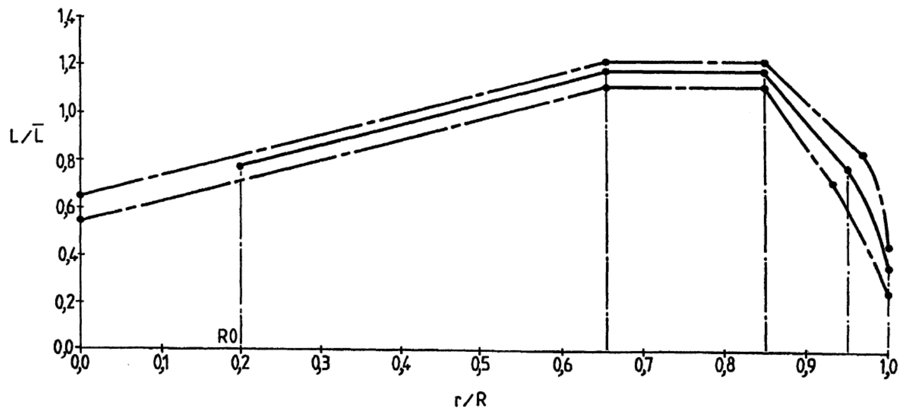

Figure 1.21: Illustration of chord law as patented by [135]

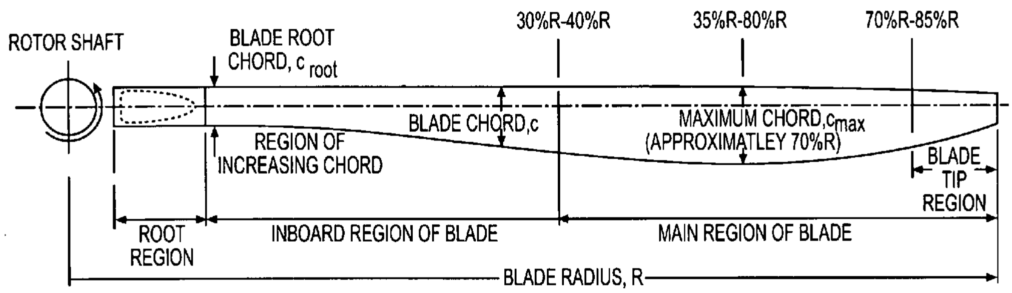

Figure 1.22: Illustration of chord law as patented by [21]

Double sweep blade

A reduction of BVI noise as described in section 1.1.3 may be obtained by using sweep on the outer part of the blade. A high sweep angle reduces the blade length that is in parallel interaction with a tip vortex, thereby modifying one of the parameters acting on BVI noise, leading to a noise level reduction. This is illustrated in Figure 1.23 that may be compared to Figure 1.12.

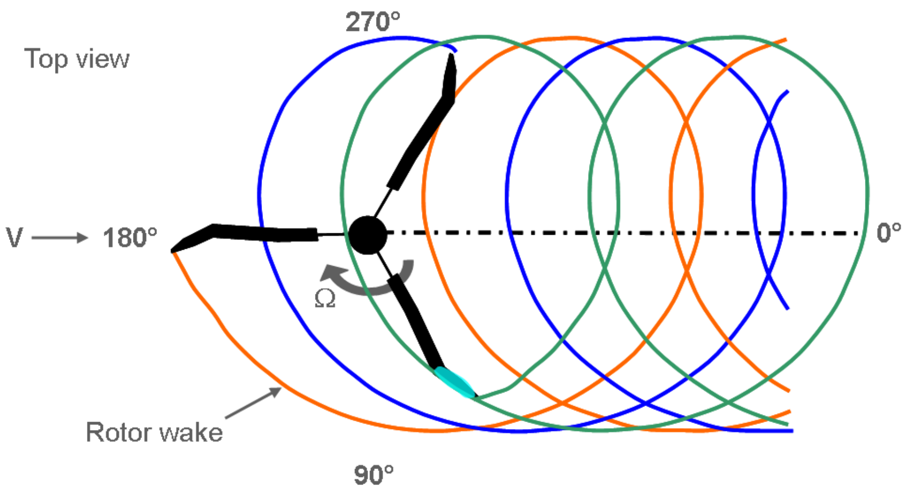

Figure 1.23: Reduction of BVI noise by a double sweep law

The aft sweep section sets back the centre of pressure of the blade. The offset between centre of pressure and pitch axis increases control loads. This may be restored by using forward sweep over a part of the blade so that the overall centre of pressure returns to the blade pitch axis. The combination of forward and aft sweep has lead to the Blue Edge blade that is patented in [57], as illustrated in Figure 1.24.

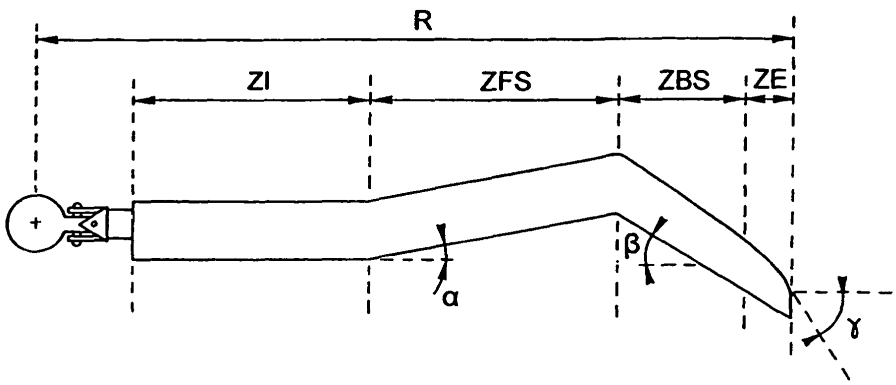

Figure 1.24: Double sweep law as introduced on the Blue Edge blade [57]

BERP blade tip

A rotor blade design that differs from the typical geometry laws described earlier is the BERP (British Experimental Rotor Program) blade [66, 104]. As illustrated in Figure 1.25, the BERP blade has a unique tip shape and uses specially designed airfoils. It was designed to cope with the conflicting requirements on the tip over advancing and retreating blade sides. The high sweep angle at the tip allows for a reduced effective Mach number over the blade tip region, thereby limiting compressibility effects on the advancing blade. However, this sweep angle would move back the centre of pressure, away from the blade elastic axis which would lead to an undesired aero-elastic coupling. This is resolved by setting the complete tip area region forward.

The discontinuity in the leading edge created by the so-called notch has two advantages. First of all, the discontinuity creates a vortex that delays separation at high angle-of-attack. Stall characteristics on the retreating blade side are thus improved by the notched shape. It also appears to help on the advancing blade side in reducing the strength of the shock wave.

The atypical design of the BERP blade tip induces different aerodynamic effects that all help in improving aerodynamic performance of the blade in high-speed forward flight.

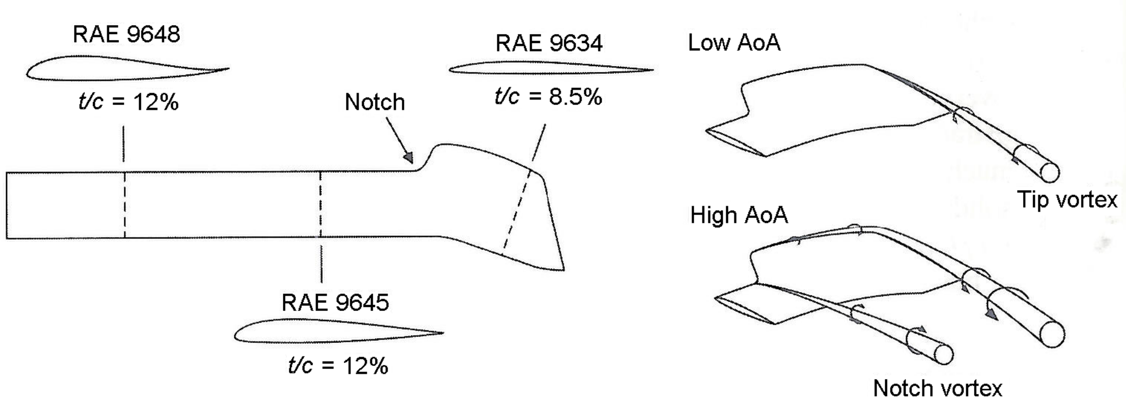

Figure 1.25: Geometry of the BERP blade and performance at low and high angle-of-attack, from [83]

Even if the performance gain in high-speed forward flight of the BERP blade was measured in wind tunnel [34] and demonstrated in flight by a world speed record in 1986, the blade planform is not always suitable. Wind tunnel tests performed at the NASA on a blade having the same planform as the BERP blade, but using different airfoils and twist law, has demonstrated a performance reduction compared to a straight blade with the same airfoils and twist [155]. This illustrates the sensitivity of rotor blade aerodynamics to geometrical parameters as well as close interactions between different geometrical parameters.

1.2.6 A former study at Eurocopter: the ORPHEE project

The ORPHEE project (Optimisation d'un Rotor Principal d'Hélicoptère par l'Étude et l'Expérimentation) was held in the beginning of the '90's with the goal of finding new blade geometries for improved performance in high speed forward flight. Four rotors have been designed and tested in the Modane wind tunnel [7] for forward flight performance and at Eurocopter's test bench for hover performance.

The two main objectives in the design process of these blades were:

- Maximize the L/D ratio at a forward flight speed of 315 km/h, corresponding to $\mu = 0.463$, and at a rotor loading of $\bar{Z} = 15$
- Increase the manoeuvrability limit by maximizing lift at stall, where stall is defined at the lift coefficient for which profile drag coefficient C_{XP} exceeds 0.028

In addition to these two objectives, a constraint was introduced to ensure that hover performance could not decrease with respect to the baseline configuration.

The ORPHEE blades

The four blades that resulted from optimizations with the above requirements are characterized by the following features:

- EC1: reference, straight blade with parabolic blade tip
- EC2: same planform as EC1, over-twist in the central blade part
- EC3: double taper, over-twist in the central blade part and reduced twist at the tip
- EC4: sabre shape, same twist law as EC2

All blades use the OA312 and OA309 airfoils and their planforms are illustrated in Figure 1.26.

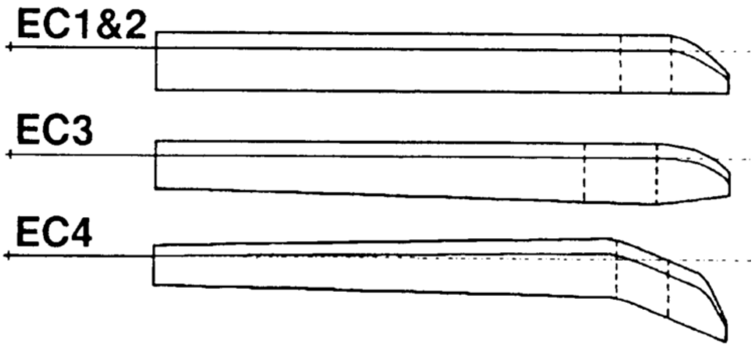

Figure 1.26: Top views of the four ORPHEE blades [28]

Wind tunnel measurements of forward flight performance of all four blades have been carried out in the Modane wind tunnel in 1992. A large matrix of flight conditions was tested corresponding to various combinations of advance parameter μ and rotor loading $\bar{Z}$. Two wind tunnel rotor command laws were used:

- American law: rotor load $\bar{Z}$ and fuselage drag are fixed while the lateral and longitudinal flapping angles, β_{1s} and β_{1c} respectively, are both set to zero, so that no blade flapping occurs. Rotor control of collective, longitudinal and lateral pitch angles as well as the rotor shaft angle α_{hub} may be used for reaching rotor equilibrium. In a high speed flight condition, this requires a high longitudinal cyclic pitch angle that can exceed rotor control capabilities.
- Modane law: may be used for high forward flight speeds as this law allows for reducing control range and loads. The rotor is now allowed for backward flapping β_{1c}, this value being set equal to the longitudinal cyclic pitch $DTS0$. The rotor shaft is tilted forward so that the tip path plane remains at a position similar to that of the American law. Again, rotor loading and fuselage drag are imposed, together with a zero lateral flapping angle.

For example, for an American law requiring 10° longitudinal pitch to set the longitudinal flapping to zero, the rotor mast may be tilted by 3°. Using a Modane law, only 5° of pitch and backward flapping may be required while the same trim is achieved by setting a rotor mast tilt angle of 8°. This is illustrated in Figure 1.27.

Measurement results

Hover performance was measured at the Eurocopter test bench. The accuracy of the F.M. in these measurements is given to be about 0.01. Figure 1.28 illustrates F.M. as a function of $\bar{Z}$ for the measurements performed at a tip speed of 220 m/s. It may be seen that the EC4 blade

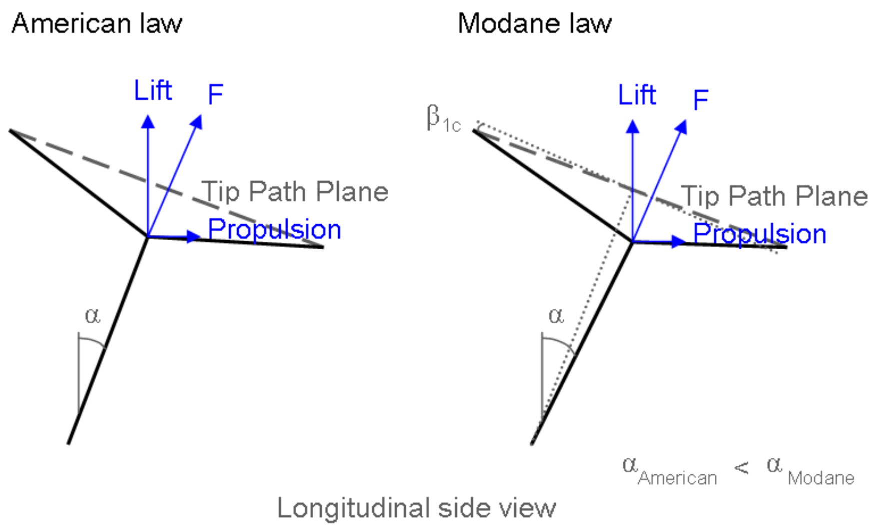

Figure 1.27: Illustration of the American and Modane rotor control laws for wind tunnel tests

has significant better hover performance than the three other blades. The EC3 blade, on the contrary, has a significantly lower F.M. for all rotation speeds and rotor loads $\bar{Z}$. The hover performance difference between the EC1 and EC2 blade is limited and within measurement accuracy, so that no conclusion may be drawn from these measurements. This is unexpected since from theory better hover performance may be expected for the steeper twist law, that of EC2. These hover measurement results are confirmed at 3 other rotational speeds.

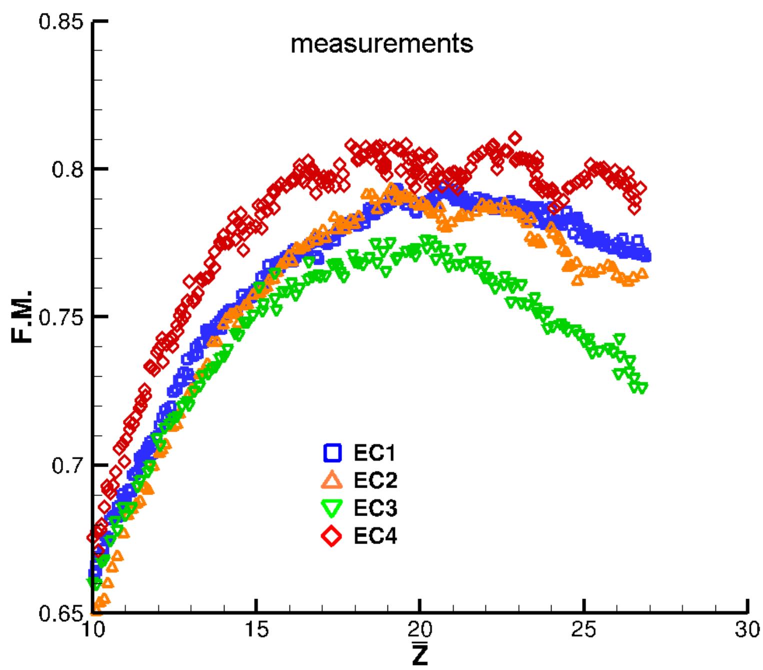

Figure 1.28: Measured F.M. as a function of $\bar{Z}$ for the four ORPHEE blades at $V_{tip} = 220$ m/s

Forward flight performance measurements were done at the Modane wind tunnel. Out of the large matrix of test points, two rotor command laws with two rotor loadings were selected. For these two laws, measurement results for four different forward flight speeds and for all four ORPHEE blades are available. Measured L/D for the four forward flight speeds and the two rotor laws are presented in Figures 1.29 and 1.30. The hierarchy of the four blades depends on flight conditions: the EC1 blade has best forward flight performance at low rotor loading and forward flight speed. With increasing μ, EC3 performance improves and surpasses that of the EC1 blade. EC4, while having poor L/D values at low $\bar{Z}$ and μ, has the best forward flight performance at high rotor loading and high forward flight speed. The EC2 blade, however, has poor performance all over the flight envelope.

Clearly, no straightforward conclusion may be drawn on forward flight performance of the ORPHEE blades. Flight conditions influence largely the hierarchy of the four blades, so that analysis of forward flight performance needs to be performed over a larger range of flight conditions.

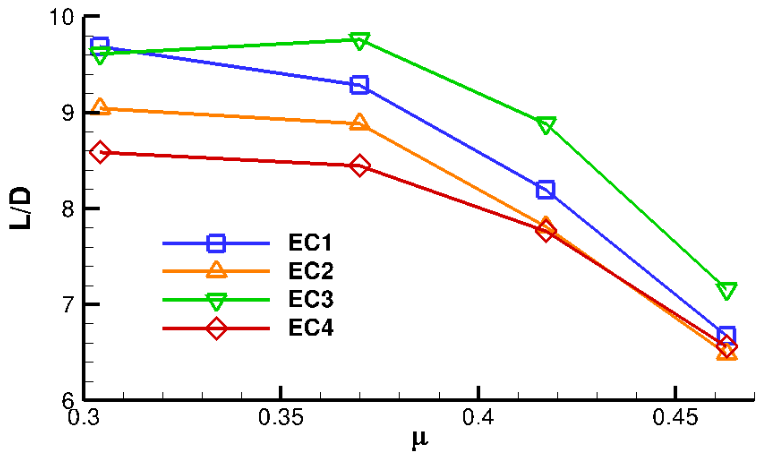

Figure 1.29: Measured L/D as a function of μ, Ω=960 rpm, $\bar{Z}$=15, C_{XS}=0.1, American law

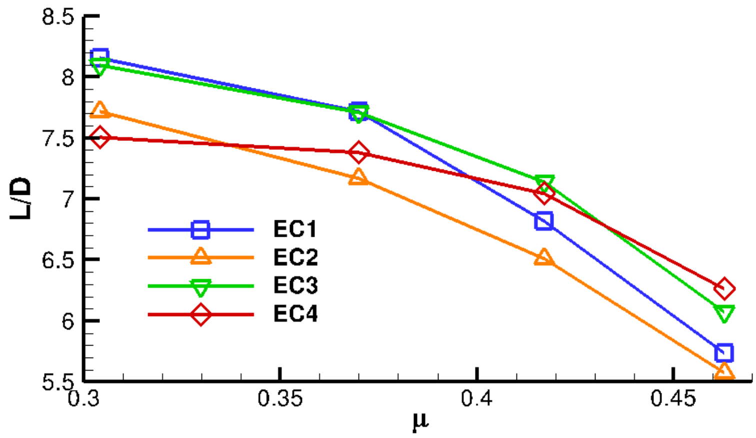

Figure 1.30: Measured L/D as a function of μ, Ω=960 rpm, $\bar{Z}$=20, C_{XS}=0.1, Modane law

1.3 State of the art of helicopter rotor blade design techniques

The aerodynamic design of helicopter rotor blades is the quest for a compromise solution of conflicting flow conditions in hover and forward flight. Industrial design will always incorporate both flight conditions as rotor performance cannot be neglected in either phase. Nonetheless, many research studies in the past were focussed on either of the flight conditions to simplify the design problem and understand the influence of geometry on various aerodynamic phenomena.

One of the first rotor blade optimizations dates back to 1987 and was carried out at NASA [146]: hover power consumption was minimized while using constraints for forward flight performance. These gradient-based optimizations of chord and twist were performed with a rotor code based on lifting-line theory.

In the last decade, the increase in computational resources has allowed for a large spread of aerodynamic rotor blade optimizations. ONERA developed an optimization loop including comprehensive rotor code HOST as well as CFD simulation tool *elsA* in 2003 [80]. First, hover optimizations of the 7A blade were carried out using a gradient-based optimizer: chord, twist, sweep and dihedral angles were optimized separately. Next, the same parameters were optimized simultaneously for both flight states by combining objectives via weighting coefficients into one cost function for gradient optimization and by a genetic algorithm [79].

To simplify the complex rotor design problem, performance improvement can be obtained from 2D airfoil shape optimization. Objectives come from conflicting flow requirements at the advancing and retreating blade positions in forward flight. Either 2D simulations may be performed at different flow conditions to create a compromise design, as done by [100] and [3]. Or, the complete blade may be simulated with only design variables on airfoil shape, as performed in [126], [82] and [81].

A way of reducing the number of cost function evaluations is the use of gradient information within the optimization method. The adjoint method solves a direct and an adjoint integration at each iteration of the optimization problem to compute gradients of cost functions with respect to design parameters [52, 53, 100]. This only holds for hover computations. A way to use gradient information in forward flight simulation is the transfer of the simulation time domain to the frequency domain, in so-called Non-Linear Frequency Domain (NLFD) simulation. This allows for the use of the adjoint equations in forward flight also. Demonstration of rotor airfoil optimizations have been presented in the last few years [41, 99, 129, 130]. While this method is very interesting in reducing the time required for a forward flight CFD simulation, the optimization method still uses a gradient optimizer with its inherent practical disadvantages.

Rotor blade optimization at the University of Bristol has been continuously extended over the last 5 years. Their optimization cycle contains CFD simulations and is based on a Feasible Sequential Quadratic Programming (FSQP) optimization algorithm, which is a gradient-based optimization method. Radial basis functions leading to mesh deformations are used in the design of airfoil shapes that are optimized for transonic flow conditions [3, 5]. An application of rotor blade optimization in hover has been demonstrated on the Caradonna-Tung rotor [37] by minimizing hover torque, while imposing constraints on blade moments and internal volume [4, 98].

As mentioned before, the multi-objective optimization for hover and forward flight simultaneously is required for industrial design of rotor blades. Multiple optimization objectives may be combined into one by using weight coefficients. This method was used by [70] in a twist optimization for hover and forward flight. Five different combinations of weighting coefficients were tested to create a limited Pareto Optimal Front. Unfortunately, in these optimizations, the solution becomes dependent on the selected weighting coefficients. Genetic Algorithms (GA; see also 3.2.1) are especially suitable for multi-objective optimization as they allow for finding the complete Pareto Optimal Front. The drawback is that GA require a higher number of geometry cost function evaluations so that extensive computational resources are needed to carry out the optimization process within an acceptable time. As a consequence, only few complete optimizations have been performed, such as in [79].

To limit the number of cost function evaluations needed by a genetic algorithm, approximate techniques may be applied, such as Surrogate Based Optimization (see also 3.3.2). This method was used in 2009 by [69] for optimizing the blade tip section using CFD. Artificial Neural Networks are used to limit the number of evaluations required in [23] to perform a sweep and anhedral optimization by using CFD. At Georgia Institute of Technology, an optimization loop was created to incorporate not only performance but also acoustics objectives. The expensive cost functions were evaluated on response surfaces [45]. In an extension, low- and high-fidelity tools are used to create high-quality response in interesting zones, while gaining evaluation time by using low-fidelity simulation tools in regions that are not optimal [46].

An industrial application of automated aerodynamic optimizations of rotor blades was published by Agusta-Westland in 2011 [92]. The optimization methodology as performed here consists of coupling genetic algorithms with panel method simulations to optimize rotor performance in hover. A demonstration is given by a simultaneous optimization of twist, chord and sweep laws. The optimization itself is performed on a surrogate model based on an Artificial Neural Network.

Figure 1.31 resumes today's state of the art as a function of optimization and simulation complexity. The high number of recent publications shows clearly that rotor blade optimization is a current research topic. In addition, it shows that forward flight performance is up until now assessed by comprehensive rotorcraft codes. Also, extensive use of CFD simulations combined with multi-objective optimization methods such as genetic algorithms is not yet common.

1.4 Chapter summary and objectives of the Dissertation

The short overview of helicopter rotor aerodynamics given in Section 1.1 has demonstrated the large differences between flow conditions in hover and forward flight. Resulting requirements on rotor blades are as different as the flow conditions encountered in the two flight cases. Whereas the hover flow state can be relatively easily understood and its influence on rotor blade geometry can be defined accurately, this does not hold for forward flight. Variations in local velocity and angle-of-attack encountered by blade sections in forward flight make that a forward flight-optimized blade is a compromise solution itself. The description of different geometry laws of section 1.2 has illustrated a hover-optimal blade shape and has reasoned geometrical choices to be expected for forward flight optimization.

Optimization of helicopter rotor blades only in either flight case remains essentially a theoretical exercise that, as shown in section 1.3, has been performed in various ways in different research centres. In recent years, research centres also extended these optimization loops to multiple objectives, either by weighting coefficients or by genetic algorithms. An industrial design of helicopter rotor blades is generally useful if the blade is designed for the two distinct flight cases. As will be further detailed later on in Section 3.2.1, genetic algorithms naturally allow optimizing for multiple objectives, making them particularly suitable for industrial optimizations. The current increase in computational resources now allows for the extensive use of genetic algorithms, even for high-fidelity simulation tools as CFD. This is why industrial optimization tools for automated rotor blade optimization finally can be designed.

In this optimization loop, typical objectives will be hover and forward flight performance. Constraints may be added for ease of production or reduction of vibrations or control loads. Reproducibility of simulation results in real flight is vital. Only then, performance gains found in the design optimization will be confirmed in flight. Accuracy of simulation tools is therefore fundamental for the correct resolution of the optimization. To assure validity of the two simulation tools, HOST and *elsA*, to be used in the present optimization loop, validation studies will be performed. Besides studies of specific elements of both tools, the ORPHEE blades (section 1.2.6) will be used to verify accuracy of the simulation tools to estimate performance differences for geometrical changes. Only when a performance difference as a

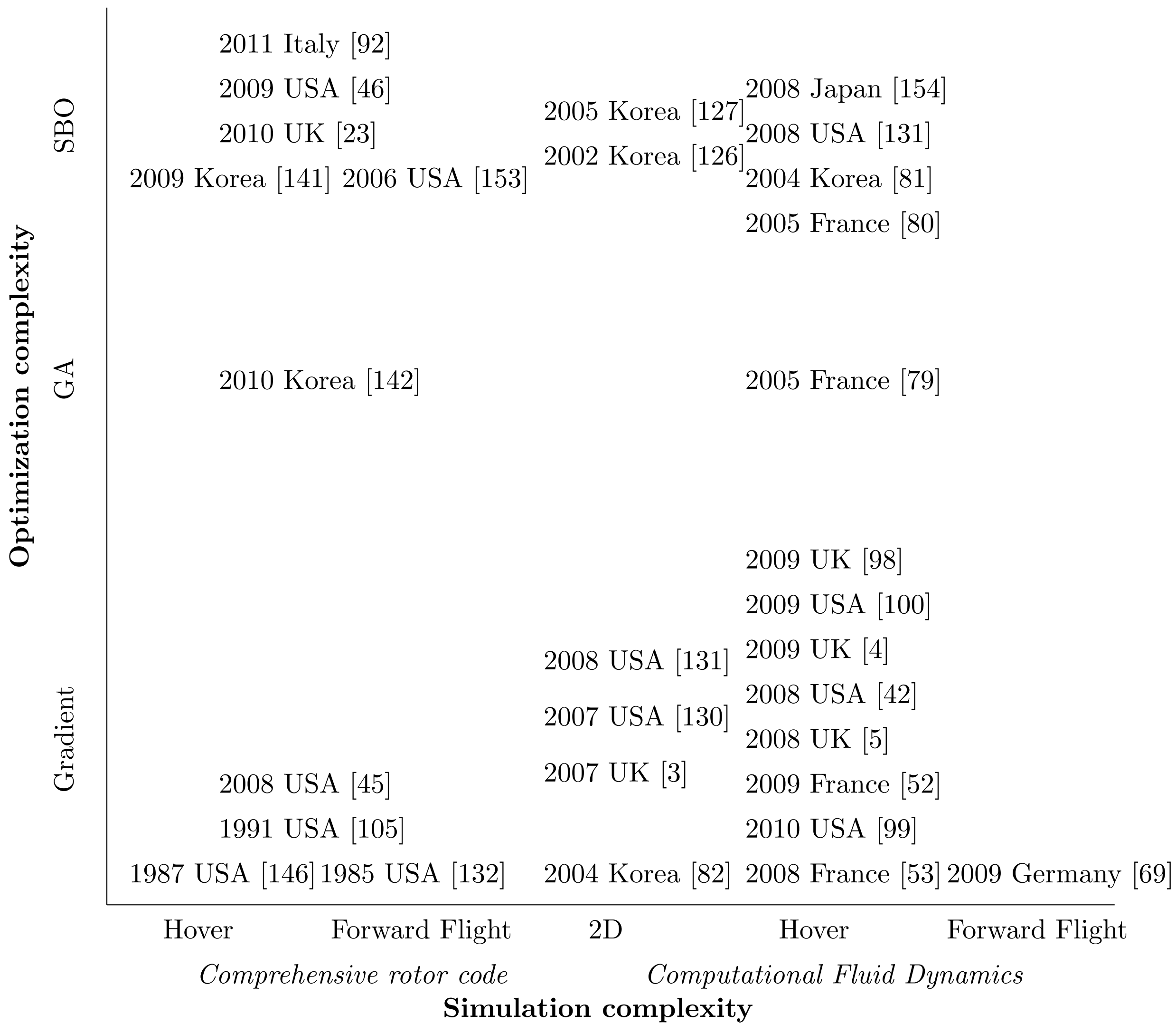

Figure 1.31: State of the art of aerodynamic rotor blade design optimization

function of a geometry modification is predicted correctly, the simulation tool may be used for optimizing that geometrical law. These various studies will be presented in chapter 2.

Since rotor blades have a high aspect ratio, their structural stiffness is low and elastic deformations occur in all flight conditions. Blade elasticity has a significant effect on the aerodynamic flow field: the positioning of the blade with respect to the wake changes when accounting for blade elasticity. Especially for a phenomenon like BVI, where the miss distance between the tip vortex and the blade is considered, blade deformation cannot be neglected. Nonetheless, the studies presented in the following are performed without taking into account for this blade deformation. Incorporation of aeroelastic effects would require a coupling between aerodynamic simulation tools and solid mechanics software. This iterative loop is very time-consuming, so that the approximation of a rigid blade is used here. The influence of this assumption will be studied, though, to assess the accuracy gain that can be expected when taken into account for blade elasticity in the future.

Blade tip design will not be considered. This is motivated on the one hand by the complicated flow physics of tip vortices that is not correctly represented by CFD simulations. Moreover, simulation of blade tips requires very fine meshes in the tip region, and is CPU-consuming. Finally, to avoid numerical dissipation of the tip vortex, uniform meshes should be used. As the resolution of the vortex core would require some 20 grid points in this small region, a uniform mesh would lead to a total of $O(10^9)$ grid points, as estimated by [138]. For the same reasons, the blade root will not be designed by the optimization loop either.

As briefly explained in section 1.3, gradient optimization is limited in the simultaneous incorporation of multiple objectives. Genetic algorithms will be used in the optimization loop designed in this work, as will be explained in chapter 3. The drawback of genetic algorithms is the relatively high number of evaluations required. Even if computational resources are now largely available and HOST and CFD simulations in hover may be performed as required, CFD simulations in forward flight are still quite time-demanding. To reduce computation time of an optimization in forward flight, advanced optimization techniques will be used. These techniques are to be incorporated and tested in the created optimization loop.

In chapter 4, the optimization loop will finally be validated. Separate and combined twist and chord law optimizations will be performed, using the two simulation tools and various optimization techniques. Results of the previously performed studies will be used for selection of parameters of the simulation tools. All optimizations will be evaluated and the best optimization parameters will be selected as well to validate the optimization strategy.

Chapter 2

Simulation tools for the prediction of rotor blade performance

To characterize the aerodynamic performance of main rotor blades within an optimization cycle, numerical simulations of different blade designs are required. It is of paramount importance that the simulations provide accurate estimations of rotor performance. Whereas exact performance prediction is interesting for foreseeing the actual capabilities of a design, for correct optimization results, prediction of performance trends as a function of design parameters is more important. A second requirement on simulation tools integrated in an optimization loop is low response time, i.e. low computational cost: typical industrial design time is of the order of hours in the pre-design phase, and should typically be a couple of days with a maximum of a week for detailed design. Thirdly, robustness of simulation methods with geometry changes is required for assuring robustness of the optimization loop. In the following of this chapter, we describe the main rotor design simulation tools in use at Eurocopter France, namely HOST and *elsA*, and discuss their advantages and applicability limits.

The Helicopter Overall Simulation Tool (HOST) developed at Eurocopter is a comprehensive rotorcraft analysis code, based on coupling of submodels for main components of a helicopter. HOST is used to compute loads, aerodynamic performance, handling qualities and acoustics impact. Aerodynamic modelling of the main rotor is based on the lifting line method and uses lift, drag and moment polars from wind tunnel measurements. The model is empirically corrected to account for specific aerodynamic phenomena occurring over the rotor disk. Typical response time is of the order of 30 seconds to two minutes on a single core processor.

Computational Fluid Dynamics (CFD) code *elsA* solves the discretized Navier-Stokes equations to simulate the flow field around a rotor. A 3D simulation of an isolated rotor naturally accounts for most aerodynamic phenomena such as airfoil stall, tip vortices or other viscous effects. Numerical computations typically require several hours for a hover computation and a couple of days for forward flight simulation at Eurocopter's processor cluster (simulation run in parallel on about 30 cores; information on computing facilities is given in the Introduction).

From the above, it appears clearly that HOST and *elsA* drastically differ in terms of accuracy and computational cost. A smart design strategy should use the unexpensive solver where it is able to predict the quantities of interest within the prescribed accuracy limits, and to switch to the expensive one otherwise. To do so, it is mandatory to accurately assess both methods and characterize their application ranges.

To this purpose, after describing numerical ingredients used by the HOST and *elsA* solvers, we perform several numerical studies presented in the following of this chapter. Precisely, we first use HOST to predict the induced velocity field around a rotor, and compare numerical results with experimental data. Then, we assess the capability of RANS solver *elsA* to correctly capture some of the relevant features of rotor flows and specifically tip vortices. Again, we select a well-documented test-case, for which detailed experimental data are available. Finally, we compare the capabilities of both solvers to predict global rotor performance by comparing their predictions to experimental data sets available for the ORPHEE blades (section 1.2.6). We consider four blades that differ in geometry and investigate the ability of HOST and *elsA* to predict the correct hierarchy in terms of performance of the four blades.

2.1 Comprehensive rotor code HOST

The Helicopter Overall Simulation Tool (HOST) developed at Eurocopter is a comprehensive rotorcraft analysis code for aeromechanics simulations. First developments date back to the '90's when two previous comprehensive codes were combined into HOST: these are the R85 rotor code, used for aerodynamic and dynamic computations of rigid or elastic blades [135] and the S80 simulation code, used for handling quality simulations of a complete helicopter. The main objective of HOST was the modular integration of both codes into a tool that can be used for three types of computation [29]:

- Trim calculations: Movements and internal state variables are expressed in terms of harmonics by HOST's kernel. The trim solution is searched for a trim law with as much parameters imposed (e.g. power, accelerations, flap angle, ...) as set free (environment and movement parameters, input control, ...). The solution is obtained by an iterative process in which a Newton method with an influence matrix is used. This influence matrix is obtained by harmonic analysis of state functions and of selected outputs and is rebuilt only when becoming inaccurate. This kind of computations is typically used for loads and rotor performance computations.

- Time domain simulations: The trim solution is integrated over time while the time variation of any parameter can be imposed. The simulation can be stopped, analyzed and resumed at any moment during the simulation. These simulations are used for flight simulators and handling quality computations.

- Linearization: Equivalent linear systems are used for the analysis of manoeuvrability or helicopter stability. The influence matrix containing responses to perturbations of input controls, movement components and internal state, is linearized after a trim calculation. The obtained linear system is used for assessing stability, representation of eigen values and computation of transfer function.

HOST has a modular structure that allows for selecting different physical models and combining geometrical elements. For instance, several models are available to describe elastic blade deformations or the induced velocity field. In the same way, helicopter elements are modular as well since comparable geometric components may use the same set of models. For example, the main and tail rotor are considered in the same fashion and may use similar models. This modular structure allows for great flexibility and consistent physical modelling.

Geometrical elements and their modelling are linked in HOST's kernel via interfaces, creating a three-layer structure. The kernel is limited to generic management routines for resolution of the system. Interfaces link models and kernel via a tree structure of relations between all elements following subsequent links. As an example, relations elements of a main rotor and their mutual relations are presented in Figure 2.1.

For rotor blade performance computations typically trim calculations are performed as often steady state flight conditions are imposed. The resolution of the trim state is done in two

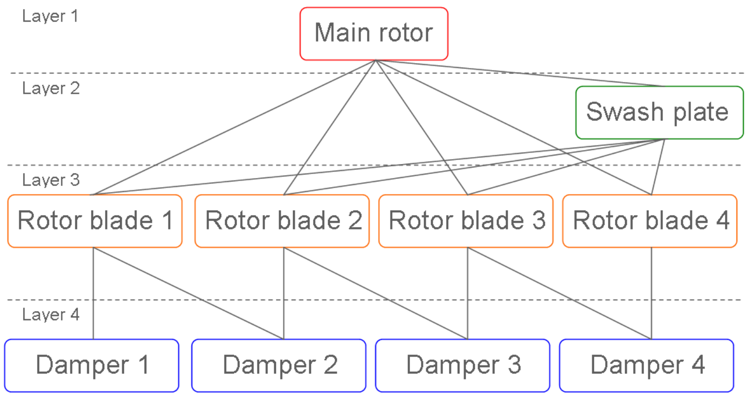

Figure 2.1: Example of arborescence of a HOST computation of a helicopter rotor, from [29]

steps: first, movements of all elements are passed from an upstream element (i.e. main rotor in Figure 2.1) towards the downstream elements (i.e. blades and swash plate, and later on to the dampers). This is the so-called kinematic pass. In a second step, loads (forces and moments) are transmitted in the upstream direction, so starting from the dampers in Figure 2.1 and moving up to the main rotor. This load path leads to first and second time derivatives of state variables of all elements. Trim is now obtained by cancelling these state variables against the researched trim state. A Newton-Raphson algorithm is used for convergence towards the requested trim condition.

The model most used in studies and optimizations presented in this work is the aerodynamic model computing blade loads. Principles of this model will be given next. As an induced velocity model is required for modelling aerodynamic loads, several examples of these models will be presented as well.

2.1.1 Aerodynamic model

For computation of aerodynamic characteristics of the rotor, HOST uses the Blade Element Theory (BET) [83]. In BET theory, blades are split up into a finite number of blade elements, see Figure 2.2. It is assumed that each of the elements acts as a quasi-2D airfoil. On this assumption, sectional loads of lift and drag are computed using 2D airfoil theory and look-up tables obtained from wind tunnel tests. The relative angle-of-attack is calculated taking into account for the induced velocity (see also Section 2.1.2). Rotor performance is then computed by integrating 2D loads over the blade span.

Three-dimensional effects are not taken into account in BET, but may be added separately later on. In HOST, optional features exist to account for some 3D effects on the blade [19]:

- *Sweep correction* The sweep correction has been introduced to account for the effect of the reduced normal component of locally incoming flow at front and aft parts of the rotor disk. It should be emphasized that blade sweep is not considered here. This correction affects maximum lift coefficient $C_{l_{\max}}$ as stall occurs at a higher angle-of-attack and adds a radial component to the drag computation [29]. The increase in maximum lift coefficient is given by:

$$C_{l_{\max}}(M,\Lambda) = \frac{C_{l_{\max}}(M,0)}{\cos(\Lambda)} \tag{2.1}$$

  where Λ is the local sweep angle and M the local Mach number.

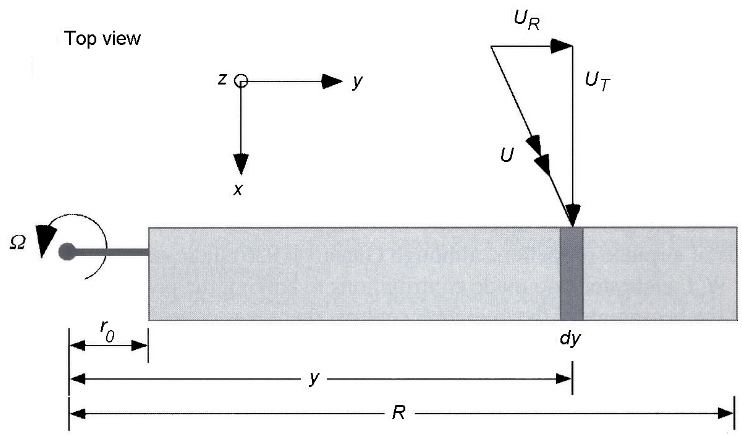

Figure 2.2: Blade element theory aerodynamic environment, from [83]

Simultaneously, sweep adds a radial contribution to drag coefficient C_d, which is a function of friction drag C_{d_f} and sweep angle Λ, related by:

$$C_d = C_{d_f} \tan(\Lambda) \tag{2.2}$$

- *Blade curvature effect* Blades may have a non-rectangular shape, especially in the tip region. To account for changes in perpendicular flow direction, dihedral and sweep angles at 25% of the chord line are used. Local Mach numbers are corrected for by the curvature angle.
- *Reynolds correction* As HOST uses wind tunnel measured polar curves for lift, drag and moment coefficients, correction of Reynolds number influence on stall characteristics is required. It appears that, as a first approximation, correction for maximum lift is not required, whereas difference in drag coefficient is approximated by an empirical formula as:

$$C_d(Re_{\mathrm{HOST}}) = C_d(Re_{\mathrm{WT}}) \frac{Re_{\mathrm{HOST}}}{Re_{\mathrm{WT}}}^{-\frac{1}{6}} \tag{2.3}$$

where the subscript *HOST* refers to HOST simulation and *WT* to wind tunnel measurement.

To take into account for lift reduction on the blade tip, the lift coefficient can be forced to zero for a small portion of the blade tip. Drag is still created by this zone, so that the effect of the tip vortex is modelled to some extent. From previous experiments, it was concluded that a 2% cut-out of the rotor tip lift would improve representation of total rotor performance [25]. Additional corrections may be added to, for example, model wake contraction in hover, or make corrections for stalled or transonic flow. As a default, all previously described corrections will be applied in subsequent HOST computations.

2.1.2 Induced velocity models

As described in Section 1.1, the local velocity encountered by rotor blades consists of three elements: local contribution of rotational velocity, forward flight velocity, which is zero in hover, and induced velocity. While contributions of rotational and forward flight velocity are easy to compute, induced velocity is amongst others a function of rotor lift and rotor longitudinal and lateral inclination angles and cannot be obtained readily. Thus, the contribution of induced velocity needs to be modelled. Several induced velocity models exist, some of which are based on global flow field parameters, whereas other models use circulation distributions to create a wake field that is advanced in time. Hereafter, we introduce induced velocity models used by HOST.

It should be noted that HOST uses information about the induced velocity to compute local velocity and angle-of-attack along the blade, in the blades reference frame, see Figure 2.3. The actual induced velocity field, however, is fully 3D and the induced velocity value and direction change drastically with observation point. This is why induced velocity models used by HOST and CFD-computed induced velocity fields cannot be compared easily: actually, an induced velocity model is an artificial way to account for the wake field to be used in lifting line theory.

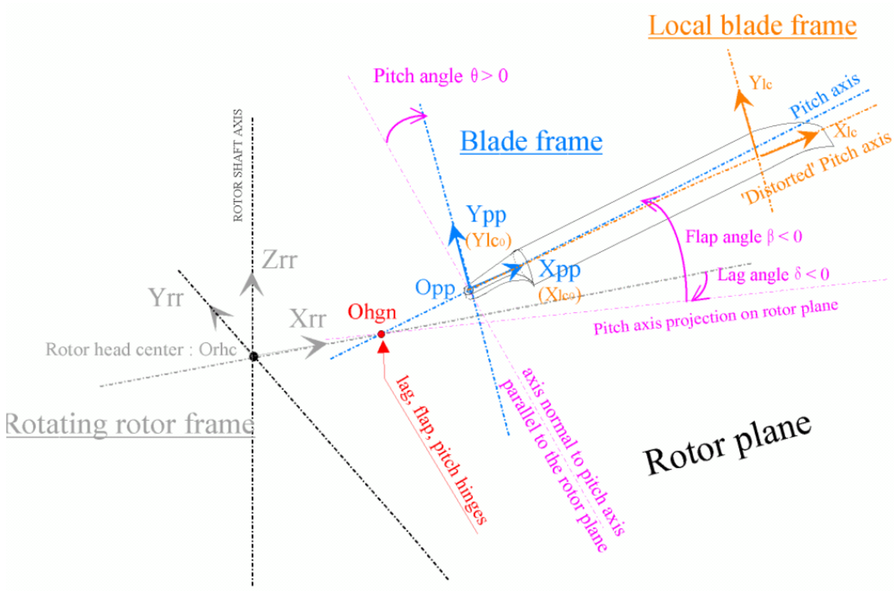

Figure 2.3: Aerodynamic reference frame used by HOST

Meijer-Drees model

In 1926, Glauert [62] proposed an induced velocity model, based on a uniform component to which a longitudinal linear part was added. This has been extended with a lateral part later on. This kind of model is said to have 3 states, referring to the three components of the induced velocity. The uniform part is based on momentum theory [83], whereas the longitudinal and lateral components are empirically obtained coefficients. The basic formula for this induced velocity model is as follows [83]:

$$\lambda_i = \lambda_0 \left(1 + k_c \frac{r}{R} \cos\psi + k_s \frac{r}{R} \sin\psi\right) \tag{2.4}$$

where:

λ_i	Inflow coefficient at element i
λ_0	Inflow coefficient of mean induced velocity
k_c, k_s	Adjustable coefficients
r	Radius of blade section [m]
R	Rotor radius [m]
ψ	Azimuth angle [°]

The mean component of the induced velocity λ_0 is computed using the following equation, based on uniform momentum theory [83]:

$$\lambda_0 = \frac{C_T}{2\sqrt{\mu^2 + \lambda_i^2}} \tag{2.5}$$

where:

C_T	Thrust coefficient
μ	Advance ratio $\mu = V_H/\Omega r$

From experiments it was found that the rotor inflow in forward flight is higher on the rear part of the rotor disk, as is the case to a lesser extent on the retreating side [83]. This information is used to construct expressions for weighting factors k_c and k_s. Various induced velocity models differ by the equations used to compute these factors. The Meijer-Drees model uses the next formulae [40]:

$$k_c = \frac{4}{3}\left(\frac{1 - \cos\chi - 1.8\mu^2}{\sin\chi}\right) \quad \text{and} \quad k_s = -2\mu \tag{2.6}$$

where χ is the wake skew angle, defined as $\chi = \tan^{-1}(\mu/\lambda)$, with λ the inflow angle of the induced velocity field.

The Meijer-Drees model is relatively easy to implement, since the computed angles are constant for a certain flight condition. This model is limited by the assumption of a linear induced velocity field.

Pitt & Peters model

The Pitt & Peters model is a so-called dynamic inflow model [106], since it takes into account for dynamic pressure differences over the rotor disk. As in the present study we perform steady flight computations, we are not concerned with dynamic changes of rotor loads so that the dynamic part of the model does not influence results. The static part of the Pitt & Peters model reduces to a linear induced velocity model of the form 2.4 for which coefficients k_c and k_s are given by [40]:

$$k_c = \left(\frac{15\pi}{23}\right)\tan\left(\frac{\chi}{2}\right) \quad \text{and} \quad k_s = 0 \tag{2.7}$$

Implementation advantages and hypothesis limitations are similar to the Meijer-Drees model.

FiSUW model

The Finite State Unsteady Wake (FiSUW) model is an implementation of the model developed by He and Peters [64] [25]. Compared to the linear fields expressed by Equation 2.4, FiSUW introduces additional states, represented by cosine and sine harmonics. The user defines the number of harmonics, allowing for selecting model complexity.

The model is based on a potential acceleration perturbation through the rotor disk caused by a lift-induced pressure discontinuity. The potential acceleration basis uses an incompressible flow assumption, which is considered acceptable for hover and low-speed forward flight, but may not hold in high-speed forward flight. In this model, no blade vortices, wake distortion or other vortex effects are considered [64]. As blade vortex interaction is not simulated, the model does not convene for aero-acoustic computations.

The potential acceleration Φ is expressed in ellipsoidal coordinates $(\nu, \eta, \bar{\psi})$ in the rotor plane, see Figure 2.4, and is computed within HOST's kernel. A suitable general solution for the potential acceleration is given by Laplace's equation. Rotor loads are thereby expressed in terms of cosine and sine components of generalized forces τ_c and τ_s by radial and azimuthal analysis in Legendre and Fourier functions as in:

$$\Phi\left(\nu, \eta, \bar{\psi}, \bar{t}\right) = -\frac{1}{2}\sum_{m=0}^{\infty}\sum_{p=0}^{\infty}\overline{P}_n^m(\nu)\overline{Q}_n^m(i\eta) \times \left[(\tau_c)_n^m(\bar{t})\cos(m\psi) + (\tau_s)_n^m(\bar{t})\sin(m\psi)\right] \tag{2.8}$$

where:

Φ	Potential acceleration
$\nu, \eta, \bar{\psi}$	Ellipsoidal coordinates
p	$n = m + 2p + 1$
n	Harmonic number of Fourier function
m	Shape number of associated Legendre function
$\bar{t}$	Non-dimensional time
$\overline{P}_n^m\ \overline{Q}_n^m$	Normalized associated Legendre functions of 1^{st} and 2^{nd} kind
$(\tau_c)_n^m$ $(\tau_s)_n^m$	Generalized rotor loads for cosine and sine terms

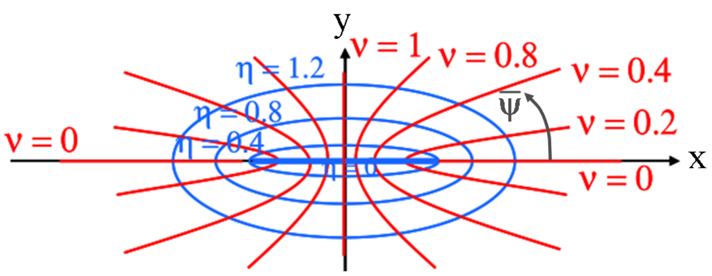

Figure 2.4: Ellipsoidal coordinates used by FiSUW, from [24]

Mass and momentum conservation relate the generalized rotor loads to unsteady and steady inflow coefficients, given by $\dot{\overline{\lambda}}_c$, $\dot{\overline{\lambda}}_s$, $\overline{\lambda}_c$ and $\overline{\lambda}_s$. These equations are given in Figure 2.5 where gain matrices L_c and L_s take into account for circulation distribution and wake skew angle. Diagonal matrix V_n^m contains the freestream velocity on its diagonal.

Vertical inflow components v_i over the rotor disk are finally expressed in terms of these inflow coefficients by:

$$v_i\left(r/R, \psi, \bar{t}\right) = \sum_{m=0}^{\infty}\sum_{p}^{\infty}\overline{P}_n^m(r/R) \times \left[(\lambda_c)_n^m(\bar{t})\cos(m\psi) + (\lambda_s)_n^m(\bar{t})\sin(m\psi)\right] \tag{2.9}$$

This cycle is iterated until convergence of rotor loads and inflow equilibrium is obtained.

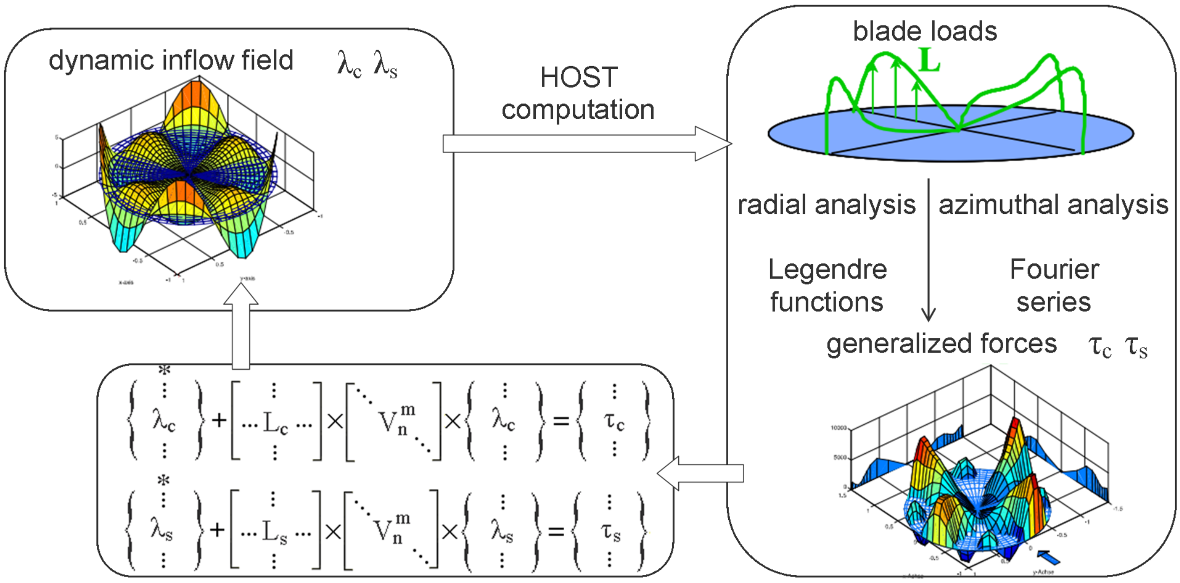

Figure 2.5: Scheme of iterative resolution of rotor airloads and induced velocity field, modified from [24]

Metar model

The Metar (French acronym for: Modèle d'Etude de l'Aérodynamique Rotor) model is specifically developed for simulation of rotor wakes in forward flight. The wake is expressed in terms of vortex filaments that trail downwards in a skewed helical movement. Wake field shape is prescribed as a function of flight conditions and momentum theory, so that this kind of method is called a rigid-wake model. This implies as well that no mutual interactions within the wake appear and that no wake contraction is considered. Incompressible flow is assumed in the derivation, having the same limitations as for FiSUW.

To start the computation process, the rotor lift distribution is calculated. Lift on each rotor blade is replaced via Prandtl's theory by a lifting line. This lifting line is discretized into 20 to 25 segments that are smaller near the blade tip, in the region where circulation distribution has a higher gradient, as illustrated in Figure 2.6.

Each of the segments is now considered to generate a discrete trailing vortex filament that trails off the blade to create a vortex sheet at every azimuthal computation step in a HOST computation. As a consequence, there are as many vortex sheets as there are blades and sheets become longer with every azimuth step. To reduce computation time, only near wake may be resolved for all vortex filaments shed off the blade. Discrete vortices along the blade are then replaced by a blade root and tip vortex after 45° of wake progression. Intensity of this single vortex filament is equal to the value of maximum circulation on the blade. As no influence on the rotor forces distribution is expected from vortex filaments far away from the rotor, the vortex sheet is cut off after a sufficient number of rotor rotations. Roll-up of vortex sheets is shown in Figure 2.7.

The rotor lift distribution is expressed in terms of circulation field $\overrightarrow{\Gamma}$, which can in turn be used for deducing the induced velocity field $\overrightarrow{v_i}$ from vector potential $\vec{\Delta}\phi$ via the Biot-Savart law:

$$\overrightarrow{v_i} = \vec{\Delta}\phi = \frac{1}{4\pi} \cdot \left(\int_{\text{lifting line}} \frac{\overrightarrow{\Gamma} \times \vec{r}}{\| r \|^3} ds + \iint_{\text{wake surfaces}} \frac{\overrightarrow{\gamma} \times \vec{r}}{\| r \|^3} dA \right) \tag{2.10}$$

where:

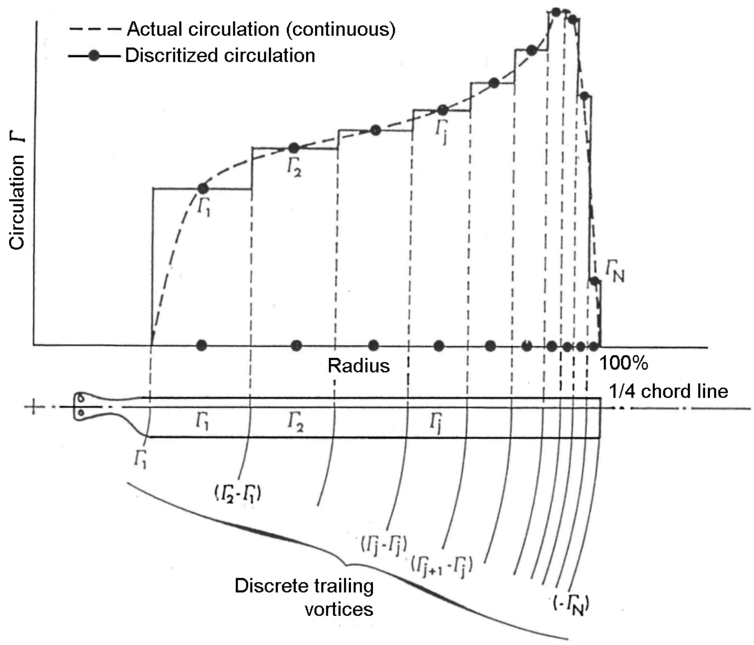

Figure 2.6: Spanwise circulation discretization on a rotor blade by Metar, from [19]

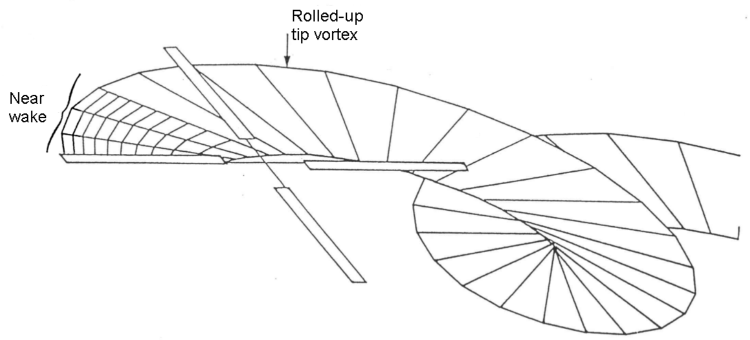

Figure 2.7: Roll-up of near and far field discretized wake, from [19]

$\vec{\Delta}\phi$	Vector potential over the rotor disk
$\overrightarrow{\Gamma}$	Circulation $\overrightarrow{\Gamma} = \frac{1}{2}cVC_l$
$\overrightarrow{\gamma}$	Circulation jump over wake surface
r	Distance between computation and integration point

Wake filaments are released from the blade at each computation step, equal to the azimuth step imposed in the HOST computation. This process is continued to create a complete wake field. Influence of the rotor wake on lift distribution is iterated until a converged solution is found, as was the case for FiSUW. A flowchart illustrating the convergence process of Metar is given in Figure 2.8.

While not specifically designed for, Metar may be used in hover as well, in which case wake contraction is added to the wake description.

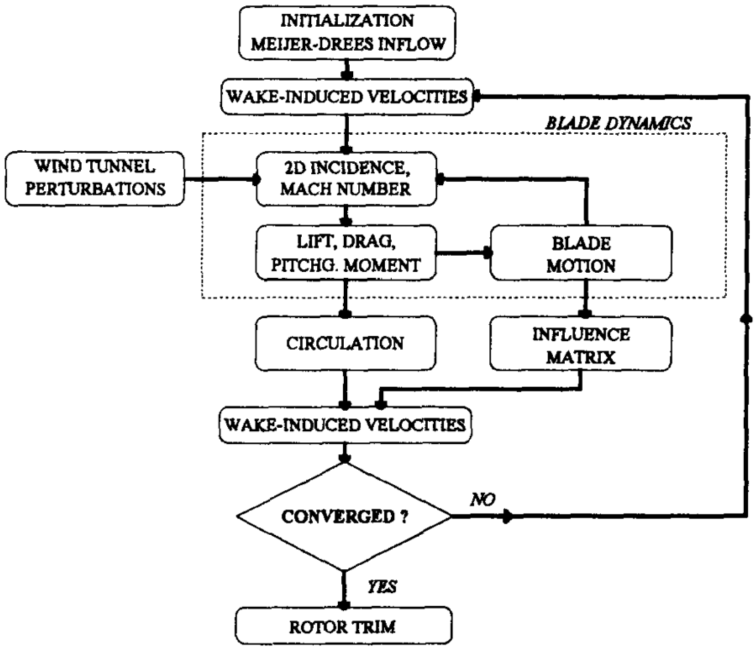

Figure 2.8: Flowchart of the Metar convergence process, from [135]

MINT model

The wake shape of a rigid-wake model like Metar is always helical and its skew angle depends on forward flight velocity. This fixed shape makes that Metar lacks interactions between wake and blades and mutual interactions that occur within the wake, as illustrated for example by pairing of vortices in Figure 1.9 of Section 1.1.3.

The rigid wake hypothesis is removed by using a free-wake model such as MINT in which position vectors of wake filaments are part of the problem resolution. The wake filaments position vector is computed from integration of local velocities encountered by filaments once being released from the blade. The solution is found by using a time-marching method. The following steps are employed for computing the wake field [32, 118]:

- To initiate the wake field, a wake structure is released from the rotor blade via the unsteady lifting line theory of Theodorsen. Meijer-Drees is used for computing aerodynamic loads during the first rotor rotation. Positions of the wake filaments are integrated in time by a one-step Runge-Kutta time-marching method.

- After one rotor rotation, the now created induced velocity field of wake filaments is used for computing aerodynamic loads on the blade. Numerical integration of induced velocities over the blade elements is done by a 4-point Gauss method. The Biot-Savart law (Equation 2.10) is again used for relating released wake filaments to blade circulation.

- The solution is stepped forward in azimuthal direction, typically with a time step equivalent to $\Delta\psi = 5°$. A sufficiently large number of rotor rotations is required for convergence of the wake field and rotor loads.

As was the case for Metar, numerical integration over the complete wake field makes that only a limited wake size can be used in a computation. In forward flight, inflow field influence on rotor loads quickly reduces when the wake is shed behind the rotor. In hover, however, the wake remains relatively close to the rotor so that a large wake field is required for accounting correctly for influence of the wake field on blade loads.

Local momentum theory model

The local momentum theory method, also called ring method, is developed for axial flow by computing a radial distribution of induced velocity.

The rotor disk is split up into a series of rings having a certain width. For each of the rings, an equilibrium solution is computed separately. For achieving equilibrium, a uniform distribution on each ring is assumed, which explains the limitation to axial flight for the model. Glauert's equation, as given in Equation 2.4, is used as a basis for the computation. The local reference frame, local angles and lift and drag coefficients are illustrated in Figure 2.9.

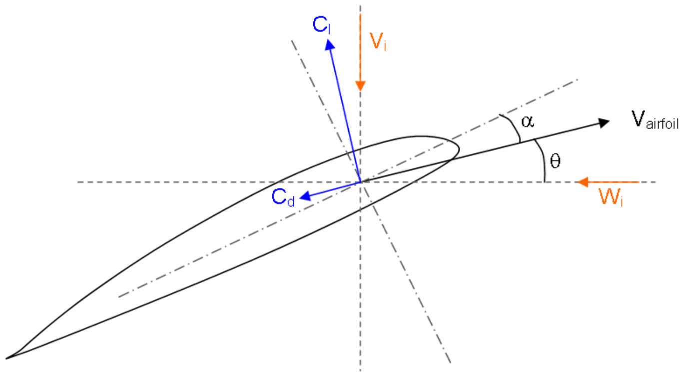

Figure 2.9: Airfoil angles and coefficients used for Ring method computation

In fact, induced velocity in axial direction V_i and in rotational direction W_i are simultaneously found by resolving the momentum conservation equation and moment of the momentum conservation equation [19]. The velocity increase due to the induced velocity is considered as a flow acceleration between far upstream and downstream sections:

$$(\dot{m}v)_{\text{downstream}} - (\dot{m}v)_{\text{upstream}} = 2\pi r dr |v_i + V_z| v_{i\infty} = \frac{1}{2} b c V_{\text{airfoil}}^2 \left(C_l \cos\theta - C_d \sin\theta\right) dr \quad (2.11)$$

$$(\dot{m}wr)_{\text{downstream}} - (\dot{m}wr)_{\text{upstream}} = 2\pi r dr |v_i + V_z| w_i r = \frac{1}{2} b c V_{\text{airfoil}}^2 \left(C_d \cos\theta + C_l \sin\theta\right) r dr \quad (2.12)$$

where:

r	radial position [m]
dr	length of radial section [m]
v_i	axial component of induced velocity [m/s]
w_i	rotational component of induced velocity [m/s]
$v_{i\infty}$	induced velocity at infinity [m/s]
V_z	axial velocity ($V_z = 0$ in hover flight) [m/s]
b	number of blades
c	airfoil chord length [m]
V_{airfoil}	local velocity encountered by airfoil due to rotation [m/s]
C_l, C_d	airfoil lift and drag coefficient
θ	airfoil pitch angle [°]

The induced velocity at the downstream position $V_{i\infty}$ (see Figure 1.2 and Equation 1.9) is computed from a wake contraction formula. Multiple formulae are available: a constant value chosen by the user, an empirical law obtained from tilt rotor experiments or a local computation of contraction.

2.1.3 Assessment in hover: comparison to ORPHEE blades measurements

Presentation of the four ORPHEE blades and their measurements was given in Section 1.2.6. To study HOST's capability to represent the hierarchy of these four blades, simulations using various computational parameters will be tested. In all cases, the goal of this study is to numerically reproduce the measurements that are illustrated in Figure 2.10. Initially, five induced velocity models are tested and compared to measurements. Based on these comparisons, the best induced velocity models are selected for further parametric studies. Namely, we check the effect of blade deformation and corrections described in Section 2.1.1. In all comparisons, we focus on hover flight performance expressed in terms of Figure of Merit (F.M.), as a function of rotor load coefficient $\bar{Z}$. Figure 2.10 shows measurements results.

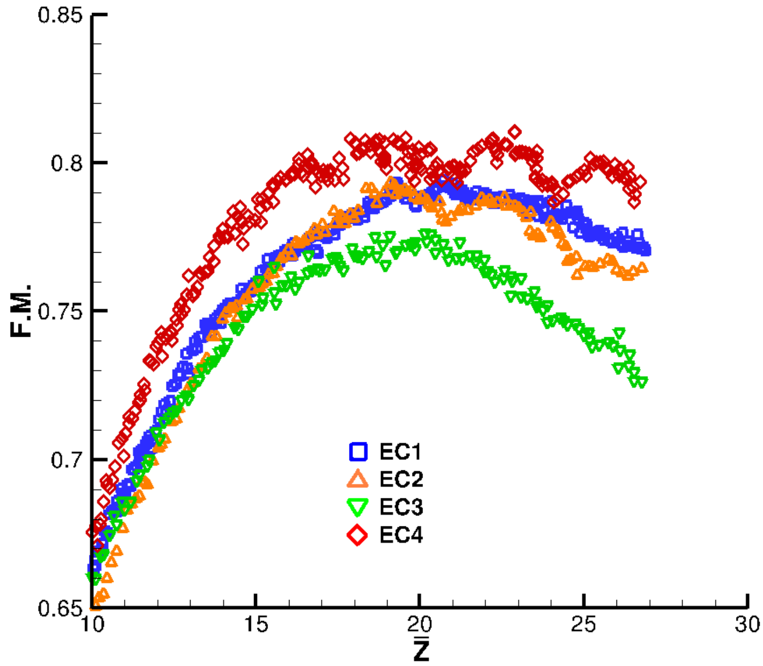

Figure 2.10: F.M. as a function of $\bar{Z}$ for the four ORPHEE blades at $V_{tip} = 220$ m/s

Effect of induced velocity models

Meijer-Drees Meijer-Drees being the simplest and oldest model, which was principally used in previous rotor designs, it is of interest to assess its capability of reproducing ORPHEE's blade hierarchy. As seen in Figure 2.11 (upper left), the EC4 blade indeed is expected by HOST to outperform the other three blades. While the EC3 blade is correctly predicted to have the worst hover performance, the difference in F.M. between EC1 and EC2 as measured is not reproduced by HOST. This discrepancy, though not measured, was already expected from theory as explained in Section 1.2.6.

Local momentum method Compared to the constant induced velocity field along the blade as given by Meijer-Drees, the Ring method should give a better representation of local induced velocity. Indeed, inflow fields vary along blades, as shown in Figure 2.12 for $\bar{Z} = 20$. But hover performance prediction is not really improved, as presented in Figure 2.11 (upper

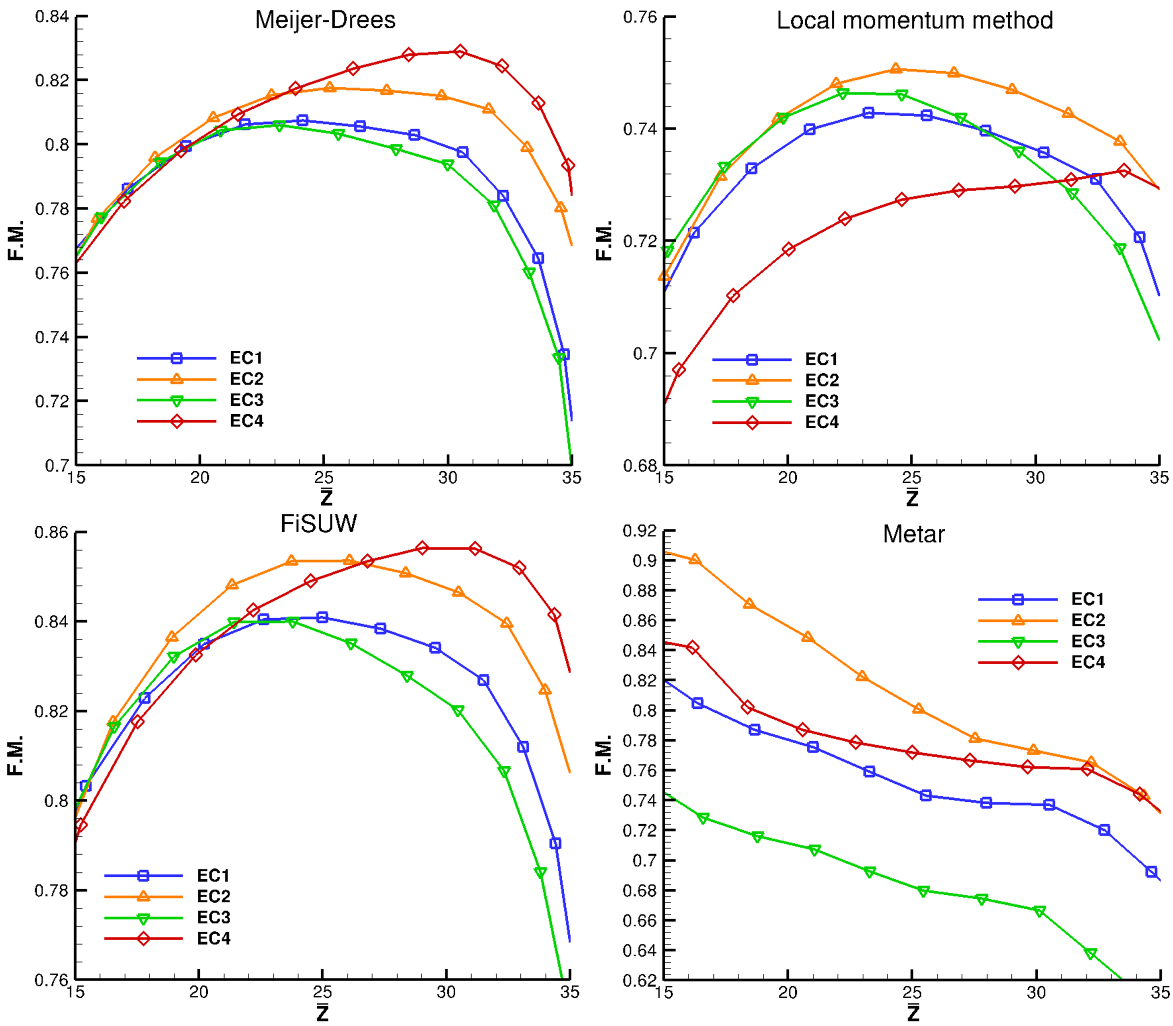

Figure 2.11: HOST simulations of four ORPHEE blades in hover with Meijer-Drees, Local momentum method, FiSUW and Metar

right), showing blade hierarchy is not predicted correctly. This may be explained by the following:

- As said in Section 1.2.2, optimal hover performance is achieved for a constant induced velocity distribution. This is achieved better by EC2, which indeed attains the highest F.M.

- High average induced velocity is foreseen for EC4. Since F.M. is inversely proportional to induced power, which is computed from average induced velocity, a higher average inflow will lead to lower hover performance. Indeed, EC4 is largely outperformed by the three other blades which can be explained by its induced velocity field.

- Differences in inflow field of EC1 and EC3 are limited compared to EC2 and EC4, and no direct link between induced velocity and F.M. is found.

Whereas the induced velocity field gives a direct explanation for hover performance as predicted by the Ring method, blade hierarchy is not correctly foreseen. This discrepancy may directly be attributed to incorrect representation of induced velocity. These conclusions hold for all options of contraction ratio (fixed coefficient, tested for 1.4, 1.6 (for which results are given here) and 1.8; contraction by an empirical law; and local contraction computation) that are proposed by HOST.

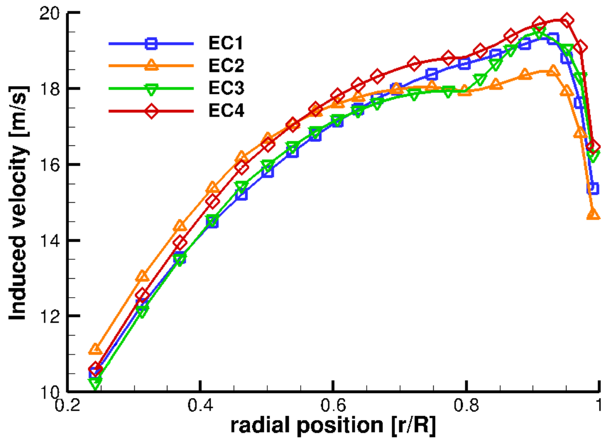

Figure 2.12: Induced velocity as predicted by HOST simulations with local momentum method of four ORPHEE blades in hover, $\bar{Z}$=20

FiSUW FiSUW predicts best hover performance for EC4, as seen in Figure 2.11 (lower left). As for Meijer-Drees, EC2 is simulated to have a higher F.M. than EC1, in contrary to measurements but expected from theory. Maximum F.M. of EC3 and EC1 are close, but EC1 retains this value for a larger range of rotor lift. Overall, blade hierarchy as predicted by FiSUW is close to measurements, only EC1 is positioned differently with respect to EC2 and EC3. The here presented results are issue from FiSUW simulations with 4 Legendre polynomials for radial distribution of the inflow field. Tests with 8 and 36 polynomials were performed but did not demonstrate improvements of blade hierarchy representation.

Metar Metar model produces unexpected curves of F.M. as a function of $\bar{Z}$ (Figure 2.11, lower right), not only because of their shape, but also for their absolute values. In terms of hierarchy, only the EC3 is correctly identified as the less performing blade. Apparently, Metar's wake shape does not correctly represent an induced velocity field in hover.

Mint Mint requires user selection of various parameters that highly influence computation time and accuracy:

- *Time step* As Mint uses a time-stepping scheme to create a wake field, a time step of vortices release and wake and equilibrium computation of $\Delta\psi = 5°$ was chosen. While a time step of 2° is required for capturing phenomena like BVI, 5° be should sufficient for creating a wake field for performance computations [32] while reducing computation time as much as possible.

- *Wake age* Since vortices and rotor wake remain close to the rotor in hover, a sufficiently long wake age needs to be considered when using Mint. Wake fields corresponding to computations with wake ages of 3 and 10 rotor rotations are presented in Figure 2.13. For a longer wake age, convergence is only found for a longer simulation duration so that the computation of 3 rotor rotations wake age is simulated over 48 rotor rotations in total and 80 rotor rotations were performed for converging the simulation with a wake age of 10 rotor revolutions. As seen in Figure 2.14, wake age has a significant influence on absolute value of average F.M. and oscillations about this performance value. Even if blade hierarchy seems to be correct, these results are obtained for a fixed collective pitch angle (10°). For a real comparison, a complete F.M. polar as a function of collective pitch angle should be created.

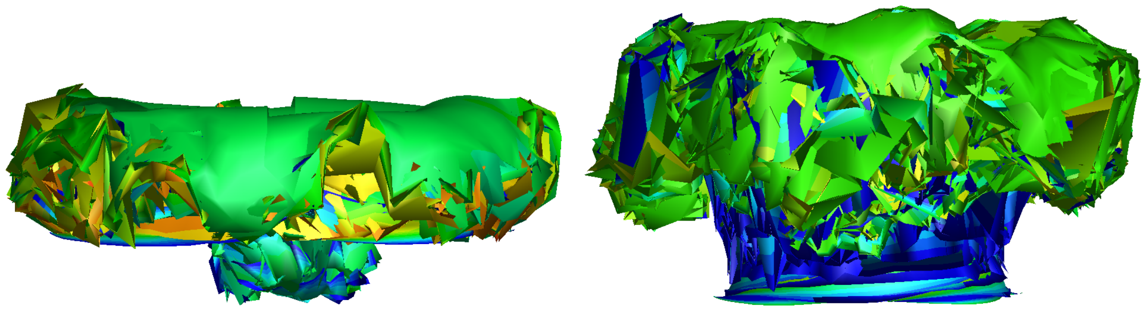

Figure 2.13: HOST simulations with Mint model of EC1 blade for (left) wake age of 3 rotor rotations, simulation duration of 48 rotor rotations and (right) wake age of 10 rotor rotations, simulation duration of 80 rotor rotations

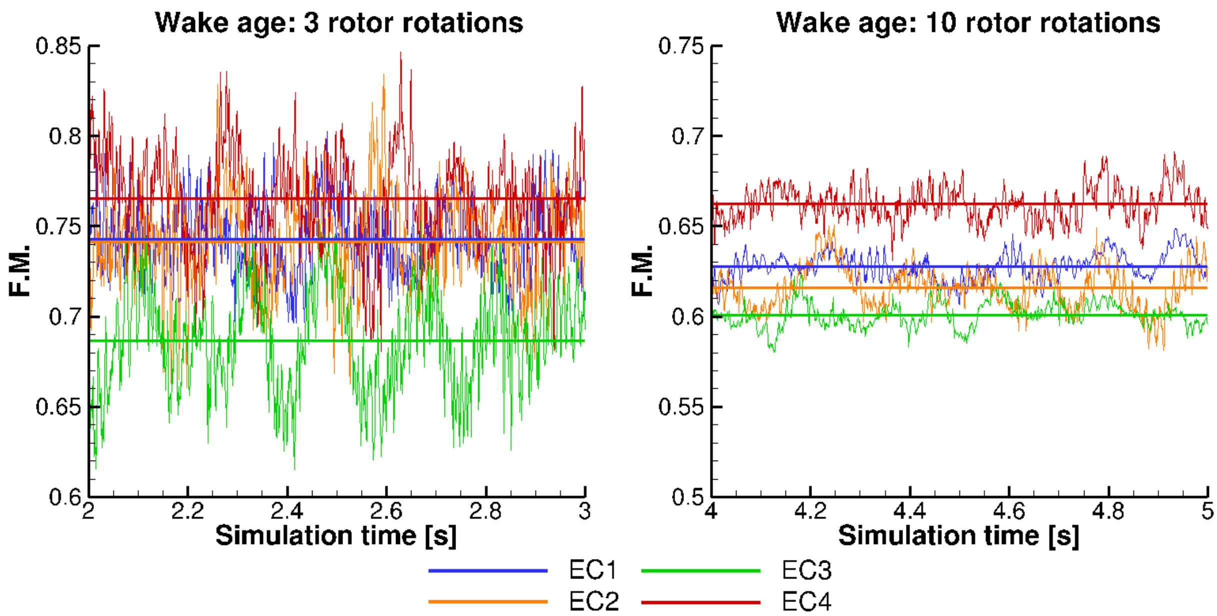

Figure 2.14: F.M. convergence for HOST simulations with Mint model of ORPHEE blades for a wake age of 3 and 10 rotor rotations

In total, computing 48 rotor rotations takes 19 hours and 80 rotations requires up to 32 hours on a single core processor. Compared to all other HOST simulations, for which simulation takes at maximum 30 seconds, Mint's simulation time is unacceptable high for optimization purposes. When parallelizing on 8 processors, the computation time would be comparable to a CFD simulation in hover. Considering the optimization background of the present study, no complete analysis of Mint's capabilities for predicting hover performance is performed.

Local induced velocity To better understand global performance predictions provided by the induced velocity models under investigation, we compare the local inflow fields along the blade radius of all models. Only [90] provides inflow measurements along a blade in hover, allowing for a qualitative comparison to numerical results from HOST. Inflow and tip vortex measurements were made on a blade with a span of 0.4m, using a NACA2415 airfoil. Three blade tips were tested: rectangular, swept and tapered. Even if image quality is not sufficient to distinguish the effect of blade tip shape, an overview of non-dimensional induced velocity along the blade is given in Figure 2.15.

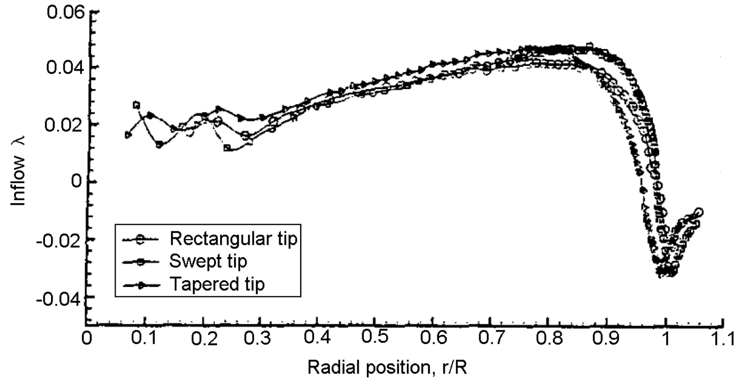

Figure 2.15: Inflow along blade radius, measurements in hover as performed by [90]

Comparing inflow field shape to induced velocity simulations of EC1 at a $\bar{Z}$ of 25 as presented in Figure 2.16, it is immediately seen that Metar's inflow reduction near the blade tip is unexpected. Even if a linear field as Meijer-Drees is not too far off with respect to measurements for the main blade part, lift loss near the tip is not reproduced by this model. FiSUW and the local momentum method provide better agreement with measurements.

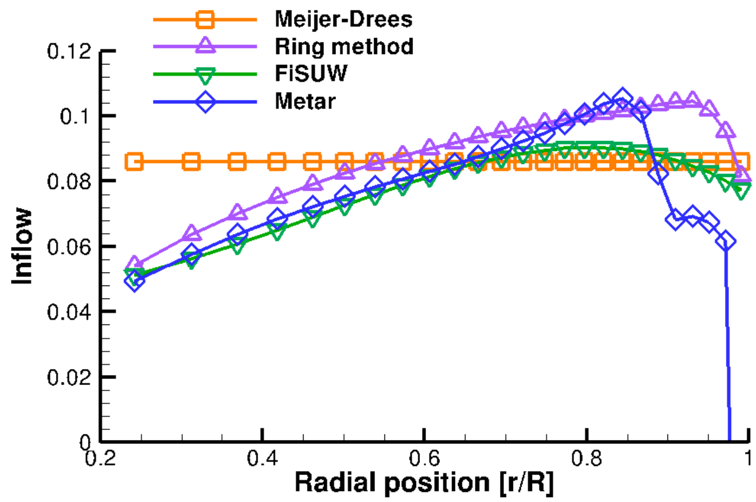

Figure 2.16: Induced velocity distributions of four induced velocity models over EC1 blade for a $\bar{Z}$ of 25, as computed with HOST

Conclusions on induced velocity field modelling Several conclusions may be drawn from this study:

- Although hover is often seen as an aerodynamically simple configuration, rotor performance is not yet predicted with sufficient accuracy by comprehensive rotor codes like HOST. This is true not only for absolute values of global performance indicators, but also for relative comparison of different blade geometries. No matter the induced velocity model, maximum F.M. is always predicted for a too high rotor load, compared to measurements. A possible explanation would be related to the use of wind tunnel data, which may not always be representative of real flight. Especially surface roughness and flow laminarity may be dissimilar between wind tunnel measurements and real flight conditions. As both affect boundary layer transition, HOST computation of stall characteristics and thus maximum rotor performance cannot be expected to be accurate. In addition, as only distinct flight conditions are tested in the wind tunnel, HOST interpolates coefficients between these conditions. Yet, linear interpolation is most likely not the best representation at some flight conditions.

- Induced velocity models influence rotor performance simulation in hover largely, again both in absolute value as in blade hierarchy prediction. Lack of precise experimental data of the induced velocity field in hover makes it difficult to locally compare inflow fields. This kind of measurements would greatly help in understanding and improving inflow field modelling for comprehensive rotor codes.

- Taking into account for the above, FiSUW is selected for performing hover computations with HOST, as this model's blade hierarchy prediction is closer to measurements than Metar and Local momentum method, and because the general shape of the inflow field is closer to hover measurements than Meijer-Drees.

Rigid vs. elastic blade modelling

Even if one of the assumptions used in the present work is that blades do not undergo elastic deformation, in real life rotor blades change shape at all flight conditions. Elastic blade modelling in HOST is based on discretized rigid elements that are connected by fictive links. Bending and torsion deformations are computed via a modal basis and are applied through these links. Impact of this elastic modelling on hover simulations using FiSUW is presented in Figure 2.17. It illustrates that differences between rigid and elastic blade modelling are minor, especially compared to the impact of induced velocity model. This conclusion was also found from rigid-elastic modelling comparison of all other tested induced velocity models. It should be noted though, that this conclusion only holds for these nearly straight blades and for this modelling approach. Different behaviour may be observed for blades with larger sweep angles.

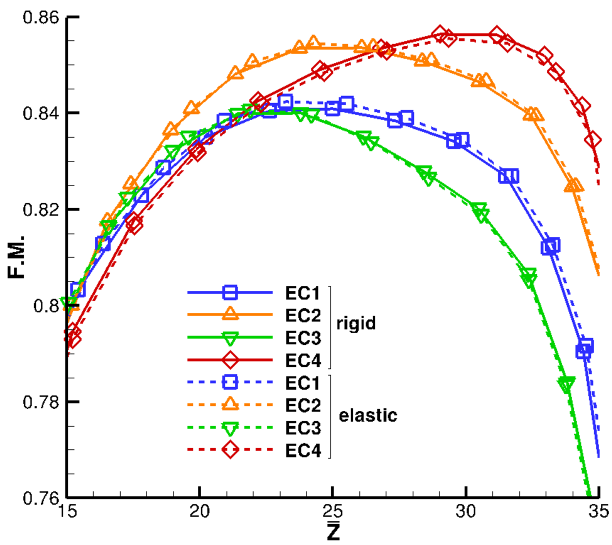

Figure 2.17: HOST simulations with FiSUW model of four ORPHEE blades in hover, rigid and elastic blade modelling

Corrections for Reynolds number effects and sweep angle

As described earlier, aerodynamic modelling in HOST may be improved by applying empirical corrections for Reynolds number effects and sweep angle. Hereafter, we retain the FiSUW model and check the effect of these corrections on predicted performance. As a default, these corrections were employed in preceding simulations, so that they will now be removed for comparison.

Reynolds correction This correction is meant to take into account stall characteristics due to Reynolds number difference in polar measurements and computational flow conditions. Its influence on F.M. is presented in Figure 2.18, showing polars with and without Reynolds correction for each of the four blades. As the Reynolds correction affects friction drag only, its influence lowers at higher $\bar{Z}$ values where drag mainly consists of induced drag. Since all four blades use the same airfoils, Reynolds correction influence may be expected comparable for all blades. Thus, blade hierarchy does not change when applying or not the Reynolds correction.

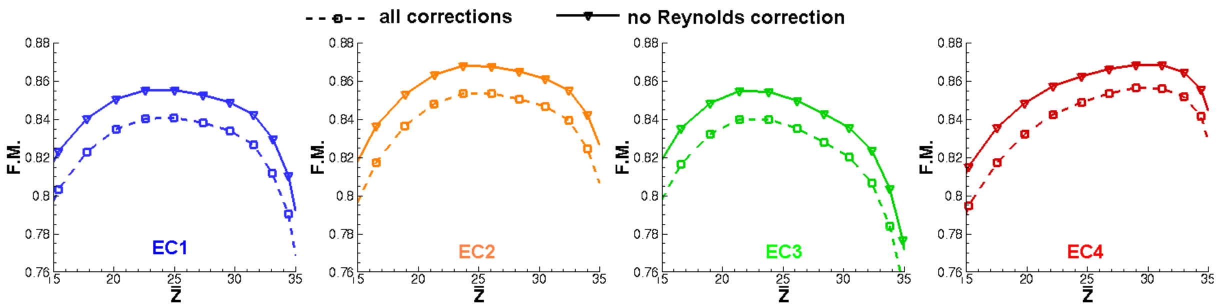

Figure 2.18: HOST simulations with FiSUW model of four ORPHEE blades in hover, with and without Reynolds correction

Sweep correction Sweep correction increases maximum lift coefficient and adds a radial drag component. As expected, EC4 is most affected by this correction, seen in Figure 2.19. Especially at high $\bar{Z}$, the correction causes an exponential increase of F.M. due to modification of maximum lift coefficient. Variation of F.M. of the other three blades comes from their blade tip shape; the only part having a certain sweep angle. Even if sweep correction influence is non-negligible for EC4, blade hierarchy does not change when applying or not this correction.

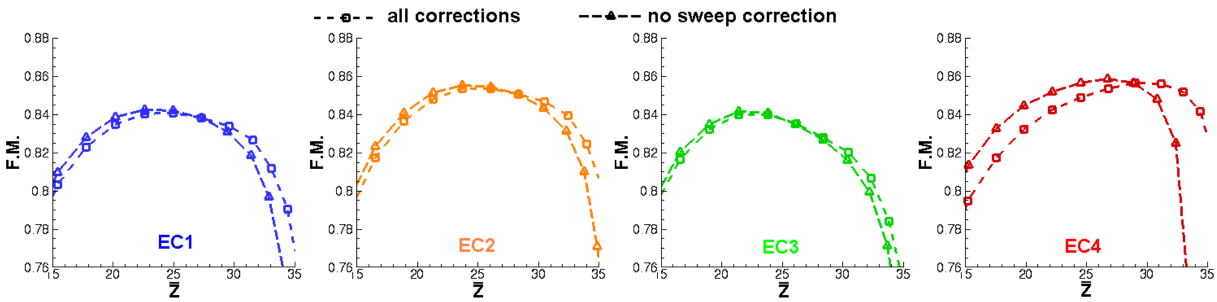

Figure 2.19: HOST simulations with FiSUW model of four ORPHEE blades in hover, with and without sweep correction

2.1.4 Assessment in forward flight: comparison to induced velocity field measurements

As explained in Section 1.1, for helicopters in forward flight the local velocity consists of forward flight velocity, local contribution of rotational velocity and induced velocity. Also local angle-of-attack of incoming flow changes with the position over the rotor disk. Induced velocity in forward flight is in the order of magnitude of 0 to 10 m/s, which is small compared to the forward flight velocity which is about 70 m/s ($\simeq$ 250 km/h) on the advancing blade and to the local contribution of the rotational velocity (ranging from about 65 m/s at 0.3R to 220 m/s at the blade tip on a 7m-radius blade rotating at 300 rpm). Thus, the absolute value of the induced velocity is less than 3% of the total local velocity at the blade tip and about 7% near the blade root.

Nonetheless, lift variation at different positions over the rotor disk and subsequent induced velocity differences lead to a significant dependency of induced velocity on local operating conditions over the rotor disk. Thus, it is important to model these effects accurately. In the following, different induced velocity models available in HOST are assessed against experimental data from the NASA. These measurements are procured in such a way that an induced velocity field equivalent to HOST's models is obtained. The main difference between measurements and HOST models is the position of the induced velocity field: while measurements were taken at different heights above the tip path plane, HOST uses induced velocity locally at the blade surface. Measurements are positioned 1 chord (6.6 cm in this case) above the blade surface near the blade tip, which increases towards the blade root due to the rotor cone angle.

NASA inflow measurements

Between 1988 and 1990, induced velocity measurements were performed at the NASA Langley Research Center [8, 9, 10, 11, 12, 13, 14, 15, 16, 17, 18]. A reduced-scale model of a helicopter rotor was placed in the 14- by 22-foot (4.2 by 6.7m) subsonic wind tunnel. Two-component Laser Velocimetry measurements were made above the rotor tip path plane (TPP) at positions located between 0.2R and 1.12R, see Figure 2.20. At each data acquisition point, at least 4096 measurements were taken, or until 1 minute of measurements had passed. The arithmetic mean of all these measurements is used in the present analysis. Induced velocity was for all cases measured at one chord above the tip path plane. Influence of this position was evaluated by reducing to 0.75 and 0.5 chord above the tip path plane for measurements of a rectangular blade for a μ of 0.23 and 0.3. Tests were also performed for 5 different values of advance parameter μ; the different tested combinations of μ and data acquisition point above TPP are given in Table 2.1.

Table 2.1: Position above the rotor tip path plane of the various inflow measurements performed by NASA

	μ	0.15	0.23	0.30	0.35	0.40
operating	V_H [km/h]	103.04	158.00	206.09	240.43	274.78
conditions	$\alpha_{shaft}[^\circ]$	-3	-3.04	-4.04	-5.70	-6.80
blade	Rectangular	$1\bar{c}$	$1\bar{c}$, $0.75\bar{c}$, $0.5\bar{c}$	$1\bar{c}$, $0.75\bar{c}$, $0.5\bar{c}$	$1\bar{c}$	$1\bar{c}$
planform	Tapered	$1\bar{c}$	$1\bar{c}$			

The four-bladed 0.86m-radius rotor was equipped with two sets of blades: rectangular and tapered ones. Rectangular blades have a linear twist law of -8° whereas tapered blades have a linear twist law of -13°. The tapered blade is illustrated in Figure 2.21. Blades were made as stiff as possible, to reduce aeroelastic effects.

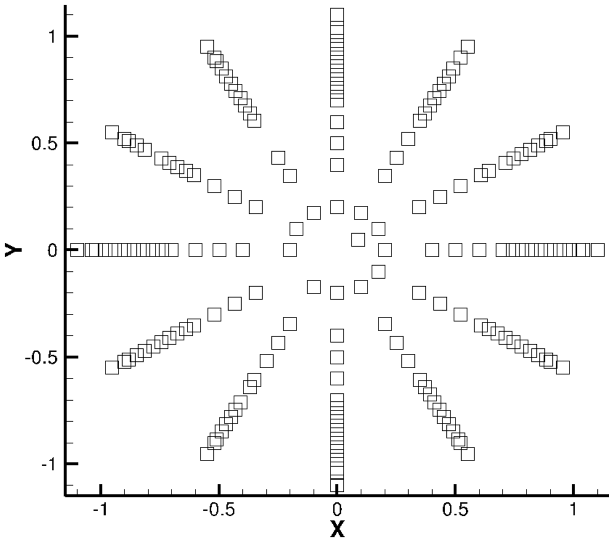

Figure 2.20: Data acquisition points over the rotor disk (rectangular blade planform, μ=0.23, measurements $1\bar{c}$ above TPP) [13]

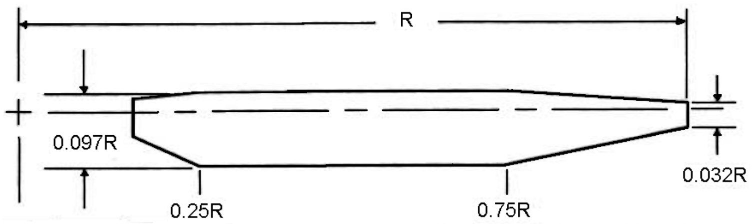

Figure 2.21: Tapered blade planform, from [25]

In the measurements, a fuselage was mounted under the rotor. As discussed in [25] and [143] and as illustrated in Figure 2.22, this slender fuselage is expected to have a small influence on rotor inflow. At the front part of the rotor, the fuselage may increase upward directed induced velocity (upwash), while effects on the rear half of the rotor are expected to be negligible due to separated flow behind the rotor shaft. In the following, and as was the case in [25], no fuselage will be simulated in the computations.

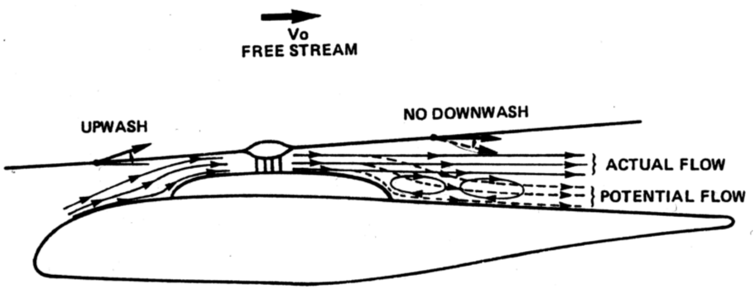

Figure 2.22: Influence of fuselage on rotor inflow, from [134]

HOST computations

The selected rotor trim for HOST computations is based on setting longitudinal and lateral flapping angles to zero while imposing the rotor thrust coefficient that was given in measurement reports. The rotor controls of collective, longitudinal and lateral pitch angles are used for finding this trim position. The forward flight speed and rotor shaft angle are imposed as well.

An azimuthal discretization of 68 positions are used for most of the simulations, except for Metar, where a maximum of 24 azimuthal positions are used. The effect of this discretization is tested and appeared to have no significant influence on results. For computations with the Mint model, an azimuthal discretization of 36 positions is used. With a rotational speed of 2113 tr/min, the time step in these simulations equals $3.94 \cdot 10^{-4}$ seconds (time required for the blade tip to travel a distance equivalent to the azimuth step of $\psi = 5°$). Numerical convergence of rotor trim is obtained after 1 second of simulation, in which a total of 35 rotor rotations are simulated. The Meijer-Drees model is used to initialize the wake during one rotor rotation. The maximum wake age kept in simulations corresponds to 3 rotor rotations.

As described in the measurement reports, in the experiment blades were made as stiff as possible to limit blade dynamic effects. Therefore, rigid blade modelling is used for the HOST computations as well. To account for the effect of a tip vortex, the lift coefficient is artificially set to zero from 0.98R on for the FiSUW, Metar and Mint models.

Sign conventions used in all images are presented in Figure 2.23. Induced velocity is given positive for flows directed upwards through the rotor (upwash).

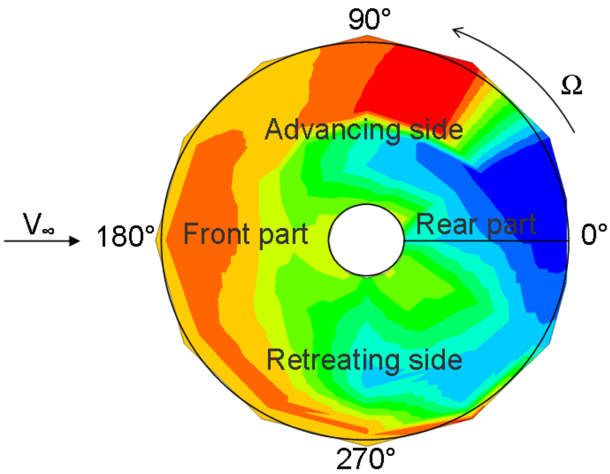

Figure 2.23: Sign convention of inflow measurements and comparisons

Out of the measurement matrix, three combinations are selected for HOST simulations:

1. Rectangular blade, $\mu = 0.23$
2. Rectangular blade, $\mu = 0.40$
3. Tapered blade, $\mu = 0.23$

As these data points contain low-speed and high-speed points, as well as both blade geometries, they will allow for giving an overview of HOST's prediction capability. As said before, the measurement position does not coincide with the height position HOST uses for the induced velocity model. The effect of measurement position on induced velocity field is examined using the measurements at 1, 0.75 and 0.5 $\bar{c}$ above the TPP as done for the rectangular blade at $\mu = 0.23$.

Rectangular blade at $\mu = 0.23$

The low-speed test case with $\mu = 0.23$, corresponding to $V_H = 158.00$ km/h for a rotor speed of 2113 rpm, is used for measuring at three different positions above the rotor tip path plane (TPP, see Section 1.1.2). As seen from measurements in Figure 2.24, the induced velocity increases in magnitude when approaching the rotor tip path plane. This is indeed expected due to the effect of wake contraction.

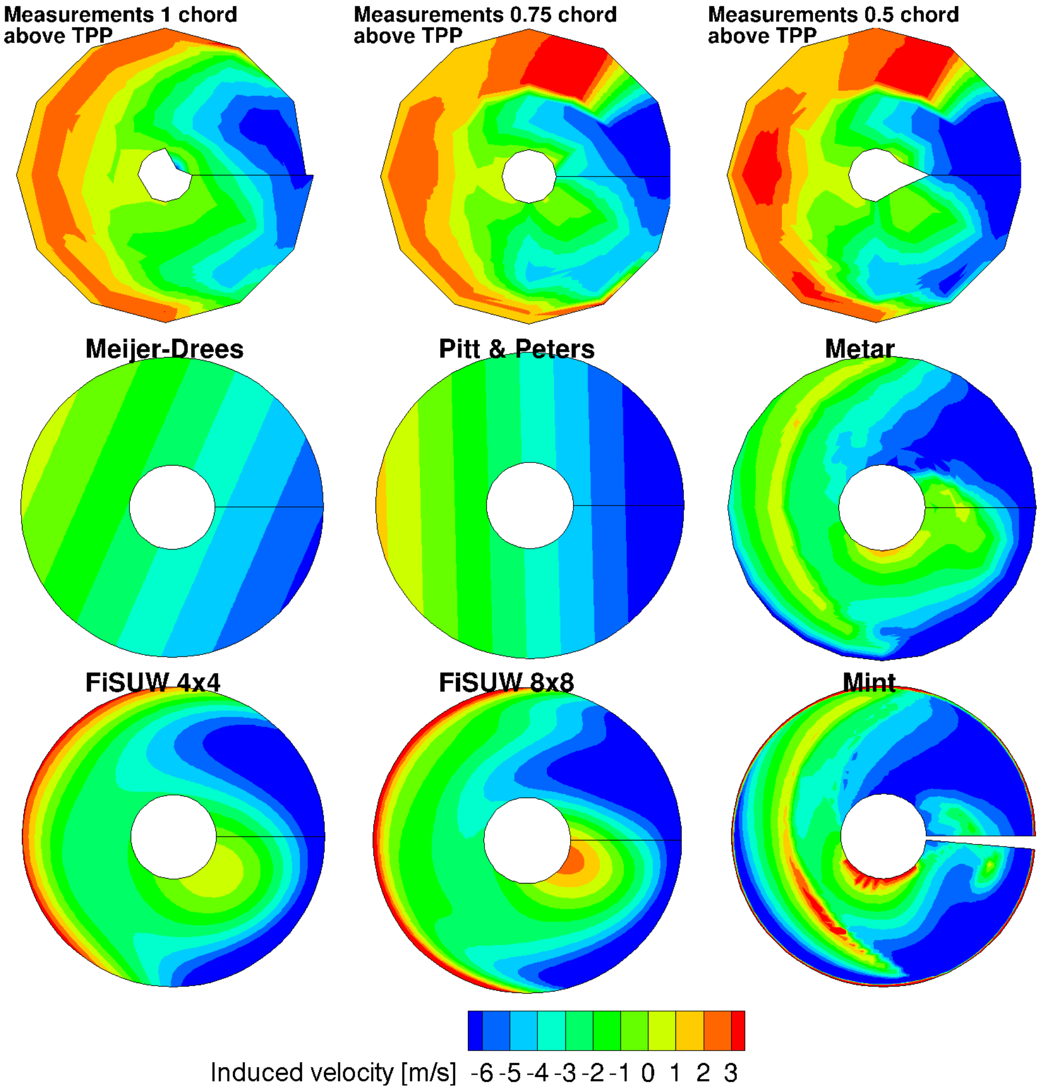

Figure 2.24: Comparison of the induced velocity field as measured by [10, 13, 15] and as computed by HOST for various induced velocity models; μ=0.23, rectangular blade

A first global conclusion of HOST computed inflow fields presented in Figure 2.24 is that the order of magnitude of all computed induced velocity fields is close to measurements. From a more local point of view, the shape of the induced velocity field as computed with HOST are very different: the Meijer-Drees and Pitt & Peters models present a tilted plane with first cosine and sine harmonics. The Meijer-Drees induced velocity field is more tilted towards the advancing side compared to Pitt & Peters, but it is difficult to justify or reject this effect with respect to measurements. The Pitt & Peters model has a stronger downwash at the rear of the rotor disk, which is somewhat closer to experiments, especially for measurements performed closer to the tip path plane. Despite correct general tendency of the induced velocity field that has been captured by these linear models, local variations are not seen.

A better description of the downwash is given by non-linear models such as Metar, Mint and FiSUW. Upwash in the front part of the rotor disk is underestimated by these models. This may in part be due to the fact that the fuselage was not taken into account, noticed as well in [25]. FiSUW predicts an upwash region near the tip on the front part of the rotor, although this area is by far too small compared to measurements. The comparable basic principles of Metar and Mint are visible in the front part, where both predict downwash near the tip at the retreating blade side, which is in contrast with experimental data. This effect is stronger for Mint than for Metar. On the rear part of the rotor disk, both FiSUW and Metar predict a zone of downwash that corresponds quite nicely with measurements, as well in terms of value as of positioning on the disk, especially when comparing with the measurements taken at $0.5\bar{c}$ above the tip path plane. This downwash zone is predicted too large by Mint.

The effect of increasing the order of the FiSUW model is considered minor. Although the downwash zone seems to be predicted somewhat better by the 8x8 version, the upwash zone near the blade attachment on the retreating blade is not seen in the measurements.

In conclusion, the Metar and FiSUW models both capture the induced velocity field, especially the downwash zone. Rotor upwash is not predicted correctly by any of the models. Linear models give a correct prediction of the induced velocity field, but these hold only as a first order estimate. The Mint model captures some of the main effects, but predicts a far too strong field in the front part and on the retreating blade side.

Rectangular blade at $\mu = 0.40$

Secondly, a high speed test case is considered with an advance ratio of 0.40 and a rotor speed of 2113 rpm, so that the forward flight speed equals 274.78 km/h. Measurements were made only at 1 chord above the tip path plane and are shown in Figure 2.25. Taking into account the two test cases for which measurements were made at 1, 0.75 and 0.5 chords above the tip path plane, it may be expected that approaching the tip path plane leads to an increase of the downwash zone, but no clear statement can be made on the upwash area.

As for the low speed test case, the linear models give a first order approximation, but they provide a poor representation of the measurements. Values predicted by the Meijer-Drees model are off with respect to experimental results.

At this speed, Metar and Mint fail to correctly simulate the induced velocity field. In particular a zone of downwash at the tip on the retreating blade is incorrect; this zone was already somewhat visible at lower forward flight speed, but is exaggerated at high speed. The zone of upwash in the inboard region on the retreating blade side is too large and induced velocity is predicted too strong. It seems that Mint amplifies the erroneous zones of the Metar computation so that this simulation is even further off with respect to experimental data.

Best prediction of the induced velocity field at high speed is given by FiSUW. The downwash area is predicted correctly, especially when taking into account for the increase expected when approaching the tip path plane. Upwash in the front part of the rotor as simulated by FiSUW does not correspond to measured data, which may again in part be due to the presence of a fuselage during the measurements. The difference between the two FiSUW generated fields (4x4 and 8x8) is very limited, so that no preference for either of the two can be stated.

Tapered blade at $\mu = 0.23$

In the tapered blade test case an advance ratio of $\mu = 0.23$ was used again, corresponding to a forward flight speed of 158.00 km/h. Experimental data and computed induced velocity field are given in Figure 2.26.

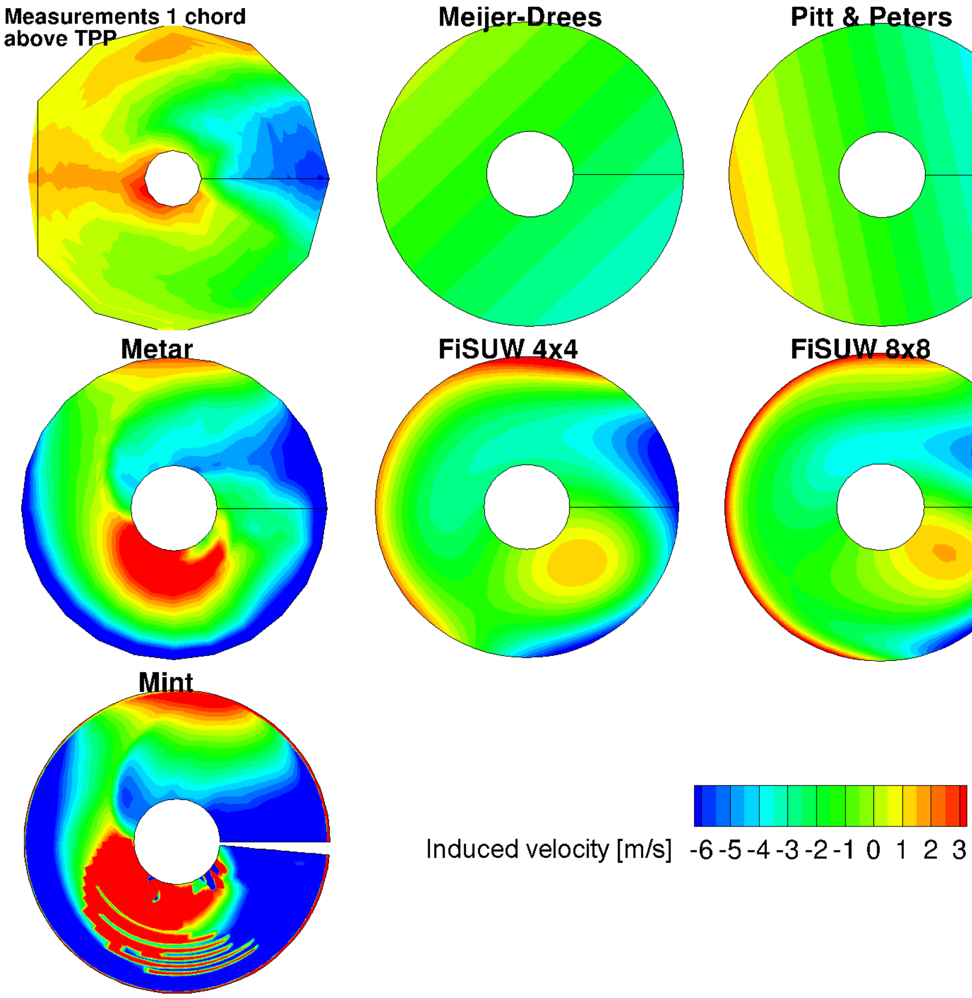

Figure 2.25: Comparison of the induced velocity field as measured by [18] and as computed by HOST for various induced velocity models; μ=0.40, rectangular blade

In general terms, all induced velocity models predict the field with better precision than for the rectangular blade. Out of the two linear models, Pitt & Peters better estimates minimum and maximum values of the induced velocity, but both remain first order estimates.

The higher-order models provide a better estimation of the induced velocity field than Meijer-Drees and Pitt & Peters. The downwash zone on the rear side of the rotor is correctly predicted by FiSUW and Metar. Mint predicts a negative induced velocity in this area, but not at the same position as measurements. Upwash over the front side of the rotor disk is predicted too strong and over a too small zone by the FiSUW model. Similar inadequacies are found from Metar and Mint, to which is added the erroneous prediction of the location of upwash: too much on the advancing blade side compared to measurements. The zone of slight upwash near the blade root is best predicted by Metar, while FiSUW and Mint simulate a too strong upward induced velocity. The location of this upwash is not correctly estimated by FiSUW.

In conclusion, the tapered test case is better reproduced by all non-linear induced velocity models than for the two rectangular blade cases. The FiSUW model again correctly predicts main aspects of the flow field. The Metar and Mint models approach the measurements as well but are particularly off in the upwash zone on the front side of the rotor disk. As was the case for previous test cases, the linear models are limited to the first order approximation that is inherent to their definition.

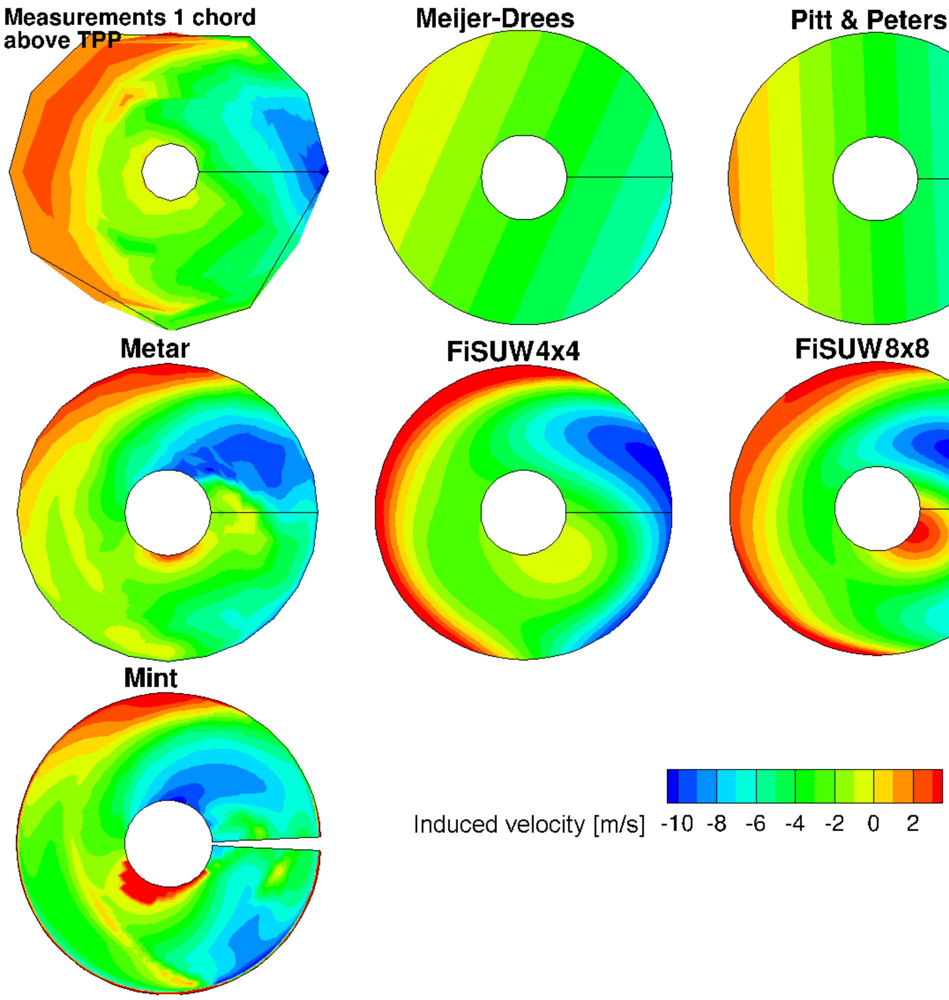

Figure 2.26: Comparison of the induced velocity field as measured by [12] and as computed by HOST for various induced velocity models; μ=0.23, tapered blade

Conclusions on induced velocity model comparison

All three test cases have demonstrated comparable tendencies that can be summarized as follows:

- Linear models are limited by their definition to a global overview of the induced velocity field. The order of magnitude of the flow field is better estimated by Pitt & Peters than by the Meijer-Drees model. Both models lack a local description of the field.

- The FiSUW model represents main characteristics of the wake field with sufficient accuracy for all test conditions.

- The prescribed and free wake models are irregular in their prediction. Whereas modelling of the tapered blade test case is relatively close to measurements, representation of both rectangular blade cases is not correct. Especially at high-speed forward flight, Metar and Mint predictions are off with respect to measurements over a large zone of the rotor disk.

As the final objective of this study is to choose an induced velocity model to be used within the rotor blade optimization loop, simulation time cannot be neglected. Table 2.2 presents average computation times of HOST simulations of an isolated rotor using different induced velocity models. It should be noted that these isolated rotor computations increase with a factor of 10 to 100 for complete helicopter simulations. So, while absolute differences are still minimal, relative differences in simulation time between induced velocity models are of importance for more complicated HOST computations.

As expected, computation time increases with computational complexity. While the simulation time remains acceptable for the linear models and FiSUW, Metar modelling significantly increases computation time. Mint requires an unacceptable computation time for predicting the induced velocity field.

Taking into account for simulation accuracy and computation time, the FiSUW (4x4) model is selected for representing the induced velocity field as required by HOST.

Table 2.2: Average computation time of HOST simulations of an isolated rotor using various induced velocity models

Model	Average computation time [s]
Meijer-Drees	0.31
Pitt & Peters	0.35
FiSUW 4x4	0.41
FiSUW 8x8	1.40
Metar	2.86
Mint	$\sim$ 14 hours

2.1.5 Assessment in forward flight: comparison to ORPHEE blades measurements

Out of the large measurement matrix of forward flight experiments of the four ORPHEE blades, two sets of data points were selected for comparison to HOST simulations. HOST equilibrium of these two equilibrium laws is given by setting free the left-hand side parameters to impose parameters on the right-hand side:

- American law: DT0 DTC DTS TETA $\rightarrow$ BC-RP=0 BS-RP=0 C_{XS}=0.1 $\bar{Z} = 15$
- Modane law: DT0 DTC DTS TETA $\rightarrow$ BC+DTS=0 BS-RP=0 C_{XS}=0.1 $\bar{Z} = 20$

where DT0, DTC and DTS are collective, lateral and longitudinal pitch angles of the rotor blades, respectively; TETA is the longitudinal pitch angle of the main rotor mast; BC-RP and BS-RP are longitudinal and lateral flapping angles of the rotor blades, C_{XS} is a drag coefficient for simulating fuselage drag and $\bar{Z}$ is the rotor load coefficient. As was the case for hover comparisons, all induced velocity models are tested first, before studying influence of elastic blade modelling and corrections. All comparisons are made for flight speeds varying from $\mu = 0.304$ ($\simeq$ 230km/h) to $\mu = 0.463$ ($\simeq$ 350km/h). Measurement results are given in Figures 2.27 and 2.28.

Induced velocity models

Meijer-Drees Computed values of forward flight performance as a function of μ are displayed in Figure 2.29 for the two rotor laws. Even though curve shapes are not the same for the American law flight case as for measurements, blade hierarchy is in good agreement with experiments for EC1, EC2 and EC3 blades at the three fastest flight conditions. EC4 blade performance, however, is overpredicted for all flight speeds. Nonetheless, the relative performance increase of EC4 predicted by HOST with Meijer-Drees, compared to EC1 and

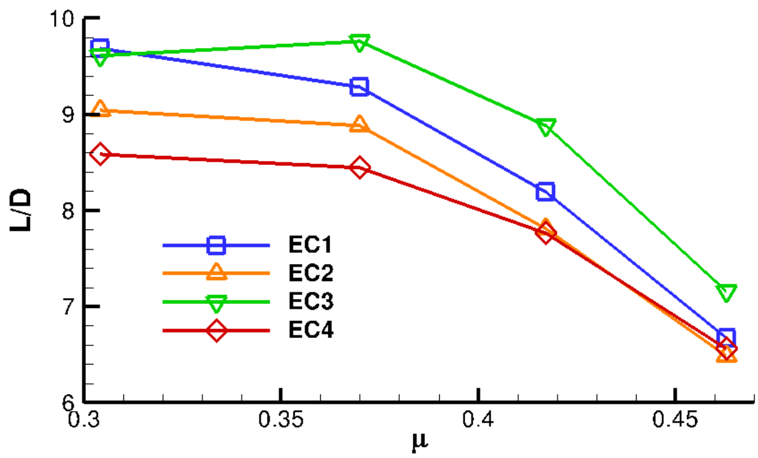

Figure 2.27: Measured L/D as a function of μ, Ω=960 rpm, $\bar{Z}$=15, C_{XS}=0.1, American law

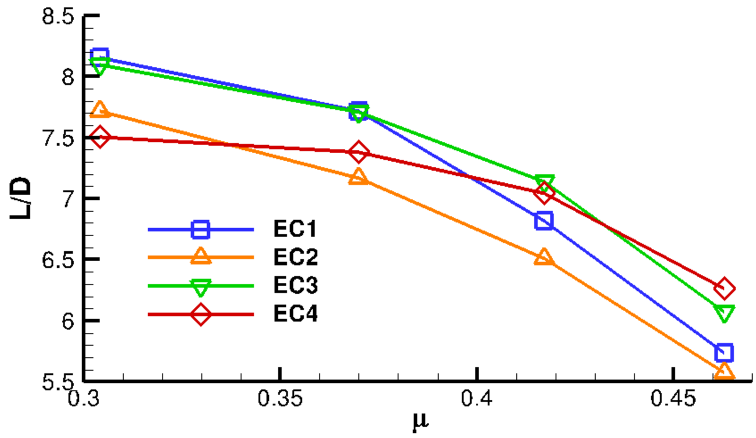

Figure 2.28: Measured L/D as a function of μ, Ω=960 rpm, $\bar{Z}$=20, C_{XS}=0.1, Modane law

EC2, is indeed seen in the measurements as well. Thus, performance of EC4 is overpredicted by the Meijer-Drees model, even if the predicted trends are more or less correct. Modane law computations overpredict EC4 performance with respect to other blades. Also, prediction of relative performance of EC1 and EC2 blades is incorrect.

Another difference of these curves compared to the wind tunnel measurements is the forward flight speed of maximum L/D. For all blades, maximum L/D of wind tunnel measurements occurs at a forward flight speed between 230 and 280 km/h. For both computed flight cases, speed of maximum L/D ratio is found between 280 and 315 km/h. This means that, even if comparable blade hierarchy is found, the aerodynamic flow field cannot be compared, as large changes in flow conditions can be expected with increasing forward flight speed.

Pitt & Peters Pitt & Peters model differs from Meijer-Drees in its description of cosine and sine components of the induced velocity field. Nonetheless, forward flight performance results are comparable, as seen from Figure 2.30. Blade hierarchy is similar to Meijer-Drees results, only absolute values are somewhat lower as computed with Pitt & Peters.

FiSUW FiSUW is chosen to use 4 Legendre polynomials for expressing radial distribution and 4^{th} order harmonics of Fourier series for azimuthal variation of the inflow field. Blade hierarchy, as presented in Figure 2.31, is predicted correctly for EC1, EC2 and EC3 of the

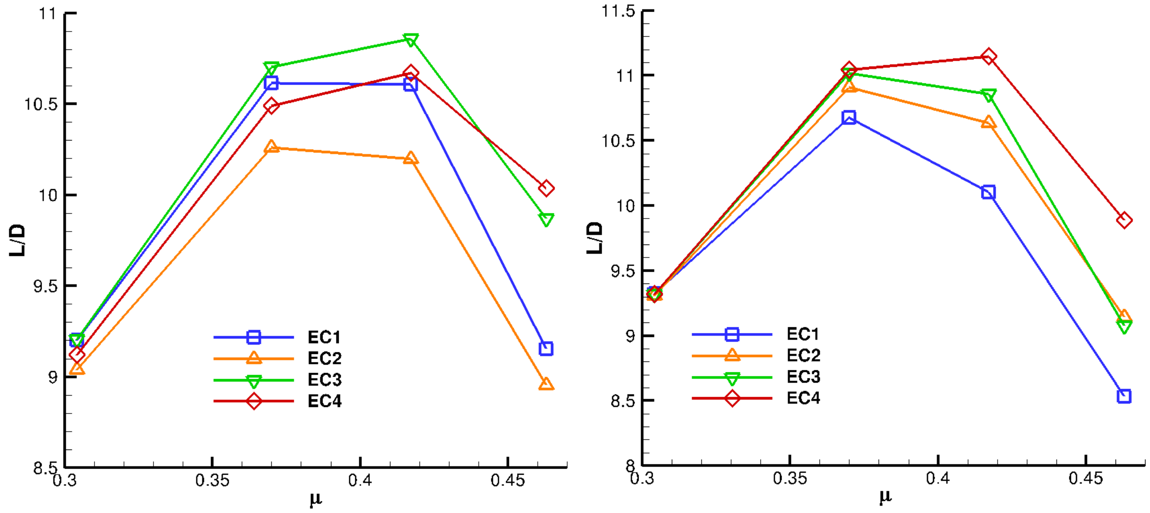

Figure 2.29: HOST simulations with Meijer-Drees of four ORPHEE blades in forward flight at $\bar{Z} = 15$, American law (left) and $\bar{Z} = 20$, Modane law (right)

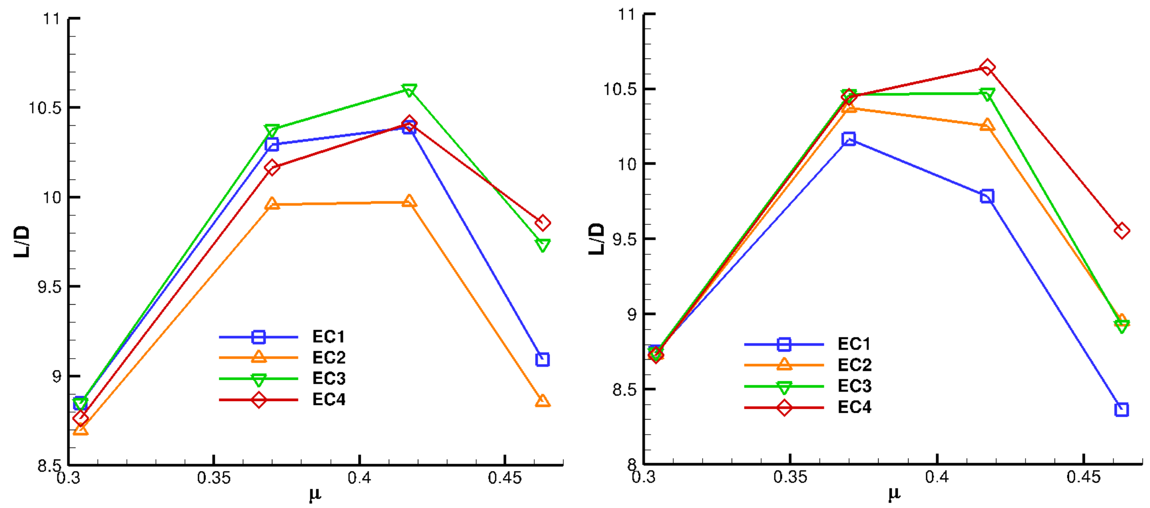

Figure 2.30: HOST simulations with Pitt & Peters of four ORPHEE blades in forward flight at $\bar{Z} = 15$, American law (left) and $\bar{Z} = 20$, Modane law (right)

$\bar{Z} = 15$ case, similar to Meijer-Drees and Pitt & Peters models. Also, EC4 performance is overpredicted at all forward flight speeds, even if this overestimation is limited at high flight speeds. Thus, at high μ FiSUW approaches measurements better than previous induced velocity models.

When flight conditions following the Modane law are considered, however, FiSUW predictions are completely off compared to measurements. The general trend of L/D ratio is incorrect as well: the EC2 blade is predicted to possess the better performance at high speed, whereas this blade has the lowest measured performance in wind tunnel experiments. Prediction of blade hierarchy between EC1, EC3 and EC4 blades at high speed is not too bad, even if the EC4 blade's performance is in reality better than EC3 at μ=0.463. At low speed, blades are predicted to have very similar performance (all blades are within 0.2 points of L/D at μ=0.304 and within 0.4 points at μ=0.37, while measured variances are 0.65 and 0.55, respectively).

The large discrepancy between measurements and FiSUW simulations is due to a perfor-

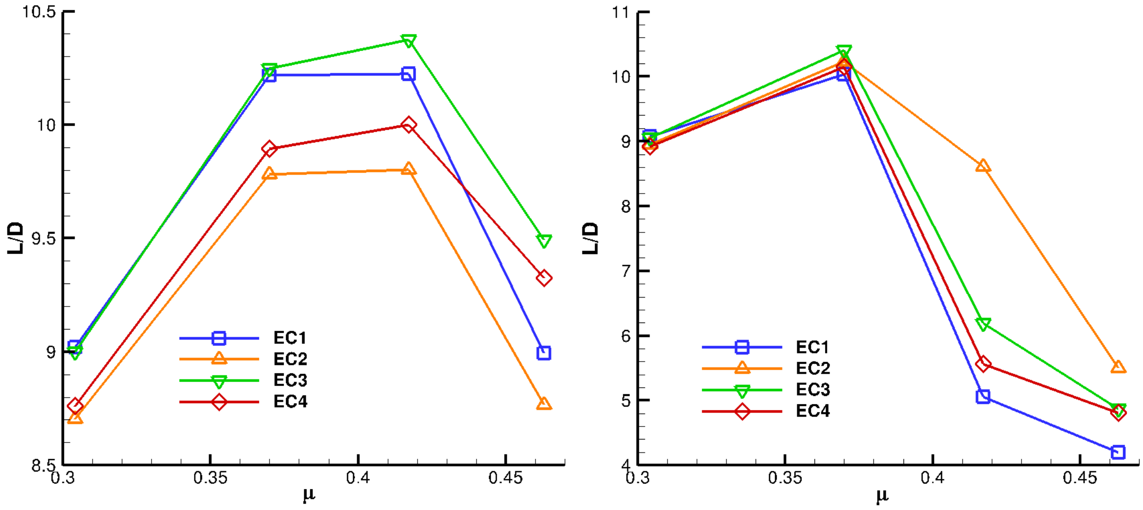

Figure 2.31: HOST simulations with FiSUW of four ORPHEE blades in forward flight at $\bar{Z} = 15$, American law (left) and $\bar{Z} = 20$, Modane law (right)

mance drop at μ=0.417 (315 km/h) for all but the EC2 blade. This is illustrated in Figure 2.32, showing L/D as a function of $\bar{Z}$ and of forward flight velocity. For both parameters, $\bar{Z} = 20$ and $\mu = 0.417$, the simulation point is exactly positioned in transition zones. Since the four rotors do not degrade their performance at identical flight conditions, comparison at these exact parameters falls completely within the transition zone. It may be questioned if such a comparison is useful and fair, since stall prediction by HOST is not expected to be accurate.

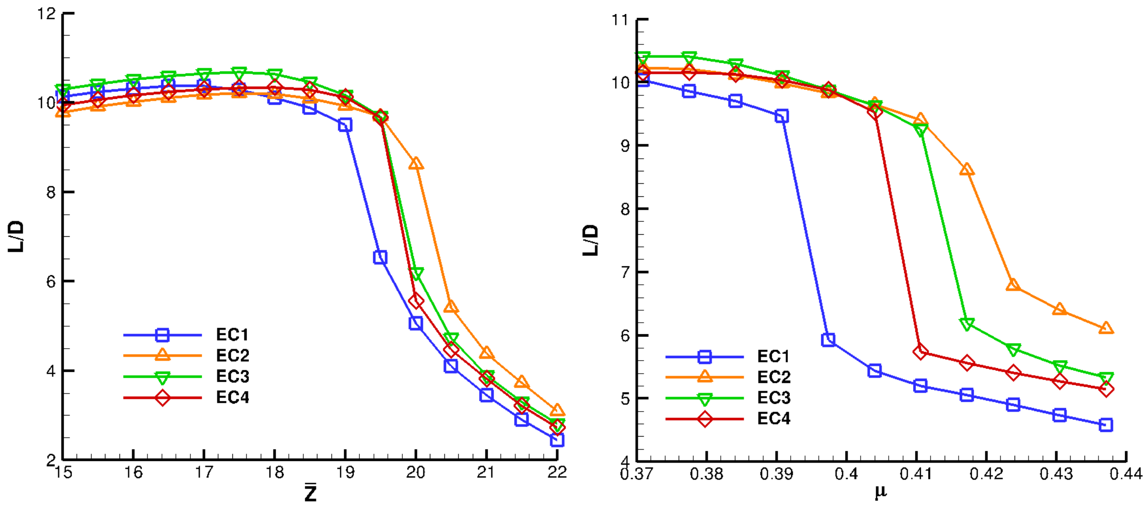

Figure 2.32: HOST simulations with FiSUW of four ORPHEE blades in forward flight with Modane law: variation of $\bar{Z}$ at forward flight speed of $\mu = 0.417$ (315 km/h; left) and variation of forward flight speed at $\bar{Z} = 20$ (right)

A possible cause for this performance drop at these demanding flight conditions is dynamic stall over the retreating blade side. This is illustrated in Figure 2.33, showing distributions of power consumption, expressed in $C_d M^3$. Power consumption for travelling along the retreating blade side of EC2 is lower than for EC1, EC3 and EC4. This suggests that dynamic stall occurs over this part of the rotor disk. Indeed, local angle-of-attack is higher for these three blades in the considered region.

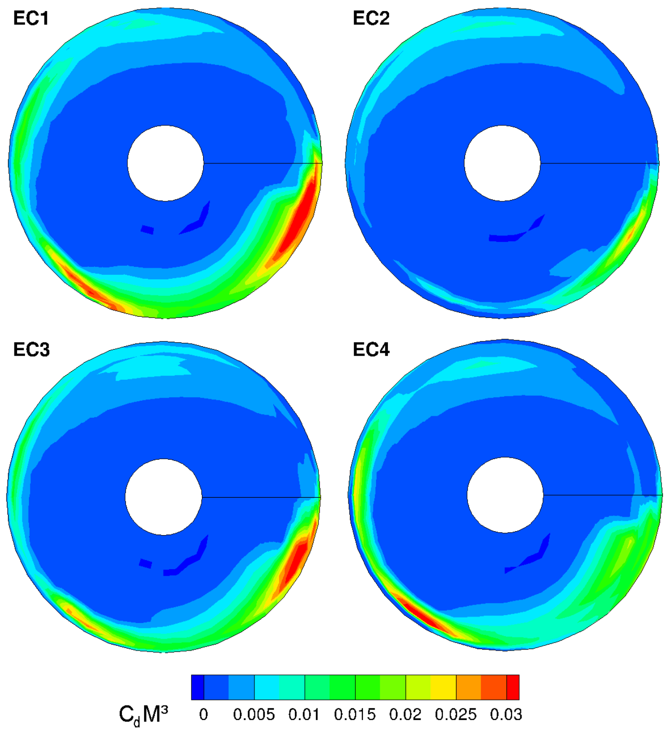

Figure 2.33: Local C_dM^3 over rotor disk of four ORPHEE blades at $\bar{Z}$ = 20 and V_H=315 km/h, Modane law, as computed by HOST with FiSUW

The effect of dynamic stall on local performance is seen in Figure 2.34. The L/D distribution shows that the EC2 blade's aerodynamic field differs from those of EC1, EC3 and EC4. Especially over the blade tip side (0.6-1R) over the retreating blade side, EC1, EC3 and EC4 blades do not contribute to an L/D increase. On the contrary, EC2 has a far smaller zone of low L/D ratio.

This example illustrates the sensitivity of HOST computations to flight conditions. Before executing an optimization, this sensitivity is to be checked to avoid a performance transition zone caused by dynamic stall.

Metar Blade hierarchy predicted by Metar is incorrect compared to measurements as shown by computational results in Figure 2.35. Only best performance by EC3 for $\bar{Z}$=15 and relative L/D increase at high μ of EC4 with respect to other blades for Modane law are estimated correctly by Metar. Absolute values of L/D are close to measurements, which is thus better estimated than previous induced velocity models, but absolute performance prediction is not of highest interest in the present study.

Mint Since a rotor wake is shed away from the rotor with forward flight speed, only a short wake needs to be simulated with Mint for considering wake-blade interactions. Here, the equivalent of three rotor rotations is used for simulating rotor wakes. In total 16 rotor rotations are simulated with a time step of $\Delta\psi = 5°$, taking on average 6 hours and 20 minutes of simulation time on a single processor. This is sufficient for computational convergence towards an equilibrium state. L/D ratio was averaged over the last rotor rotation.

Assessing performance prediction by Mint, see Figure 2.36, no blade hierarchy is estimated accurately for either of the 8 flight conditions. In contradiction with measurements, EC3 is estimated to have worst overall performance and EC4 is predicted best in all flight conditions. A single positive point may be found for the forward flight speed of maximum L/D, which

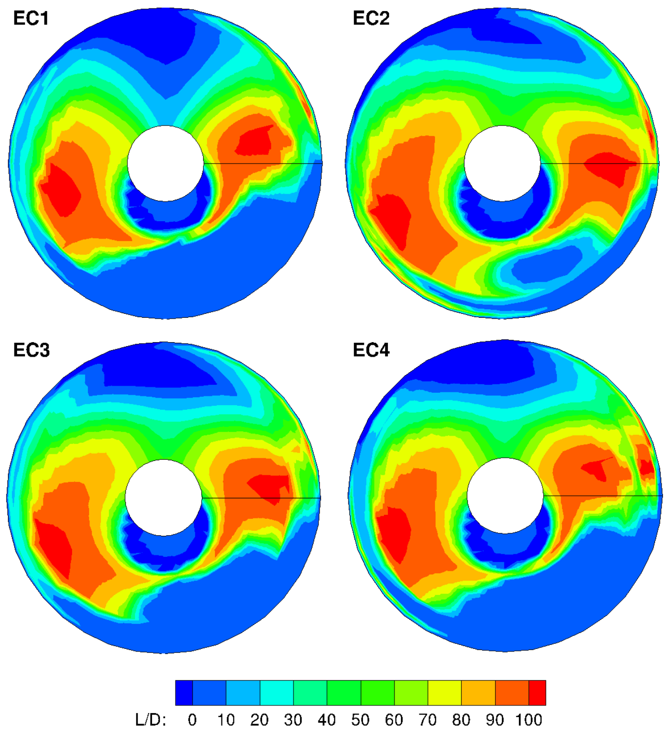

Figure 2.34: Local L/D ratio over rotor disk of four ORPHEE blades at $\bar{Z} = 20$ and V_H=315 km/h, Modane law, as computed by HOST with FiSUW

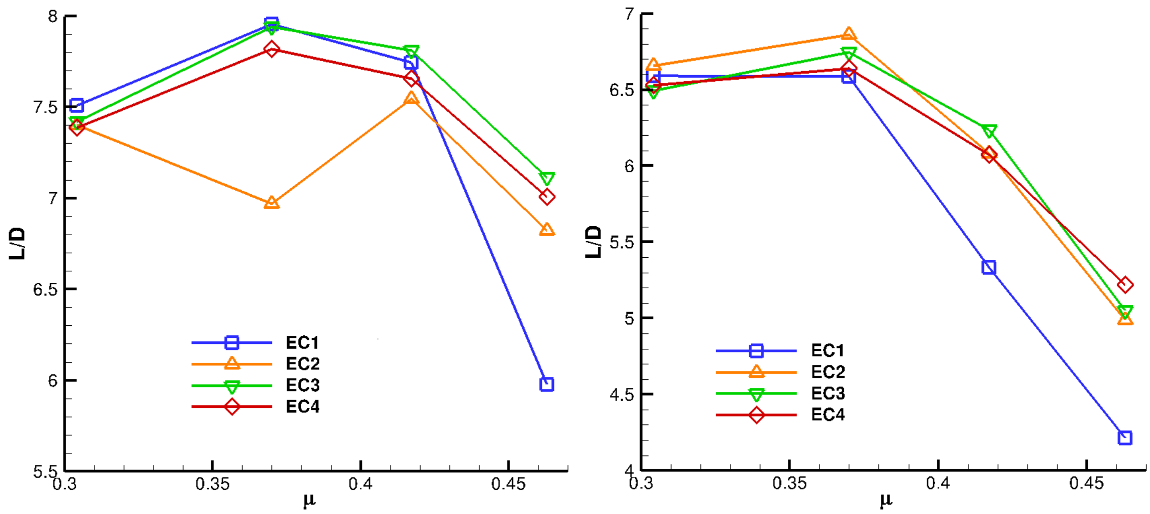

Figure 2.35: HOST simulations with Metar of four ORPHEE blades in forward flight at $\bar{Z} = 15$, American law (left) and $\bar{Z} = 20$, Modane law (right)

corresponds better to measurements than all other induced velocity models.

Conclusions on induced velocity field modelling Since flight conditions have a strong influence on computed rotor performance, and since correct prediction for all 8 simulation points is not found in this study, selecting one induced velocity model is not easy. Wake models Metar and Mint are directly eliminated as their blade hierarchy prediction was wrong for all 8 flight conditions. Differences between Meijer-Drees and Pitt & Peters are small, but in favour of Pitt & Peters, so that Meijer-Drees is excluded as well. Finally comparing Pitt

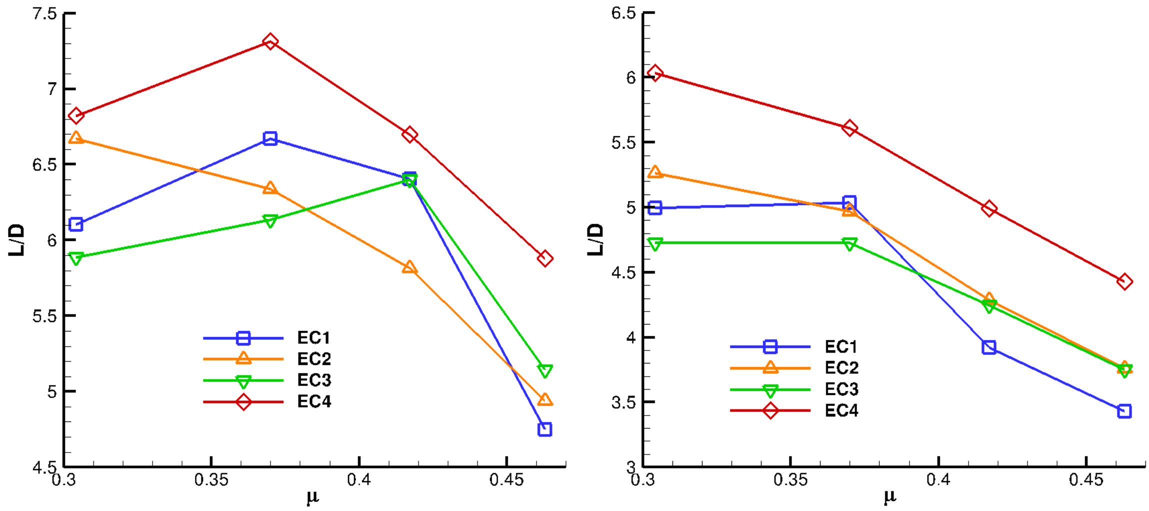

Figure 2.36: HOST simulations with Mint of four ORPHEE blades in forward flight at $\bar{Z} = 15$, American law (left) and $\bar{Z} = 20$, Modane law (right)

& Peters with FiSUW, for American law flight conditions FiSUW predicts blade hierarchy better since EC4 performance is less overestimated. For Modane law, neither of the models predicts blade hierarchy correctly, even if FiSUW is particularly off due to sensitivity to simulation conditions. Both Pitt & Peters and FiSUW will be used for assessing blade elasticity modelling.

Some general conclusions that hold for all induced velocity models may be drawn from this study:

- Forward flight speed at which maximum L/D ratio is computed does not correspond to measured flight conditions of maximum L/D. This implies that flow conditions and rotor equilibrium are different, so that comparison of local aerodynamic characteristics is difficult.

- Except for wake models, absolute L/D values are overpredicted compared to measurements.

- No matter the induced velocity model, EC4 performance is systematically overestimated with respect to other blades, suggesting this is due to other computational parameters than inflow field modelling.

- Performance prediction at high rotor load and high forward flight speeds, such as $\bar{Z} = 20$ and $\mu > 0.37$, is difficult due to inherent HOST limitations of representing physical phenomena as rotor stall or transonic flow that occur in these flight conditions.

As these items are generic for all induced velocity models, other HOST parameter than inflow modelling are expected to influence forward flight performance prediction.

Rigid vs. elastic blade modelling

Influence of blade deformations is studied for Pitt & Peters and FiSUW. Blade hierarchy does not alter with elastic blade modelling at $\bar{Z} = 15$ with FiSUW; in the other three cases blade deformation modelling changes performance predictions significantly, as seen in Figures 2.37 and 2.38. Pitt & Peters predict a noteworthy L/D increase of EC4 at high μ for the American law. This effect is not seen with FiSUW. Modane law simulation with FiSUW changes largely

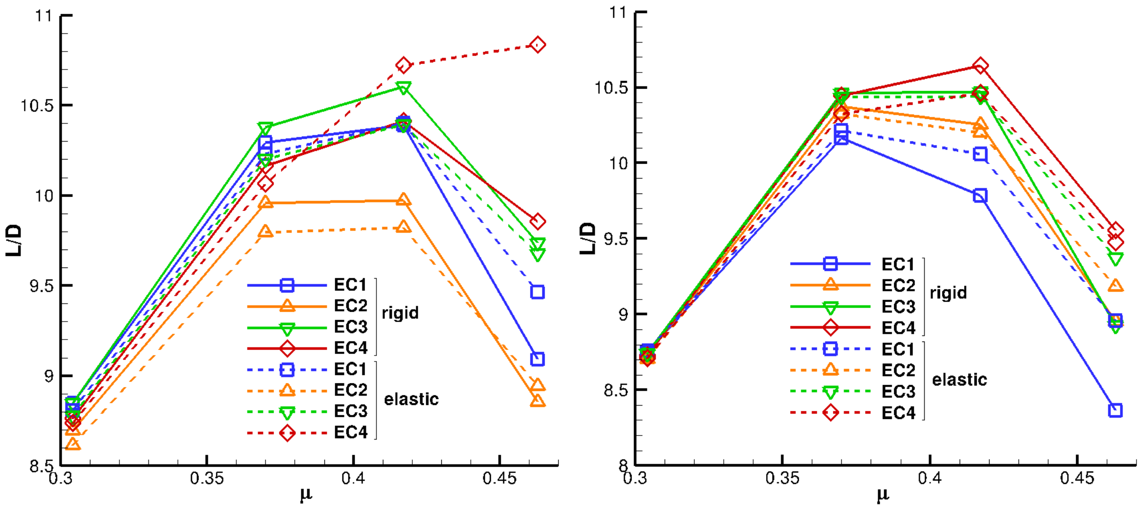

Figure 2.37: HOST simulations of rigid and elastic blades with Pitt & Peters of four ORPHEE blades in forward flight at $\bar{Z} = 15$, American law (left) and $\bar{Z} = 20$, Modane law (right)

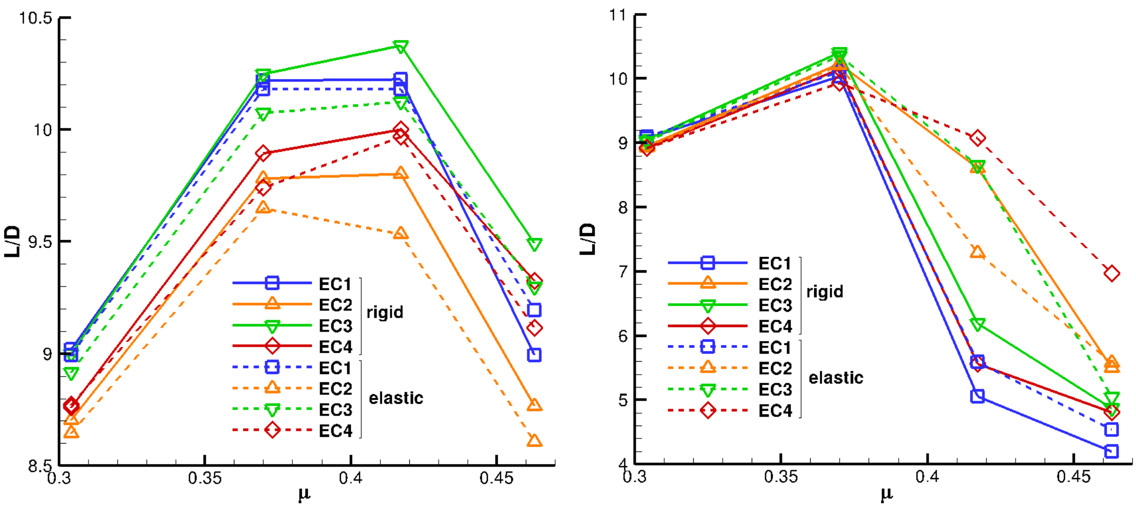

Figure 2.38: HOST simulations of rigid and elastic blades with FiSUW of four ORPHEE blades in forward flight at $\bar{Z} = 15$, American law (left) and $\bar{Z} = 20$, Modane law (right)

when incorporating blade deformation modelling, which may be explained by sensitivity to flight conditions, as already explained earlier.

These comparisons illustrate that inflow and blade deformation modelling are closely related in forward flight simulations. Concluding on modelling of blade deformation requires a deeper analysis.

HOST corrections

As was done for hover computations with HOST, influence of Reynolds and sweep corrections is tested for rigid-blade FiSUW computations for both wind tunnel laws.

Reynolds correction Removing the Reynolds correction increases L/D with on average 1 point, as illustrated in Figures 2.39 and 2.40. For the American law, the correction has a constant influence for all blades, except for high speed forward flight on EC1. Only at this flight condition blade hierarchy is altered; no explanation is found for this discrepancy. Effect by Reynolds correction on computations at $\bar{Z} = 20$ differs per blade but blade hierarchy is not modified at any flight speed.

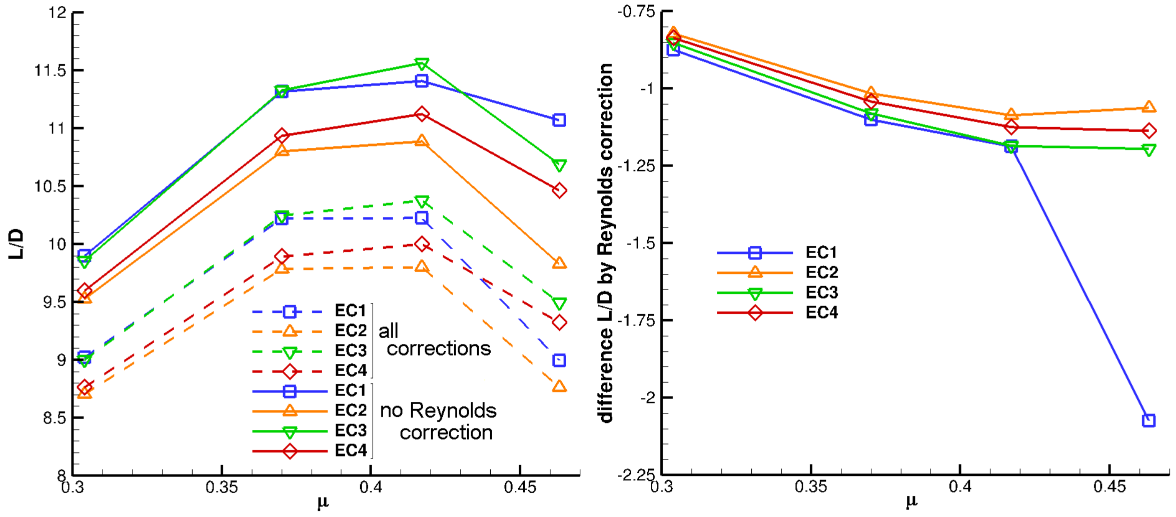

Figure 2.39: HOST simulations with FiSUW model of four ORPHEE blades in forward flight at $\bar{Z}$=15, American law, with and without Reynolds correction

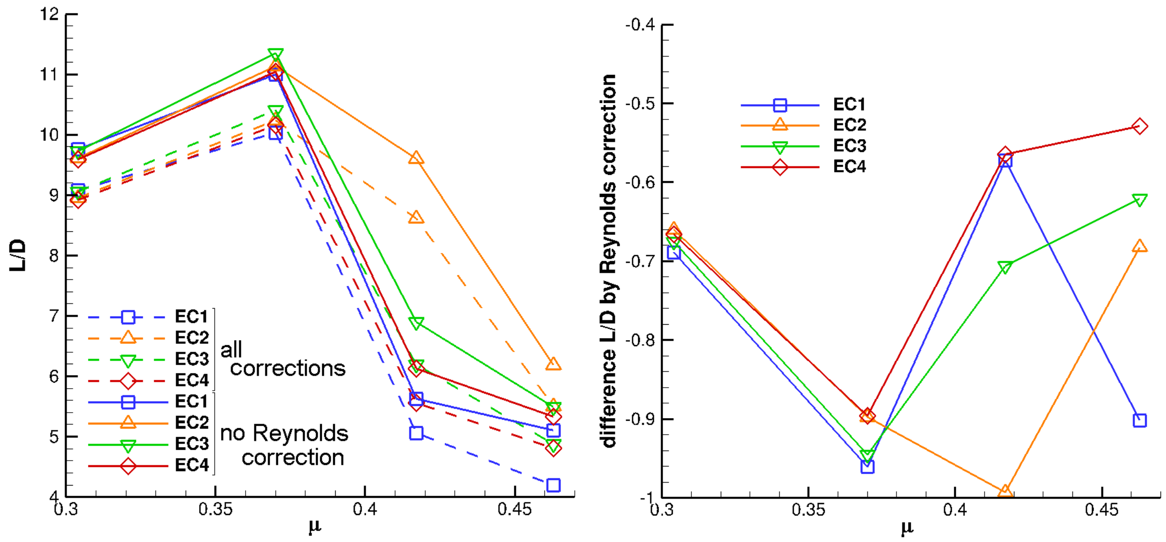

Figure 2.40: HOST simulations with FiSUW model of four ORPHEE blades in forward flight at $\bar{Z}$=20, Modane law, with and without Reynolds correction

Sweep correction The effect of sweep correction in HOST on forward flight performance depends completely on flight conditions, as demonstrated in Figures 2.41 and 2.42. For $\bar{Z} = 15$, influence of the sweep correction is limited and nearly constant for all four blades so that blade hierarchy does not alter with this correction. For Modane law computations, however, L/D values change significantly when removing the sweep correction. Blade hierarchy alters as well but not for the better.

As removing the sweep correction can completely alter forward flight performance to implausible values, it is recommended to apply this correction.

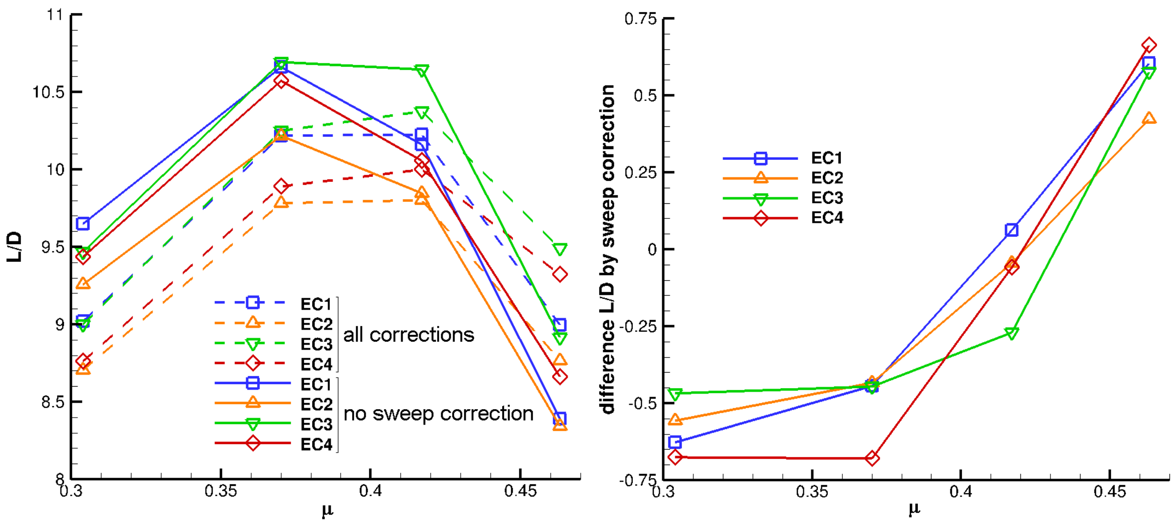

Figure 2.41: HOST simulations with FiSUW model of four ORPHEE blades in forward flight at $\bar{Z}$=15, American law, with and without sweep correction

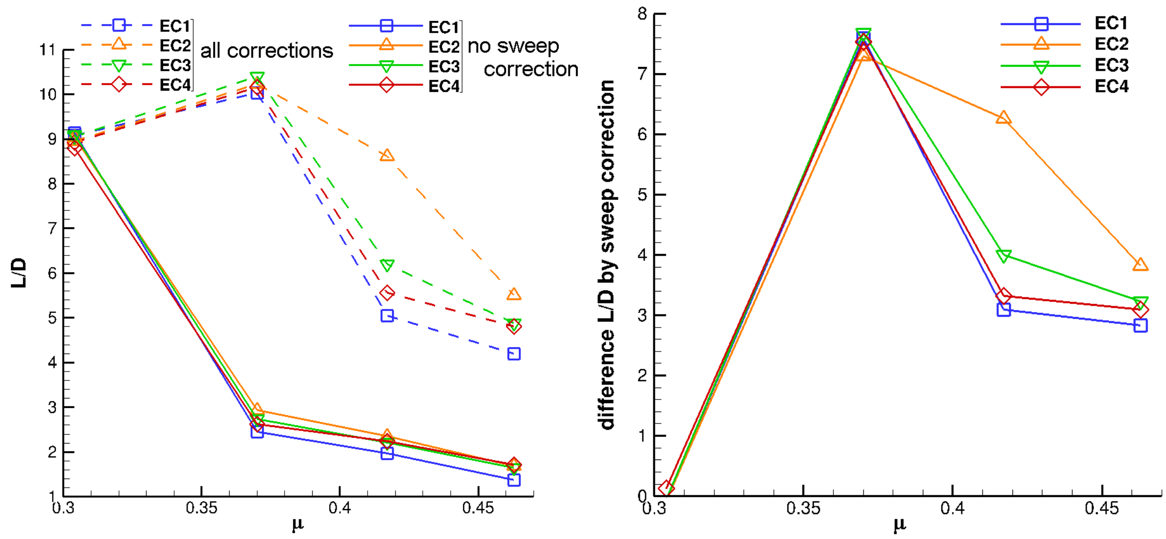

Figure 2.42: HOST simulations with FiSUW model of four ORPHEE blades in forward flight at $\bar{Z}$=20, Modane law, with and without sweep correction

2.1.6 Summary of rotor performance simulations using HOST

Even if hover is often considered to be a simple flow configuration, HOST simulations do not predict rotor hover performance accurately. No matter the induced velocity model, blade hierarchy is not predicted accurately for any of the tests performed. In general, maximum F.M. of EC1 and EC3 is simulated too close compared to measurements, and EC2 is systematically predicted to have better hover performance than EC1, which was expected from theory, but was not measured. Nonetheless, both Meijer-Drees and FiSUW approximate measured hover performance, especially when accounting for the theoretically expected F.M. difference between EC1 and EC2. As the shape of radial variation of induced velocity as calculated by FiSUW is closer to inflow measurements, this model is preferred over Meijer-Drees, even if on global performance no effect is seen.

From forward flight simulations, combination of the induced velocity field study and ORPHEE blade comparisons designate FiSUW as the best induced velocity model. It represents in general better the induced velocity field over a rotor disk, as shown by comparison to NASA inflow measurements. Additionally, global rotor performance prediction is in general better predicted by Pitt & Peters and FiSUW. Combining both studies leads to the conclusion that FiSUW is best suitable for forward flight simulations with HOST.

Elastic blade modelling was compared to rigid blade simulations for rotor performance in hover and forward flight. For hover computations, no significant changes of global performance were found, whereas forward flight performance was more severely affected by blade elasticity. No conclusions on elastic blade modelling are drawn at this stage; deeper analysis would be required for that.

Finally, concerning tested aerodynamic corrections, both the Reynolds and sweep correction are recommended for HOST simulations since they generally improve the accuracy of the predicted performance.

A final remark may be given as a warning for selecting design conditions of optimization points, as performance values were seen to completely change blade hierarchy with varying flight conditions. It is recommended to perform parameter sweeps about chosen flight conditions (forward flight speed, rotor loading, fuselage drag coefficient) before starting an optimization to be sure being off such sensitive flight conditions that can completely change blade performance.

2.2 Computational Fluid Dynamics code *elsA*

The Computational Fluid Dynamics (CFD) code *elsA* developed at ONERA [35] is the second simulation tool considered in this work for computing rotor performance. Hereafter, we first recall the governing equations we use to model the flow around helicopter rotors (Section 2.2.1). For computational cost reasons, we restrict our attention to the Reynolds-Averaged Navier-Stokes (RANS) equations closed by a suitable turbulence model. Turbulence models are presented in Section 2.2.2. We investigate the influence of numerical schemes on the computed solution. Candidate numerical schemes are described in Section 2.2.3. To complete the theoretical description of CFD simulations, some details on the specific computational set-up of rotor performance simulations are given in Section 2.2.4.

Two validation studies of *elsA* are presented in Sections 2.2.5 and 2.2.6. First, the influence of mesh refinement, numerical scheme and turbulence model is investigated and assessed against wingtip vortex measurements for a well-documented flow over a low aspect ratio wing. We focus in particular on the representation of the tip vortex. This study allows for understanding influential parameters and selecting parameters best adapted for further studies. The second study concerns numerical simulation of the four ORPHEE blades in hover and forward flight. Again, a sensitivity analysis of computational parameters is performed. The final goal of this Section is to provide criteria for computational settings to be used in rotor blade optimization, as presented in 2.2.7.

2.2.1 Numerical simulation of Navier-Stokes equations

The Navier-Stokes equations are based on conservation of mass, momentum and energy. For compressible flow, they can be given as follows [108]:

- Mass conservation

$$\frac{\partial \rho}{\partial t} + \frac{\partial(\rho u_j)}{\partial x_j} = 0 \tag{2.13}$$

- Momentum conservation

$$\frac{\partial(\rho u_i)}{\partial t} + \frac{\partial(\rho u_i u_j)}{\partial x_j} = -\frac{\partial p}{\partial x_i} + \frac{\partial \tau_{ij}}{\partial x_j} \tag{2.14}$$

- Energy conservation

$$\frac{\partial(\rho E)}{\partial t} + \frac{\partial(\rho H u_j)}{\partial x_j} = -\frac{\partial q_j}{\partial x_j} + \frac{\partial(\tau_{jk} u_k)}{\partial x_j} \tag{2.15}$$

where we make use of Einstein notation for repeated subscripts, and where:

ρ	density $[kg/m^3]$
t	time $[s]$
u_i	components of velocity vector $\mathbf{v}$ $[m/s]$
x_j	components of Cartesian coordinate vector $\mathbf{x}$ $[m]$
p	pressure [Pa]
E	total energy [J]
H	total enthalpy [J]
q_j	components of heat flux vector $\mathbf{q}$ $[W/m^2]$
τ_{jk}	components of symmetrical viscous stress tensor τ $[m^2/s^2]$

Total energy E, internal energy e, total enthalpy H and specific enthalpy h are related by:

$$E = e + \frac{1}{2}u_k u_k \qquad H = h + \frac{1}{2}u_k u_k \qquad h = e + \frac{p}{\rho} \tag{2.16}$$

The Navier-Stokes equations contain more variables than equations, so that additional equations are required for system closure. Closure is achieved by adding constitutive laws for viscous stress tensor τ, heat flux vector $\mathbf{q}$ and an equation of state to relate thermodynamics variables.

For Newtonian flows, viscous stress tensor τ_{ij} is given by:

$$\tau_{ij} = 2\mu_d S_{ij} + \lambda \frac{\partial u_k}{\partial x_k}\delta_{ij} \tag{2.17}$$

and

$$S_{ij} = \frac{1}{2}\left(\frac{\partial u_i}{\partial x_j} + \frac{\partial u_j}{\partial x_i}\right) \tag{2.18}$$

where δ_{ij} is the Kronecker delta symbol, S_{ij} the deformation rate tensor, equivalent to the symmetric part of the velocity gradient tensor and scalars μ_d and λ are the dynamic viscosity and second viscosity coefficients, respectively. By Stokes' hypothesis, $3\lambda + 2\mu_d = 0$, Equation 2.17 simplifies to:

$$\tau_{ij} = 2\mu_d\left(S_{ij} - \frac{1}{3}\frac{\partial u_k}{\partial x_k}\delta_{ij}\right) \tag{2.19}$$

The heat flux vector $\mathbf{q}$ is represented through Fourier's law:

$$q_j = -\kappa \frac{\partial T}{\partial x_j} \tag{2.20}$$

with κ the thermal conduction coefficient, related to μ_d via Prandtl's number $P_r = \mu_d c_p/\kappa$ which is taken equal to 0.72, so that Equation 2.20 may be written as:

$$q_j = -\frac{\mu_d c_p}{P_r}\frac{\partial T}{\partial x_j} \tag{2.21}$$

Dynamic viscosity coefficient μ_d is related to temperature by Sutherland's law:

$$\mu_d = \mu_{\text{ref}}\left(\frac{T}{T_{\text{ref}}}\right)^{3/2}\frac{T_{\text{ref}} + S_t}{T + S_t} \tag{2.22}$$

where reference temperature T_{ref} equals 273.15 K, viscosity μ_{ref} at T_{ref} equals $1.711 \cdot 10^{-5} kg \cdot m^{-1}s^{-1}$ and S_t is the Sutherland temperature, equal to $110.4K$ in air. Sutherland's law holds for temperatures below 1500 K [108].

For the equation of state, we assume that air behaves like a thermally and calorically perfect gas, so that the following equations hold:

$$e = c_v T \qquad h = c_p T \qquad p = \rho R T \tag{2.23}$$

where R is the specific gas constant, which, under our hypotheses, is equal to $287.04\ Jkg^{-1}K^{-1}$.

Typical Reynolds number for rotor flows are in the order of magnitude of $10^6 - 10^7$. At these Reynolds numbers, initially laminar flow transitions to turbulent flow. Turbulence can be described as an irregular motion having a wide range of time and space scales [150]. Large-scale turbulent eddies are produced from mean flow disturbances and contain most kinetic energy. This energy is transferred to small-scale eddies, which are several orders of magnitude smaller than large-scale eddies, that dissipate energy through molecular viscosity to heat. Interactions between all turbulence scales and with the mean flow appear by fluctuations of different amplitudes, frequencies and directions. In fact, large-scale eddies carry along small-scale disturbances so that turbulence at a given position depends on its time-history. Turbulent eddies are strongly rotational and most of their vorticity resides in small-scale eddies. In conclusion, turbulence is three-dimensional and time-dependent.

Mean flow is modified by turbulence in several ways. First of all, turbulent diffusion increases transport efficiency of mass, momentum and heat. This may reduce flow separation and wake size around obstacles, both limiting drag. On the other hand, higher skin friction drag is found for turbulent flows compared to laminar flows due to increased motions perpendicular to the surface [26].

Three principal ways of resolution of turbulent flow exist:

1. Complete resolution of all turbulent space- and time-scales is called Direct Numerical Simulation (DNS) and is today applied on theoretical test cases of low-Reynolds number and simple geometries. It may be demonstrated [150] that the number of numerical operations required for resolution of all turbulence scales by DNS is in the order of $Re^{9/4}$. For high Reynolds numbers encountered in helicopter rotor flows, the computational cost associated with DNS is prohibitive for this kind of simulations for the next years, or even decades.

2. Larger scale turbulent eddies are simulated in Large Eddy Simulation (LES), whereas small scale eddies are modelled by so-called subgrid-scale models. It is based on the general idea that large-scale eddies are directly modified by the mean flow and carry most of the Reynolds stresses, whereas smaller eddies have nearly-universal characteristics, making them more suitable to model [150]. Mesh requirements for computing large-scale eddies today remain unfeasible for application within an optimization loop for

rotor flows.

3. The Navier-Stokes equations are decomposed in time-averaged and fluctuating parts in Reynolds Averaged Navier-Stokes (RANS). Only the averaged equations are simulated so that fluctuations of the flow field, typically due to turbulence, are neglected. Influence of turbulence on the mean flow is modelled by turbulence models, reducing grid requirements to mean flow simulation scales. Today, this is the only acceptable solution for rotor flow simulation in terms of grid requirements.

   Whereas RANS resolution resolves an averaged flow field, leading to a steady state solution, unsteady RANS (URANS) simulations may be employed for solving unsteady flow phenomena, such as rotor flow in forward flight. In this case, the mean flow field is computed at different physical time-steps; for helicopter rotors corresponding to azimuthal positions of the rotor blades. Fluctuations due to mean flow field variations may be captured, but turbulence fluctuations are not simulated and turbulence models still only model its influence on the mean flow field.

In the following of this Dissertation, we retain the RANS or URANS approach to study helicopter rotor flows. Using, as usual, Favre averaging to cope with compressible flow equations (see [97] or [150] for details), these write:

- Mass conservation

$$\frac{\partial \bar{\rho}}{\partial t} + \frac{\partial \bar{\rho}\widetilde{u_j}}{\partial x_j} = 0 \tag{2.24}$$

- Momentum conservation

$$\frac{\partial \bar{\rho}\widetilde{u_j}}{\partial t} + \frac{\partial \bar{\rho}\widetilde{u_i}\widetilde{u_j}}{\partial x_j} = -\frac{\partial \bar{p}}{\partial x_i} + \frac{\partial}{\partial x_j}\left(\widetilde{\tau_{ij}} - \bar{\rho}\widetilde{u_i'' u_j''}\right) \tag{2.25}$$

- Energy equation

$$\frac{\partial \bar{\rho}E^*}{\partial t} + \frac{\partial \bar{\rho}\widetilde{u_j}H^*}{\partial x_j} = -\frac{\partial}{\partial x_j}\left(q_{L_j} + q_{T_j}\right) + \frac{\partial}{\partial x_j}\left(\widetilde{u_j}(\widetilde{\tau_{ij}} - \bar{\rho}\widetilde{u_i'' u_j''})\right) + \frac{\partial}{\partial x_j}\left(\frac{1}{2}\bar{\rho}\widetilde{u_k'' u_k'' u_j''} - \overline{\tau_{ij} u_i}\right) \tag{2.26}$$

where:

$E^* = \tilde{e} + \frac{1}{2}\widetilde{u_i}\widetilde{u_i} + k$	
$H^* = \tilde{h} + \frac{1}{2}\widetilde{u_i}\widetilde{u_i} + k$	
q_{L_j}	laminar transport of heat, obtained with laminar Prandtl number $Pr_L = c_p\mu_d/\kappa$
$q_{T_j} = \overline{\rho u_j'' h''}$	turbulent transport of heat
$\widetilde{\tau_{ij}}$	Favre-averaged Reynolds stress tensor

The Favre-averaged Reynolds stress tensor $\widetilde{\tau_{ij}}$ is function of Favre-averaged and fluctuating parts by: $\overline{\tau_{ij}} = \widetilde{\tau_{ij}} + \overline{\tau_{ij}''}$. This last term can be neglected since $|\widetilde{\tau_{ij}}| << |\overline{\tau_{ij}}|$.

Preceding equations are general formulations, creating a universal basis for CFD-codes. For application on rotor simulation, additional terms appear for mesh movement and rotation. Description of these terms is given in [76].

2.2.2 Turbulence modelling

Turbulence appears in several terms in Equations 2.24 to 2.26: $\widetilde{\tau_{ij}}$ is the Favre-averaged Reynolds stress tensor, $\overline{\tau_{ij} u_i}$ represents molecular diffusion, $\frac{1}{2}\bar{\rho}\widetilde{u_k'' u_k'' u_j''}$ turbulent transport of turbulence kinetic energy and q_{T_j} is the turbulent heat flux vector. Turbulence kinetic energy is contained in k of E^* and H^*.

Modelling of these terms is for example described in [150]. Next paragraphs focus on modelling of the Reynolds stress tensor, as no general closure equations for this term exists. Yet, this term incorporates the effect of turbulent fluctuations on the mean flow, thereby increasing momentum transport in the mean flow. This symmetric tensor of 6 unknowns needs to be modelled for computing the RANS equations. Two turbulence models are tested: one is based on the Boussinesq hypothesis; the other models all 6 unknown terms. A theoretical description of both models is given next.

Menter's $k-\omega$ model

Boussinesq proposed to model the Reynolds stress tensor by introducing turbulent viscosity μ_t by analogy of the viscous constraint tensor [150]:

$$\bar{\rho}\widetilde{\tau_{ij}} = -\widetilde{\rho u_i'' u_j''} = 2\mu_t \widetilde{S_{ij}^D} - \frac{2}{3}\rho\bar{k}\delta_{ij} = \mu_t\left(\frac{\partial \widetilde{u_i}}{\partial x_j} + \frac{\partial \widetilde{u_j}}{\partial x_i}\right) - \frac{2}{3}\rho\bar{k}\delta_{ij} \tag{2.27}$$

where δ_{ij} is the Kronecker delta symbol, S_{ij}^D the deviatoric part of the viscous constraint tensor $\widetilde{S_{ij}}$ that tends to distort it and $\tilde{k}$ the turbulence kinetic energy $\tilde{k} = \frac{1}{2}\widetilde{u_i'}^2 = 1/2 \cdot \left(\widetilde{u_i'}^2 + \widetilde{u_j'}^2 + \widetilde{u_k'}^2\right)$. The term $\frac{2}{3}\rho\bar{k}\delta_{ij}$ is added to avoid the singular solution $\rho\bar{k} = \widetilde{\rho u_i'' u_i''}/2 \equiv 0$.

With all other variables known by earlier presented equations, Reynolds stress tensor modelling now is reduced to expressing eddy viscosity μ_t. Various turbulence models are based on the Boussinesq hypothesis. The $k-\omega$ model of Menter will be pointed out here, more information on others may be found in for example [26, 150].

As turbulence models are intended to simulate the effect of turbulence on the mean flow, dissipation of turbulent structures into thermal and internal energy is often modelled. This dissipation may be represented by for example turbulent dissipation ϵ $[m^2/s^3]$ or turbulent dissipation rate ω $[s^{-1}]$ which represents the rate at which turbulent kinetic energy is converted into thermal and internal energy per unit volume and time. These dissipation quantities and turbulent kinetic energy k are related via:

$$\omega = \frac{\epsilon}{C_\mu k} \tag{2.28}$$

where C_μ usually equals 0.09. In the $k-\omega$ model, eddy viscosity μ_t is related to turbulence kinetic energy k and specific dissipation rate ω by:

$$\mu_t = \frac{k}{\omega} \tag{2.29}$$

The specific $k-\omega$ model used in the following is the one of Menter [94] that uses the Jones-Launder $k-\epsilon$ model [74] rewritten in $k-\omega$ variables in the outer part of the boundary layer. The inner part of the boundary layer is described by the $k-\omega$ formulation of Wilcox [150]. This choice allows to combine the low sensitivity to free-stream boundary conditions of the $k-\epsilon$ model with the robustness and accuracy of $k-\omega$ in the near-wall region.

The required quantities k, ω and ϵ rewritten in ω variable are modelled as follows in Navier-Stokes formulation, so neglecting Reynolds or Favre-averaging [94]:

$$\frac{\partial \rho k}{\partial t} + \frac{\partial \rho u_j k}{\partial x_j} = P_k - \beta^* \rho\omega k + \frac{\partial}{\partial x_j}\left[(\mu_d + \sigma_{kn}\mu_t)\frac{\partial k}{\partial x_j}\right] \tag{2.30}$$

$$\frac{\partial \rho \omega}{\partial t} + \frac{\partial \rho u_j \omega}{\partial x_j} = \gamma_1 P_\omega - \beta_1 \rho \omega^2 + \frac{\partial}{\partial x_j}\left[(\mu_d + \sigma_{\omega 1}\mu_t)\frac{\partial \omega}{\partial x_j}\right] \tag{2.31}$$

$$\frac{\partial \rho \omega}{\partial t} + \frac{\partial \rho u_j \omega}{\partial x_j} = \gamma_2 P_\omega - \beta_2 \rho \omega^2 + 2\rho\sigma_{\omega 2}\frac{1}{\omega}\frac{\partial k}{\partial x_j}\frac{\partial \omega}{\partial x_j} + \frac{\partial}{\partial x_j}\left[(\mu_d + \sigma_{\omega 2}\mu_t)\frac{\partial \omega}{\partial x_j}\right] \tag{2.32}$$

where σ_{kn} is σ_{k1} for the original $k-\omega$ model, and σ_{k2} for the transformed $k-\epsilon$ model. In these equations, constants ω, β and γ as well as definitions of turbulence production terms P_ω and P_k are given in [95]. The same reference presents blending function F_1 to define values of constants of $k-\omega$ model (subscript 1) and of transformed $k-\epsilon$ model (subscript 2). These constants depend on turbulent length scale and wall-distance.

Onto this model, the Shear Stress Transport (SST) correction proposed by Menter [94] is applied to improve the representation of turbulent shear stress in boundary layers subject to an adverse pressure gradient. It uses Bradshaw's assumption that principal shear-stress in a boundary layer is proportional to turbulent kinetic energy. In regions of adverse pressure gradient flows where production is larger than dissipation, the SST correction modifies the expression of μ_t of equation 2.29 into the following:

$$\mu_t = \frac{a_1 k}{\Omega_{\text{abs}}} \tag{2.33}$$

where Ω_{abs} is the absolute vorticity and constant a_1 equals 0.3. Blending function F_2 used for the SST correction and model constants are given in [94].

Limitations of the Boussinesq hypothesis Although the Boussinesq hypothesis provides a relatively simple way of computing the Reynolds stress tensor, it has multiple limitations [39]:

- Assuming a linear relation between $\widetilde{u_i' u_j'}$ and $\widetilde{S_{ij}^D}$ is only a first order approximation;
- Isotropy of Reynolds stresses is assumed;
- Physically, the Boussinesq hypothesis gives a diffusive nature to Reynolds stresses, leading to a stabilizing effect on unsteady phenomena. Though, in reality the Reynolds stress tensor would add to turbulence unsteadiness;
- Eddy viscosity is no physical fluid property;
- The value of μ_t has to be defined in every location of the flow field. This implies that μ_t only depends on local properties at a given instant, whereas spatial and temporal memory are ignored.

Due to these limitations, Boussinesq turbulence models especially fail in simulating (amongst others) flows of rotating fluids and three-dimensional flows [150].

Reynolds Stress turbulence model

Turbulence models based on second-order closure lead to the solution of a transport equation for the 6 independent components of the Reynolds stress tensor and do not use the Boussinesq hypothesis. A transport equation for the turbulence scale is also needed to close the system. The Reynolds Stress Model (RSM) retained for the present simulations is the one developed by Speziale, Sarkar and Gatski (SSG-model) [61]. Typically, RSM models use a Reynolds stress transport equation. Assuming homogeneous turbulent flows at high Reynolds numbers so that dissipation is approximately isotropic, the system of Reynolds stress transport equations is given as follows [61]:

$$\frac{\partial \overline{\tau_{ij}}}{\partial t} = -\overline{\tau_{ik}}\frac{\partial \widetilde{u_j}}{\partial x_k} - \overline{\tau_{jk}}\frac{\partial \widetilde{u_i}}{\partial x_k} - \Pi_{ij} + \frac{2}{3}\epsilon\delta_{ij} \tag{2.34}$$

where pressure-strain correlation Π_{ij} and scalar dissipation rate ϵ are given by:

$$\Pi_{ij} = p\widetilde{\left(\frac{\partial u_i}{\partial x_j} + \frac{\partial u_j}{\partial x_i}\right)} \tag{2.35}$$

$$\epsilon = \frac{\mu}{\rho}\widetilde{\frac{\partial u_i}{\partial x_k}\frac{\partial u_i}{\partial x_k}} \tag{2.36}$$

The particularity of this model with respect to other RSM models is its expression for the pressure-strain redistribution term Π_{ij}. This term redistributes the Reynolds stresses over all flow directions, and contributes significantly to the (an)isotropy of the model.

Menter's equation for ω [94] with SST correction is added to close the system of equations and allows for direct comparison of the two presented turbulence models.

2.2.3 Numerical schemes

Numerical resolution of the compressible RANS equations, as given in Equations 2.24 to 2.26, is achieved in *elsA* by space- and time-discretization using a finite-volume formulation. The present Section provides a brief description of these discretization methods, and introduces in particular two space discretization schemes that will be used in validation studies later on. More information on discretization methods may be found in [76, 78].

In the following, the compressible RANS equations are written in integral form and notation is alleviated by leaving out Reynolds- and Favre-averaged notations:

$$\frac{d}{dt}\int_{\Omega(t)} \mathbf{W} d\Omega + \oint_{\partial\Omega(t)} \Big[\mathbf{Fc}(\mathbf{W},\mathbf{s}) + \mathbf{Fd}(\mathbf{W},\mathbf{gradW})\Big]\cdot \mathbf{n} d\Sigma = \int_{\Omega(t)} \mathbf{T}(\mathbf{W},\mathbf{gradW}) d\Omega \tag{2.37}$$

where $\mathbf{W}$ is the conservative variables vector (of mean and turbulence field), $\mathbf{Fc}$ contains convective fluxes corresponding to first-order space derivatives, $\mathbf{Fd}$ corresponds to diffusive fluxes of second-order space derivatives, source term $\mathbf{T}$ contains inertial forces in relative reference frame formulation, Ω is the volume of a mesh cell and $\partial\Omega$ its boundary, having normal external unit $\mathbf{n}$ and velocity $\mathbf{s}$.

The system of equations 2.37 is discretized on a structured mesh of hexahedron cells of volume V and with closed surface $\partial\Omega$ given by:

$$V(\Omega)(t) = \int_{\Omega(t)} d\Omega \tag{2.38}$$

$$\partial\Omega(t) = \sum_{l=1}^{6} \Sigma_l(t) \tag{2.39}$$

where Σ_l represents boundary l of a hexahedron cell.

Equation 2.37 may be rewritten in semi-discrete form by replacing volume integrals by cell average values and surface integrals by summation over cell boundaries. The semi-discrete formulation on a mesh fixed in time may be written as follows:

$$\frac{d}{dt}\mathbf{W}_\Omega = -\frac{1}{V(\Omega)}\left[\sum_{l=1}^{6}\mathbf{F}(\mathbf{W_\Omega},\mathbf{W_{\Omega_l}})\cdot\mathbf{N_{\Sigma_l}} - V(\Omega)\mathbf{T}_\Omega\right] = -\frac{1}{V(\Omega)}\mathbf{R}_\Omega \tag{2.40}$$

where:

$\mathbf{W}_\Omega$	numerical approximation of average value in cell Ω
$\mathbf{F}(\mathbf{W_\Omega},\mathbf{W_{\Omega_l}})$	numerical flux (sum of convective and diffusive fluxes); function of $\mathbf{W}_\Omega$ and numerical approximation $\mathbf{W}_{\Omega_l}$ computed in a neighbour cell with coinciding boundary Σ_l
$\mathbf{N_{\Sigma_l}}$	external vector normal to Σ_l: $\mathbf{N_{\Sigma_l}} = \int_{\Sigma_l(t)}\mathbf{n}d\Sigma$
$\mathbf{T}_\Omega$	approximation of source term $\mathbf{T}$
$\mathbf{R}_\Omega$	numerical modelling residual term composed of divergence of numerical and source term fluxes

In this semi-discrete formulation, the space discretization is given by flux differences through cell boundaries. Numerical flux vector $\mathbf{F}$ is split in convective and diffusive fluxes $\mathbf{Fc}(\mathbf{W},\mathbf{s}) + \mathbf{Fd}(\mathbf{W},\mathbf{gradW})$. Diffusive flux $\mathbf{Fd}$ is modelled by a first-order central-difference scheme and its discretization is described in [76]. Convective flux $\mathbf{Fc}$ is modelled by a spatial discretization scheme. Two schemes are presented, followed by an overview of two time integration methods used in rotor simulations.

Spatial discretization schemes

In this Dissertation, two numerical schemes are selected for comparison: the classical Jameson scheme and the more recent AUSM+ scheme. Both are briefly presented next in two-dimensional formulation, following the notation illustrated in Figure 2.43.

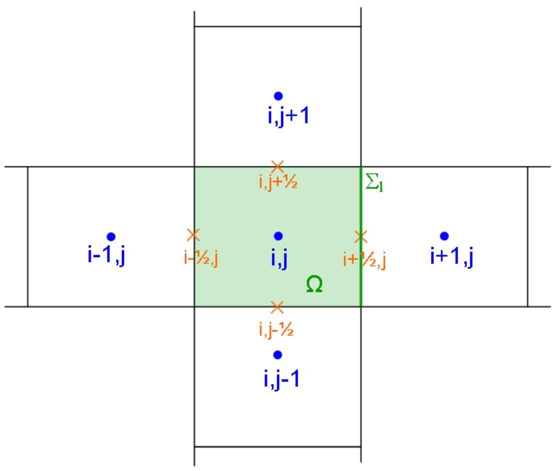

Figure 2.43: Numerical discretization for 1st order directional scheme

Jameson's scheme The second order central-difference Jameson scheme uses a simple-centred discretization of flux averaging over two cells separated by common boundary Σ_l. As this discretization leads to an unconditionally unstable scheme, numerical dissipation terms are added. Numerical flux term $\mathbf{F}$ is written by Jameson as [72, 76]:

$$\mathbf{F}_{\text{Jameson}}(\mathbf{W_\Omega}, \mathbf{W_{\Omega_l}}) \cdot \mathbf{N_{\Sigma_l}} = \frac{1}{2}\Big[\mathbf{Fc}(\mathbf{W_\Omega}) + \mathbf{Fc}(\mathbf{W_{\Omega_l}})\Big] \cdot \mathbf{N}_{\Sigma_l} - \mathbf{D}_{\Sigma_l} \tag{2.41}$$

where $\mathbf{W_\Omega}$ and $\mathbf{W_{\Omega_l}}$ are numerical approximations of average values in cell Ω and neighbour cell Ω_l, respectively, separated by common boundary Σ_l. Artificial dissipation flux is represented by $\mathbf{D_{\Sigma_l}}$.

In semi-discrete finite-volume formulation, Equation 2.41 becomes:

$$\frac{d}{dt}\mathbf{W_\Omega} = -\frac{1}{V(\Omega)}\left[\sum_{l=1}^{6} \frac{1}{2}\left[\mathbf{Fc}(\mathbf{W_\Omega} + \mathbf{FcW_{\Omega_l}})\right] \cdot \mathbf{N_{\Sigma_l}} - \mathbf{Di} - \mathbf{Dj} - V(\Omega)\mathbf{T_\Omega}\right] \tag{2.42}$$

where $\mathbf{Di}$ and $\mathbf{Dj}$ are artificial dissipation terms in i and j direction. These dissipation operators include a second-order dissipation term for low-order dissipation close to discontinuities to prevent the appearance of spurious oscillations, and a fourth-order dissipation term for dumping high-frequency errors throughout the computational domain. Dissipation in i-direction and on cell boundary $\Sigma_{i+\frac{1}{2},j}$ may be written as:

$$\mathbf{Di}_{i+\frac{1}{2},j} = \varepsilon^{(2)}_{i+\frac{1}{2},j}(\mathbf{W}_{i+1,j} - \mathbf{W}_{ij}) - \varepsilon^{(4)}_{i+\frac{1}{2},j}(\mathbf{W}_{i+2,j} - 3\mathbf{W}_{i+1,j} + 3\mathbf{W}_{i,j} - \mathbf{W}_{i-1,j}) \tag{2.43}$$

Coefficients $\varepsilon^{(2)}_{i+\frac{1}{2},j}$ and $\varepsilon^{(4)}_{i+\frac{1}{2},j}$ are adapted by coefficients χ_2 and χ_4 to modify dissipation locally:

$$\varepsilon^{(2)}_{i+\frac{1}{2},j} = \chi_2 r_{i+\frac{1}{2},j} + \nu^{(i)}_{i+\frac{1}{2},j} \tag{2.44}$$

$$\varepsilon^{(4)}_{i+\frac{1}{2},j} = \max\left(0, \chi_4 r_{i+\frac{1}{2},j} - \varepsilon^{(2)}_{i+\frac{1}{2},j}\right) \tag{2.45}$$

where coefficient $r_{i+\frac{1}{2},j}$ is a scaling factor (called spectral radius) and sensor $\nu^{(i)}_{i+\frac{1}{2},j}$ allows for detecting discontinuities. At Eurocopter France, default values for coefficients χ_2 and χ_4 are 0.5 and 0.032, respectively.

AUSM+ scheme The Advection Uptream Splitting Method (AUSM) is an upwind scheme, for which the numerical flux is the sum of a numerical convective flux and numerical pressure flux expressed on the boundary surface of cells i and $(i+1)$ as given by [87, 91]:

$$\mathbf{F}_{i+1/2} = \mathbf{F}^c_{i+1/2} + \mathbf{P}_{i+1/2} \tag{2.46}$$

For one-dimensional upwinding, convective and pressure terms on the cell boundary are given as follows:

$$\mathbf{F}^c_{i+1/2} = \mathbf{M}_{i+1/2}\, \mathbf{a}_{i+1/2}\, \mathbf{\Phi}_{i+1/2} \tag{2.47}$$

$$\mathbf{P}_{i+1/2} = \mathbf{p}_{i+1/2}\, (0, 1, 0)^T \tag{2.48}$$

where $\mathbf{M}$ and $\mathbf{a}$ represent local values of Mach number and speed of sound, respectively, and $\mathbf{\Phi}$ is the conservation variables vector $[\rho, \rho u, \rho h]^T$. Local Mach number $\mathbf{M}_{i+1/2}$ and pressure

$\mathbf{p}_{i+1/2}$ are computed from values on left and right sides of the interface, denoted $_L$ and $_R$, respectively:

$$\mathbf{M}_{i+1/2} = \mathcal{M}_L^+ + \mathcal{M}_R^- \tag{2.49}$$

$$\mathbf{p}_{i+1/2} = \mathcal{P}_L^+ \, p_L + \mathcal{P}_{R+1}^- \, p_{R+1} \tag{2.50}$$

Split Mach number $\mathcal{M}^\pm$ and pressure $\mathcal{P}^\pm$ are a function of the Mach number and given by:

$$\mathcal{M}^\pm(M) = \begin{cases} \frac{1}{2}(M \pm |M|) & \text{if } |M| > 1 \\ \pm\frac{1}{4}(M \pm 1)^2 & \text{otherwise} \end{cases} \tag{2.51}$$

$$\mathcal{P}^\pm(M) = \begin{cases} \frac{1}{2}(1 \pm \operatorname{sign}(M)) & \text{if } |M| \geq 1 \\ \frac{1}{4}(M \pm 1)^2(2 \mp M) & \text{otherwise} \end{cases} \tag{2.52}$$

Expressing mass fluxes, split Mach number and pressure differently makes that a family of AUSM-schemes exists [58]. One of those, the one implemented in *elsA*, is called AUSM+ [86]. The difference between AUSM+ and the above described AUSM scheme lies in the expression of split Mach number and pressure. The split Mach number can be found by replacing Equation 2.51 with:

$$\mathcal{M}^\pm(M) = \begin{cases} \frac{1}{2}(M \pm |M|) & \text{if } |M| > 1 \\ \pm\frac{1}{2}(M \pm 1)^2 \pm \beta(M^2 - 1)^2 \text{ with } \beta = \frac{1}{8} & \text{otherwise} \end{cases} \tag{2.53}$$

In the same way, instead of Equation 2.52, split pressure is now described as:

$$\mathcal{P}^\pm(M) = \begin{cases} \frac{1}{2}(1 \pm \operatorname{sign}(M)) & \text{if } |M| \geq 1 \\ \frac{1}{4}(M \pm 1)^2(2 \mp M) \pm \alpha M(M^2 - 1)^2 \text{ with } \alpha = \frac{3}{16} & \text{otherwise} \end{cases} \tag{2.54}$$

Details of AUSM+ scheme are presented in [86] and the particular implementation done in *elsA* is detailed in [91]. As this implementation differs somewhat from the original scheme for low-Mach preconditioning, *elsA*'s version of the scheme will be referred to as AUSMp in the rest of this work.

As AUSM is a first-order scheme, Monotone Upstream-centred Schemes for Conservation Laws (MUSCL) extrapolation is used for extension to second-order. The idea is to extend the stencil used by adding gradient information of left and right cells. In particular, states of both cells are defined on cell boundary $i + 1/2$ by $\mathbf{P}^L_{i+1/2}$ and $\mathbf{P}^R_{i+1/2}$:

$$\mathbf{P}^L_{i+1/2} = \mathbf{P} + 0.5 \, \text{slope}_i(i) \tag{2.55}$$

$$\mathbf{P}^R_{i+1/2} = \mathbf{P} - 0.5 \, \text{slope}_i(i+1) \tag{2.56}$$

where slope_i indicates the slope in i-direction by:

$$\text{slope}_i(i) = \Psi(\mathbf{P}_i - \mathbf{P}_{i-1}, \mathbf{P}_{i+1} - \mathbf{P}_i) \tag{2.57}$$

Function Ψ refers to limiter functions that avoid spurious oscillations close to discontinuities. In the present Dissertation, the Van Albada limiter will be used, which is defined as:

$$\Psi(a,b) = \frac{(b^2+\epsilon)a + (a^2+\epsilon)b}{a^2+b^2+2\epsilon} \tag{2.58}$$

where ϵ is a very small, fixed value and a and b refer to conservative fluxes on the left and right cells, respectively.

Time integration methods

The system of semi-discrete RANS equations of 2.40 needs to be integrated in time. In rotor simulations, two time integration methods are used: backward Euler and Gear time-stepping. In fact, backward Euler is used for steady state simulations, such as hover simulation. For forward flight simulation, a physically unsteady solution is sought. Here, Gear time-stepping is used for creating sub-iterations between physical time steps. Both methods will be introduced next.

Backward Euler Backward Euler is an implicit integration scheme meaning a local time-step is used in each mesh cell, which depends on its size and local flow velocity. Only the converged state has a physical meaning. In this scheme, conservation variable vector $\mathbf{W}$ at new integration step $n+1$ depends on its state of iteration n by:

$$\mathbf{W}^{(n+1)} - \mathbf{W} = -\frac{\Delta t}{V(\Omega)}\mathbf{R}_\Omega^{(n+1)} \tag{2.59}$$

The residual $\mathbf{R}_\Omega$ at time $(n+1)$ represents the difference between time steps n and $(n+1)$ and may be given as follows:

$$\mathbf{R}_\Omega = \sum_{i=1}^{6} = (\mathbf{F}_n)_{\Sigma_i} - V(\Omega)\mathbf{T}_\Omega \tag{2.60}$$

The residual is obtained by a first-order linearization at iteration n:

$$\mathbf{R}_\Omega^{(n+1)} = \mathbf{R}_\Omega^{(n)} + \left.\frac{\partial \mathbf{R}}{\partial \boldsymbol{\Omega}}\right|_n \Delta\boldsymbol{\Omega}^{(n)} + \mathcal{O}(\Delta t^2) \tag{2.61}$$

Inserting Equation 2.61 into 2.59 leads to:

$$-\mathbf{R}_\Omega^{(n)} = \left(\left.\frac{\partial R}{\partial \mathbf{W}}\right|_n + \frac{V(\Omega)}{\Delta t}\right)\Delta\mathbf{W}_n \tag{2.62}$$

For resolution, the Jacobian matrix $\partial\mathbf{R}/\partial\boldsymbol{\Omega}$ is decomposed by the LU-SSOR technique, described in [156]. This first-order accurate scheme is unconditionally unstable for centred spatial discretization schemes such as Jameson if no artificial dissipation would be added. The scheme may be stable at specific conditions for upwind schemes such as AUSMp.

Numerical convergence is here considered if residual term $\mathbf{R}_\Omega$ has reduced with 3 orders of magnitude.

Gear time-stepping For resolution of unsteady flows, advancing in time requires a physical time-step that is common for the complete computational domain. At each physical time-step, sub-iterations are performed for resolving flow conditions at that position. For rotor simulations, physical time-stepping corresponds to advancing azimuthal blade positions with

$\Delta\psi$ and at each blade position, sub-iterations are performed for resolving the flow state. Gear's scheme is a second-order accurate backward linear multi-step method, given by:

$$\mathcal{H}(\mathbf{W}^{n+1}) = \frac{V(\Omega)}{\Delta t^n}\left[\frac{3}{2}\mathbf{W}^{n+1} - 2\mathbf{W}^n + \frac{1}{2}\mathbf{W}^{n-1}\right] + \overline{\mathbf{R}}_\Omega^{(n+1)} = 0 \tag{2.63}$$

where $\mathcal{H}$ is an unsteady residual operator. The resolution of nonlinear system 2.63 can be approximated by an iterative Newton method. Denoting physical iterations by n and sub-iterations at each physical position by m, this approximation is given by:

$$\left.\frac{\partial\mathcal{H}(\mathbf{W}^{n+1})}{\partial\mathbf{W}^{n+1}}\right|_m \Delta\overline{\mathbf{W}}_\Omega^m = -\mathcal{H}(\mathbf{W}^{n,m}) \tag{2.64}$$

where $\Delta\overline{\mathbf{W}}_\Omega^m = \overline{\mathbf{W}}_\Omega^{n,m+1} - \overline{\mathbf{W}}_\Omega^{n,m}$. In a similar manner as presented for Equation 2.59, inserting Equation 2.64 into 2.63 gives:

$$\left(\frac{3}{2}\frac{V(\Omega)}{\Delta t^n}\mathbf{I} + \left.\frac{\partial\mathbf{R}}{\partial\mathbf{W}}\right|_m\right)\Delta\overline{\mathbf{W}}_\Omega^{n,m} = -\mathcal{H}(\mathbf{W}_\Omega^{n,m}) \tag{2.65}$$

where $\partial\mathbf{R}/\partial\mathbf{W}$ is the Jacobian matrix obtained from linearization of flux terms.

2.2.4 Rotor simulations with *elsA*

CFD simulations of helicopter rotors need to predict three-dimensional, viscous and unsteady flow phenomena on complex geometries. Comparisons of pressure distributions obtained from experiments and main helicopter rotor computations by *elsA* are presented in [51]. *elsA* computations of fuselage and rotor blades are performed and compared to wind tunnel data in [115].

Rotor head and blade root geometries are very complex and require a specific meshing strategy, which can hardly be automated. Rotor simulations are therefore performed on a so-called isolated rotor, meaning blade roots are not represented. Blade geometry is thus represented from the first airfoil section of the blade on. A consequence of this limitation is a recirculation area in the blade root zone, where in real life flow could partially be blocked by geometrical parts. This is acceptable in a preliminary design stage, but blade roots need to be represented for detailed design of inboard blade sections. As for optimization automatic mesh generation is required and preliminary designs are created, blade roots may be neglected so that isolated rotor simulations are performed.

Two automatic blade grid generation softwares are available at Eurocopter, the so-called VIS12 and Autogrid codes. The first originates from the ONERA code that provided mesh generation and a CFD solver based on coupled Euler/boundary layer resolution. VIS12 here refers to the mesh generation part which is based on a mono-block topology, meaning the complete domain around one blade consists of one mesh block. Grid generation starts with C-meshes around airfoil sections along the blade, which are inter-connected. Outer points are extended to the complete computational domain and several optimization loops are performed to distribute points equally in space. This mesh type is illustrated in Figure 2.44.

Autogrid generates a O-mesh around the solid blade surface and uses a so-called butterfly topology on blade leading and trailing edges. This blade mesh is extended to 2 chords upstream and downstream of the blade, 0.5 chord in the inner part of the blade root and 2 chords in the extension of the blade tip. A cylindrical background grid is generated and Chimera techniques are used to interpolate between the two meshes. Advantages of Chimera meshes are the flexibility of mesh generation and the possibility to move mesh blocks with respect to others. Main drawback of Chimera meshes is the requirement of information transfer between

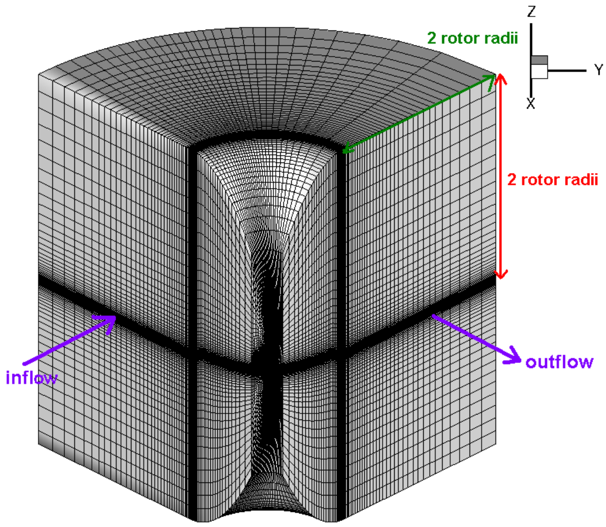

Figure 2.44: Example of VIS12 mesh for hover rotor simulations

neighbour blocks [22]. Top- and sideviews of a rotor blade Chimera mesh are presented in Figure 2.45.

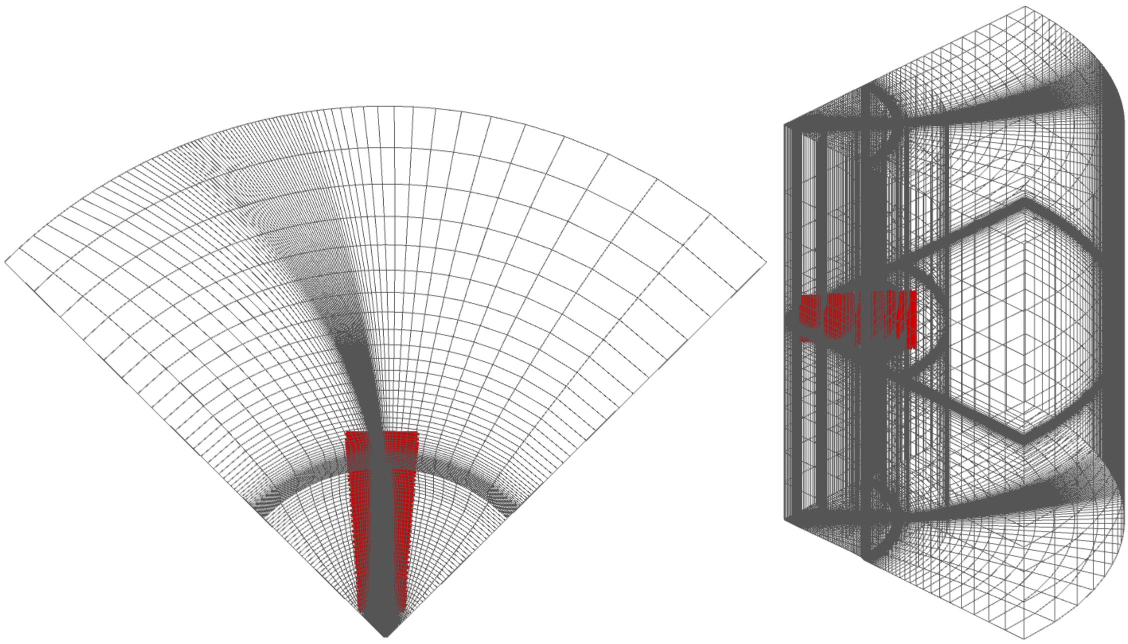

Figure 2.45: Top- (left) and sideview (right) of an Autogrid Chimera mesh: background (grey) and blade mesh (red)

Different aerodynamic phenomena occur in hover and forward flight making that different types of simulations are performed. Details of CFD simulations in hover and in forward flight are provided in next Sections.

Hover flight simulations with *elsA*

In hover, all blades encounter identical flow conditions, no matter their azimuthal position. This flow field is simulated as a steady-state problem in which only one blade is represented.

A hover mesh then only contains a domain around this single blade and periodicity conditions are imposed on lateral boundaries so that outflow is re-injected. A typical hover mesh is illustrated in Figure 2.44, showing physical domain size and periodicity boundary conditions.

On resulting boundaries, the so-called Froude boundary condition is imposed. This boundary condition is based on the Froude equation that relates rotor induced velocity created by rotor thrust as follows:

$$v_i = \sqrt{\frac{T}{2\rho_\infty A}} \tag{2.66}$$

where v_i is the mean induced velocity through the rotor disk, T represents rotor thrust, ρ_∞ is the density at the farfield (Froude's theory assumes incompressible flow) and A is the rotor disk surface. According to Froude's theory, the surface of an infinite lower boundary has half the size of the rotor disk. Through this lower boundary, flow streams at two times the velocity given by Equation 2.66, which is numerically reproduced by a potential sink boundary. Over the remaining boundaries, a condition is imposed to let the flow stream into the domain. The inflow velocity equals:

$$\overline{V} = -\frac{A}{4\pi r^3} v_i \bar{r} = -\frac{A}{4\pi r^2}\sqrt{\frac{T}{2\rho_\infty A}}\overline{e}_r \tag{2.67}$$

where vector notation and $\overline{e}_r$ refer to the vector between a point on the boundary with respect to the rotor disk centre.

Forward flight simulations with *elsA*

CFD simulations of helicopter rotors in forward flight are unsteady computations of isolated rotors. In these simulations, both a rotating and forward flight velocity need to be imposed. This can be achieved in two ways:

1. Rotate and move all mesh blocks with rotational and forward flight velocities. Possible for non-Chimera and Chimera meshes.

2. Fix the background mesh and rotate blade meshes within this background. Forward flight velocity is added either by moving all mesh blocks or as a boundary condition. Possible for Chimera meshes only.

At Eurocopter, the second solution is selected for its easier computational set-up.

The initial flow state, either given by initial conditions or by mesh movements, only contains rotational and forward flight velocity components but no rotor wake. Typical computational sequences for progressively refining wake resolution are done as follows:

- 3 rotor rotations at $\Delta\psi = 10°$: 108 time-steps
- 2 rotor rotations at $\Delta\psi = 5°$: 144 time-steps
- 1 rotor rotation at $\Delta\psi = 1°$: 360 time-steps

This sequence requires in total 612 physical time-steps, which is less than 2 or 3 rotor rotations on $\Delta\psi = 1°$ that would be required for convergence. Analysis of rotor performance is done on the $\Delta\psi = 1°$ simulation over a simulation period equal to 360° divided by the number of blades and by summation of forces on all blades.

In forward flight, rotor equilibrium is found by variations of blade pitch, flapping and lead-lag angles over a rotor rotation, as well as a static inclination angle of the rotor mast

(Section 1.1.2). These rotor motions are obtained from a HOST equilibrium computation and inserted into *elsA* in terms of harmonics. A precise description of rotor harmonics and their insertion into a CFD computation is given by [125]. In *elsA*, two ways exist of applying these harmonics: on mono-block meshes, *elsA* deforms the grid at each azimuth step to place the blade at its correct position. On Chimera meshes, blade grids are rotated about all three axes within the background mesh. Updating of Chimera interpolation coefficients is then required at all azimuthal steps.

2.2.5 Numerical simulation of a wingtip vortex

We now assess numerical results provided by *elsA* against a well-documented test case, namely, flow measurements over and directly behind a half-wing as tested in the NASA Ames wind tunnel and as described by [43]. A 4-feet chord, 3-feet span half-wing with a NACA0012 airfoil was placed in a wind tunnel with a 32x48 inch test section, as illustrated in Figure 2.46. Chord based Reynolds number of test conditions equals $4.35 \cdot 10^6$.

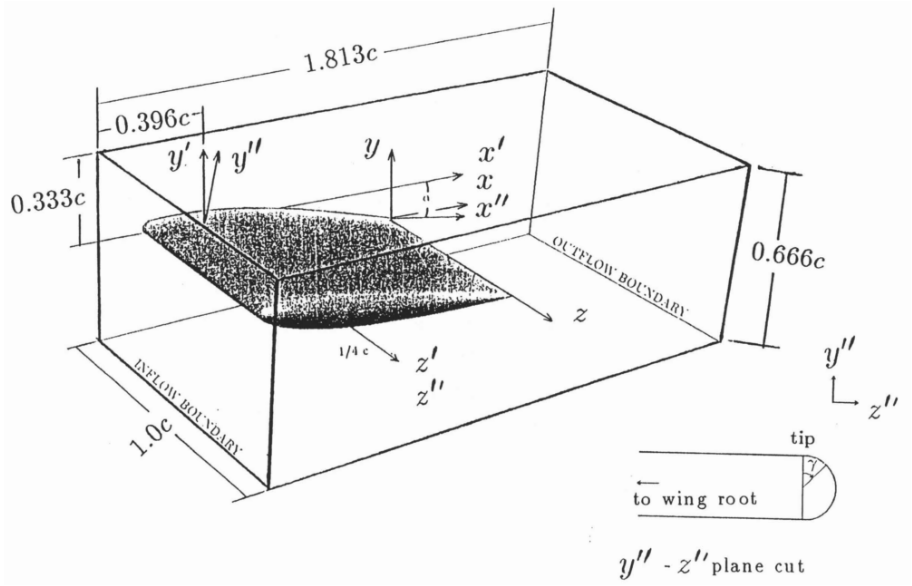

Figure 2.46: NACA0012 airfoil positioned in wind tunnel, from [43]

This test case has been selected for its complete measurement matrix containing not only the mean flow but also all six components of the Reynolds stress tensor. Measurements were performed on the wing and in the wake, until $0.678\bar{c} = 0.83$m behind it, so that vortex formation is precisely documented. In addition, chord based Reynolds number is in the same order of magnitude as that of a rotor blade tip, so that a comparison would be feasible, even though Mach number does not correspond ($M_{\text{half-wing tip}} \sim 0.15$ vs. $M_{\text{rotor blade tip}} \sim 0.5-0.9$) and measurements were taken at an angle-of-attack of 10°.

Correspondence of turbulence field of a wingtip vortex over a fixed wing and helicopter rotor blade is demonstrated by [113] and [112]. Turbulence measurements in the wake of a single-bladed rotor by the latter show similarities to fixed wing measurements for Reynolds stresses $\overline{u_i'u_j'}$ and $\overline{u_j'u_k'}$ and Reynolds strain rates $\frac{\partial u_i}{\partial y} + \frac{\partial u_j}{\partial x}$ and $\frac{\partial u_j}{\partial z} + \frac{\partial u_k}{\partial y}$. Qualitative analysis of these turbulences measurements demonstrates a clear correlation between fixed wing and helicopter rotor tip vortex turbulence. Even if Reynolds and Mach numbers of both experiments do not correspond, turbulence patterns remain the same for both types of tip vortices. From these studies, it can be concluded that the fixed wing measurements of [43] can be considered representative of a helicopter rotor tip vortex for this methodology comparison.

To compare experiment and computations, three measurements planes will be used, as illustrated in Figure 2.47. The first plane ($x/\bar{c}$ = -0.1975) cuts the region where the boundary layer wraps up around the wingtip, showing thereby vortex formation. At $x/\bar{c}$ = 0.005, the measurement plane is positioned just behind the trailing edge, in the region where the vortex is shed into the wake. The vortex is still surrounded by the boundary layer. The third plane is located behind the wing ($x/\bar{c}$ = 0.246) where the vortex is completely rolled up and has started its decay. Numerical dissipation of the vortex is expected to affect computed mean flow characteristics of this plane.

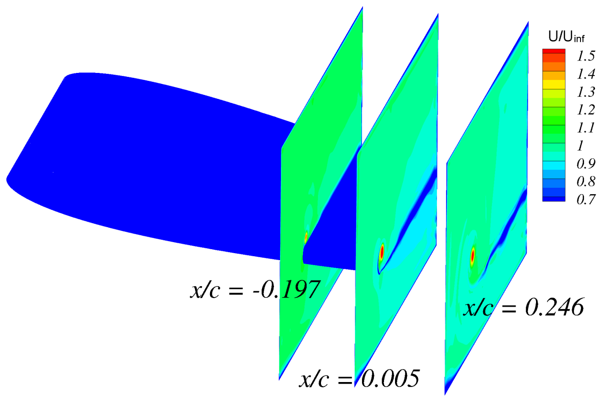

Figure 2.47: Longitudinal velocity at three measurement planes, at $x/\bar{c}$ = -0.197, $x/\bar{c}$ = 0.005 and $x/\bar{c}$ = 0.246

The objective of this study is to assess the influence of numerical parameters on computed tip vortices. Measurements will be compared to numerical simulations to study influence of various numerical parameters:

1. Mesh refinement: numerical solutions on three meshes with different degrees of refinement are evaluated.

2. Numerical scheme: the Jameson scheme is tested for three combinations of (χ_2,χ_4): Eurocopter default settings of (0.5, 0.032), reduction of χ_4 to (0.5, 0.016) and reduction of χ_2 to (0.0, 0.032). In addition, the Jameson scheme is tested against AUSMp, with and without the Van Albada limiter.

3. Turbulence model: $k - \omega$ and SSG-ω are compared.

All computations are steady-state RANS simulations and are performed using multigrid techniques to accelerate convergence.

Boundary conditions

Before studying the influence of various numerical parameters, numerically reproduced pressure coefficients are compared to measurements. Whereas the Ames' wind tunnel has a relatively short straight inlet section, as illustrated in Figure 2.48, numerical simulations were performed on a wind tunnel mesh having 6 chords ahead and behind the half-wing. This should allow numerical flow to accommodate before reaching the half-wing.

In preliminary simulations, a pressure distribution shift was found over the half-wing, as illustrated on the left-hand side of Figure 2.49. This discrepancy was found to be due to boundary layer creation on walls ahead of the half-wing, as illustrated on the right-hand side. Wind tunnel confinement, created by thick boundary layers ahead of the half-wing, leads to an axial velocity increase at the section of interest. This in turn causes the observed pressure distribution shift.

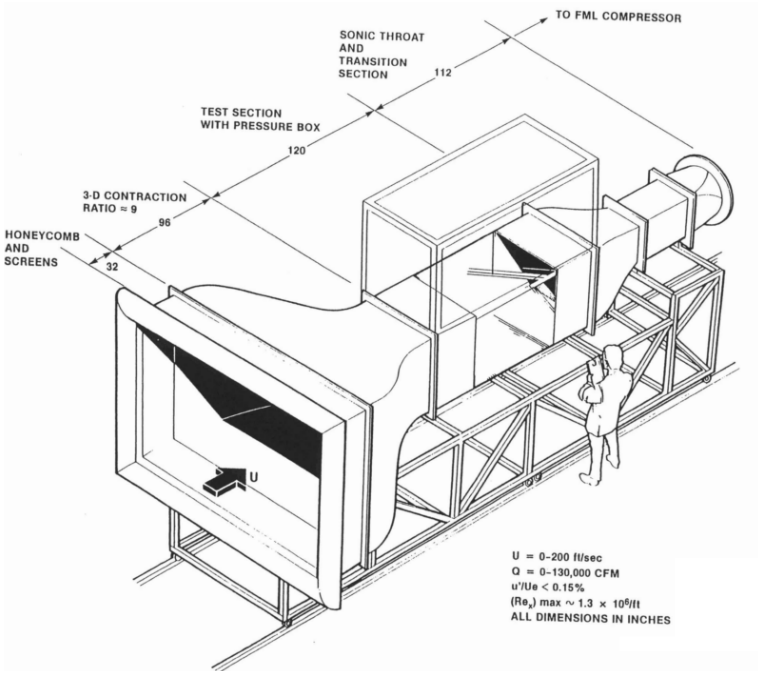

Figure 2.48: Ames' wind tunnel facility, from [43]

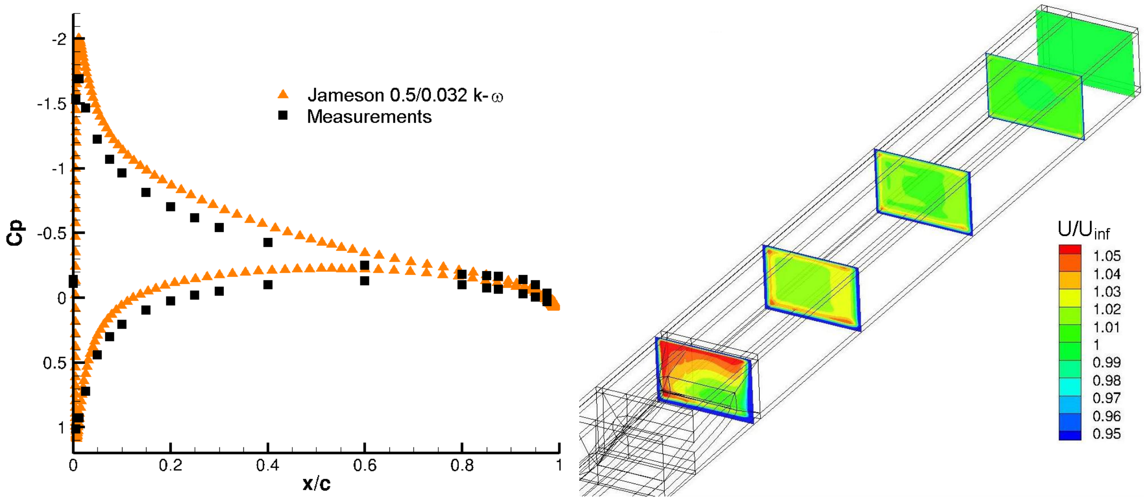

Figure 2.49: Pressure distribution comparison of simulations and experiment (left) and axial velocity at different positions in the inlet of the numerical wind tunnel (right)

As a solution, wall slip conditions were imposed on walls ahead of the half-wing up until a position comparable to that of the start of the test section used for experiments ($x/\bar{c}$ =-2.2), as indicated in Figure 2.48. In addition, inlet conditions imposing a velocity vector, normalized total pressure, normalized total enthalpy and turbulence field were chosen. This turbulence field depends on turbulence modelling and is given by turbulence kinetic energy k and turbulence dissipation rate ω for the $k-\omega$ model and the 6 components of the Reynolds stress tensor plus ω for RSM-SSG. In the numerical wind tunnel outlet boundary, only a static pressure was imposed, equivalent to 0.9 times the inlet total pressure. This value was chosen such that pressure distribution coherency between measurements and simulations was found. These pressure coefficients are compared at two positions along the wing span in Figure 2.50. Numerical results are computed on the medium grid, using the $k-\omega$ model and both numerical schemes. At $z/\bar{c} = 0.25$, numerical results are in good comparison with experimental data. This is also observed for other wing sections along the straight part of the wingtip. However, some discrepancies are perceived on the wingtip, in the zone where the vortex is formed (corresponding to $z/\bar{c} = 0.666$).This pressure distribution comparison shows that wind tunnel walls are taken into account correctly and that simulated confinement is comparable to that of the measurements.

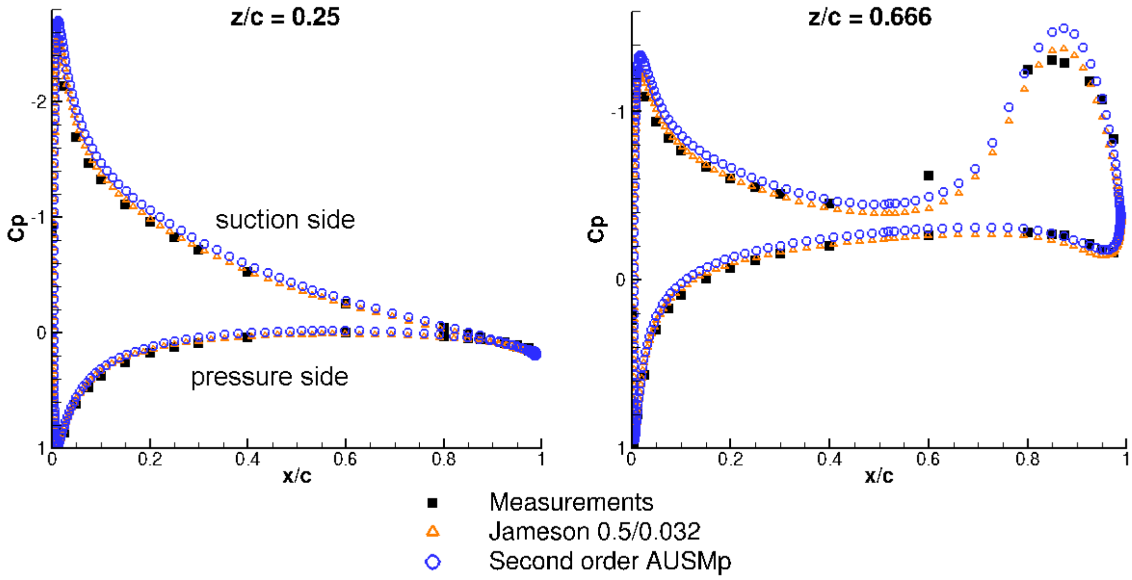

Figure 2.50: Comparison of measured pressure distributions at $z/\bar{c} = 0.25$ (left) and $z/\bar{c} = 0.666$ (right) to those obtained from computation on medium grid, with $k-\omega$ model and two numerical schemes

Mesh study

Three numerical meshes were created for studying influence of mesh size within the tip vortex, in boundary layers over the wing and wind tunnel walls and in the complete computational domain. Surface mesh of half-wing and wind tunnel walls and a mesh slice at $x/\bar{c} = 0$ are illustrated in Figure 2.51. Main characteristics of the three meshes are given in Table 2.3. According to [54], a minimal mesh spacing of $0.003\bar{c}$ is required in the vortex core. This is obtained for the refined mesh in both y- and z-direction, for the medium mesh only in y-direction and for the coarse mesh for neither of the directions.

Table 2.3: Comparison of numerical meshes for simulation of NACA0012 half-wing

	coarse mesh	medium mesh	refined mesh
Max spacing in x-direction [$\bar{c}$]	0.1	0.1	0.02
Max spacing in y-direction [$\bar{c}$]	0.01	0.0056	0.0028
Max spacing in z-direction [$\bar{c}$]	0.0095	0.0034	0.0015
First node distance on wing [m]	$5 \cdot 10^{-6}$	$1 \cdot 10^{-6}$	$1 \cdot 10^{-6}$
First node distance on wind tunnel walls [m]	$10 \cdot 10^{-6}$	$5 \cdot 10^{-6}$	$3 \cdot 10^{-6}$
Max y^+ value on wing	2.3	0.6	0.5
Max y^+ value on wind tunnel walls	6	4.8	1.7
Number of blocks	109	109	142
Total mesh size	$5 \cdot 10^6$ nodes	$19 \cdot 10^6$ nodes	$33 \cdot 10^6$ nodes

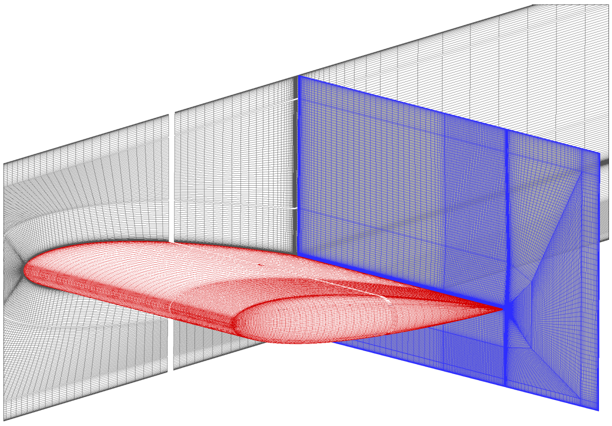

Figure 2.51: Surface mesh on wind tunnel wall and wing, mesh at $x/\bar{c} = 0$

Grid convergence is tested on these three meshes. Figure 2.52 shows iso-contours of normalized axial velocity on the plane located at $x/\bar{c} = 0.005$ obtained on the three meshes. Computations have been carried out here using RSM model and Jameson scheme with artificial viscosity coefficients (0.5, 0.032). Although the shape of the vortex is well represented in all simulations, mesh refinement has an important influence on results. Only the refined grid result captures the vortex size and core position correctly. The coarser the grid, the more iso-velocity lines are spread out. This also leads to an incorrect vortex core velocity prediction.

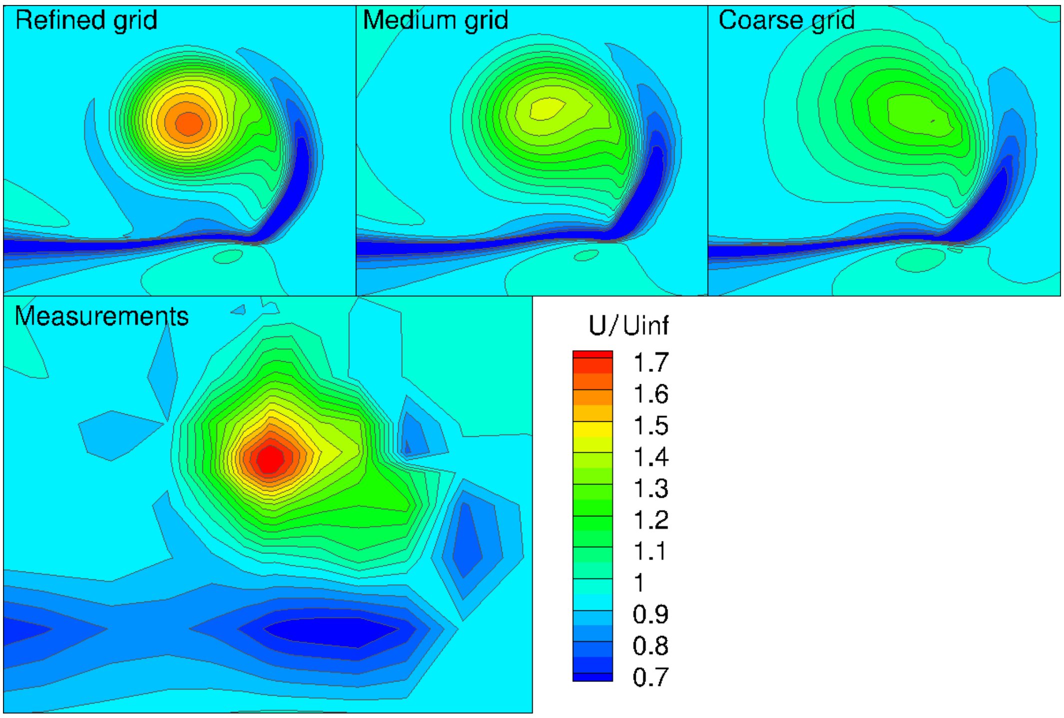

Figure 2.52: Comparison of normalized axial velocity at $x/\bar{c} = 0.005$ with RSM model and Jameson (0.5, 0.032)

Axial flow acceleration in the vortex core is visualized in Figure 2.53, showing axial velocity along a line parallel to the wing trailing edge and crossing the vortex core. These simulations were all performed with the Jameson scheme (0.5, 0.032) and $k-\omega$ model. It is clear that better simulation of the velocity peak in the vortex core is obtained for more refined meshes. This conclusion is hereby confirmed for both turbulence models.

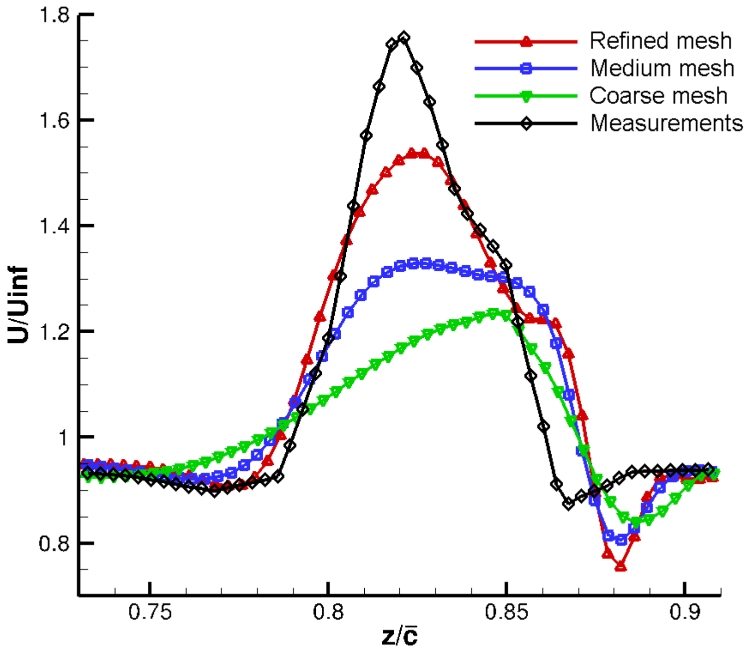

Figure 2.53: Comparison of measured and simulated normalized axial velocity at $x/\bar{c} = 0.005$ along a line parallel to the trailing edge, crossing the vortex core. Simulations with $k-\omega$ model and Jameson (0.5,0.032)

Even though mesh refinement in the vortex core region advised by [68] is attained for the refined mesh, grid convergence may not yet be established, since a difference of 12% on the peak velocity is found when passing from the medium to the refined grid. It is thus possible that an even more refined grid further improves computational results.

It can be concluded that a refined grid is of utmost importance for correct simulation of a tip vortex. Insufficiently refined grids do not allow capturing typical vortex characteristics, such as acceleration in the core, even though boundary layer roll-up that creates the vortex is simulated with relative accuracy. Nevertheless, for helicopter rotor simulations of practical interest, using such refinement is not viable. An alternative approach is to increase the accuracy of the discretization scheme.

Spatial discretization scheme

Effect on vortex formation by numerical scheme and its adjustment parameters is illustrated in Figure 2.54. Jameson scheme was tested for three combinations of coefficients χ_2 and χ_4: (0.5, 0.032), (0.5, 0.016) and (0.0, 0.032). Second-order AUSMp scheme was assessed with and without the Van Albada limiter. All these computations were performed on the medium grid and with the eddy viscosity turbulence model. The figure shows that the AUSMp scheme without Van Albada limiter and the Jameson scheme with the lower choice for χ_4 (0.5, 0.016) provide a better resolution of the vortex core, which also improves agreement with measurements. Concerning the Jameson scheme, modifying dissipation coefficient χ_2 seems to have no effect on the result. It may be concluded that the discontinuity sensor is not switched on in present simulations. The χ_4 coefficient needs to be reduced to limit dissipation. However, numerical stability imposes a lower limit on this value, as a computation with $\chi_4 = 0.008$ diverged. The AUSMp scheme is always less dissipative than the Jameson scheme, even for the lowest tested value of χ_4. Adding the Van Albada limiter was expected to have no effect, since flow is fully subsonic and no discontinuities are formed. Yet, the Van Albada limiter influences computational results to a high extent. It reduces axial velocity in the vortex core already on the wing surface leading to a smaller vortex. For this reason, succeeding computations are carried out without any limiter.

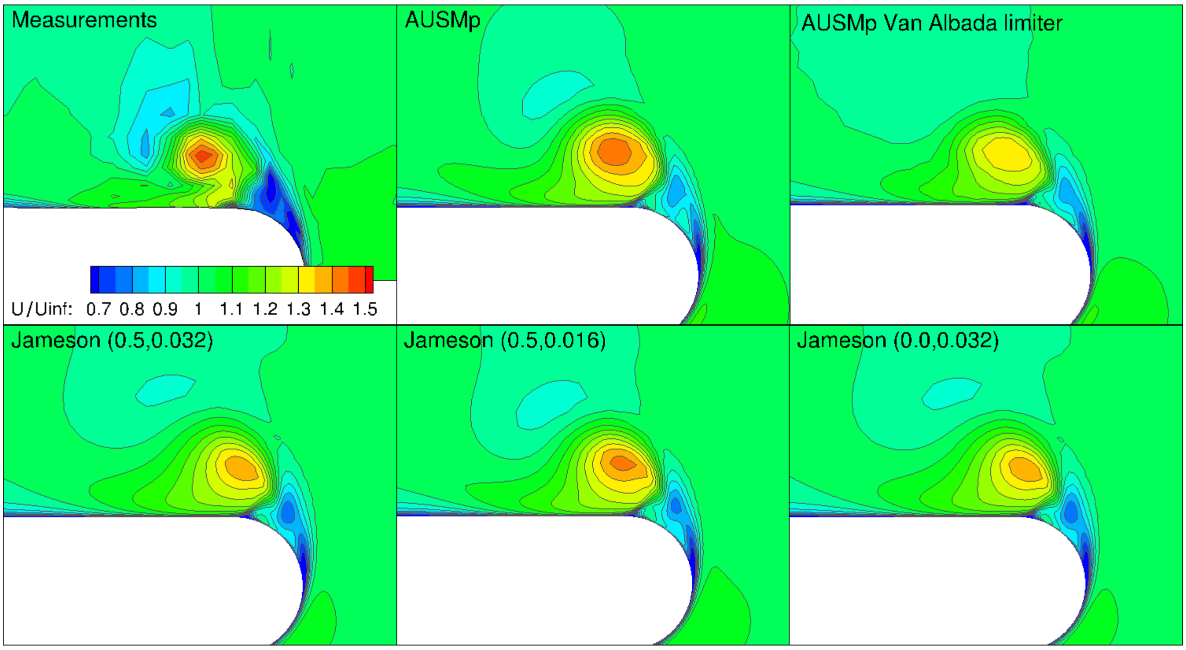

Figure 2.54: Comparison of normalized axial velocity at $x/\bar{c}$ =-0.197 on medium grid and $k-\omega$ turbulence model, for two numerical schemes with various parameters

At $x/\bar{c}$ = 0.005 the vortex shed in the wake starts being dissipated both by physical and numerical effects. On the refined grid, the central-difference Jameson scheme dissipates the vortex more quickly than the AUSMp scheme, as shown by the results of Figure 2.55: it compares results of AUSMp scheme with those of Jameson scheme with dissipation coefficients (0.5, 0.032). Similar conclusions are obtained for both turbulence models under investigation. In conclusion, to improve a tip vortex simulation, the numerical scheme should be as less dissipative as possible. The AUSMp scheme fulfils this requirement better than the Jameson scheme, although lowering the χ_4 value also helps in reducing numerical dissipation. Adding the Van Albada limiter has a non-negligible influence on the computation and should better be avoided if computational stability allows.

Turbulence modelling

In this section, formation and transport of the wingtip vortex by using eddy viscosity $k-\omega$ and SSG$-\omega$ turbulence models are investigated. All subsequent results have been obtained on the refined grid and using the AUSMp scheme. For analysis, we consider numerical results along the three planes of Figure 2.47, and we compare with corresponding measured quantities.

At $x/\bar{c}$ =-0.197, the boundary layer wraps up along the wingtip while the viscous vortex core accelerates, as seen in the measurements in Figure 2.56. The acceleration process is predicted by both turbulence models, as demonstrated by inspection of the computations illustrated in Figure 2.56. The represented quantity is axial velocity normalized with upstream velocity. Surprisingly, core velocity increase is somewhat better predicted by $k-\omega$ than by the SSG model. Yet, the zone of decreased axial velocity, on the rounded side of the wingtip, is better calculated by RSM. Moreover, the vortex core position is very well predicted by

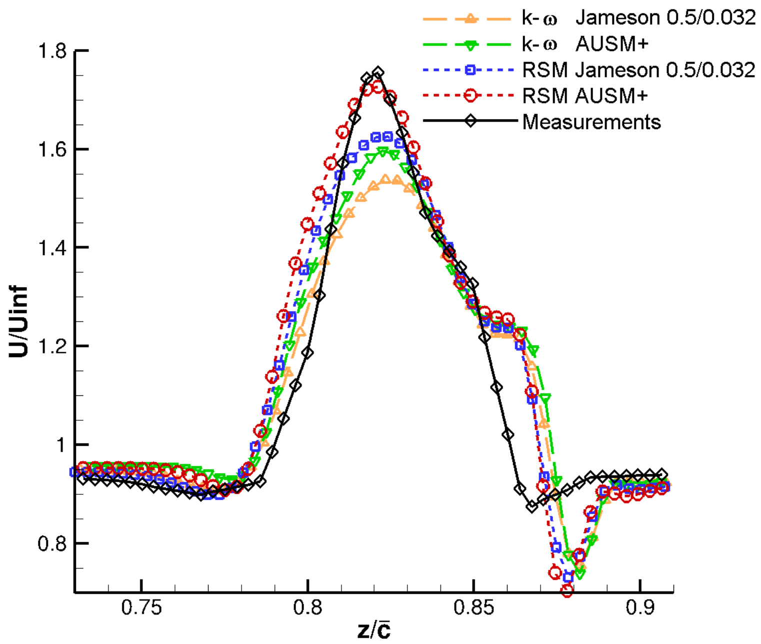

Figure 2.55: Comparison of measured and simulated normalized axial velocity at $x/\bar{c} = 0.005$ along a line parallel to the trailing edge, crossing the vortex core. Simulations on refined grid with $k-\omega$ and RSM turbulence models and Jameson (0.5, 0.032) and AUSMp

the RSM model, whereas the eddy viscosity model is less accurate. Furthermore, comparable results can be found in [47]. In this article the eddy viscosity model, $k-\epsilon$ in this case, also predicts a too high axial velocity in the vortex core at $x/\bar{c}$ =-0.197. This is even more significant for the non-linear version of the $k-\epsilon$ model. The RSM model of the cited article shows similar features as current computations.

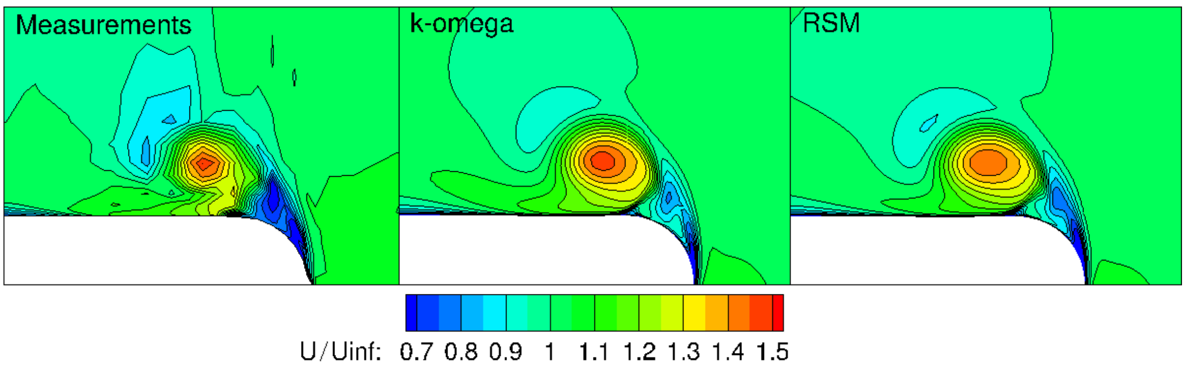

Figure 2.56: Comparison of normalized axial velocity at $x/\bar{c}$ =-0.197 on refined mesh with AUSMp scheme and two turbulence models

From the trailing edge on, differences between the two turbulence models are accentuated. Figure 2.55 shows normalized axial velocity through the vortex core in the plane $x/\bar{c} = 0.005$ for both turbulence models. Comparing the $k-\omega$ model with SSG, for refined grid and AUSMp, we see that the second order turbulence model better predicts core acceleration and provides results in close agreement with measured data for the core velocity.

Normal Reynolds stresses, being by definition all three equal for eddy viscosity models, are expected to be the major cause of differences between the two turbulence models. A comparison of these stresses for the two turbulence models on the plane $x/\bar{c} = 0.005$ and computed on the refined grid with AUSMp is given in Figure 2.57. Even though both turbulence models do not predict very well normal Reynolds stresses, the $k - \omega$ model seems to be far more dissipative than the SSG model.

Nonetheless, it cannot be concluded that this over-prediction of normal stresses holds for all eddy viscosity models, as shown from [47]. In this article, the $k - \epsilon$ model appears to dissipate less than the $k - \omega$ model here employed. On the other hand, both simulated vortices seem to be too large compared with experiments. This appears to be the case as well in the previously cited article. Yet, the $k - \omega$ model again overestimates this effect and has the largest zone of increased normal axial stress, compared to the SSG model, and to the results of $k - \epsilon$, non-linear eddy viscosity and second moment closure models of [47]. Apparently, the axial normal stress prediction of the $k - \omega$ model is particularly off with respect to other computations.

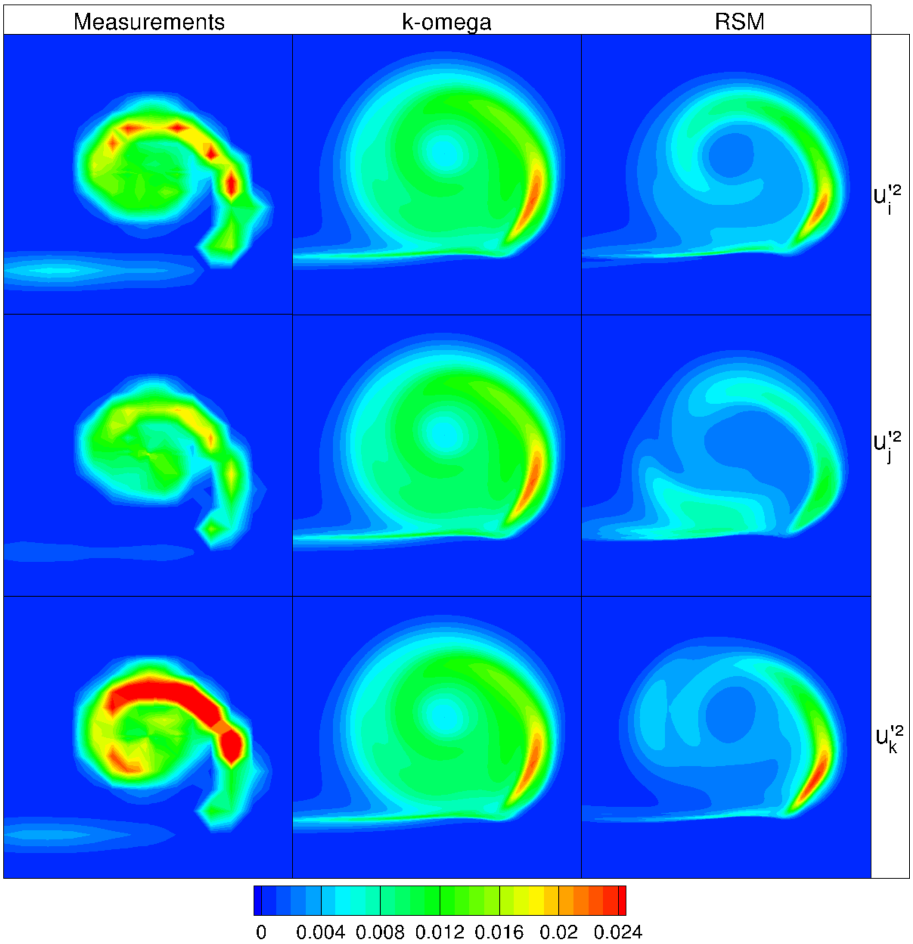

Figure 2.57: Comparison of normalized normal Reynolds stresses $u_i'^2/U_\infty^2$, $u_j'^2/U_\infty^2$ and $u_k'^2/U_\infty^2$ at $x/\bar{c} = 0.005$ for two turbulence models on refined grid computations with AUSMp

Somewhat further downstream, at $x/\bar{c} = 0.246$ as illustrated in Figure 2.58, where vortex dissipation has started, both turbulence models predict a too fast decay of vortex strength compared to experiments, decay being more significant for the $k - \omega$ model. Actually, the eddy viscosity model dissipates more quickly axial velocity, due to an overprediction of turbulent dissipation. Similarly to results at $x/\bar{c} = 0.005$, vortex axial velocity is flattened out for the $k - \omega$ case, compared to relatively good prediction provided by SSG. Nevertheless, also the RSM simulation suffers from a too high dissipation. Note however that this too high dissipation may also be due to numerical scheme or grid effects.

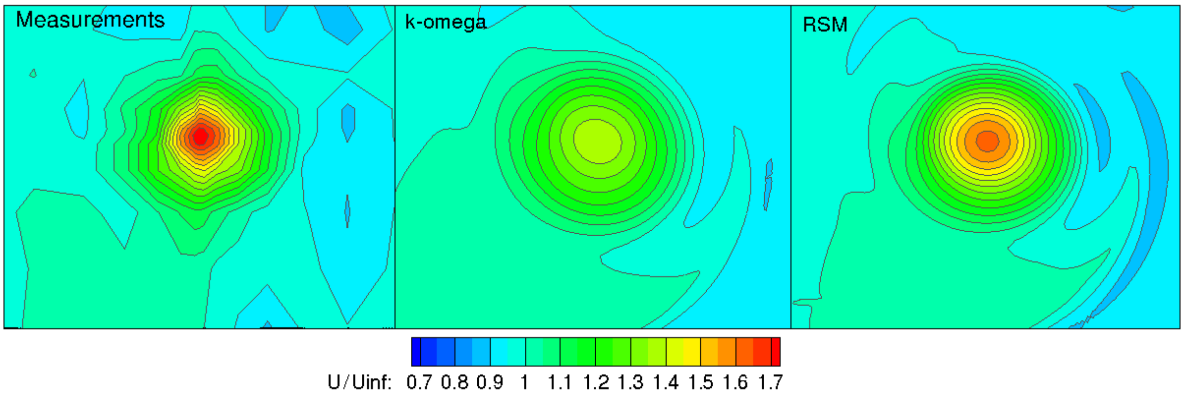

Figure 2.58: Comparison of normalized axial velocity at $x/\bar{c} = 0.246$ for 2 turbulence models on refined grid and with AUSMp scheme

In summary, the results indicate that RSM-SSG improves simulation accuracy, especially in the zone downstream of the trailing edge. The second order turbulence model limits vortex decay, even if dissipation in the vortex core is still too fast compared to measurements. Nonetheless, even though the benefits of the SSG model seems to come essentially from its lower dissipation, quantitative behaviour of the turbulent stresses is still in relatively poor agreement with experiments.

Conclusions on wingtip vortex simulations

Besides this qualitative assessment of wingtip vortex simulations, for industrial use of these methods, especially within an optimization loop, CPU time consumption is to be assessed as well. Computation time increases when switching from $k - \omega$ turbulence modelling to RSM by approximately 35%. AUSMp reduces CPU consumption with roughly 10% with respect to the Jameson scheme.

The numerical study investigated the capability of an industrial code to correctly describe formation and transport of a wingtip vortex. Simulations show that the numerical scheme has a very significant influence on the results of a CFD simulation of a wingtip vortex, of the same order of that of the chosen turbulence model. Fine grids and low dissipative schemes are essential for correctly capturing of at least the mean velocity field in the near wake. Second-order closures perform better than standard eddy viscosity models, even if the present simulations did not reveal a significant improvement over eddy viscosity models in the representation of turbulent stresses. Improvements seem to be mainly due to the reduced amount of turbulent dissipation introduced by the higher-order closure. Finally, in spite of the huge number of grid points composing the refined mesh used for this study, complete grid convergence was still not achieved. Use of high order, low dissipative schemes [84] and/or mesh adaptation [120] may open the way to accurate wingtip simulations while limiting grid refinement requirements.

2.2.6 Numerical simulation of the ORPHEE blades

To assess the ability of CFD software *elsA* to accurately evaluate rotor performance as a function of blade geometry variations, computations of the four ORPHEE blades are carried out. Hover and forward flight simulations are performed and default settings of the *elsA* software in use at Eurocopter are applied. It will be shown later that these default settings are often not the best choice for achieving accurate performance predictions. Hereafter, several sensitivity studies are carried out to check the impact of numerical settings on solution accuracy. These include mesh resolution, transition and turbulence modelling. As was seen in the wingtip vortex study, the AUSMp spatial discretization scheme significantly reduces numerical dissipation without increasing computational cost and will be used in all of the following computations.

First, hover simulations are presented. As a default at Eurocopter, a hover mesh is created with automatic blade mesh tool VIS12. As this tool appeared to deliver refined meshes of insufficient quality, mesh generation software Autogrid was acquired. A mesh study is performed using this software. Default computations are performed as fully turbulent, meaning laminar-turbulent transition is not modelled. Effect of incorporation of transition modelling is tested on a VIS12 mesh, as only this mesh topology allows for transition modelling in today's version of *elsA*. Finally, the influence of turbulence modelling on performance prediction is evaluated by comparing computations with $k-\omega$ and SSG turbulence models.

Secondly, forward flight simulations are assessed. Again, we check the effects of blade mesh refinement and turbulence modelling. Finally, an analysis of local flow behaviour is performed to examine causes of global performance differences between the four ORPHEE blades.

At the end of this section, we state some recommendations on best computational settings for prediction of rotor performance.

Hover simulations

A typical hover simulation at Eurocopter is executed on a VIS12 mesh, using a $k-\omega$ turbulence model and with AUSMp as numerical scheme, following the computational set-up that was detailed in Section 2.2.4. Mesh tool VIS12 creates C-meshes around airfoil sections which are extended towards the complete computational domain as illustrated in Figure 2.44. Hereafter, we consider a default mesh containing 173 nodes around the airfoil, 69 in spanwise direction out of which 33 nodes over the blade surface and 57 in the direction perpendicular to the blade surface. This leads to a total mesh size of 680 409 nodes. Computational convergence is considered within 3000 iterations as residuals are reduced by at least 3 orders of magnitude.

Simulation results of all four blades are compared to experimental data in Figure 2.59. The computation correctly predicts the superior performance of the EC4 blade. However, differences in numerical performance of EC1 and EC2 is much greater than the difference observed in experiments. Also, the hierarchy of EC1 and EC3 has changed in the computation, compared to measurement data.

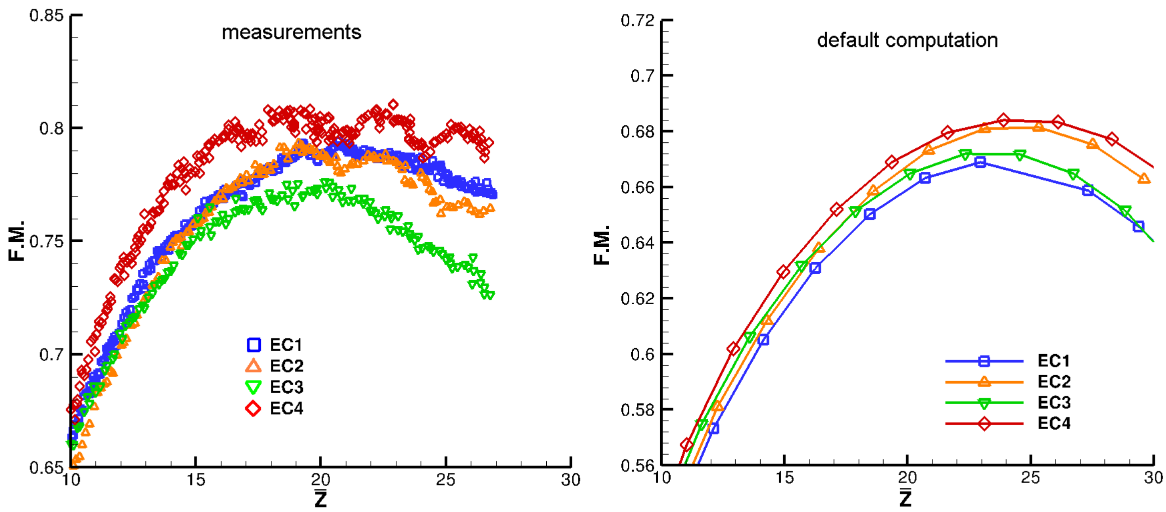

Figure 2.59: Experimental (left) and computed (right) blade hierarchy. Computations on VIS12 mesh with $k-\omega$ model, no transition modelling

In the following, tests are performed to try to improve prediction of blade hierarchy in hover by modifications to this default CFD computation.

Influence of transition modelling The position at which transition occurs is expected to influence friction drag and flow separation, thereby modifying rotor torque and dynamic stall characteristics, as described in [51, 67]. Flow solver *elsA* allows prescribing the chordwise position of the transition point on the airfoil. Precisely, an intermittency function γ is used to switch from laminar to turbulent flow, as given by:

$$\mu_{\text{eff}} = \mu_l + \gamma\mu_t \tag{2.68}$$

Up until the transition point, the intermittency function equals 0 so that the effective viscosity μ_{eff} is equal to the laminar viscosity. From the transition position onwards, γ becomes 1 and turbulent viscosity μ_t is also considered.

This model only works with eddy viscosity turbulence models and *elsA*'s current implementation is limited to meshes with a C-topology. Various transition models available in *elsA* were tested in [51]. In the present study, the influence of the transition point on blade performance hierarchy is evaluated by prescribing an intermittency function. On the suction side, γ is 0 up until the position of highest $z_{\max}$ which depends on airfoil shape and flow angle-of-attack. On the pressure side, a linear relation between collective pitch angle and transition position is given. These positions are illustrated in Figure 2.60.

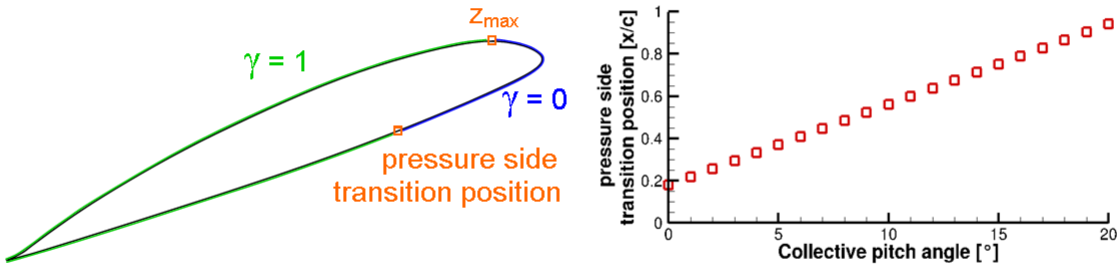

Figure 2.60: Transition position as imposed in computations

Figure 2.61 compares the previous fully turbulent computation with a computation with imposed transition. As seen, higher absolute values of F.M. are found when transition is modelled. This may be due to lower friction drag over the laminar part on the leading edge when imposing the transition point. Unfortunately, since transition can be imposed only when C-type meshes are used, and since in the following we use Autogrid meshes with a O4H topology, transition modelling is abandoned in the following. Nevertheless, even if absolute performance values are closer to measurements when modelling laminar-turbulent transition, relative blade hierarchy is not altered.

Influence of mesh size As VIS12 appeared to generate fine meshes of poor quality for tapered blades with sweep, Numeca's software Autogrid was acquired. Autogrid generates a 5-block O4H grid around the blade, referred to as the blade mesh, composed of an O-shaped blade mesh around the airfoil and H-meshes on top, bottom and leading and trailing edge sides of this O-mesh. Precisely, three blade meshes of increasing density are created, referred to as coarse, medium and refined meshes. Table 2.4 provides the number of grid points in each direction for the three meshes, and Figure 2.62 illustrates these variables. Blade meshes are inserted in a cylindrical background mesh via chimera interpolations [76]. Three increasingly fine background meshes are created, of which mesh sizes are given in Table 2.4 and corresponding grid variables are seen in Figure 2.63.

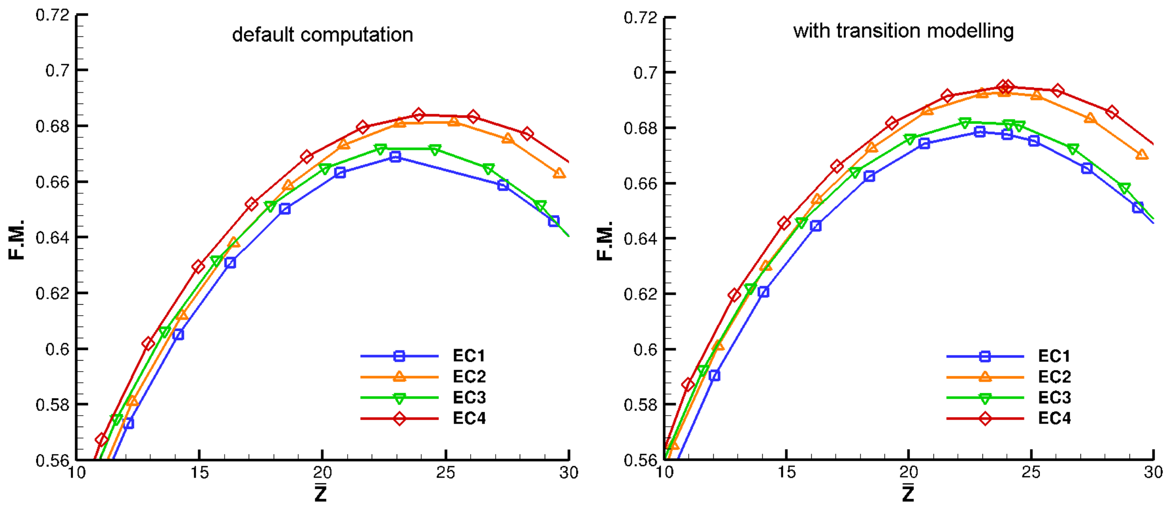

Figure 2.61: Blade hierarchy of fully turbulent computations (left) and computations with transition modelling (right), coarse VIS12 mesh, $k-\omega$ turbulence model, no transition modelling

Table 2.4: Mesh sizes of blade and background meshes for ORPHEE hover simulations

	Blade mesh			Background mesh			
	coarse	medium	refined	coarse	medium	refined	
O-mesh	176	176	288	77	99	115	rotation
spanwise - blade	31	43	51				
spanwise - root	5	5	5	104	116	152	spanwise
spanwise - tip	9	17	21				
perpendicular	42	46	50	91	109	135	height
total	464 652	766 377	1 553 001	728 728	1 251 756	2 359 800	total

For all computations, 8000 iterations of the steady flow solver were carried out on 12 cores. These were not sufficient to achieve complete convergence of the F.M. parameter, especially for fine grids and high blade pitch angles, corresponding to higher values of $\bar{Z}$ and stronger wake structures, since the present steady RANS model is not able to capture unsteady physical phenomena like vortex shedding. Nevertheless, F.M. fluctuations were only on the order of about 2% of the absolute value and, most importantly, they had no influence on the hierarchy between different blades. For this reason, and in order to reduce computational costs in view of subsequent (costly) optimization runs, we retained 8000 iterations as a sufficient stop criterion to achieve valuable information on the quantity of interest (F.M.).

Blade hierarchy of computations on the three meshes are compared to experiments in Figure 2.64. The effect of incomplete convergence on fine grids at high pitch angles is clearly seen as blade hierarchy is less well predicted on the refined mesh than by coarse mesh computations.

Figure 2.65 shows the effect of mesh refinement for each of the blades separately. Clearly, mesh convergence is not completely achieved. The influence of mesh refinement is smaller for the EC2 blade than for others.

Influence of turbulence modelling A final test is performed to evaluate the effect of turbulence modelling on hover CFD simulations. Computational results using the SSG turbulence model on refined grids are presented in Figure 2.66. It appears that F.M. computation by *elsA* in this configuration leads to completely incorrect orders of magnitude of global rotor

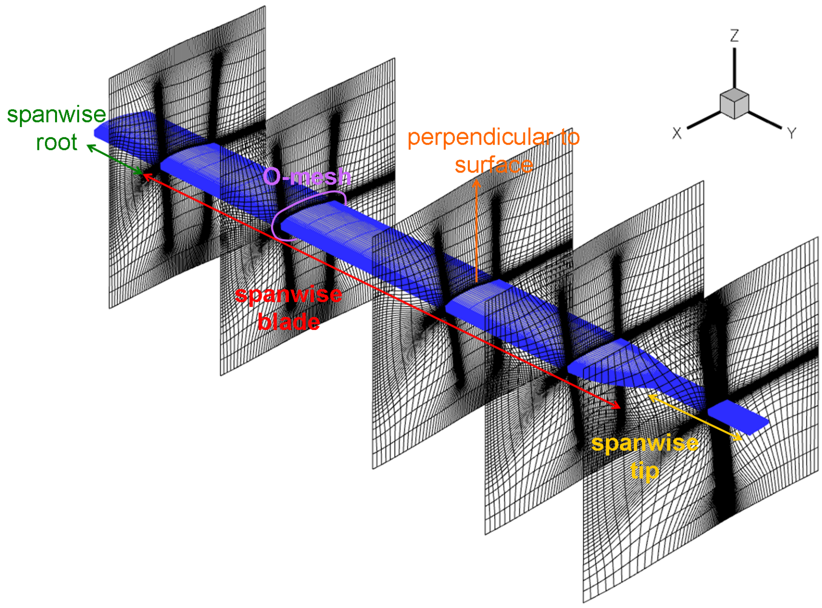

Figure 2.62: Mesh size indications for hover blade meshes, shown on blade surface grid and slices of coarse EC1 blade mesh

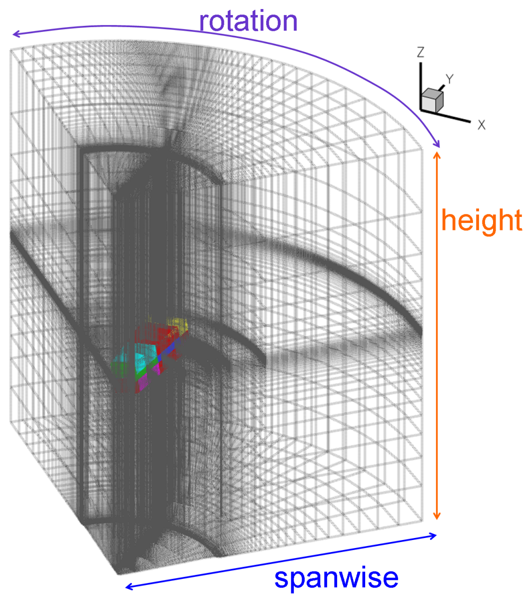

Figure 2.63: Mesh size indications for hover background meshes, shown on a coarse mesh

performance. In addition, blade hierarchy is inversed, with EC4 computed to have worst performance. As the SSG model worked correctly for earlier computations, it seems that its implementation is not adapted for rotor hover computations in the present version of *elsA*.

Forward flight simulations

Whereas for HOST evaluation simulations were performed at 4 forward flight speeds and using 2 wind tunnel laws, forward flight CFD simulations are done only for the 4 speeds of the American law as this law is more representative of a typical industrial design point. Rotor lift $\bar{Z}$ and simulated fuselage drag corresponding to these flight conditions are inserted

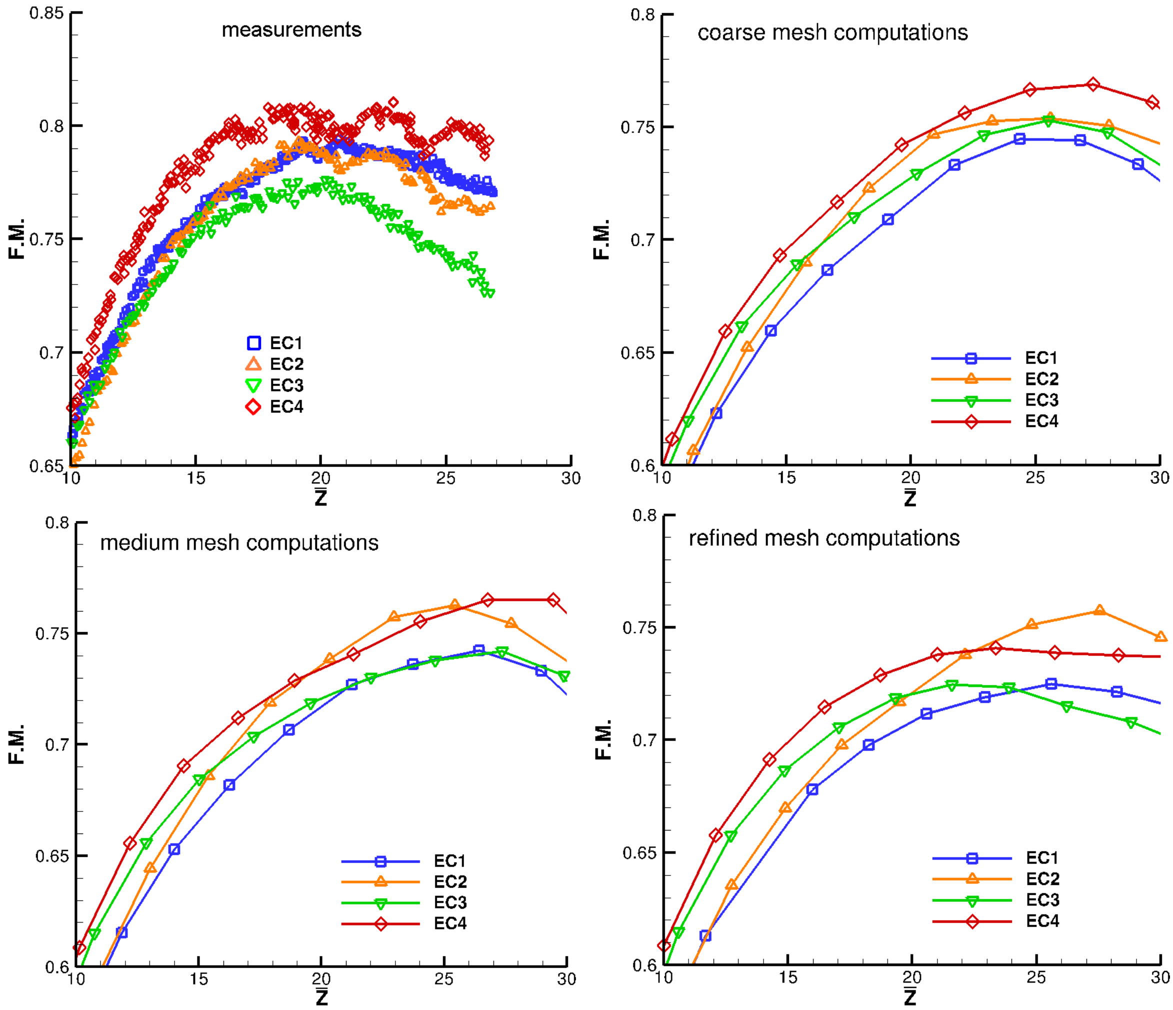

Figure 2.64: Comparison of blade hierarchy of ORPHEE blades as experimentally obtained to CFD computations on three Autogrid meshes

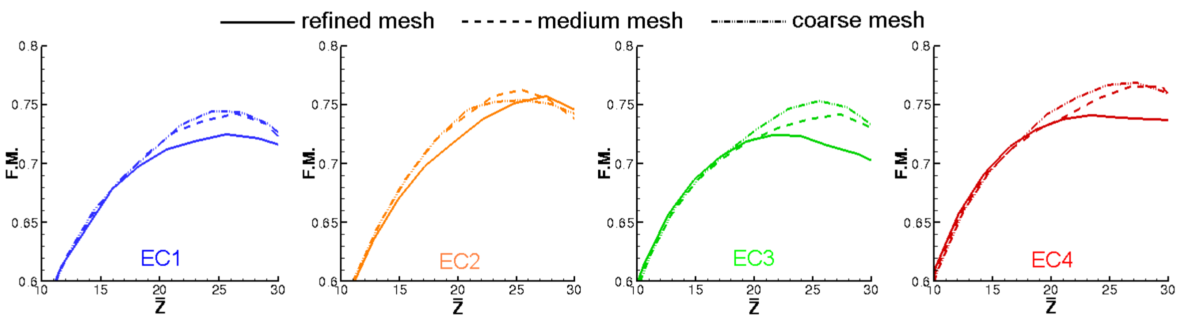

Figure 2.65: Effect of mesh refinement on hover performance per blade

in CFD simulations via rotor harmonics calculated by a preliminary HOST computation. Blade pitching, flapping and lead-lag motions are performed by blade mesh motions within the background mesh. Consistency of the expected CFD-simulated rotor lift is checked a posteriori. URANS computations are performed using Gear's second order time discretization with 40 sub-iterations at each physical time step. This is enough to achieve a reduction of 2 orders of magnitude of the residual in inner sub-iterations.

Initialization of the lowest forward flight speed ($V_H = 230$ km/h) is done by imposing this

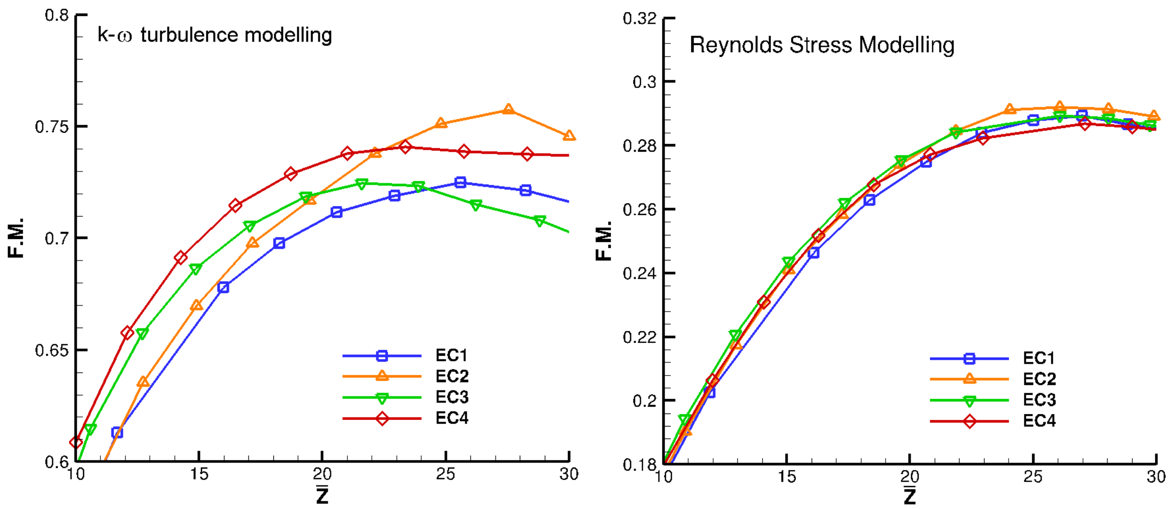

Figure 2.66: Blade hierarchy as computed on refined grid with $k-\omega$ (left) and SSG$-\omega$ (right) turbulence models

speed in all mesh nodes. For higher forward flight speeds ($V_H \geq 280$ km/h), this initialization leads to numerical divergence. Therefore, these computations are initialized on the flow field obtained from the $\Delta\psi = 10°$ solution of a lower flight speed.

Initially, as was done for HOST simulations, CFD computations were meant to compute L/D-ratio for comparison to wind tunnel measurements. Despite multiple tests, it was not possible to extract drag forces over rotating meshes using the present version of the *elsA* code. Thus, another measure for rotor performance was selected. A commonly used parameter for assessing rotor performance is the rotor torque coefficient $\bar{C}$ defined as:

$$\bar{C} = \frac{100Q}{\frac{1}{2}\rho b\bar{c}R^2V_{\text{tip}}^2} \tag{2.69}$$

where Q is the rotor torque [Nm]. $\bar{C}$ is thus a measure for the power required to rotate the blades in the air. In the following, wind tunnel measurements and simulations are compared via the ratio $\bar{Z}/\bar{C}$. This ratio is similar to the L/D ratio, as shown hereafter.

During the ORPHEE wind tunnel measurements $\bar{C}$ was measured as well, $\bar{Z}/\bar{C}$ results are presented in Figure 2.67.

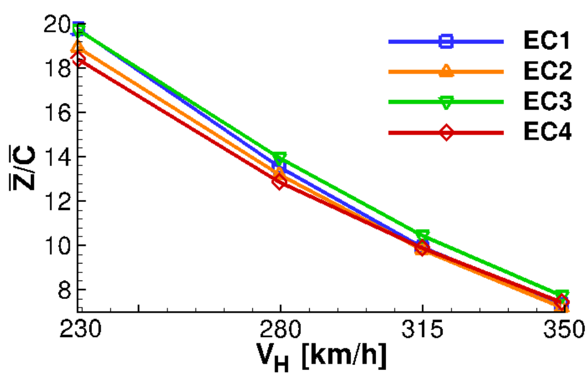

Figure 2.67: Wind tunnel measurements of $\bar{Z}/\bar{C}$ of ORPHEE blades

Absolute values being more apart for different forward flight speeds, the left part of Figure 2.68 shows $\bar{Z}/\bar{C}$ values normalized by reference blade EC1. A similar normalization of L/D

ratios is shown on the right side, showing comparable blade hierarchy for both performance parameters. There is a difference between EC1 and EC4 at high speed, as EC4 outperforms EC1 at 315 and 350 km/h for the $\bar{Z}/\bar{C}$ variable, but not for L/D. Also at $V_H = 315$ km/h a small difference can be perceived between EC2 and EC4: EC4 has slightly less good forward flight performance compared to EC2 when using L/D as a measure, whereas it has better performance when using the $\bar{Z}/\bar{C}$ expression. Keeping these slight alterations in mind, switching from L/D to $\bar{Z}/\bar{C}$ is acceptable as another measure of forward flight performance.

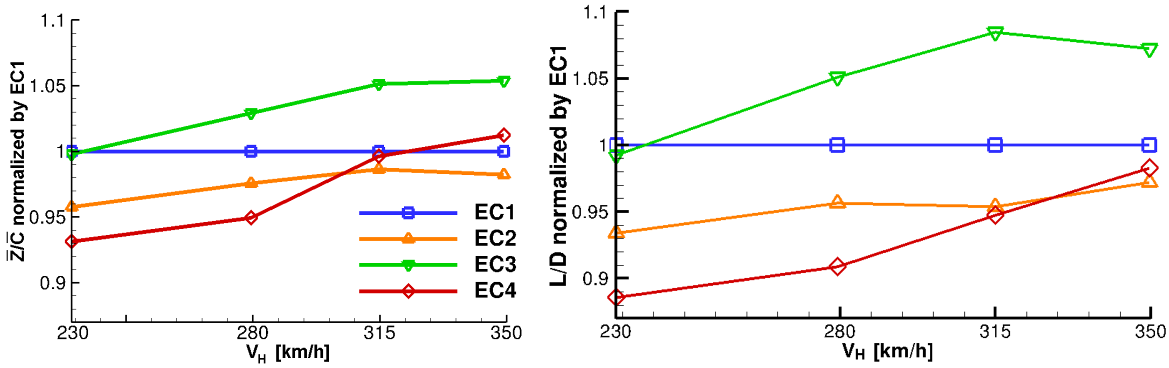

Figure 2.68: Wind tunnel measurements of $\bar{Z}/\bar{C}$ and L/D ratio normalized by reference EC1 blade

Influence of mesh size Mesh influence on forward flight simulation results is checked by carrying out computations on the set of blade meshes of increasing density used previously for hover simulations. A new background grid was created, shown in Figure 2.69, composed of 8 276 190 nodes, of which 155 in height direction, 195 in radial direction and 260 in rotational direction. The background grid was the same for all of the subsequent computations as refinement of the background grid leads to additional mesh cells throughout the domain, and computational cost becomes prohibitive.

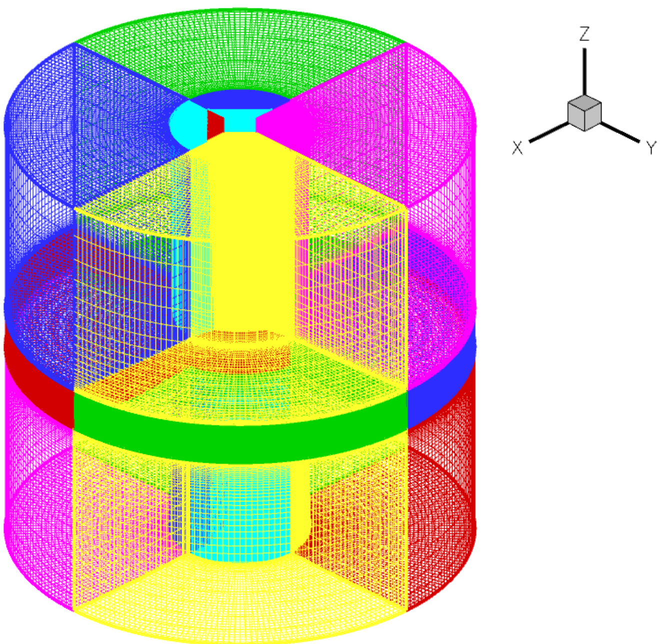

Figure 2.69: Background mesh used for forward flight simulations

Unsteady forward flight computations are stopped when a periodic variation of global parameters, such as $\bar{Z}$, is achieved. Figure 2.70 shows for a typical calculation a 4/revolution periodicity matching the blade passing frequency of a four-bladed rotor. The convergence series of 3 rotor rotations at $\Delta\psi = 10°$, 2 rotor rotations at $\Delta\psi = 5°$, and 1 rotor rotation at $\Delta\psi = 1°$ is shown here for coarse mesh simulations of the EC1 blade, but conclusions hold for other blade geometries and mesh sizes.

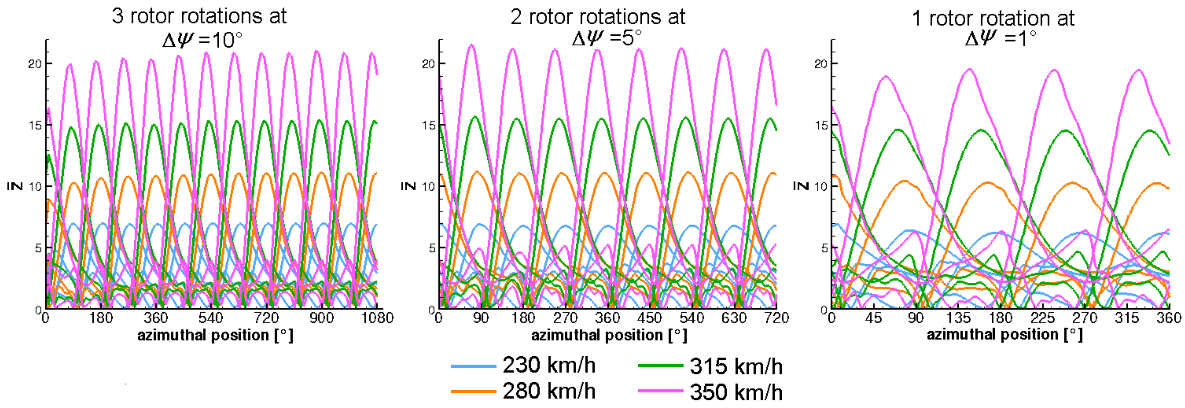

Figure 2.70: Computational convergence of $\bar{Z}$ on coarse EC1 mesh for four forward flight speeds

Simulation results expressed in global rotor performance by $\bar{Z}/\bar{C}$ are presented in Figure 2.71 for the three meshes and wind tunnel measurements. Correct prediction of blade hierarchy is found for low forward flight speeds of 230 and 280 km/h and for EC1, EC2 and EC3 blades. Performance of EC4 is overestimated on all three meshes. At high forward flight speed, from $V_H = 315$ km/h on, numerical solutions differ significantly from experiments and even blade hierarchy predictions are no longer correct. Reasons for this discrepancy will be examined next. No significant difference in global performance prediction is found for the three blade mesh sizes. The 350 km/h computation of EC4 on the medium grid did not converge, explaining this missing point.

Mesh density influence may also be assessed by comparing variations of $\bar{Z}/\bar{C}$ over a rotor rotation for the three meshes. This is shown for EC1 at $V_H = 230$ and 280 km/h in Figure 2.72. It illustrates that only small differences are observed by mesh refinement, so that blade mesh density does not affect computational results when considering global coefficients.

High speed forward flight results discrepancy Whereas blade hierarchy prediction at low forward flight speeds of 230 and 280 km/h is correct of EC1, EC2 and EC3 blades and on all blade meshes, this does not hold for higher speeds. A possible cause of this discrepancy is now investigated.

In forward flight, a rotor trim of blade pitching, flapping and lead-lag motions is required for force and moment equilibrium, as was explained in Section 1.1.2. In CFD computations, this trim is imposed by blade motions given by rotor harmonics as obtained from a HOST simulation. For HOST and CFD simulations, the same flight conditions are to be used. Yet, similar rotor harmonics and flight conditions might lead to different rotor forces (lift, drag) as computation principles differ. Therefore, we check a posteriori that the lift predicted by CFD is consistent with the expected value, used as an input for the HOST computation.

For all HOST simulations, a rotor lift of $\bar{Z} = 15$ was imposed. Average values and azimuthal variations of $\bar{Z}$ of all 4 forward flight speeds as computed on the coarse mesh of the EC1 blade are presented in Figure 2.73. It illustrates that at low forward flight speeds of 230 and 280 km/h, an average $\bar{Z}$ close to 15 is obtained. At $V_H = 315$ km/h, however, a strange variation of $\bar{Z}$ over a rotor revolution is found: this solution is no longer periodic. Yet, similar

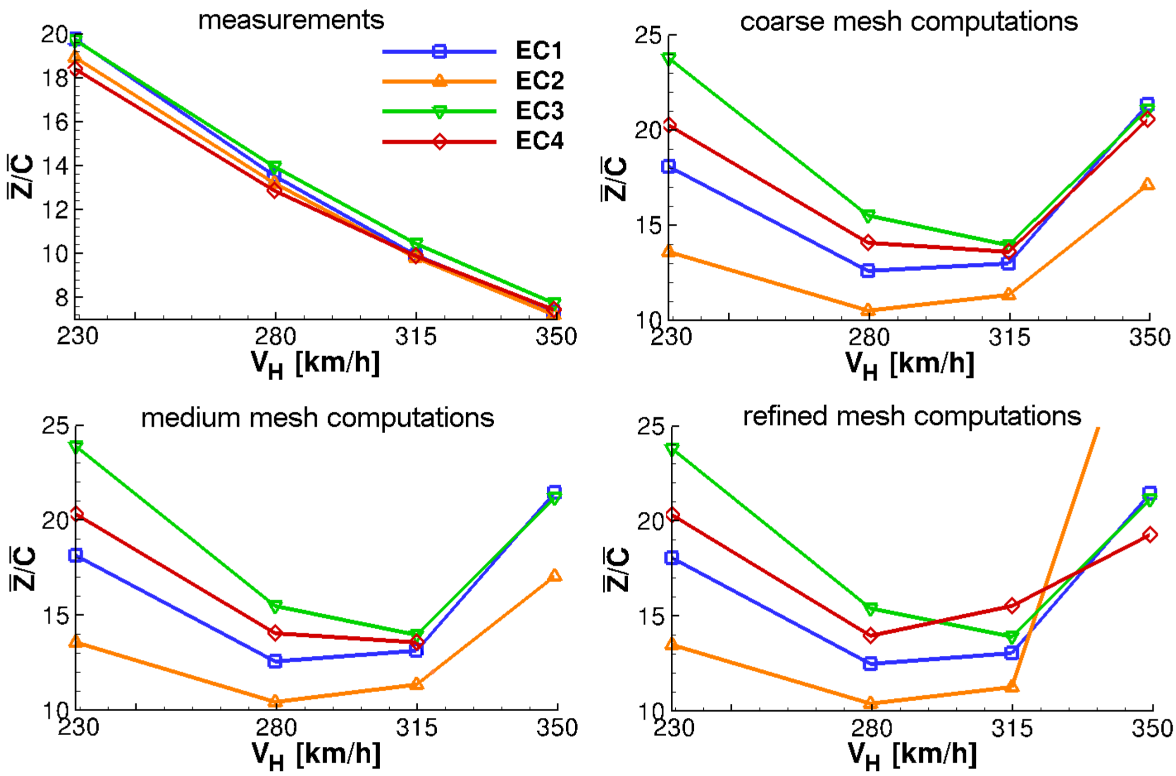

Figure 2.71: Wind tunnel measurements and CFD simulation results on all meshes of $\bar{Z}/\bar{C}$ of ORPHEE blades. Attention on different y-axis scales for measurements and computations

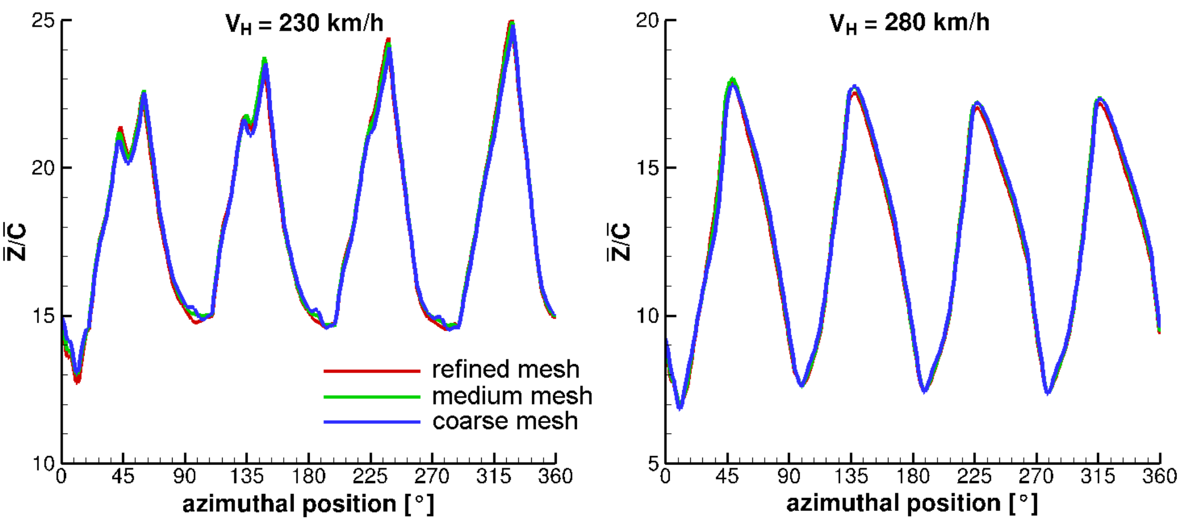

Figure 2.72: Variation along a rotor rotation of $\bar{Z}/\bar{C}$ of EC1 blade as computed on all three meshes at V_H = 230 (left) and 280 (right) km/h, $\Delta\psi = 1°$

behaviour is observed for all simulations at $\Delta\psi = 1°$ on all four blades and each of the mesh refinements. No explanation has been found up to now for this discrepancy. At the fastest point, lift periodicity over a rotor rotation is again found, but at a far too high $\bar{Z}$ compared to required flight conditions.

Table 2.5 displays average $\bar{Z}$ values of all forward flight computations. In general terms, no matter mesh refinement nor blade geometry, average $\bar{Z}$ is too high for V_H = 315 and 350 km/h. This means that aerodynamic conditions of measurements and simulations are

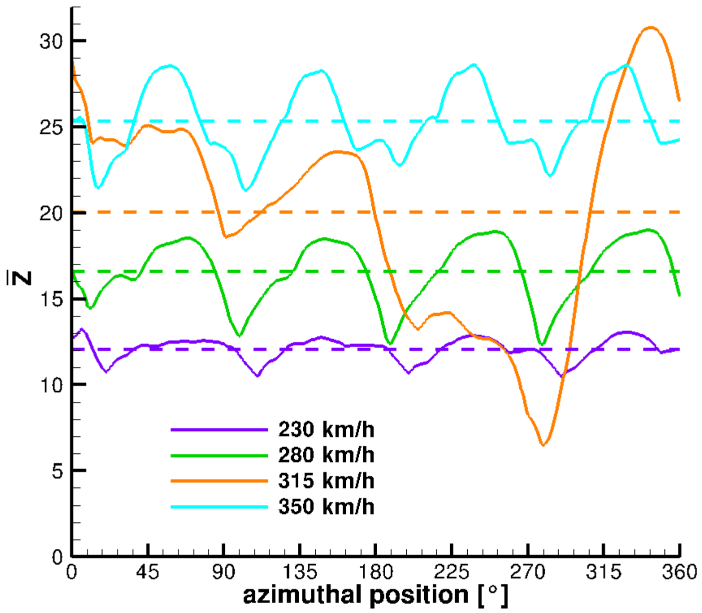

Figure 2.73: Variation along a rotor rotation (—) and average (- - -) value of $\bar{Z}$ of EC1 blade as computed on coarse mesh for 4 forward flight speeds

completely different.

Table 2.5: Average $\bar{Z}$ values as computed by *elsA*

	mesh	230 km/h	280 km/h	315 km/h	350 km/h
	coarse	12.07	16.61	20.06	25.33
EC1	medium	12.07	16.62	20.08	25.06
	refined	12.03	16.60	19.97	24.88
	coarse	12.75	17.56	21.24	27.33
EC2	medium	12.73	17.57	21.22	26.98
	refined	12.70	17.56	21.02	6.62
	coarse	11.60	15.34	18.29	23.70
EC3	medium	11.57	15.34	18.32	23.61
	refined	11.52	15.31	18.27	23.46
	coarse	11.31	15.34	18.76	24.12
EC4	medium	11.30	15.36	18.84	-
	refined	11.27	15.37	18.83	23.66

It appears that rotor harmonics predicted by HOST result in completely different local flow conditions in a CFD simulation at high speed forward flight. Therefore, it must be concluded that simple injection of HOST rotor harmonics into a CFD simulation is only possible for lower forward flight speeds, up until 280 km/h, corresponding to $\mu \leq 0.37$. At higher forward flight speeds, iterative coupling between CFD results and HOST rotor harmonics prediction is required to perform the CFD simulation at correct flight conditions.

Effect of mesh refinement on local flow characteristics The influence of mesh refinement on local flow is now further examined for low forward flight speed conditions. Precisely, we investigate the numerical representation of the vortex wake by means of the Q-criterion, which is computed as a function of symmetric ($\mathbf{S}_{ij}$) and asymmetric ($\mathbf{\Omega}_{ij}$) components of velocity gradient tensor $\nabla \mathbf{u}$ [49]:

$$Q_{ij} = \frac{1}{2}\left(||\mathbf{\Omega}_{ij}||^2 - ||\mathbf{S}_{ij}||^2\right) \tag{2.70}$$

where $||\mathbf{S}_{ij}|| = [\mathrm{tr}\mathbf{S}\mathbf{S}^{\mathbf{T}}]$ and $||\mathbf{\Omega}_{ij}|| = [\mathrm{tr}\mathbf{\Omega}\mathbf{\Omega}^{\mathbf{T}}]$. The Q-criterion is positive when rotation $\mathbf{\Omega}_{ij}$ dominates strain and shear $\mathbf{S}_{ij}$, thereby representing pure rotational components of vortices.

Figures 2.74 and 2.75 show top and side views of instantaneous iso-surfaces of $Q_{\text{criterion}} = 10$ for simulations on the three meshes of the EC1 blade at $V_H = 280$ km/h. No visual differences between these images are observed, which could be explained by the fact that only blade meshes are refined, whereas the background mesh is the same. We expect to observe a longer wake if a finer background mesh is used.

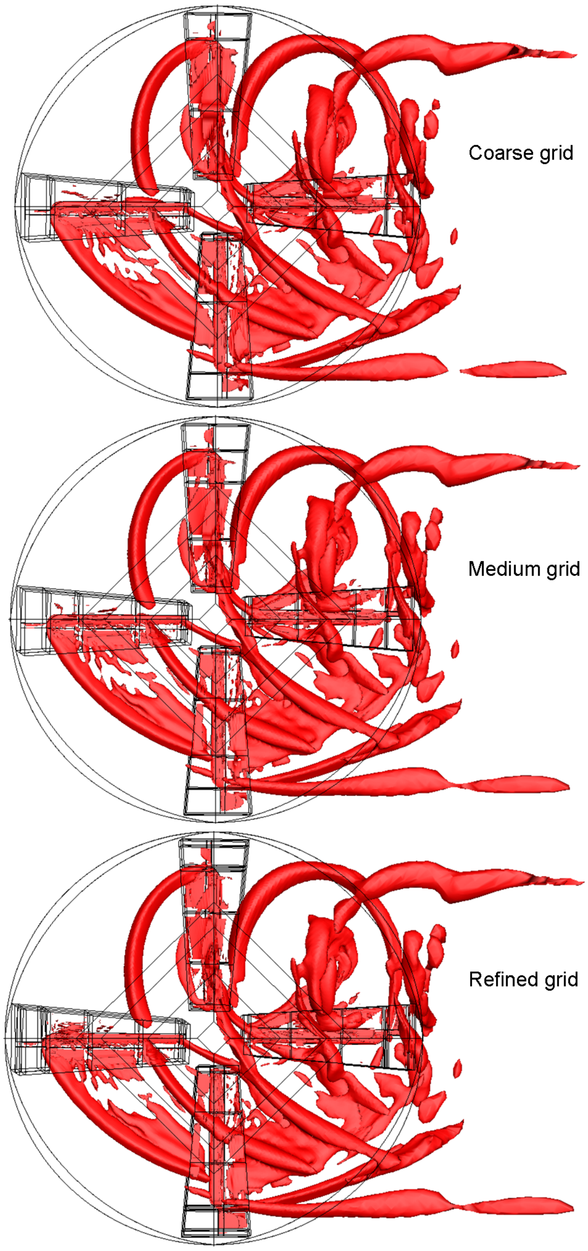

Figure 2.74: Top view of iso-surface of $Q_{\text{criterion}} = 10$ for EC1 blade at $V_H = 280$ km/h on coarse, medium and refined meshes

Figure 2.76 shows the pressure coefficient over a blade section at 0.85R of the advancing

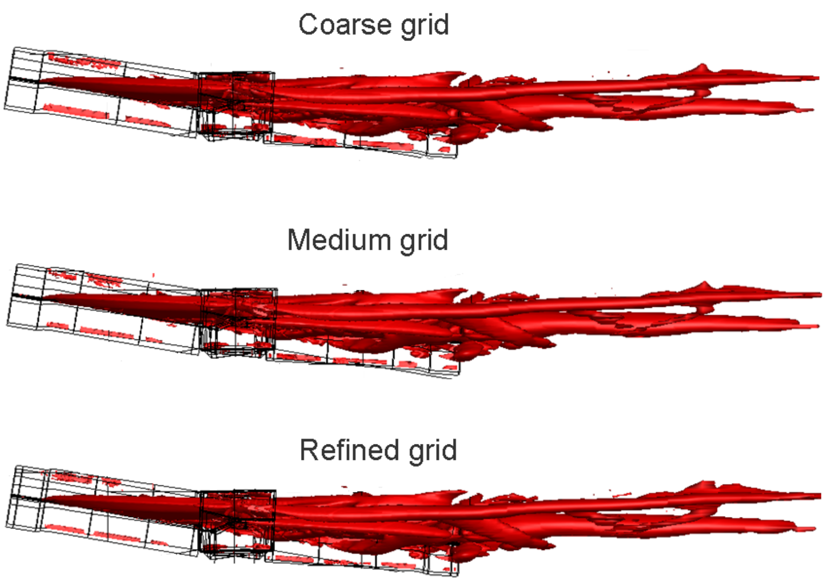

Figure 2.75: Side view of iso-surface of $Q_{\text{criterion}} = 10$ for EC1 blade at $V_H = 280$ km/h on coarse, medium and refined meshes

blade side ($\psi = 90°$), which is computed as:

$$C_p = \frac{p_{\text{static}} - p_\infty}{1/2 \rho V_\infty^2} \tag{2.71}$$

where the local reference speed is the sum of the local contribution of rotational velocity (0.85 V_{tip}) and the forward flight speed. This mesh comparison shows that also close to the blade no significant differences in lift generation are observed between the three meshes. At this position, the airfoil has a low angle-of-attack and generates almost no lift. The shock wave, near 0.1 $x/\bar{c}$, is positioned similarly for all three meshes. Apparently, not only the wake structure is the same no matter the here tested blade mesh refinement, also lift generation is unaltered.

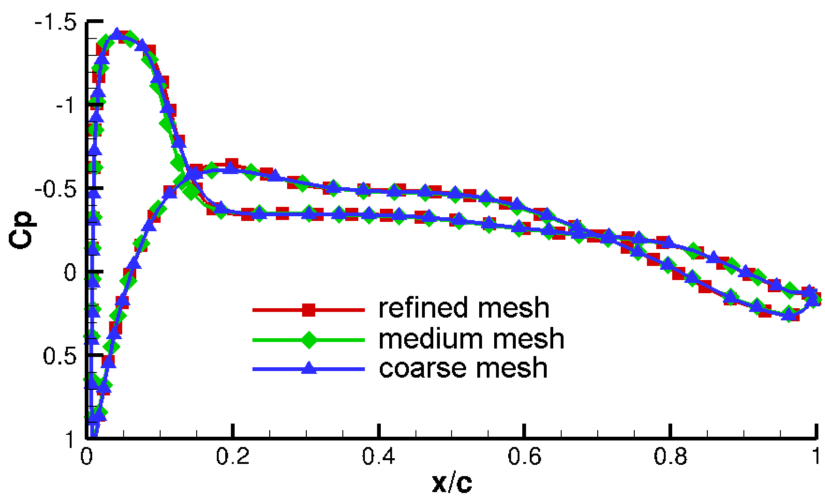

Figure 2.76: Pressure coefficient distribution over 0.85R blade section of advancing blade on coarse, medium and refined meshes of EC1 blade

Computational cost comparison To complete the mesh study, the relation between mesh refinement and computational cost is investigated. Mesh refinement evidently increases computational time. However, since the same background grid was used for all computations, and this background grid contains more grid nodes than blade meshes, influence of blade mesh refinement on total mesh size is small. In fact, the complete medium mesh has only 1.12 times more mesh nodes than the coarse mesh, and the refined mesh is increased with a factor 1.27 compared to the medium mesh. In addition, total computation time depends on the distribution of mesh blocks over processors. Mesh sizes, number of processors, time per iteration, total computation time and total CPU time are presented in Table 2.6.

Table 2.6: Computation time averages of all blades and all forward flight speeds per mesh size

	coarse mesh	medium mesh	refined mesh
Total mesh size	10 371 983	11 578 883	14 725 379
CPU	23	24	32
Time/iteration	3min 55s	4min 19s	4min 42s
Total time	$\sim$ 40h	$\sim$ 44h	$\sim$ 48 h
Total CPU time	$\sim$ 920h	$\sim$ 1055h	$\sim$ 1535 h

Conclusion on mesh study To conclude on the mesh influence study, a first remark is that blade hierarchy is correctly predicted for EC1, EC2 and EC3 on all meshes and at low forward flight speed (V_H = 230 and 280 km/h). Only small differences between the three blade meshes are observed, both in terms of global performance results as in variations over a rotor rotation, so that the coarse mesh will be retained for the following computations. Better results could be obtained by refining the background grid, but this would increase computational costs significantly. In view of optimization, we seek again for a compromise between simulation reliability and computational cost.

Analysis of local aerodynamics To assess blade hierarchy differences by analysis of local aerodynamic flow fields, a flight case is selected for this local comparison: computations performed on coarse meshes at a forward flight speed of 280 km/h. Pressure distribution and frictionlines and -magnitudes are extracted at three azimuthal positions of the blades, giving an overview of local flow properties on blades at different positions. Rotation and forward flight direction as well as advancing and retreating blade sides of images to follow are indicated in Figure 2.77.

Local comparison of pressure distribution $\bar{Z}$ values of the four blades at V_H =280 km/h on coarse mesh simulations were 16.61, 17.56, 15.34 and 15.34 for EC1 to EC4 blades, respectively. More lift is thus generated on EC1 and in particular EC2, compared to EC3 and EC4. This is expected to be seen from the pressure distribution. Pressure coefficients are computed by Equation 2.71 where V_∞ now refers to the blade tip speed due to rotation (211 m/s). Figure 2.78 shows pressure distributions of all four blades. Lift appears to be created mainly over the advancing and front parts of the rotor disk. The high positive pressure coefficient observed on the leading edges of advancing blades indicates that stagnation points are located on or close to the suction side rather than on the pressure side. This is due to the low angle-of-attack of advancing blades, which is related to rotor equilibrium. As expected, larger zones of low pressure coefficient are found for EC1 and EC2, which have higher $\bar{Z}$ values.

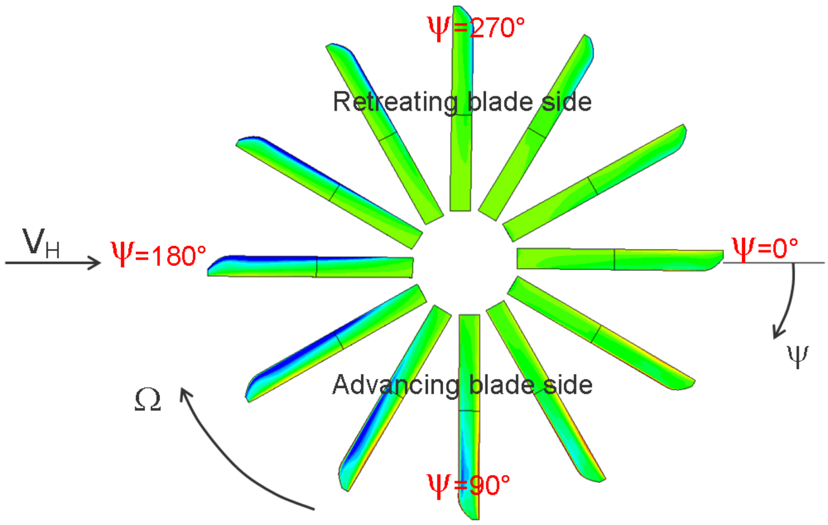

Figure 2.77: Rotation and forward flight direction for local flow field analysis

Local comparison of friction lines Friction lines are illustrated in Figure 2.79, where blade surfaces are coloured by the magnitude of wall friction τ_w, computed as:

$$\tau_w = \sqrt{{\tau_{w_x}}^2 + {\tau_{w_y}}^2 + {\tau_{w_z}}^2} \qquad (2.72)$$

Friction lines show on all rotors attached flow on the advancing blade side. On the retreating blade sides, a small zone of flow separation may be observed on blade tips at $\psi = 300°$ of EC1, EC2 and, on a smaller zone, of EC4.

On the retreating blade side, highly three-dimensional flow is observed, as seen in Figure 2.80, that shows friction lines on the four blades at $\psi = 270°$. Results are similar for all of the four blades. Attached flow is only found on the complete outboard side of the blades, from about 0.8R on. Somewhat more inboard, between approximately 0.6-0.65 and 0.8R, trailing edge stall is recognized from reversal of friction lines. Radial positions of these zones differ somewhat between blades, but this may have various causes: stalled flow is directly related to local angle-of-attack and thus to blade pitch angle, which differs from one blade to another via rotor harmonics. As said, different $\bar{Z}$ values are found on the four blades, meaning different rotor trims are used leading to different pitch angles as well.

From theory, see Equation 1.19, the diameter of the inversion circle should equal 0.37R, whereas reversed friction lines are seen on inboard blade sections up until approximately 0.6R. Reversed friction lines may not only be due to reversed flow, but also to stalled flow. This might be the case for some part of the inboard sections, but concluding on exact flow characteristics remains difficult due to large blade-wake interactions that will also appear in this zone, in addition to flow hysteresis of earlier azimuth positions and flow three-dimensionality.

In conclusion, interesting and unexpected local aerodynamic characteristics may be seen from these friction lines. Unfortunately, they do not allow for explaining performance differences, mainly because of different rotor loadings and trims that make comparisons of these relatively small local flow variations unfair.

2.2.7 Summary of rotor performance simulations using *elsA*

Comparison of wingtip vortex measurement data with CFD computations has given indications on the capability of the *elsA* code to capture fine physical phenomena as the turbulent structure of a wingtip vortex. Whereas local flow simulations of this fixed-wing test case are

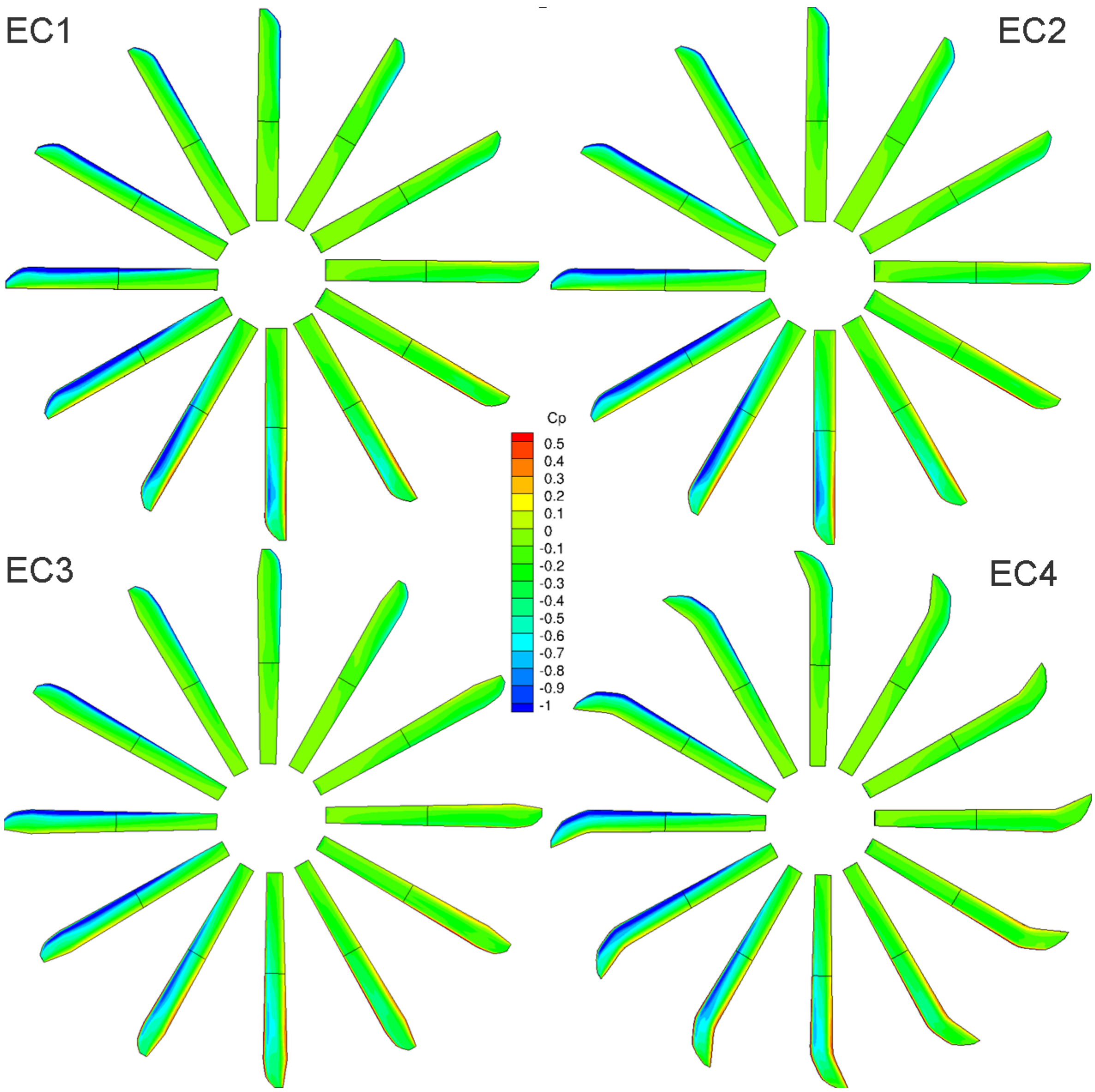

Figure 2.78: Pressure distribution of ORPHEE blades as simulated on coarse meshes at V_H=280 km/h

quite precise, global performance prediction of rotor blades is not as accurate. Physical phenomena appearing over helicopter rotors seem difficult to capture and wake dissipation already observed in the fixed wing test case is expected to highly influence rotor performance results. In addition, implementation of the non-Boussinesq turbulence model within *elsA* turned out to be inadequate for rotor applications.

The wingtip vortex study demonstrated that mesh refinement is required for capturing typical vortex characteristics such as acceleration in the vortex core. Yet, the mesh study performed for rotor blade simulations has shown that both in hover and in forward flight a satisfactory representation of global rotor performance parameters and, most of all, of blade hierarchy, can be achieved already on relatively coarse grids. Fine meshes are required for capturing fine physical phenomena like wingtip vortices, but the preceding numerical experiments show that for predicting global rotor performance coarser meshes are sufficient.

Concerning the numerical scheme, rotor simulations are recommended to be performed with AUSMp and Van Albada limiter. Higher order schemes are an interesting means for reducing numerical dissipation and should be considered in the future.

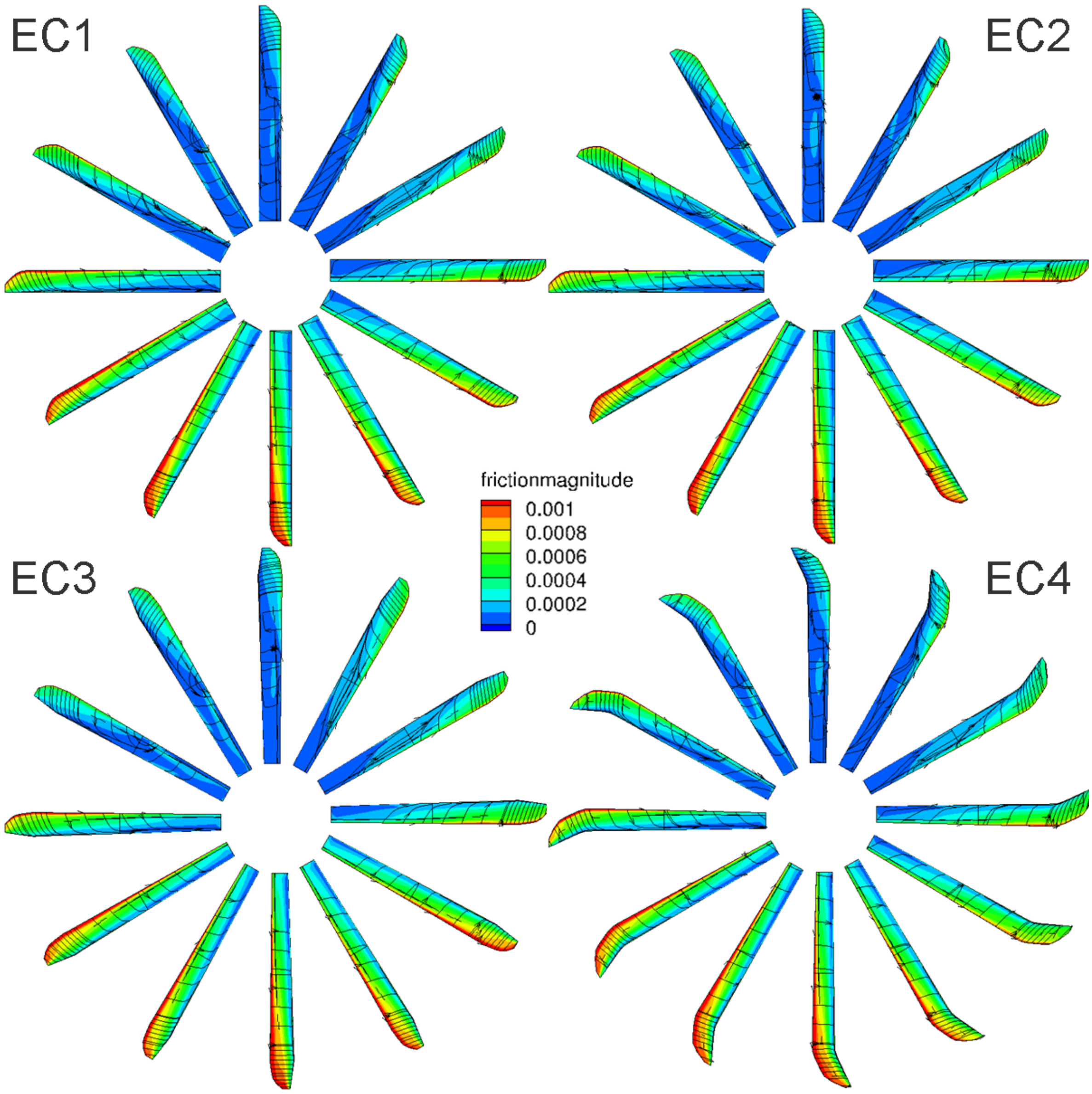

Figure 2.79: Frictionlines and frictionmagnitude of ORPHEE blades as simulated on coarse meshes at V_H=280 km/h

Another conclusion for optimization purposes via forward flight CFD-simulations is that at high speed coupling with a flight mechanics code is required for finding the correct rotor equilibrium. At low forward flight speed ($V_H \leq 280$ km/h, or $\mu \leq 0.37$), rotor equilibrium conditions imposed into the HOST simulation for obtaining rotor harmonics were reasonably recovered in the CFD simulation results. However, at higher forward flight speeds, different rotor flight conditions were retrieved by *elsA* so that aerodynamic flow fields are unlike. For rotor blade optimization in forward flight with *elsA* either low forward flight speeds need to be chosen as a design point or coupling with HOST is required for finding the correct rotor trim. This weak-coupling between HOST and *elsA* is described in [27] and improves rotor trim but requires three additional CFD simulations for convergence. As forward flight CFD simulations are already time-consuming on their own, this is today too demanding in an optimization loop. In addition, typical design points are often below a μ of approximately 0.35, for which the rotor trim was found correctly. Therefore, today, it is recommended to perform rotor blade optimizations at forward flight velocities of $\mu \leq 0.37$.

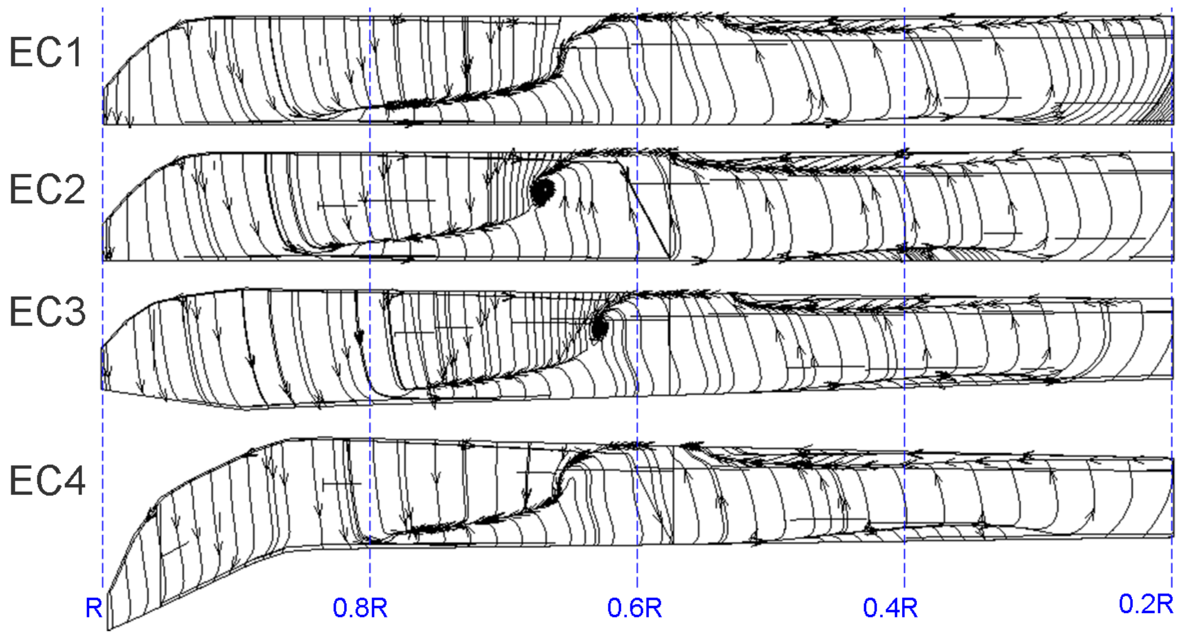

Figure 2.80: Frictionlines on retreating blades ($\psi = 270°$) as simulated on coarse meshes at V_H=280 km/h

2.3 Conclusions on rotor performance simulations

The simulation tools available at Eurocopter for rotor performance evaluation are HOST and *elsA*. Various studies have been performed to assess the ability of both tools to accurately predict rotor performance at a low computational cost. Experimental data of the four ORPHEE blades, with varying geometries, has allowed for the assessment of blade hierarchy prediction of both simulation methods. Even if measurements set similar hover performance for EC1 and EC2 blades, theory and all performed computations designate EC2 to provide higher F.M. compared to EC1. In the following, this more logical hierarchy is considered true.

HOST was seen to provide accurate relative prediction of hover performance of EC2, EC3 and EC4, but EC1 performance was underestimated compared to EC2 and EC3. In forward flight, EC1, EC2 and EC3 blade hierarchy was correctly predicted for moderate rotor loading and diverse forward flight speeds. In this flight case, EC4 performance is systematically overestimated. Elastic blade modelling did not improve this representation in either flight case, but induced velocity model choice highly influenced rotor performance results. Comparison to measured induced velocity data showed that FiSUW best models the induced velocity field. In addition, this model also provides good results in the ORPHEE study and is therefore recommended in all HOST simulations for rotor performance estimation.

In short, HOST provides correct relative prediction of chord and sweep laws in hover, and of twist and chord laws in forward flight. Effect of twist is not correctly estimated in hover, which may be due to the 2D hypothesis which does not hold on outer blade parts. The sweep variation is not correctly foreseen in forward flight, which is likely to be related to blade elasticity.

CFD simulations become far more difficult when switching from a fixed-wing case to a helicopter rotor. This difference in fixed and rotary wing prediction accuracy is reflected by NASA's 2013 Fundamental Aeronautics Program in which research projects are launched to achieve a 35% improvement of rotor performance prediction [164].

Today, CFD allows for correctly predicting hover performance hierarchy of EC2, EC3 and EC4, just as was the case for HOST simulations. Despite tests on transition and turbulence modelling and mesh refinement, no improvement of EC1 performance prediction was obtained.

In forward flight, only low-speed cases ($\mu \leq 0.37$) can be executed without iterating between HOST-obtained rotor harmonics and the CFD flow field. These low-speed flight cases compute EC1, EC2 and EC3 performance in agreement with measurements. Again, EC4 performance is overestimated.

Concerning CFD simulations in an optimization loop, it is recommended to use relatively coarse meshes, the $k - \omega$ turbulence model, no transition modelling and the AUSMp numerical scheme. These parameters are considered leading to best results obtained with today's version of *elsA* while accounting for computational cost. Future implementation of in particular higher-order numerical schemes and adaptive mesh refinement is expected to limit wake dissipation and thereby improve CFD simulations of helicopter rotors.

In conclusion, both simulation methods today allow for predicting chord and sweep laws in hover, and twist and chord laws in forward flight. As the simulation tools are based on different computational principles, different aerodynamic aspects are taken into account by each tool. In particular, 3D effects are naturally considered only by CFD. Today, the two tools are complimentary and prediction of improved rotor performance by both tools increases simulation confidence. In addition, whereas improvements of HOST's predictivity are expected to be restricted due to inherent model limitations, predictivity of CFD simulations is expected to improve in coming years. The use of CFD in the optimization loop is thus justified as an outlook to the future.

Chapter 3

Optimization strategies

A multi-objective minimization problem may be defined as [89]:

$$\min \mathbf{F}(\mathbf{x}) = \min \left[F_1(\mathbf{x}), \ldots, F_p(\mathbf{x})\right]^T \tag{3.1}$$

subject to:

$$\begin{cases} g_j(\mathbf{x}) \leq 0 & \text{for } j = 1, \ldots, m \\ h_i(\mathbf{x}) = 0 & \text{for } i = 1, \ldots, e \end{cases}$$

where:

$\mathbf{F}(\mathbf{x}) \in \mathbb{R}^p$	vector of objective functions in objective space $\mathbb{R}^p$
$\mathbf{x} \in \mathbb{R}^n$	vector of design variables with n independent variables in parameter space $\mathbb{R}^n$
g_j	inequality constraints
h_i	equality constraints
p	number of objective functions
m	number of inequality constraints
e	number of equality constraints

The optimization goal is to find the best sets of parameters $\mathbf{x}$ within the feasible design space $\mathbf{X}$ leading to the minimum of $\mathbf{F}$. The feasible design space may be defined as all combinations of parameters for which constraints are not violated, so that:

$$\left\{\mathbf{x} \,\middle|\, g_j(\mathbf{x}) \leq 0,\ j = 1, \ldots, m \quad \text{and} \quad h_i(\mathbf{x}) = 0,\ i = 1, \ldots, e\right\} \tag{3.2}$$

In multi-objective design problems, there is no definition for a single optimal solution. As for practical optimization problems a single optimal design has to be chosen, this selection may be performed either a priori or posterior to the optimization. In the first case, the different objectives are assigned a weight and combined into a function, for example a weighted average of the different objectives. In the second case, the optimization method searches for so-called Pareto Optimal solutions that will be defined next. The user may then express his preferences for objectives posterior to the optimization run.

Pareto Optimal Front A feasible solution $\mathbf{x}^* \in \mathbb{R}^n$ is called a Pareto Optimal solution [159]:

$$\text{iff} \nexists \mathbf{y} \in \mathbb{R}^n \quad \text{such that} \quad \mathbf{F}(\mathbf{y}) \prec \mathbf{F}(\mathbf{x}^*) \tag{3.3}$$

where the notation $\mathbf{F}(\mathbf{y}) \prec \mathbf{F}(\mathbf{x}^*)$ means that $\mathbf{F}(\mathbf{y})$ is dominated by $\mathbf{F}(\mathbf{x}^*)$ [160]. In words, a point is Pareto Optimal if no other point exist that improves at least one objective function without detriment to another [89]. Pareto Optimal points are said to dominate other points in the design space. The Pareto Optimal Set (POS) containing all Pareto Optimal solutions is defined as:

$$\text{POS} = \left\{ \mathbf{x} \in \mathbb{R}^n | \nexists \mathbf{y} \in \mathbb{R}^n, \mathbf{F}(\mathbf{y}) \prec \mathbf{F}(\mathbf{x}) \right\} \tag{3.4}$$

The Pareto Optimal Front (POF) is then the image of the Pareto Optimal Set in objective space $\mathbb{R}^p$:

$$\overline{P} = \text{POF} = \left\{ \mathbf{F}(\mathbf{x}) | \mathbf{x} \in \text{POS} \right\} \tag{3.5}$$

Even if Pareto Optimality is clearly defined, the assessment of numerical representation of Pareto Optimal Fronts is not straightforward as various measures on performance quality may be given [44, 85, 101, 103, 152, 161, 162]. The most important ones may be summarized as follows:

- Convergence: it measures the distance between the true Pareto Optimal Front, denoted $\overline{P}$, and so far best optimization solutions X'. This metric may be expressed as follows in the objective space:

  $$\mathbf{M}_1(X') := \frac{1}{|X'|} \sum_{a' \in X'} \min \left\{ ||a' - \overline{a}||; \overline{a} \in \overline{P} \right\} \tag{3.6}$$

  This metric can only be used if the true POF is known. Its value tends towards zero when the optimization algorithm reaches convergence.

- Distribution: a uniform distribution of points along the Pareto Optimal Front is preferred. This is often quantified by a distance metric:

  $$\mathbf{M}_2(X') := \frac{1}{|X' - 1|} \sum_{a' \in X'} \left| \left\{ b' \in X'; ||a' - b'|| > \sigma \right\} \right| \tag{3.7}$$

  For larger values of $\mathbf{M}_2$, less points are found within a distance σ, so that points are better distributed along the front. The metric depends on the value of σ prescribed by the user.

- Spread: maximize the extent of the Pareto Optimal Front to include a wide range of solutions, as described by:

  $$\mathbf{M}_3(X') := \sqrt{\sum_{i=1}^{m} \max \left\{ ||a'_i - b'_i||; a', b' \in X' \right\}} \tag{3.8}$$

  Where m is the number of individuals in the Pareto Optimal Front. The larger $\mathbf{M}_3$, the greater the distance between outer points of the front, meaning larger spread.

A graphical representation of the geometrical meaning of preceding measures is given in Figure 3.1.

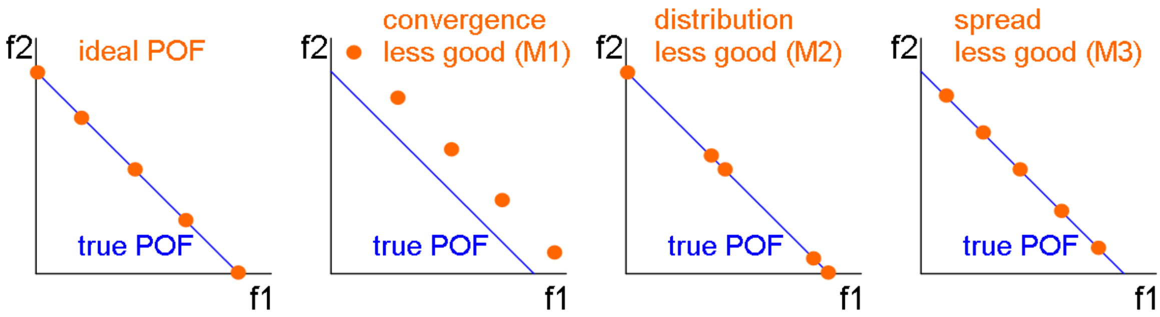

Figure 3.1: Metrics for performance assessment of Pareto Optimal Fronts on convergence, distribution and spread

The present chapter contains four sections: first, requirements specific to an optimization strategy for the current design problem are given. Some requirements are related to the complexity of rotor blade optimization, while other are closely linked to industrial implementation. To develop an optimization loop that is useful for Eurocopter's specific needs, a good balance between optimization result quality and industrial requirements on time and cost is to be found.

From discussion of these requirements, an optimization method is selected in Section 3.2.

Recent advances in development of optimization strategies may allow for reduction of optimization time and computational cost, which are both of importance for industrial application. These techniques are discussed in Section 3.3.

Finally, Section 3.4 summarizes the optimization strategy that is assessed in the next Chapter.

3.1 Requirements on an optimization strategy for aerodynamic design of helicopter rotor blades

To develop an optimization strategy specific for the aerodynamic optimization of helicopter rotor blades, requirements on this type of optimizations are defined first, followed by some priorities. These criteria are specific to Eurocopter's industrial needs and may differ from choices found in literature.

An optimization strategy for aerodynamic, industrial design of helicopter rotor blades should be able to tackle optimization problems with the following characteristics:

Multiple design parameters A blade geometry definition is generated from parametric laws (see a description of this tool in Section 4.1). The number of parameters per geometry law (chord, twist, sweep, etc) typically ranges between 2 and 10. Depending on selected parameterization, a blade optimization simultaneously considers 5 to 30 parameters.

Multiple objectives Current optimizations will typically incorporate at least two objectives on aerodynamic performance in hover and forward flight conditions. A compromise design needs to be found for creating a blade that is industrially feasible. In the future, additional objectives on other rotor blade design characteristics may be included, such as acoustics, vibrations, loads and production goals.

Complex constraints Inequality constraints need to be incorporated in the optimization to control other-than-aerodynamic performance criteria such as blade mass, loads and production feasibility. In most cases, inequality constraints are considered. No equality constraints are incorporated for the moment.

Multi-physics simulations Optimization loops include simulation tools for hover and forward flight performance evaluation. To incorporate objectives on acoustics, vibrations or manufacturing, additional methods may be incorporated in the future. As these simulation tools may range from in-house developed codes to commercial software, the optimizer should see the simulation tools as black box functions, so that new methods can be easily added to the optimization loop.

Robust optimal solutions The flight envelope of a helicopter is based on large variations, often expressed in terms of forward flight speed and mass. A blade design with very well performing characteristics in a single flight condition is thus not interesting for industrial exploitation. Instead, a globally well performing rotor blade design is preferred. Performance of optimized blade geometries thus needs to be robust when slightly modifying flight conditions.

Pareto Optimal Front Finding many Pareto Optimal solutions is more interesting than retrieving only one blade geometry. From an industrial point of view, a selection from Pareto Optimal solutions allows for incorporating criteria that are not yet included in the optimization loop or that cannot be designated in objective or constraint values. In addition, a Pareto Optimal Front eases assessment of relations between parameters and objectives.

Computational cost Eurocopter has access to the large EADS computation cluster HPC3 for CFD simulations (see Introduction for details). HOST simulations are performed on small internal clusters of a dozen processors. These facilities allow for parallel simulations.

Return time The aerodynamic design of a rotor blade consists of two main phases: predesign and detailed design. In the first stage, the return time has to be in the order of hours, to quickly evaluate a large variety of possibilities. For detailed design, a longer return time is accepted, but still needs to be in the order of days, with a typical maximum of a week.

In the present work, the most important requirements that will guide the selection of the optimization method are: to obtain robust and globally optimal solutions, to find an approximation of the Pareto Optimal Front for multi-objective design problems, and to be able to incorporate multiple simulation tools without prerequisites.

3.2 Optimization method

An optimization method may be defined as a mathematical procedure involved in a process of making a design as effective as possible [163]. A large variety of optimization methods exists, each with different characteristics in terms of solution search, final proposed solution and time required to obtain this solution. Optimization methods may be classified in several ways. Hereafter, we distinguish global vs. local methods and the way multiple objectives are considered.

Local optimization methods start their search for an optimum at a certain point in the design space and seek to improve objectives from this point on. Often, gradient information is used to advance towards the optimum [31], so that local optimization methods typically need a relatively low number of function evaluations to find a local optimum. However, the final solution depends on the initial search position and global optima may not be found, especially if multiple extremes are present (multimodal problems).

On the contrary, global optimization methods search at a large variety of positions within the design space to find global optima. These methods may be either deterministic or heuristic

[157]. The first one converges quickly but mathematical requirements on the optimization problem restrict its application. Heuristic, or stochastic, methods randomly generate feasible design points [136]. No gradient information is used to advance towards optimal solutions. Instead, the optimizer searches for relations between objective and parameter values to find globally optimal solutions.

Another way to classify multi-objective optimization methods is by the way they assign preferences to each of the objectives of the design problem. Three groups of optimization methods may be distinguished, each having its own way of assigning preferences to the objectives [89]:

1. A priori articulation of preferences: the user designates relative importance of objectives before starting the optimization;

2. A posteriori articulation of preferences: a set of mathematically equivalent solutions is returned to the user who chooses a single solution;

3. Progressive articulation of preferences: the decision-maker continuously provides an input during the optimization run.

Two main types of optimization methods are found in literature of aerodynamic design optimization of helicopter rotor blades: gradient methods [3, 6, 71, 80, 146] and genetic algorithms [23, 71, 73, 80, 92]. Genetic algorithm methods have been employed only in recent years, as they require a high number of cost function evaluations, thus requesting more computational power.

The choice for an optimization method can in practice be reduced to these two methods, as they may be labelled in different categories by the classifications as presented above: gradient methods are local optimization methods, whereas genetic algorithms are global methods. And where gradient methods need a priori preferences for combining multiple objectives, genetic algorithms return the Pareto Optimal Front, leaving to the designer the selection of an optimal solution.

To choose between both methods, their compliance with the requirements presented earlier is discussed:

Multiple design parameters Both methods are able to treat multiple design parameters. The adjoint method, available in *elsA* [36, 77], permits the concurrent gradient computation for a large number of parameters requiring only one additional cost function evaluation. Genetic algorithms also handle multiple parameters at once, but it may be expected that a higher number of objective evaluations are required for the optimizer to understand relations between objectives and all parameters. Both methods only handle continuous design variables. Even if both optimization methods may cope with this requirement, gradient methods are expected to be more efficient.

Multiple objectives Gradient methods require the specification of preferences on the different objectives before running an optimization. The finally proposed solution thus depends on these preferences, often given as weighting factors to the objectives. On the contrary, genetic algorithms naturally account for multiple objectives and try to optimize for all objectives simultaneously. Therefore, genetic algorithms are more suitable when multi-objective optimization is required.

Complex constraints Exact implementation may differ, but normally both optimization methods are able to deal with inequality constraints.

Multi-physics simulations Gradient information may or not be available in simulation tools. Whereas *elsA* allows for computing gradients within the code by an adjoint method, this is not possible in HOST. Simulation methods that may be included in the optimization loop in the future may not provide gradient data either. Numerical approximation of the gradient may be inaccurate and become quickly expensive for highly-dimensional design spaces. For this reason, genetic algorithms that use simulation tools as a black box are preferred over gradient methods.

Robust optimal solutions Gradient methods are local search methods [31], meaning their final solution depends on the start position. Genetic algorithms, on the contrary, start and continue to explore the complete design space, thereby searching for a global optimum. Even if optimization convergence cannot be proven for genetic algorithms, finding a global optimum rather than a locally positioned best performance is of high importance in industrial rotor blade design. Genetic algorithms are thus preferred for this criterion.

Pareto Optimal Front Genetic algorithms naturally account for multiple objective and return all Pareto Optimal solutions to the user. The engineer then can choose out of these best design solutions. Gradient methods would only return a single best solution, depending on the weighting coefficients. To obtain a Pareto Optimal Front by a gradient method, multiple optimizations with different combinations of weighting coefficients would need to be carried out. Moreover, this technique may fail for non-convex Pareto fronts. As obtaining the Pareto Optimal Front is preferred to incorporate additional requirements in the final choice, genetic algorithms are preferred over gradient methods.

Computational cost and return time Parallel simulations greatly reduce return time. Computation facilities allow for parallel simulations both for HOST and *elsA* of which computation times were given in the Introduction in Table **1**. In practice, typically 8 parallel HOST simulations can be performed. Using a typical HOST computation time of 1 minute, this means that 480 simulations may be performed in 1 hour. Within the stated optimization return time of a couple of hours, typically 1000 to 2000 simulations can be performed (neglecting optimization treatment). In case of serial optimization, only 125 to 250 blade geometries could have been tested within the same time span. For CFD, this is even stronger, as computational facilities allow for more parallel simulations. The increased computational cost of parallel simulations is considered of less importance than its related return time reduction. The higher computational power required for genetic algorithms may thus be greatly relieved by parallelization. As resulting return time is of highest importance, no preference for either optimization method is given for this criterion.

Given the preceding discussion, rotor blade optimizations will be carried out using genetic algorithms. A short description of this optimization method is presented next, followed by some details on the two software codes used.

3.2.1 Genetic algorithms

Genetic Algorithms (GA) are family of evolutionary algorithms, and as their names suggest, these algorithms are based on evolutionary principles. By analogy to biological evolution, definitions of elements of genetic algorithms are given as follows [160]:

- Individual: solution candidate, consisting of a parameter set and representing a possible solution by objective and constraint values
- Population: set of individuals living in the same generation
- Generation: subsequent loop iteration in the optimization

- Fitness: quality of an individual to fulfil optimization requirements in terms of objectives and constraints

Basic principles of genetic algorithms are presented in Figure 3.2 and can be described by [88, 137, 160]:

1. Initial population: An initial set of individuals is created by attributing design variables to each of them.

2. Evaluation: Cost function evaluation of all individuals to acquire objective and constraint information.

3. Fitness assignment: Quality assessment of individuals to fulfil optimization requirements. Several techniques have been proposed [137, 160], out of which a popular one is ranking (or non-dominated sorting): Pareto Optimal solutions of the current population receive the highest rank, Pareto Optimal solutions of the resulting population are ranked at level 2, and so forth until all individuals have received a relative ranking compared to other individuals.

4. Selection: Individuals to be used for creating the new generation are selected; a large variety of selection techniques exist [50, 88, 137, 160]. The goal here is to find individuals of the Pareto Optimal Front while maintaining diversity over the complete population. The risk is to converge towards a single solution and losing information on widely different solutions. A possible technique is to degrade fitness of individuals having many neighbours (high niche count). Another way is to include elitism, in which the best individual(s) of the current population is (are) directly included in the next generation, without genetic operator actions that could change its properties.

5. Crossover: Individuals are combined together to create new individuals, as illustrated in Figure 3.3. In this image, individuals are represented by a binary string, but real coded algorithms exist as well. The crossover probability decides at what point the parameter string is cut to combine parents together. In this example, two parent individuals create two children by cutting the binary string at one point, but various other methods of recombination exist [88].

6. Mutation: Obtained individuals are mutated according to the mutation probability. This step is important for searching for new interesting zones and to avoid getting stuck in a local optimum. Again, various mutation techniques have been proposed [88, 160]. The mutation probability typically has a low value to avoid a random search.

7. Stop criterion: As optimization convergence or stagnation of multi-objective problems is difficult to determine, often a user-fixed number of generations or evaluations is performed.

These basic principles are altered according to precise implementations of genetic algorithms. Variations may include population size change during the optimization and many propositions for selection, crossover and mutation are found in literature [88, 160].

3.2.2 Optimization software

At Eurocopter, two implementations of genetic algorithms are available: the in-house coded algorithm NSGA-II [50] and the MOGA algorithm available in the Design Analysis Kit for Optimization and Terascale Applications (DAKOTA), which is developed at Sandia National Laboratories [1, 2]. Some details on both methods are given next.

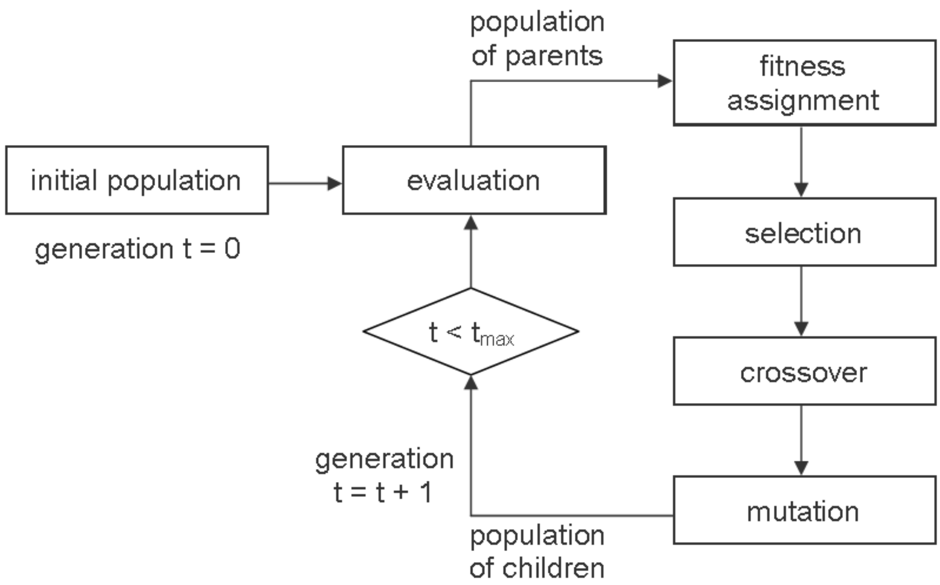

Figure 3.2: Schematic overview of a genetic algorithm

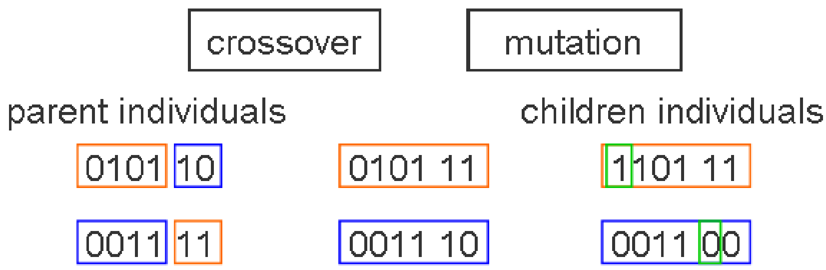

Figure 3.3: Creation of children individuals by crossover and mutation

The second version of the Non-dominated Sorting Genetic Algorithm, NSGA-II, is an update of NSGA which is computationally faster and includes elitism and a crowding operator to maintain diversity [50]. In fact, NSGA-II has a computational complexity of $\mathbf{O}(pN^2)$ (where p is the number of objectives and N the number of individuals), compared to NSGA which required $\mathbf{O}(pN^3)$ operations. More important for the current application are improvements for preservation of diversity. A crowding distance is computed which is a function of the average distance to adjacent solutions having the same rank. Within the same rank, solutions being more crowded, so having closer neighbours, are discarded in favour of less crowded individuals. This should improve spread along the population. Finally, elitism is included by comparing the current population to best non-dominated solutions found in previous generations. This should help in improving optimization convergence.

In various studies [85, 159, 161], NSGA-II is presented as a standard choice for a genetic algorithm, having in general good performance for a large variety of test problems.

Optimization toolkit DAKOTA contains, besides optimization algorithms, tools for parameter studies, uncertainty quantification and sensitivity analysis. It is developed to be coupled to any simulation method which is considered as a black-box. A full overview of DAKOTA's capabilities can be found in the user and reference manuals [1, 2]. In this manuscript, only here employed methods are described. In particular, DAKOTA's Multi-Objective Genetic Algorithm (MOGA) of global optimization library JEGA is described.

In comparison to the general principles of genetic algorithms presented above, recommended settings of MOGA include individual selection by domination count, meaning individuals are assigned the number of other individuals they dominate. A higher number refers to a fitter individual. For crossover the below-limit operator is suggested, which only keeps designs that are dominated by less than a user-specified number of other individuals. A significant difference compared to NSGA-II is the use of so-called niche pressure to encourage differentiation along the Pareto Optimal Front. This secondary selector requires solutions to be separated by a user-defined distance. Finally, various mutation possibilities are proposed. Even if a convergence tracker based on fitness is available in MOGA, all optimizations are executed with a stop criterion on the total number of evaluations. Due to crossover and niching implementations, MOGA changes population size over subsequent generations. This size can only be specified for the initial population. For practical control of the optimization cost, the total number of function evaluations is specified.

3.3 Advanced optimization techniques

Optimization algorithms always require a certain number of objective function evaluations, which may be costly in terms of total CPU time (which is a function of number of processors and computation time) and computational time, particularly for flow optimization problems. The number of function evaluations required for converging to an optimum depends greatly on the optimization method.

For industrial design purposes, return time of an optimization loop is of great importance. Therefore, techniques that allow for reducing the total optimization time are interesting in industrial application. This reduction may be achieved by accelerating solution convergence and/or by reducing the number of function evaluations. To this purpose, it is possible to apply optimization techniques, called Design and Analysis of Computer Experiments (DACE) [59]. Specifically, we focus on: Design of Experiments and Surrogate Modelling. The first allows for distributing points in the design space to span it as largely as possible with as few simulations as possible. The second technique is a way of representing objective functions by means of approximation by analytical functions. Besides replacing a costly objective function evaluation within an optimization loop by a low-cost function, the construction of surrogate models also allows for better understanding of relations between design parameters and objectives. Both techniques will be introduced in subsequent Sections. Design of Experiments and Surrogate Models may be combined into Surrogate Based Optimization or other hybrid strategies. These methods are described in Section 3.3.3.

3.3.1 Design of Experiment

A Design of Experiment (DoE) can be defined as a sampling plan in the parameter space [109]. An effective DoE should provide most possible information about the design space structure by using the smallest possible number of function evaluations. In precise wording, a DoE executed by deterministic computer experiments is called a Design and Analysis of Computer Experiments (DACE). Throughout this manuscript both DoE and DACE will be used.

A DoE can be used for several applications, each allowing in a different way to reduce the total optimization time [2]:

1. To select a good starting point for optimization algorithms through a preliminary exploration of the design space and detection of regions of interest. This should allow to improve convergence towards the optimum.

2. To provide information for surrogate modelling, to be used for subsequent optimization.

3. To investigate the influence of variables on simulation output (sensitivity analysis). Improved understanding of relations between parameters and objectives helps for example in analyzing relative importance of parameters and selecting suitable parameter ranges.

For all purposes, a DACE is used as an intelligent way to cover the design space. Several techniques are available (see [60] for a review). One of them is Latin Hypercube Sampling (LHS). In LHS, the domain of all design parameters n is split into k equally spaced parts. A sample point is then placed in each level of each independent parameter [48], see the example in Figure 3.4. An advantage of LHS is that the number of samples equals the number of partitions k and is thus independent of the number of design variables. A weakness is that for each given DoE problem, multiple LHS sampling results exist. Some results give a better spread than others and no check for best spread is included in the method. Nonetheless, LHS is very effective to sample highly dimensional design spaces and leads to a smaller variance of the sample mean than random sampling, as well as a good spread over the design space [59, 109]. Another advantage of LHS is that different sample points cannot have the same value for a certain parameter [60]. In the following, LHS is selected for these advantages and for its common usage in optimizations [60, 109].

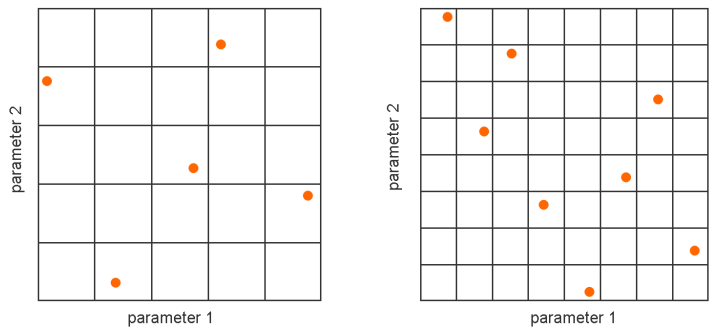

Figure 3.4: Example of a two-dimensional Latin Hypercube Sampling design with 5 (left) and 8 (right) partitions

3.3.2 Surrogate modelling

A surrogate model, also called a metamodel or a response surface model, represents data by analytical functions. Surrogate models express objective functions in terms of design variables. For each simulation result, objective and constraint, a separate metamodel is generated which is a function of all design variables. Assuming this function correctly represents simulation outputs, the optimization can be performed on this cheap model, replacing the costly simulation, as illustrated in Figure 3.5.

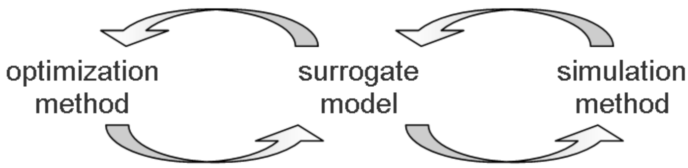

Figure 3.5: Optimization on surrogate model

The main requirement on a surrogate model is that it provides an accurate representation of the actual functions by using a small number of data points. Figure 3.6 shows how 2 different metamodels are found from one data set. Evidently, optimization on these two models would not lead to comparable results, showing the sensitivity of optimization to metamodel quality. Since its development in the '70's, a large variety of models has been created [124]. Often employed models are based on polynomial functions [60], radial basis functions [114], kriging [119] and neural networks [147]. Even if several review papers exist [60, 109, 122, 124], surrogate model construction highly depends on the particular design problem. In literature, rotor blade optimization has been carried out by using metamodels based on polynomial functions [45] and an artificial neural network [23, 92].

Since metamodelling leads to the construction of an approximated response surface, hereafter we refer to these techniques as Response Surface Modelling (RSM).

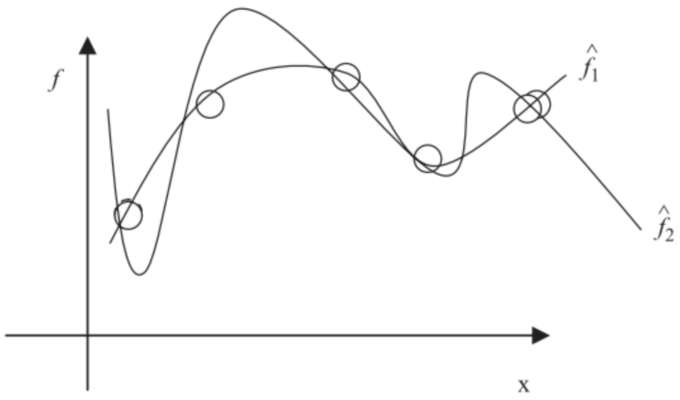

Figure 3.6: Two possible surrogates consistent with the data, from [109]

DAKOTA offers local and global surrogate model formulations. For local methods, various simple local models are combined to generate an overall model of the complete design space [109]. In a global method, it is assumed that a global form over the complete design space exists. Figure 3.7 illustrates the relation of rotor power as a function of twist and chord values at the blade tip. It shows that this function is smooth, continuous and that a simple function could describe this response surface. From present numerical tests, and from literature comparison, it is decided to prefer global surrogate models.

Out of DAKOTA's global metamodelling possibilities [2], two surrogate models are selected: a polynomial, attractive for its simplicity [56], and Gaussian Process modelling [128].

Polynomial response model Polynomial model description may include linear, quadratic or cubic functions $\hat{f}(\mathbf{x})$, which are given as follows for n design variables:

$$\hat{f}_{\text{linear}}(\mathbf{x}) \approx c_0 + \sum_{i=1}^{n} c_i x_i \tag{3.9}$$

$$\hat{f}_{\text{quadratic}}(\mathbf{x}) \approx c_0 + \sum_{i=1}^{n} c_i x_i + \sum_{i=1}^{n} \sum_{j \geq i} c_{ij} x_i x_j \tag{3.10}$$

$$\hat{f}_{\text{cubic}}(\mathbf{x}) \approx c_0 + \sum_{i=1}^{n} c_i x_i + \sum_{i=1}^{n} \sum_{j \geq i} c_{ij} x_i x_j + \sum_{i=1}^{n} \sum_{j \geq i}^{n} \sum_{k \geq j}^{n} c_{ijk} x_i x_j x_k \tag{3.11}$$

In fact, the number of data points N required to construct the polynomial is related to

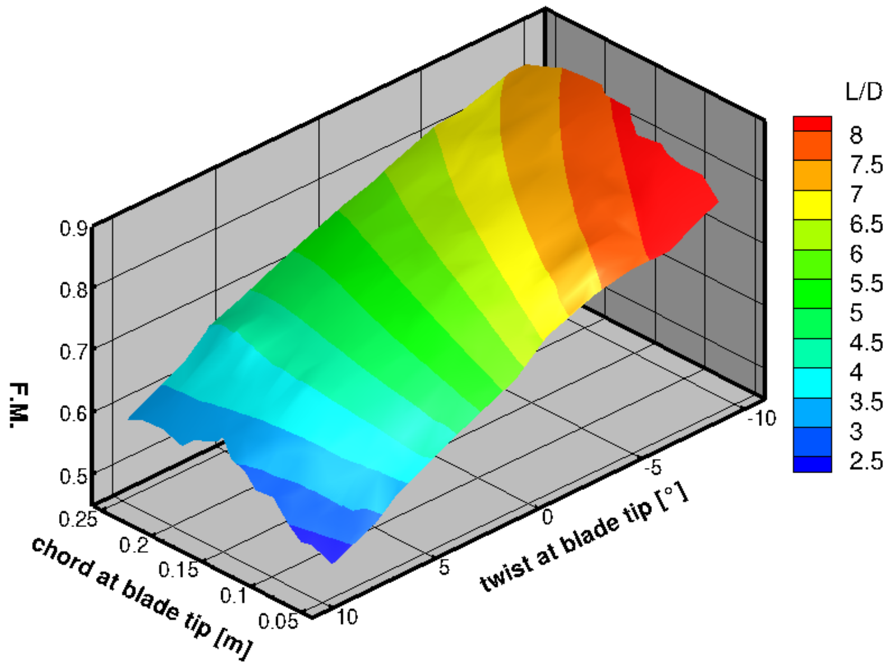

Figure 3.7: F.M. and L/D as a function of twist and chord at blade tip, HOST computations on 7A blade

the number of design variables n and to the polynomial order by the following relations:

$$N_{\text{linear}} = n + 1 \qquad N_{\text{quadratic}} = \frac{(n+1)(n+2)}{2} \qquad N_{\text{cubic}} = \frac{n^3 + 6n^2 + 11n + 6}{6} \tag{3.12}$$

If more than the required number of points are available, a least-squares regression approach is employed to solve the linear system.

These relations show a fast increase of the number of data points required for polynomial construction. In fact, for 10 design variables, at least 22 data points are required to build a quadratic polynomial function and 286 for a cubic function. As typically the number of data points used for the first surrogate model is below 200, and the number of design variables might be above 10, cubic polynomial function modelling is unfeasible for this design problem. However, quadratic and linear modelling is possible. According to DAKOTA's user manual [2], polynomial modelling is especially useful for modelling a small portion of the design space as this often can be described by lower-order functions. An advantage is the smoothing of data noise by least-squares fitting of data points. It is stated that global modelling is possible if the response surface has a linear, quadratic or cubic polynomial shape [2].

Gaussian Process modelling Gaussian Process modelling as implemented in DAKOTA has many similarities with Kriging. In contrast to polynomial surfaces, Gaussian Processes are nonparametric surrogate models meaning no a priori knowledge of the response data is required [2]. These models combine a set of mean functions with local shape modifications of the form [2, 59, 158]:

$$\hat{f}(\mathbf{x}) \approx \sum_{j=0}^{L} \beta_j \mathbf{B}_j + z(\mathbf{x}) \tag{3.13}$$

where $\mathbf{B}_j$ is the mean function of order L with coefficients β_j given by a constant, linear or quadratic trend functions. This function should capture large scale variations of the surrogate. Error function $z(\mathbf{x})$ is a stochastic process with zero mean, variance σ^2 and covariance described by a Gaussian correlation function. Formulations for these terms are given in [2, 123, 158]. Thanks to the wide range of fluctuation functions, these models should be able to accurately predict highly nonlinear and irregular behaviour [157].

Gaussian Process implementation in DAKOTA has features to overcome ill-conditioning of the correlation matrix due to multiple closely positioned data points [2]. A Gaussian Process surrogate model can be constructed from N_{linear} data points on, but preferably $N_{\text{quadratic}}$ points should be used.

3.3.3 Hybrid strategies

In preceding sections, two simulation methods (HOST and *elsA*) and two optimization techniques (genetic algorithm optimization and advanced optimization techniques including DoE and RSM) have been discussed. We can imagine various combinations of these methods to optimize rotor blade geometries as efficiently and effectively as possible. We call such combinations "optimization strategies" [136]. These include for instance hierarchical optimization, which employs low- and high-fidelity simulation tools, respectively HOST and *elsA*, within the same optimization loop.

One important point to be taken into account in building an optimization strategy for helicopter rotors is that a genetic optimization based entirely on CFD simulations is not feasible: genetic algorithms require a high number of objective function evaluations and CFD-simulations are too CPU-costly for massive employment. Thus, for incorporating CFD-simulations in an industrial optimization loop, employment of surrogate models is needed. For best metamodel quality, Surrogate Based Optimization is proposed in the following: the design space is first investigated by a metamodel created from data points obtained from a Design of Experiment. Then, this surrogate model is updated in interesting zones, often where optimal solutions are found.

Another interesting strategy is to create a response surface from combination of low- and high-fidelity simulation tools. A low-cost low-fidelity metamodel is then updated by costlier high-fidelity simulations in interesting regions only.

Finally, different optimization methods can be employed subsequently for solution refinement. For example, a global search method can be used first to explore the design space, followed by a local search for optimal solutions. Various other sequences can be imagined.

These strategies are discussed next.

Surrogate Based Optimization

Surrogate models should provide a sufficiently accurate description of system optima and be able to discriminate between different designs [75]. Model quality may be validated by computing the root mean square error from data points that were not used for surrogate construction or by cross-validation in which subsets are temporarily left out to compute model quality of remaining data points [109]. In most optimizations, surrogate models based on the initial DoE will not be accurate enough in the region of interest as only a few simulated data points are available. In Surrogate Based Optimization, the metamodel is improved in this interesting region by adding more data points in subsequent update cycles.

To set up a Surrogate Based Optimization (SBO), both earlier presented techniques are combined: DoE is used to explore the design space for a global surrogate model initialization. The actual optimization is then performed on the metamodel, which is updated in subsequent iterations by real objective function evaluations, as illustrated in Figure 3.8.

As response surface based optimization is very cost-efficient, genetic optimizations are performed. In the following, 10 generations of 200 individuals will be used within these

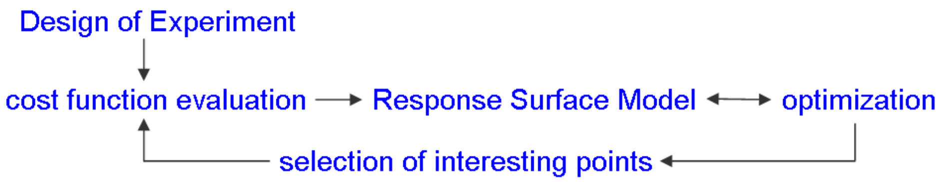

Figure 3.8: Illustration of Surrogate Based Optimization

optimizations as this should result in an extended Pareto Set.

Even if this SBO set-up seems simple, many questions on its practical use are found:

- How many data points should be used in the Design of Experiments phase? This question has not often been discussed in literature as it is highly problem dependent. Each type of metamodel may require a different number of sample points to construct an accurate surrogate. In addition, practical limitations on maximum number of parallel simulations will play a role in this decision. In the end, the number of data points should be sufficiently high to identify interesting zones from this first surrogate model on. On the other hand, the number of data points should be as low as possible to avoid using computational power to evaluate data points with poor performance. Only practical tests for typical design problems will allow choosing suitable DoE sizes.

- How many surrogate model update cycles should be performed? References [111] and [110] discuss this subject by using information on prediction variance of Kriging metamodels [139]. Variance allows to estimate how valuable an additional data point at a certain position would be. Statistics are then used to decide on performing another update cycle. In practice, as for the number of data samples in the DoE, the number of update cycles is directly related to available computational resources and optimization return time.

- How to select sample points to update the surrogate model? Surrogate model improvement will mostly be required in the region of interesting objective values, but additional points elsewhere in the design space may help to continue design exploration. If information on added value of extra data points is not available, points may be chosen out of the Pareto Optimal Front obtained from optimization on the metamodel. For a large POF, this selection may be performed by domination count or by imposing a certain distance between update points to assure their spread. In case of selection out of the POF, no additional design exploration is added during surrogate updates and the region of interest is to be defined from the first surrogate model construction on.

These questions are still open and represent research subjects. Problem dependency makes it difficult to define generic SBO-settings. DAKOTA incorporates methods of uncertainty quantification that allow for computing the prediction variance, which should help in choosing additional data points. In a first stage, however, only points taken out of the Pareto Optimal Front will be selected to update the response surface.

Combined low-/high-fidelity response surface

Combining simulation tools of variable fidelity may be used to reduce the number of high-fidelity simulations required to find optimal solutions. The low-fidelity tool is then used to explore the design space and designate interesting zones where high-fidelity simulations are performed. When switching from low- to high-fidelity simulation, design parameters may even be adapted to better match the design problem [117].

An example of this multi-fidelity metamodel optimization is presented in [46] and its architecture is illustrated in Figure 3.9. As seen in Chapter 2, different simulations methods lead to different performance values for the same blade geometries. To combine low- and high-fidelity simulations into one surrogate model, objective values are scaled by factor $s(\mathbf{x})$ which is a function of low- and high-fidelity responses by:

$$s(\mathbf{x}) = \frac{f_{\text{high}}(\mathbf{x})}{f_{\text{low}}(\mathbf{x})} \tag{3.14}$$

The actual optimization is then performed on a metamodel which is built from low-fidelity simulations and on which scaled high-fidelity simulations are added.

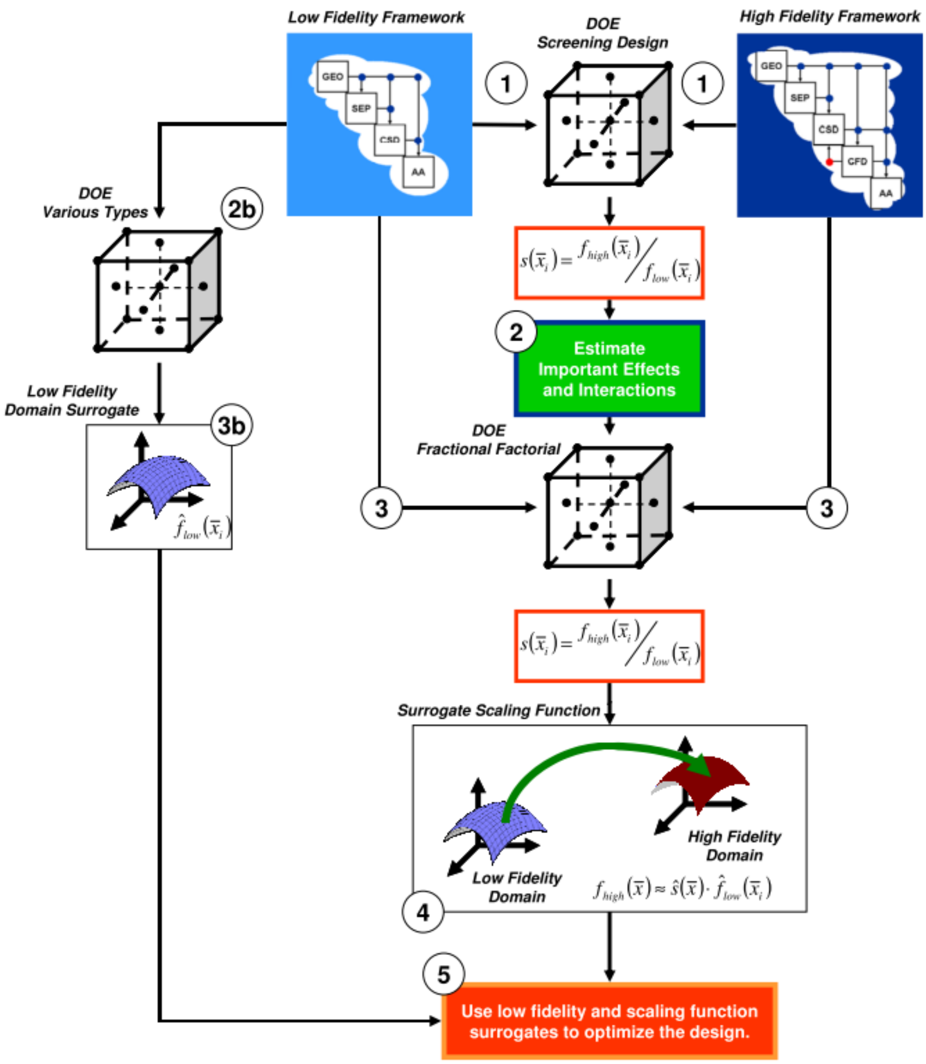

Figure 3.9: Combination of low- and high-fidelity simulation tools in Surrogate Based Optimization, from [46]

This seems a very promising technique that combines the advantages of both simulation tools into one optimization. However, optimization on this combined surrogate only provides interesting optimal solutions if the metamodel is of sufficient quality. Scaling of high-fidelity results to fit within the low-fidelity metamodel is the first need to construct a combined surrogate model. Secondly, the shape of these response surfaces would have to be similar as well. If not, the optimizer would not know in which direction to search for better solutions.

An extensive sensitivity study of rotor performance as a function of blade geometry variations by several simulation methods is provided by [151]. Assessed simulation methods include HOST computations with different induced velocity models: Ring method, Pitt & Peters, FiSUW, Metar and Mesir (free wake model [96]), a DLR developed panel method and CFD simulations neglecting viscosity effects (Euler equations) and Navier-Stokes on a coarse and refined grid. These CFD simulations are performed with DLR code FLOWer [102] but it may be expected that similar results would be found using *elsA*. As no panel method or inviscid CFD simulations are used within the current optimization loop, these methods are excluded out of this discussion.

The baseline 7A blade (see Section 4.2.1) was computed in hover and forward flight at $\mu = 0.38$, in both cases for creating a lift force corresponding to $\bar{Z} = 15$. Computed rotor power differed greatly from a simulation method to another. In hover, lowest computed rotor power equals about 60 kW for the free wake model in HOST, whereas the highest rotor power of more than 100 kW was found for coarse grid CFD simulations. For forward flight conditions, computed rotor power varies between about 100 kW for fine grid CFD simulations and HOST with FiSUW up to just over 120 kW for a HOST computation with Metar. Variations of computed rotor power with simulation method are not consistent between hover and forward flight simulations. These comparisons thus concern the relative difference of rotor performance as computed by various simulation methods. Despite these variations, a combined surrogate model could be constructed using scaling functions.

The paper also provides a rotor performance sensitivity study when modifying geometry. Anhedral, sweep, chord and twist variations are applied to the outer 20% of the 7A blade. For anhedral and sweep angle variations, relative performance variations show similar behaviour for HOST simulations with Pitt & Peters, Ring method and FiSUW, compared to CFD simulations. HOST computations with wake models behave differently, especially for sweep variations in hover. Response surface gradients of these design parameters would be different for these simulations compared to others. For chord variations in forward flight, very similar rotor power tendencies are found. In hover, chord should be reduced to decrease rotor power consumption, as computed for all simulation methods. Nonetheless, gradients are predicted to be low for CFD simulations, somewhat higher for HOST with Pitt & Peters, Ring method and FiSUW and much higher for HOST simulations with wake models. Finally, twist variations of [151] are shown in Figure 3.10. For all simulations, in hover and in forward flight, parabolic response surfaces are found. In forward flight, twist angles for which minimum rotor power is found are positioned relatively close together, and vary between -5° and -8°. Rotor performance variations are largest for twist variations in hover, meaning a strong relation exists between hover performance and twist distribution. But, the twist angle at which best rotor performance in hover is found now largely depends on the simulation method: HOST simulations with Pitt & Peters, Ring method and FiSUW predict best rotor performance for a tip twist angle of approximately -6°. Yet, CFD simulations on a coarse grid calculate best hover performance for a tip twist angle of -16°. In addition, a difference of 4° in optimal twist angle between coarse and fine grid viscous CFD simulations is observed. This illustrates on the one hand side the large dependency of hover power by tip twist angle, and on the other side the difficulty of correctly predicting this dependency by different simulation methods. In the end, predicted performance as a function of twist is directly linked to the inflow angle of the flow seen by the airfoil. This in turn is closely related to the induced velocity field. A final conclusion is thus that prediction of induced velocity field differs largely from a simulation method to another, leading to disparities in optimal twist angle.

In this study, no interference effects of geometrical parameters are taken into account, which would lead to even more complicated response surfaces. The paper finishes with rotor blade optimizations, executed separately for hover and forward flight performance. These

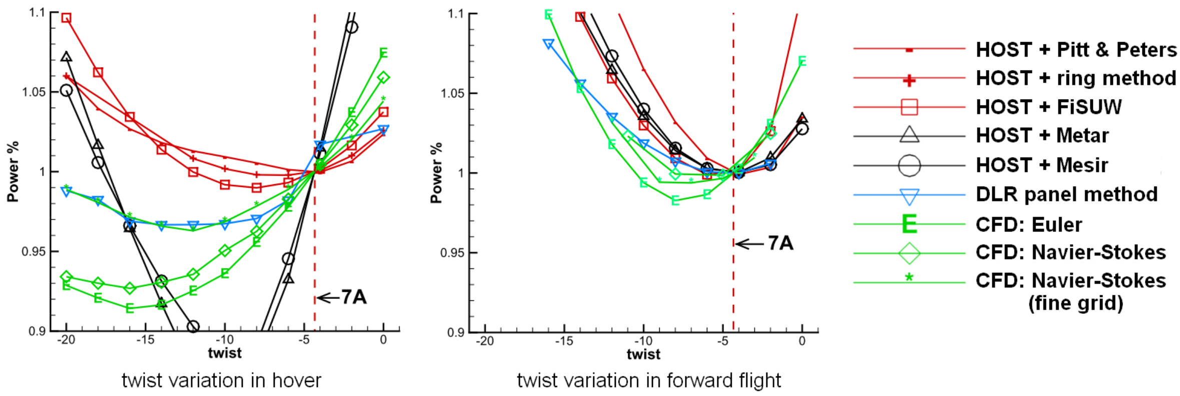

Figure 3.10: Relative rotor power consumption as a function of twist variations, from [151]

optimizations are executed for all simulations methods and resulting blade geometries are compared. It is observed that obtained blades differ in terms of sweep, anhedral and chord, even if most often reduced chord sections are seen at the blade tip. Obtained twist laws are not presented.

This paper presents a very interesting study on differences in performance prediction for different simulation methods. It shows that large computed performance differences are observed for tested methods. These could still be combined into a multi-fidelity surrogate model by applying scaling functions. For anhedral, sweep and chord, response surfaces obtained from different simulations method would have a similar shape and thus only a value offset. But, for twist variations, obtained surrogate models would have a significantly different shape when changing simulation method. Creating a multi-fidelity metamodel for twist variations would thus not be possible. Yet, twist is an important design parameter, which is seen from the large variations of rotor performance in this paper. Based on its high importance and too large differences between simulation methods for twist variations, the idea of a combined low-/high-fidelity response surface is discarded in the following.

Combination of different optimization methods

Another type of hybrid strategy is the subsequent use of different optimization methods to take advantage of each of them. In general, first a global optimization is performed to identify interesting zones. This is then followed by a local search method to find the optimal solution.

An example is given by [107] in which a genetic algorithm is employed to design a yacht fin keel. This design includes 22 parameters and is simultaneously optimized for maximum lift and minimum drag. Standard genetic algorithm optimizations are then compared to a combined GA + gradient method optimization. For the local search, weighting factors are assigned to combine both objectives into one objective function. A better converged Pareto Optimal Front is found for the hybrid optimization strategy, compared to simple genetic algorithm optimization. In fact, the local search phase increases the lift force by 4% and reduces drag by another 1%, compared to optimal genetic algorithm solutions. As expected, gradient optimization allows for finding locally optimal solutions.

The hybridization of a genetic algorithm and a deterministic optimization method is demonstrated on airfoil and wing tip shape optimization by [55, 140]. As CFD-simulations are used in this optimization, the global search phase is performed on a surrogate model of Artificial Neural Networks (ANN). This metamodel is updated in interesting zones as described earlier as a Surrogate Based Optimization. To switch from the global to local search phase, a stop criterion is implemented, based on the percentage of individuals within a certain distance to the best individual. This should lead to one interesting region on which the so-called derivative-free trust-region method is applied for local search. For the airfoil optimization application, it is demonstrated that the stop criterion has a large influence on optimization results. When this criterion is too strict, hybridization does not significantly reduce optimization time. For a too tolerant criterion, the global optimization has not yet defined a clear region of interest and improvement by local search is difficult. Comparing local optimization only, genetic algorithm optimization only and combined genetic algorithm and local optimization, it is observed that no optimal design is found for the local method. Yet, optimal solutions for Surrogate Based Optimization and global + local optimization are similar and only a slight performance improvement is obtained from the hybridization by local search. In conclusion, defining a stop criterion that balances optimization time and convergence is complicated, making practical implementation of this hybridization tricky.

These two examples illustrate potential advantages as well as difficulties in practical implementation. Two disadvantages of this hybridization strategy for industrial rotor blade optimizations are encountered in the second design phase:

- An interesting feature of genetic algorithms is their ability to find various Pareto Optimal solutions. This information is lost if only a single starting point is chosen for local refinement. If not, all Pareto solutions could be used for local optimizations, but this would lead to considerable computational cost. In addition, multiple objectives should be combined into one objective function by weighting factors. The final solution thus depends on these factors. The hybridization of a multi-objective optimization method with a single-objective optimization method thus always leads to information loss.

- Often, local search methods do not allow for simulation parallelization. Even if in total fewer simulations would be required for the local search phase than for continued search by genetic optimization, total return time may not be in favour of local search due to simulation parallelization for genetic algorithms.

In conclusion, the hybridization of genetic algorithms with local search methods to refine solutions locally is interesting to improve optimization convergence, but practical implementation appears tricky and no significant return time gain is expected.

Besides this hybrid strategy, other combinations of optimization methods and techniques can be imagined. In particular, initialization of a genetic optimization could be done on a Design of Experiment, rather than a stochastic initialization. This could improve design exploration without additional computational cost.

3.4 Proposed optimization strategy

Important requirements for industrial optimization of rotor blades include locating globally optimal solutions, finding the multi-objective Pareto Optimal Front and employment of multiple simulation tools as a black box. From these prerequisites, genetic algorithms are selected.

Typically acceptable return times are in the order of hours in the pre-design phase and a couple of days for detailed design. Low-fidelity HOST computations usually take less than a minute. For both design stages, many HOST simulations can be performed within the prescribed time. Massive employment of HOST within a genetic optimization loop is thus no problem. But, high-fidelity CFD-simulations take some hours for a hover computation and up to 3 days for a forward flight computation. Therefore, use of advanced optimization techniques is required to perform CFD-based optimization. A possible solution is Surrogate Based Optimization for which fewer simulations as well as less update cycles are required, both leading to a lower return time.

The intelligent use of low- and high-fidelity simulation tools could lead to a further reduction in optimization time. An optimization strategy based on a combined low- and high-fidelity response surface was discussed. This combination is attractive as costly high-fidelity simulations are only performed to update the surrogate model in interesting zones. Differences in performance values between low- and high-fidelity simulations could be resolved by scaling functions. But, as explained earlier, it appears that not only performance values differ, also gradients of rotor performance as a function of geometry variations are not uniform for HOST and CFD simulations, especially for twist variations. This implies that shapes of response surfaces are not coherent and combined surrogate models cannot be constructed.

Another optimization strategy is the subsequent employment of different optimization methods. In particular, two examples of design space exploration by global search methods, followed by a local refinement optimization were discussed. In both examples, further improvement by the local search phase was demonstrated. But, practical implementation appeared difficult due to the definition of a method switch criterion. In addition, multi-objective information is lost when continuing with a local optimization method.

Combining the ideas of both optimization strategies, a Multi-Fidelity Optimization (MFO) strategy for rotor blade design is proposed, see also Figure 3.11:

1. Perform an explorative low-fidelity genetic algorithm optimization.

2. Based on low-fidelity Pareto Optimal solutions, parameter bounds for the high-fidelity phase may be reduced.

3. By inspection of the low-fidelity optimization progress, an extended set of near-optimal blade geometries can be selected. These geometries should not consist of Pareto Optimal solutions as these blades will most likely be no longer Pareto Optimal when switching to high-fidelity simulation. Instead, these geometries should provide a large set of parameter combinations that allow the high-fidelity optimization to still search for optimal solutions and at the same time initialize on good-performance blade geometries.

4. Perform a high-fidelity Surrogate Based Optimization, using the reduced parameter limits and initializing on near-optimal blade geometries obtained from selection of low-fidelity computed solutions.

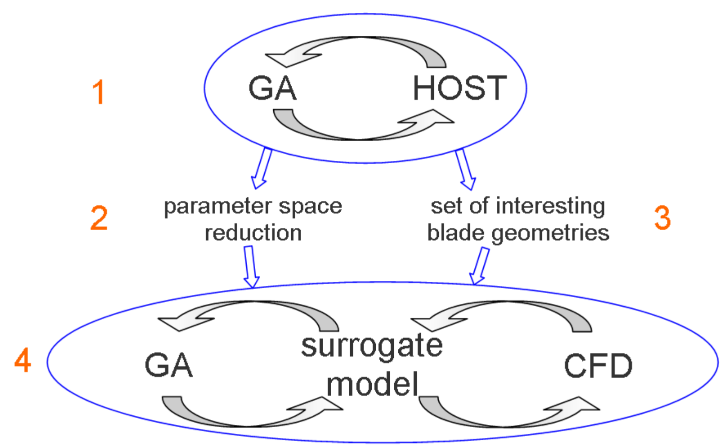

Figure 3.11: Illustration of Multi-Fidelity Optimization strategy

This multi-fidelity optimization strategy has two factors that should lead to improved optimization convergence compared to a CFD-based SBO. First, reducing the parameter space allows the MFO to consider less non-optimal blade geometries. In addition, the surrogate model is used to describe a smaller portion of the design space and is thus expected to have a better quality for a given number of simulations. Secondly, initializing on an extended set of good performance blade geometries allows for finding optimal solutions more quickly than with a DoE. Again, the response surface is constructed only in this interesting region. Fewer update cycles should be required to converge to optimal solutions as the initial design is already close to optimal.

In conclusion, for the pre-design phase, HOST-based genetic algorithm optimizations are recommended to fulfil optimization requirements within the allocated return time. For detailed design, employment of CFD simulations is required. To converge to optimal solutions by using as less simulations as possible, a Multi-Fidelity Optimization strategy is proposed: HOST-based genetic algorithm optimization results are used to reduce the design space and to initialize a CFD-based SBO on near-optimal blade geometries. The high-fidelity SBO is expected to require fewer update cycles to find Pareto Optimal solutions.

Chapter 4

Rotor blade optimization

The last Chapter of this Dissertation combines the simulation and optimization methods presented in preceding chapters into a rotor blade optimization loop. Precisely, HOST and *elsA* are used as low- and high-fidelity simulation methods, and computational parameters determined earlier in Chapter 2 are used for these simulations. Optimization runs are based on multi-objective genetic algorithms, or on a genetic algorithm combined with a surrogate model.

This chapter consists of two main sections: first, a description of the optimization loop is presented, along with implementation details. Then, in the second section, twist and chord laws of the 7A blade are optimized. Various optimizations are performed, combining in different ways both simulation tools, HOST and *elsA*, and both optimization techniques, genetic algorithm and Surrogate Based Optimization. First, HOST-based genetic optimizations are carried out to validate the optimization loop and study objective selection as well as the parameterization used to represent blade geometry. For this low-cost simulation tool, fully genetic optimization is compared to Surrogate Based Optimization. For SBO, we investigate the impact of response surface method and the number of HOST simulations required to create high quality surrogate models. Finally, both simulation tools and both optimization techniques are combined in the Multi-Fidelity Optimization strategy described in section 3.4.

This chapter finishes with conclusions on all tests performed to validate the optimization loop.

4.1 Optimization loop description

The optimization loop links optimization methods and simulation tools by exchanging design parameters, values of the objective functions and constraint information, as shown on the left-hand side of Figure 4.1. As described in previous chapters, two optimization methods, NSGA-II and the DAKOTA library, are connected with two objective evaluation tools, HOST and *elsA*. A generic optimization loop architecture is required to include both methods and to allow for continued linking of tools later on. In general terms, the optimization loop will have a structure as presented in the right part of Figure 4.1, in which information between optimization and simulation methods is exchanged via text files.

Interfaces are written to integrate optimization and simulation methods in the loop, so that tools are not modified. These interfaces are described next, followed by a short description of the blade geometry generation tool.

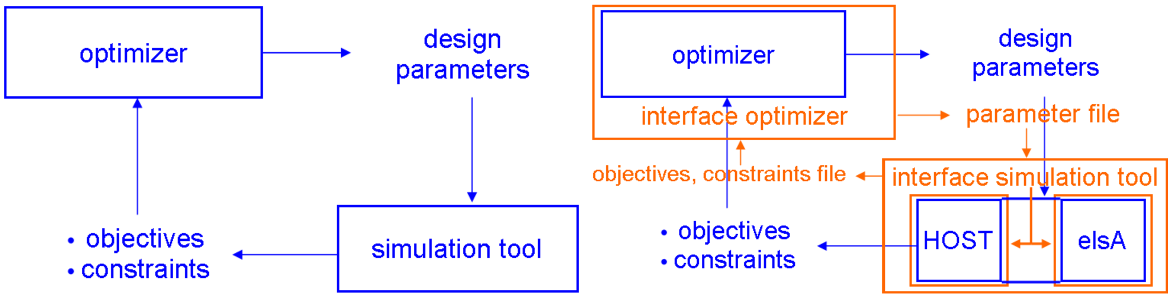

Figure 4.1: Generic architecture of optimization loop and interfaces

4.1.1 Solver/optimizer interfaces

In-house coded optimizer NSGA-II is adapted to read and write the discussed text files containing parameter information and objectives and constraints function values. The DAKOTA optimization library is encapsulated by an interface that performs this task so that new versions of this library can be inserted without modification.

Simulation interfaces for HOST and *elsA* are encapsulated by an overall simulation interface that enables combined use of both solvers within the same optimization loop. Tasks performed by this overall simulation interface are illustrated in Figure 4.2.

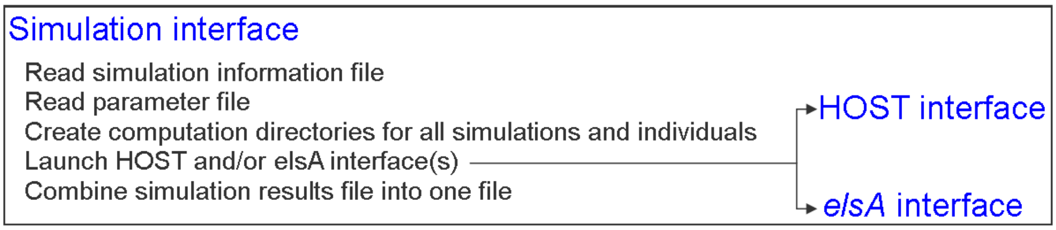

Figure 4.2: Overview of simulation interfaces

Both solver interfaces need to handle all actions required to prepare and launch simulations and analyze their results. These steps are illustrated in Figures 4.3 and 4.4. For forward flight simulations with *elsA*, both solver interfaces are called sequentially: first a HOST computation is performed to obtain the harmonics required for rotor trim, which are then inserted into the *elsA* computation. For both solvers, in case of simulation failure, high objective values and violated constraint values are assigned to the individual.

The simulation interfaces are coded in C as this allows for easy text treatment, which is a principal task of these interfaces. The overall simulation interface contains some 1000 lines of code (comments included), while the HOST and *elsA* interfaces are about 1500 and 1200 lines, respectively.

4.1.2 Blade geometry generation

An in-house developed tool, called bladesee, is used to create blade geometry descriptions for HOST and *elsA*. A text file describes the blade geometry in terms of separate laws for twist, chord, dihedral, sweep and airfoil relative thickness along the blade radius. All laws are combined into one blade geometry, which is written in two file formats: one for HOST and one for *elsA*.

A large variety of laws is possible within bladesee, out of which the most frequently used are:

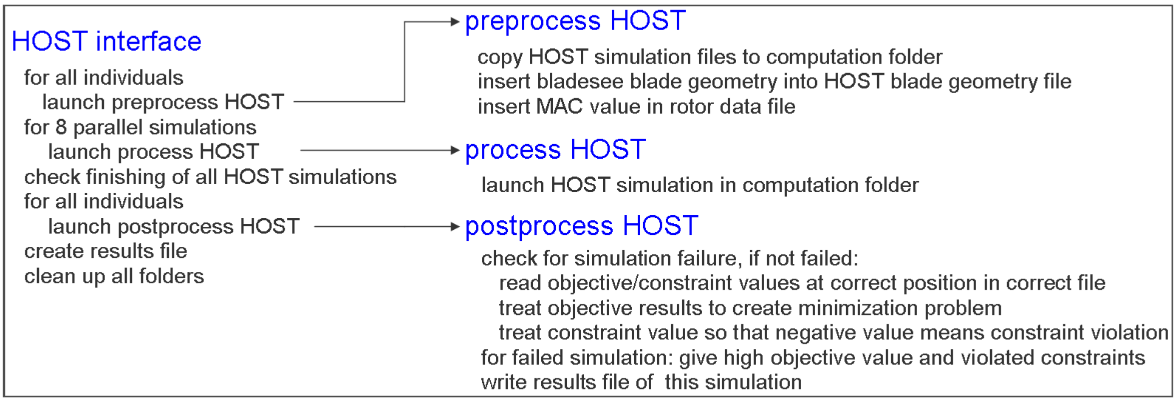

Figure 4.3: Overview of HOST interface

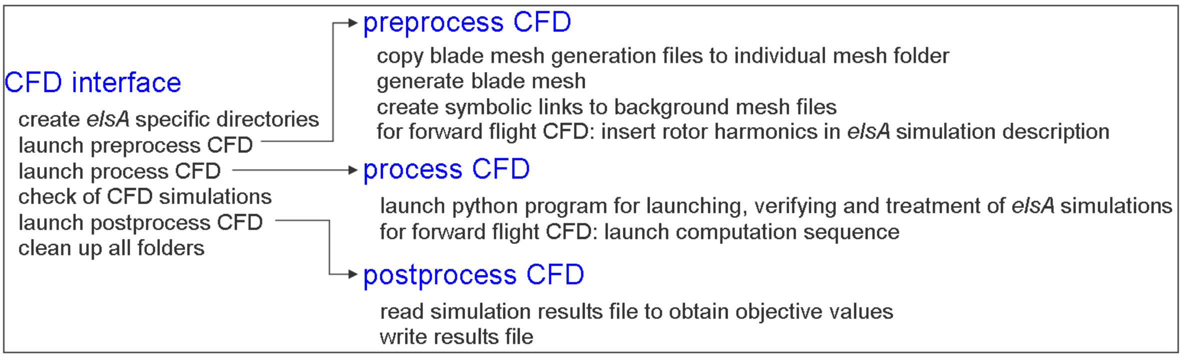

Figure 4.4: Overview of *elsA* interface

- Linear law: radial position and values are given for two extreme points.

- Bézier law: Bézier curves describe the blade parameter, for which a user-selected number of control points are given. A Bézier curve is given as follows:

$$\mathbf{B}(t) = \sum_{i=0}^{n} \mathbf{b}_{i,n}(t)\mathbf{P}_i \tag{4.1}$$

  where $\mathbf{P}_i$ are control points of the Bézier curve and $\mathbf{b}_{i,n}(t)$ are Bernstein basis polynomials of degree n that are given as:

$$\mathbf{b}_{i,n}(t) = \binom{n}{i} t^i (1-t)^{n-i} \quad , i = 0 - n \tag{4.2}$$

  Bézier curves do not pass through control points, except for outer points.

- SP2: a two-point parabolic law using a parameter α for controlling the curve shape, defined as $f(x)$ in point x located between two points x_0 and x_1 of values $f(x_0)$ and $f(x_1)$ by:

$$f(x) = f(x_0) + \alpha(x - x_0) + \left[f(x_1) - \left\{ f(x_0) + \alpha(x_1 - x_0) \right\} \right] \left(\frac{x - x_0}{x_1 - x_0} \right)^2 \tag{4.3}$$

Multiple subsequent laws may be used for the same geometrical parameter, i.e. a twist law may be described in the inboard part of the blade by a linear section, followed by a Bézier curve.

This tool has two main advantages: no mutual relations between parameter laws are given, allowing for a large flexibility of geometry description; and secondly a single input file is required to generate geometry descriptions for both simulation tools HOST and *elsA*. This means that coherency between the two blade geometry descriptions is assured.

4.2 Combined twist & chord optimization

As described in Chapter 3, the final goal of this work is to perform a Multi-Fidelity Optimization (MFO). This MFO starts with a design space exploration by a genetic optimization with inexpensive solver HOST. Then, a CFD-based SBO is initialized on well-performing blade geometries obtained from the HOST-based optimization. Before reaching this final goal, several intermediate validation steps are performed:

1. Perform HOST-based genetic algorithm optimizations
2. Perform HOST-based surrogate based optimizations to validate against GA
3. Perform multi-fidelity optimization with HOST-GA and CFD-SBO

As CFD simulations are too costly for full genetic algorithm optimization, only SBO will be performed with *elsA*. Validation of SBO against GA thus needs to be performed using HOST. The precise tests performed and test case are detailed next.

4.2.1 Description of optimization runs

To validate the optimization loop and study the influences of different variables, various tests of increasing complexity are performed. Precisely, the optimization strategy is assessed through the following steps:

1. Genetic algorithm optimizations with HOST
    - Study objective influence: compare minimizing rotor power to maximizing rotor aerodynamic performance (F.M. and L/D)
    - Study parameter influence: compare parameterization of Bézier laws with and without parameters on radial positioning of inner control points
    - Perform twist, chord and combined twist & chord law optimizations using the objective function and parameterization selected at preceding steps
2. HOST-based Surrogate Based Optimization
    - Study influence of size of initial DoE: test three different sizes
    - Study influence of response surface update frequency
    - Study influence of number of added simulations used for response surface update
    - Perform combined twist & chord law SBO optimization with selected parameters and compare to GA optimizations
3. Multi-fidelity optimization
    - Perform HOST-based genetic optimization to explore the design space and use optimization results to initialize a CFD-based SBO optimization

The evaluation associated to each step is detailed in next sections.

Optimization set-up

Optimizations are run to improve rotor performance. The 7A blade is selected as the baseline design. This choice is motivated by the large database of pressure measurements available for an extended range of flight conditions. The 7A blade is a rectangular wind tunnel blade with a span of 2.1m and constant chord section of 0.14m. Twist law and radial distribution of airfoils are illustrated in Figure 4.5.

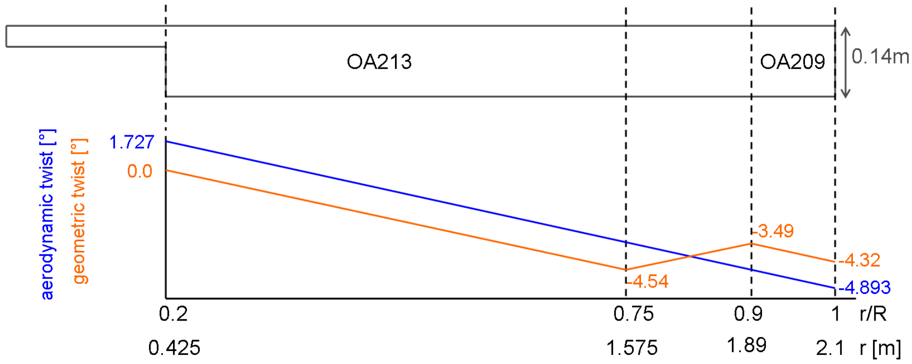

Figure 4.5: Geometry description of 7A blade: twist law and airfoil positioning

In literature, forward flight optimization of the 7A blade was carried out for high-speed performance, at a design point of $\mu = 0.4$ and $\bar{Z} = 12.56$ [71, 79]. However, since the calculations of Chapter 2 showed that the simulation tools used in this study (HOST and *elsA*) do not predict correct trends at high-speed flight conditions, we choose a design point at a somewhat lower forward flight speed. The selected point, characterized by $\mu = 0.3$ and $\bar{Z} = 15$, has been investigated experimentally for the 7A blade. For these experiments, the rotor equilibrium law in use was the Modane law. Measured forward flight performance results at these conditions are given in Table 4.1.

Hover performance measurements of the 7A blade do not exist so that no comparison of either global or local performance can be made.

Table 4.1: Measurements of forward flight performance of 7A blade at $\mu = 0.3$, $\bar{Z} = 15$, $C_{XS} = 0.1$, $\Omega = 1022$ rot/min, Modane law

L/D	8.6147
$\bar{Z}/\bar{C}$	18.64
Rotor power [kW]	55.644

Optimization parameters Variations to the 7A blade are made by varying twist and chord laws. In a first stage, these laws are optimized separately to understand relations between parameters and objectives. Then, both laws are combined within the same optimization to study interaction effects between both families of geometrical parameters. Twist and chord distributions are parameterized by Bézier laws with 6 control points. The design variables are then the radial distribution of these Bézier points and the associated twist or chord values. The radial position of the first and last Bézier point being fixed, we are left with 10 design parameters per geometry law. These laws and parameter limits are illustrated on the left-hand side of Figure 4.6. This parameterization allows for a large variety of radial distributions, as shown in Figure 4.7.

In an attempt to reduce the number of design parameters, a second Bézier parameterization using fixed radial coordinates for the inner Bézier control points is also tested. The right image

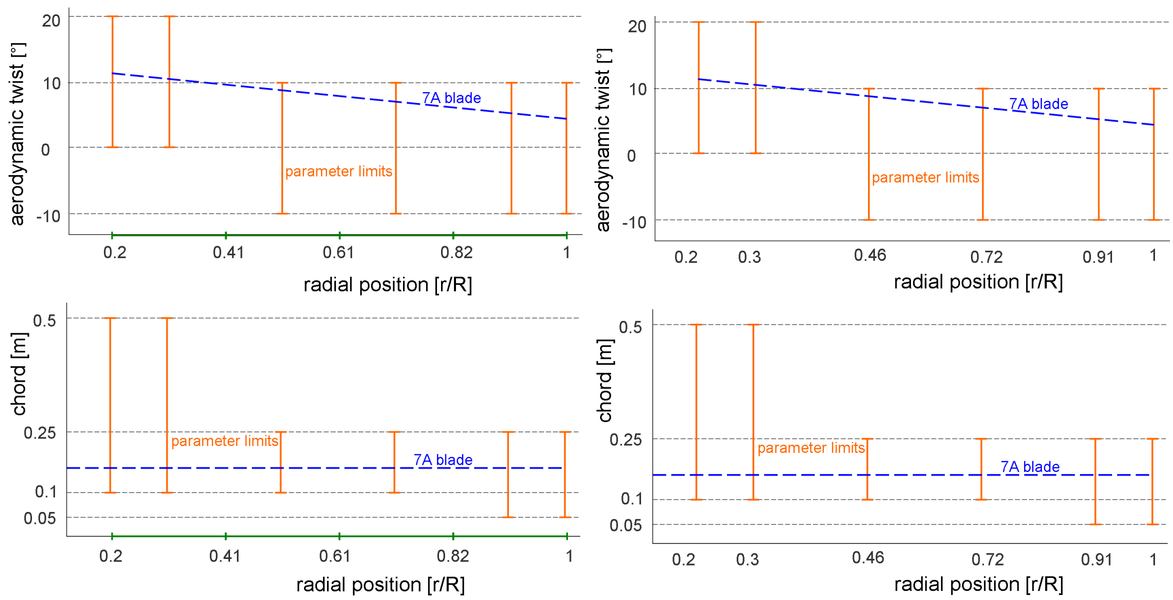

Figure 4.6: Parameter limits for twist (top) and chord (bottom) laws, with (left) and without (right) radial positioning of inner Bézier control points

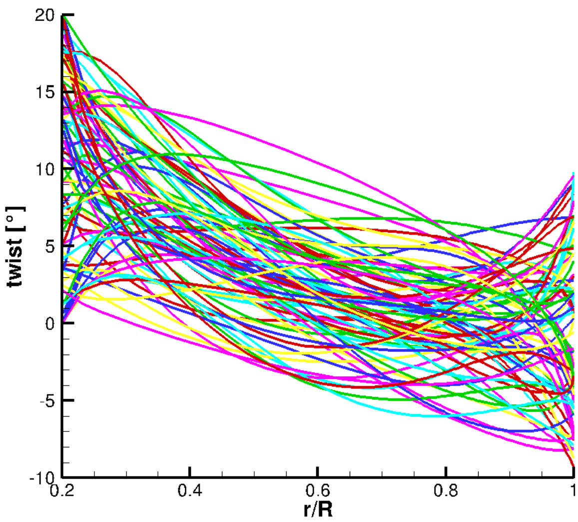

Figure 4.7: Random generation of 80 twist laws using Bézier law with 6 control points

of Figure 4.6 illustrates the main feature of this parameterization that involves only 6 design parameters.

Optimization objectives and constraints Two sets of objectives are tested in HOST-based optimizations to check for influence of this choice on optimization results:

- Maximize F.M. in hover and L/D in forward flight
- Minimize rotor power in hover and in forward flight

Where the F.M. objective simultaneously modifies lift and drag characteristics, rotor power minimization only considers rotor drag. Therefore, lift is constrained to a fixed value in hover to avoid an optimized rotor creating nearly no lift. In forward flight HOST simulations, measurement conditions are used in the computational set-up. In CFD-based optimizations, F.M. may be used for hover simulations, but as earlier shown, drag computations in forward flight are not realistic. Therefore, in forward flight the ratio of lift and torque coefficients $\bar{Z}/\bar{C}$ is maximized for fixed flight conditions.

In chord optimizations, a constraint is added on the Mean Aerodynamic Chord (MAC), which is computed as follows under the assumption of constant local lift coefficient c_l along the blade [83]:

$$\text{MAC} = \frac{\int_0^R cr^2 dr}{\int_0^R r^2 dr} \tag{4.4}$$

This constraint should avoid large differences in blade mass which would seriously affect design of rotor head parts. The 7A blade having a constant chord of 0.14m, the MAC is constrained between 0.13 and 0.15m in optimizations.

HOST simulations All HOST rotor simulations within the optimizations are executed with FiSUW for modelling induced velocity, as earlier selected. Here, respectively 4 harmonic terms and 4 polynomials are used for azimuthal and radial distributions. All simulations assume a rigid blade and default corrections are turned on, as prescribed from Chapter 2.

HOST computed hover performance is presented in Figure 4.8. Maximum F.M. equals 0.808 and is achieved at a collective pitch angle of 13.5°, corresponding to a rotor loading of $\bar{Z} = 21$. Rotor power consumption at this point equals 138.6 kW. In all optimizations, a rotor loading of $\bar{Z} = 21$ is imposed, and collective pitch angle may be altered to find the rotor equilibrium. This would be equivalent to designing a rotor for lifting a specific mass.

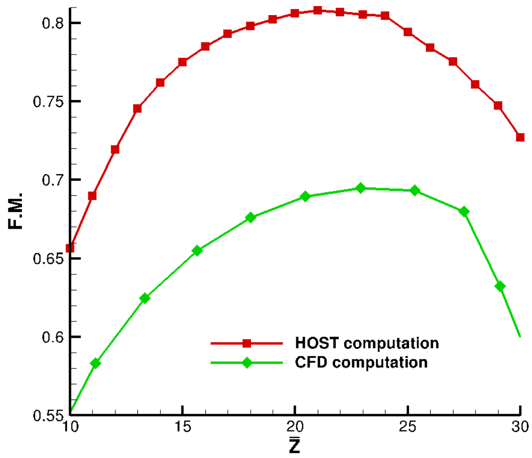

Figure 4.8: Figure of Merit as a function of $\bar{Z}$ as computed by HOST and CFD

HOST computation of forward flight performance of earlier described flight conditions (Table 4.1) equals 7.526 in terms of L/D and power consumption equals 71.28 kW. Figure 4.9 illustrates variations of forward flight speed and $\bar{Z}$ as a function of rotor performance. No discontinuity is seen in these variations, as was the case earlier in Section 2.1.5, so that this design point can be used without any problem.

***elsA* simulations** For CFD simulations, meshes with similar characteristics as medium size meshes of the ORPHEE study (Section 2.2.6) are used. In fact, blade meshes contain 795 201 mesh nodes, hover background mesh blocks total 679 679 nodes and forward flight background

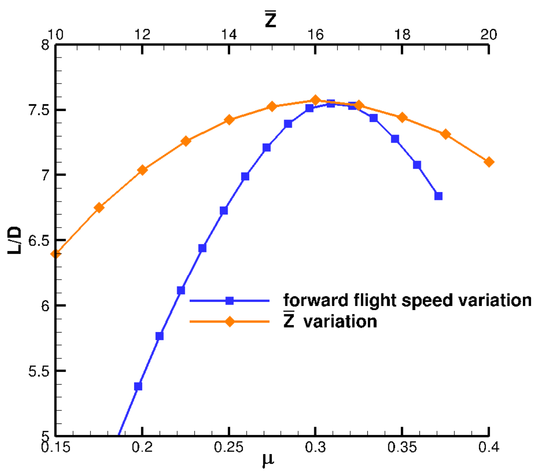

Figure 4.9: L/D as a function of forward flight speed and $\bar{Z}$, as computed by HOST

meshes contain 9 641 775 nodes. Illustrations of hover and forward flight meshes are given in Figures 4.10 and 4.11.

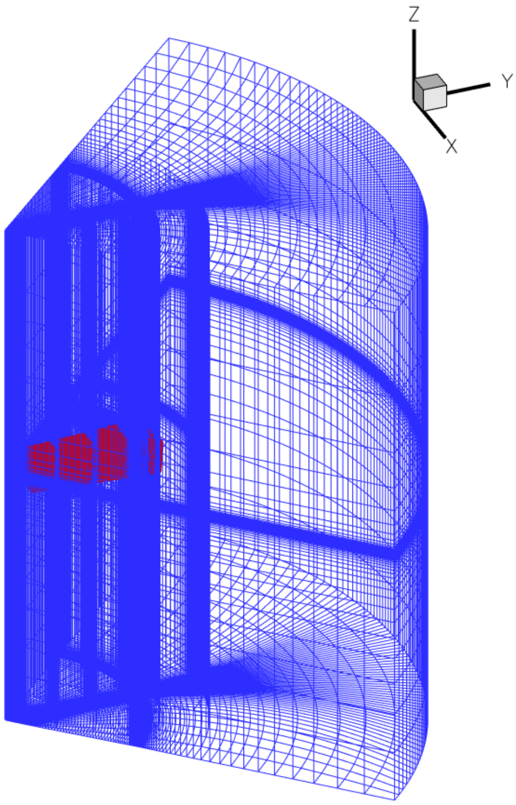

Figure 4.10: Overview of hover mesh of 7A blade

In all computations, earlier selected numerical parameters are used: numerical discretization by the AUSMp scheme and the $k-\omega$ model with SST correction for turbulence modelling.

Reference simulations of the 7A blade in hover and forward flight result in a maximum F.M. of 0.695 (see Figure 4.8) and a CFD computed $\bar{Z}/\bar{C}$ of 21.9.

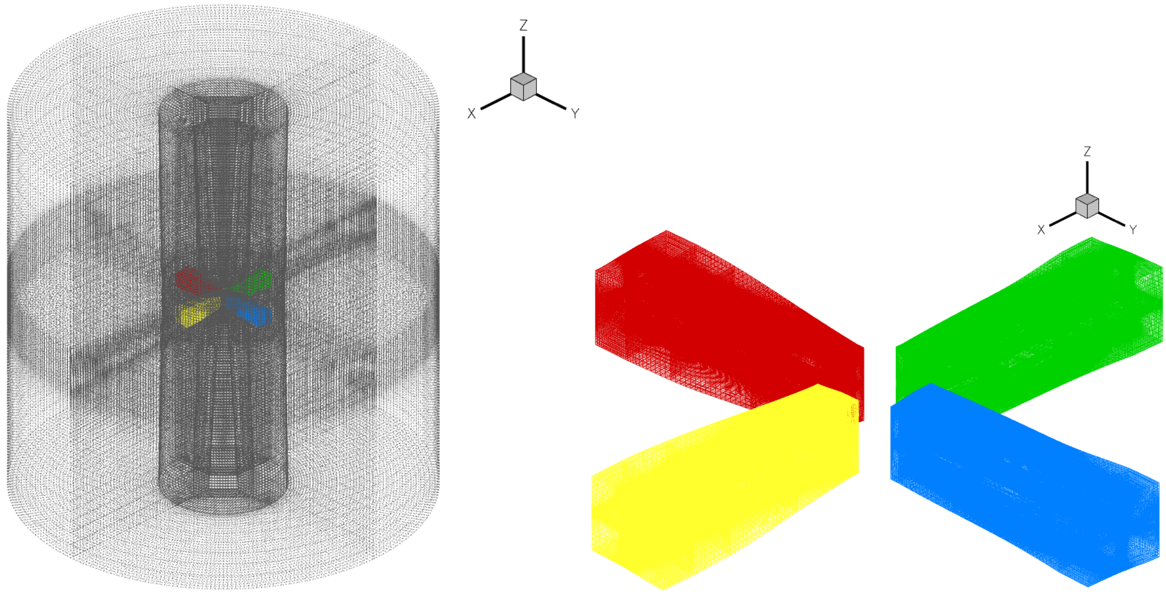

Figure 4.11: Overview of forward flight mesh of 7A rotor: background mesh (left) and blade meshes (right)

4.2.2 Genetic algorithm optimizations

Validation of genetic algorithm optimizations would be too costly for CFD-simulations, so this is done by HOST-based optimizations. In a first step, different two-objective optimizations of twist, chord and combined twist and chord distribution are performed to assess the best choice of optimization objectives. Then, these objectives are used to evaluate the influence of adding or removing parameters on radial positioning of Bézier control points. These first tests are performed with large optimization sets of 80 individuals and 20 generations to insure a good convergence of the genetic algorithm. Finally, the best objectives and parameterization are used for single- and multi-objective optimizations of combined twist and chord laws. Optimization convergence is evaluated to give estimates on the number of full cost function evaluations required for finding Pareto Optimal solutions.

Wherever possible, Pareto Optimal Fronts are compared via the performance metrics on spread and distribution presented in Equations 3.7 and 3.8. For the spread metric, as a default a σ of 0.5 is chosen. The metric on convergence cannot be used here since no theoretical Pareto Optimal Front exists. A quick analysis of optimization convergence is presented in Figure 4.12: criteria remain almost unchanged between generations 15 and 20. As this optimization uses 20 design variables, it is expected that optimizations of twist or chord law only, involving a lower dimensional space, could converge within a smaller number of generations. A more complete study on the number of evaluations required for optimization convergence will follow once objectives and parameterization are fixed.

Genetic algorithms use probabilities to advance the optimization and find better individuals. In fact, in all current optimizations, a crossover probability of 90% and a mutation probability of 10% are used. In addition, a certain seed value is given for random initialization of the first generation. The influence of the initial seed is tested on 10 identical optimizations as shown in Figure 4.13. The number of individuals in the Pareto Optimal Front (POF) ranges from 22 to 42 and performance indicators differ as well: the spread metric $\mathbf{M_3}$ ranges from 12.4 to 22.4 and the distribution metric $\mathbf{M_2}$ goes from 0.89 to 1.23. Visual inspection may easily confirm the large range of values of the spread metric. This dispersion is inherent to genetic algorithms. In the following, typically only one optimization will be carried out as will be the case in practical use of the optimization loop. In results analysis, this seed probability

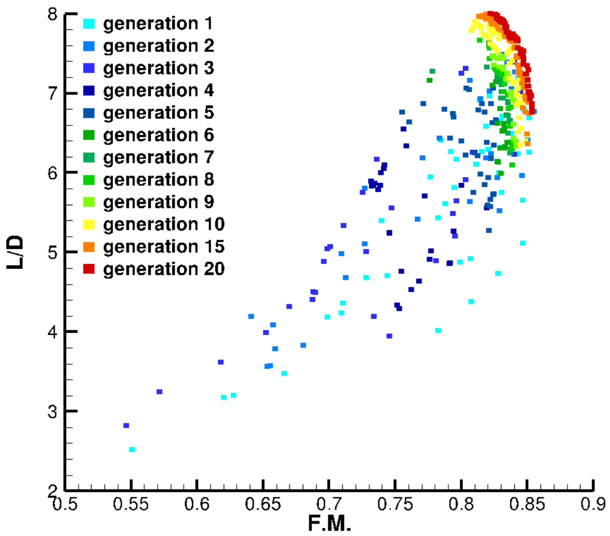

Figure 4.12: Optimization convergence of combined twist & chord optimization (maximize F.M. and L/D, 20 parameters

should be kept in mind to avoid concluding on differences between optimizations which could simply be due to different initializations and probabilities during the optimization.

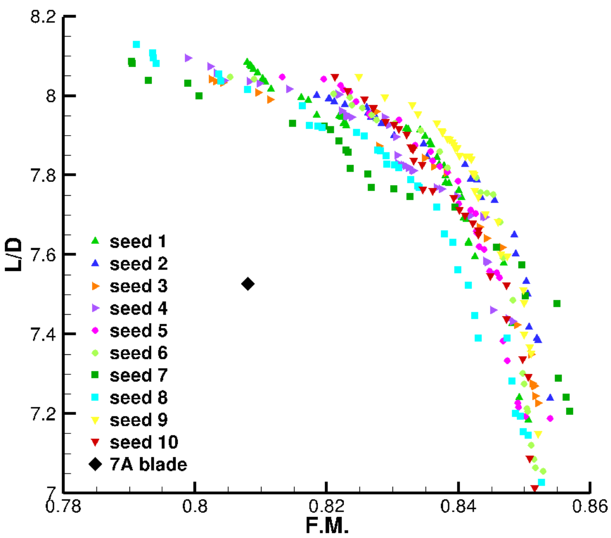

Figure 4.13: Pareto Optimal Front solutions of combined twist & chord optimizations with 20 different seed values (maximize F.M. and L/D, 20 parameters)

Influence of objectives

Two sets of objectives were tested to assess its influence on optimization outcome:

- Maximize F.M. in hover and L/D in forward flight
- Minimize rotor power in hover and in forward flight

As a first result, the number of individuals contained in the Pareto Optimal Front are presented in Table 4.2 for the different optimization runs. For all parameter sets, minimization of rotor power leads to a smaller Optimal Set of solutions compared to objectives on F.M.

and L/D. This might be due to the fact that F.M.-L/D objectives both can alter lift- and drag-distributions to improve rotor performance, whereas objectives on rotor power are only related to drag reduction.

Another difference in these objective sets is the order of magnitude, related to sensitivity of the optimization. As rotor power is typically 2 to 3 orders of magnitude larger than F.M. and L/D, slight changes in rotor blade geometry may result in noticeable rotor power gains. This may be the cause for the far smaller number of individuals in the Pareto Optimal Front of rotor power optimizations.

Table 4.2: Number of individuals in Pareto Optimal Front of twist, chord, combined twist & chord optimizations with two objective sets

	maximize F.M.-L/D	minimize rotor power
twist optimization	51	45
chord optimization	48	9
twist and chord optimization	36	5

Pareto Optimal Fronts of twist, chord and combined twist & chord optimizations with both objective types are recomputed in terms of both objective sets and presented in Figure 4.14. The left image, showing all Pareto Optimal Fronts in terms of F.M.-L/D, illustrates clearly that all optimizations results represent an improvement over the baseline for these performance variables. Optimizations with same parameters but different objective functions are positioned closely together, which means that similar gains are obtained with both choices of the objectives. Only for chord optimizations, the F.M.-L/D optimization achieves better convergence of the POF. A difference between both objective sets is the extent of POF, which is considerably larger for optimizations on F.M.-L/D.

When expressing Pareto Set solutions of all optimizations in terms of rotor power, it is noticed that not all solutions are Pareto Optimal anymore; even more, several solutions of F.M.-L/D chord and twist & chord optimizations have a lower performance than the reference blade. This discrepancy between objective sets may be explained as follows: as in all cases a rotor trim of $\bar{Z} = 21$ is required, F.M. and L/D are not function of lift but of drag only. Yet, rotor power is a function of rotor torque. Drag and power consumption are tightly related over most of the rotor disk: torque results of an integration of rotation-opposing forces over the rotor disk. In hover, drag and torque are therefore equivalent measures. However, in forward flight, a difference exists between rotor torque and rotor drag in the inversion circle (see Section 1.1.3). This difference is due to an altered coordinate system, as explained via Figure 4.15: within the inversion circle, drag is directed in the forward moving direction of the rotor. In the rotor reference frame, this drag thus helps in advancing the rotor. Yet, in the local coordinate system, drag in the inversion circle is opposed to the rotation direction and increases torque. In short, whereas drag over the reversed flow sections adds to rotor torque, this same drag lowers rotor drag. In this zone, the results of optimizations to minimize rotor drag (F.M. and L/D) or rotor torque (rotor power) are not the same. This explains why rotor blades designed for minimizing rotor power also work well in terms of rotor drag, thus L/D, whereas blades optimized for L/D do not necessarily perform well expressed in terms of rotor power.

The effect of difference between rotor drag and torque in the inversion circle is mainly seen for chord optimizations. For twist, both objective sets of twist optimizations have similar POFs. Indeed, no matter the twist angle at blade sections within the inversion circle, local drag force will not differ significantly as flow is separated anyway. However, chord length directly affects the local drag force. This explains why only optimizations with chord design variables are sensitive to the difference between rotor torque and rotor drag.

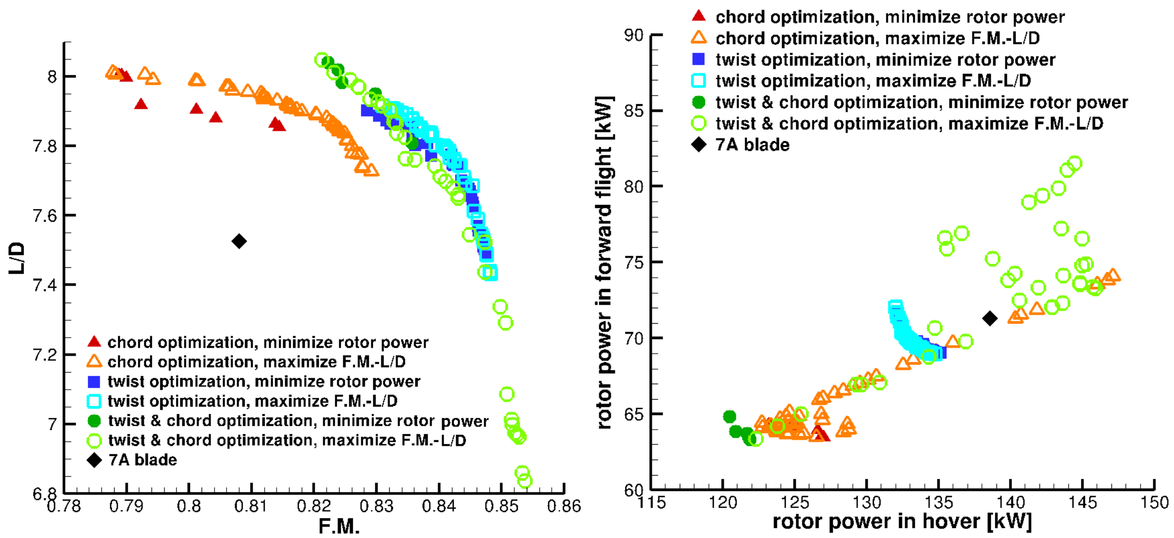

Figure 4.14: Comparison of POF of objective sets (F.M. - L/D vs. rotor power) optimizations HOST-recomputed in terms of F.M.-L/D (left) and in terms of rotor power (right)

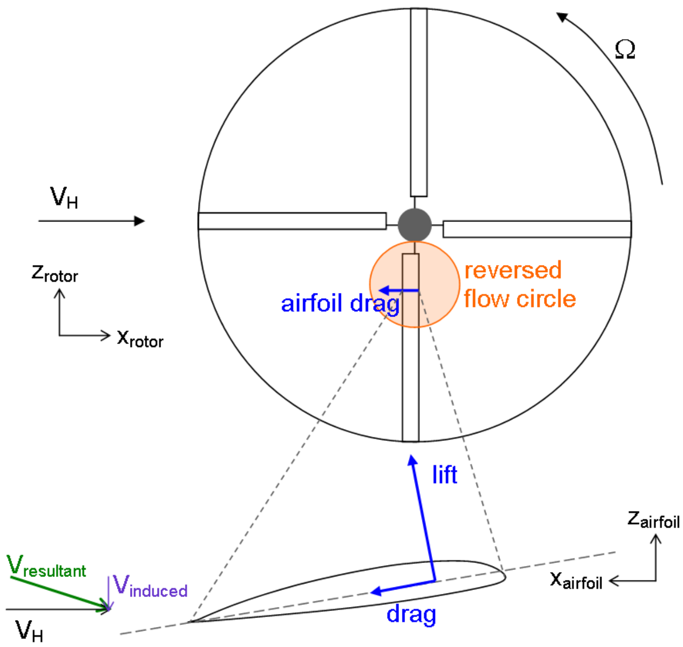

Figure 4.15: Difference in rotor and airfoil coordinate system within inversion circle

Figures 4.16 and 4.17 illustrate all twist and chord laws corresponding to Pareto Optimal solutions. Twist law optimizations result in blade designs that are comparable, no matter the optimization objective. This was expected since the corresponding POF are located at approximately the same position for both objective spaces. The lateral shift of twist law solutions is due to different collective pitch angles to obtain the requested $\bar{Z}$ of 21. Chord optimizations support the hypothesis of difference in drag consideration in the inversion circle by the two objectives: for rotor power minimization, mainly solutions with reduced chord sections at the blade root are found.

In conclusion, optimizations with objectives on minimizing rotor power or maximizing rotor aerodynamic performance result in similar solutions for twist laws, whereas divergences

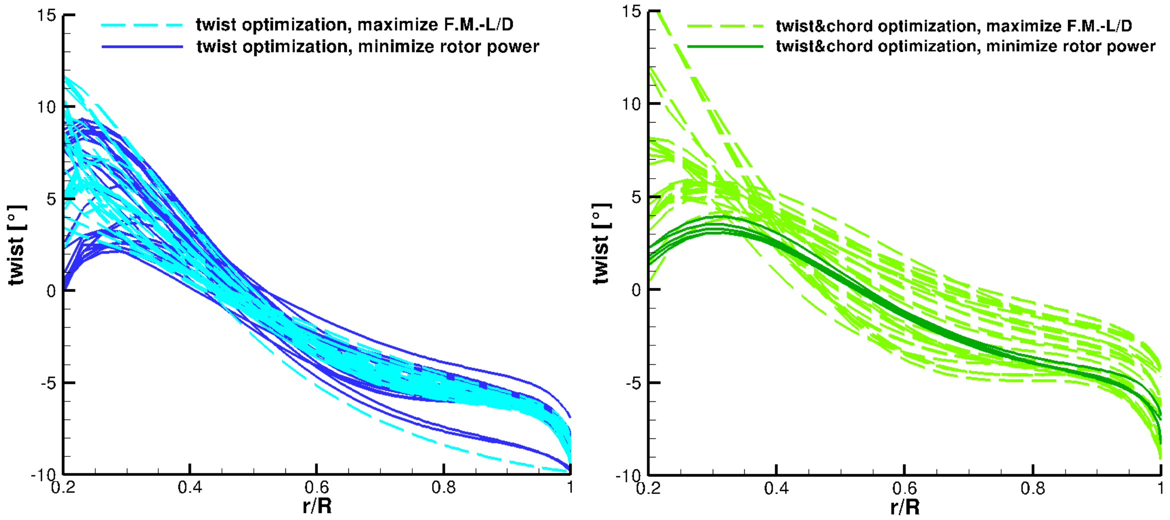

Figure 4.16: Pareto Set comparison of twist laws of both objective sets (F.M. - L/D vs. rotor power) of twist optimizations (left) and twist & chord optimizations (right)

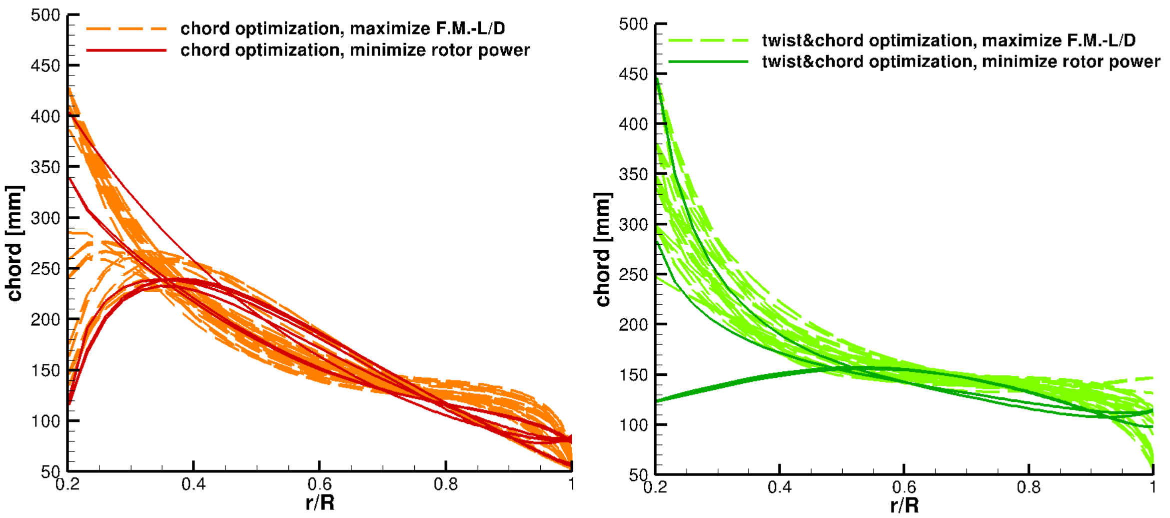

Figure 4.17: Pareto Set comparison of chord laws of both objective sets (F.M. - L/D vs. rotor power) of chord optimizations (left) and twist & chord optimizations (right)

are observed for chord law optimizations due to different treatment of drag in the inversion circle. More extended and better distributed Pareto Sets for F.M.-L/D optimizations make this objective set more interesting for analysis. These objectives are selected here for continuing optimization tests. Yet, as described in Section 2.2.6, forward flight CFD simulations cannot be classified as a function of L/D but need to be optimized for $\bar{C}$ which is related to rotor power.

As a final remark, these conclusions hold for isolated rotor simulations with HOST. When accounting for fuselage drag and interference, different rotor trims may be found, possibly affecting rotor performance. Additional studies are required for assessing this influence.

Influence of the parameterization

Surrogate model generation by data fit models is considered appropriate for optimization problems with up to 30-50 design variables [2]. For the current design problem (maximum 20 parameters for combined twist & chord laws) this value is not yet achieved. But, additional geometry descriptions of for example sweep law and airfoil positioning may approach this limit. Another potential disadvantage of larger parameter sets is that response surface generation takes more time. Finally, relations between objectives and parameters are more complicated, making analysis more difficult. For these reasons, it is of interest to reduce the number of design variables. To maintain flexibility of geometry law selection, Bézier laws will still be used but radial positioning of control points will no longer be a design variable, as illustrated on the right-hand side of Figure 4.6. Optimizations are executed as before with objectives on F.M.-L/D using this new parameterization. Resulting POFs are presented in Figure 4.18. Visual inspection of these POFs is confirmed by performance metrics $\mathbf{M}_2$ and $\mathbf{M}_3$ on POF distribution and spread given in Table 4.3. A higher value of $\mathbf{M}_2$ indicates that less points are located within a zone of size $\sigma = 0.5$, resulting in a better distribution along the POF. $\mathbf{M}_3$ has a larger value for a POF with a larger spread between outer points. Both image and table show that spread is increased when removing parameters on radial positioning of Bézier control points for chord and combined twist & chord optimizations. Distribution along the POF is improved for separate twist and chord optimizations without radial positioning. Finally, POF are located at comparable positions in the objective space. In conclusion, similar Pareto Optimal results are found with both parameterizations, even if slight differences between fronts are observed. This exercise also illustrates difficulty in comparing Pareto Optimal Fronts, due to unequal positioning as demonstrated by disparate results for performance metrics.

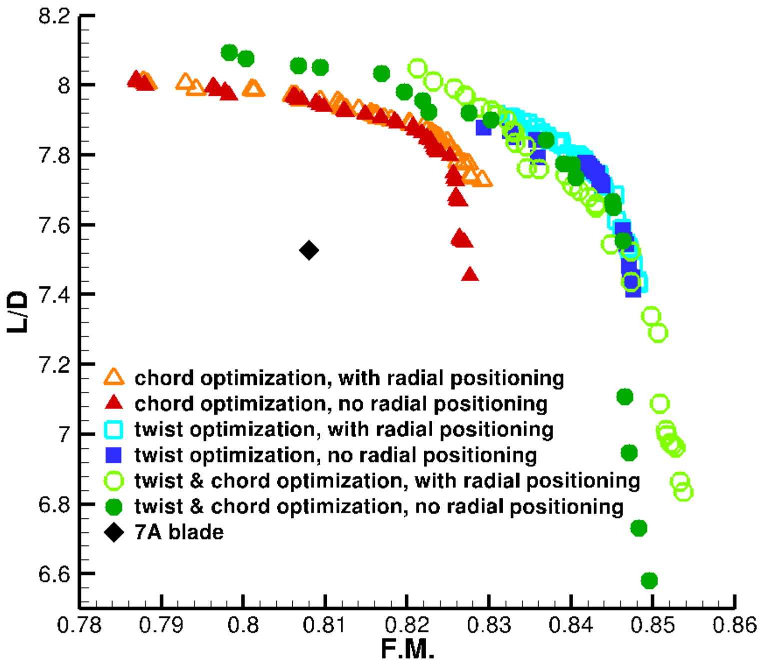

Figure 4.18: Comparison of POF individuals of F.M.-L/D optimizations with and without radial positioning of Bézier control points

Besides comparing Pareto Solutions in the objective space, assessment of blade geometries corresponding to these optimal individuals allows for studying the effect of parameterization. Figures 4.19 and 4.20 show twist and chord laws as obtained by optimizations with and without parameters on radial positioning. A first conclusion is that similar geometry laws are found for both parameterizations, except for chord laws of the combined twist & chord optimization, where different solutions are found. These individuals appear to correspond to the POF-extension in forward flight performance. A more important conclusion is that, in all cases, no visual difference is observed for blade geometry laws with either of the two parameterizations.

Table 4.3: Number of individuals in and performance metrics of Pareto Optimal Front of optimizations with and without parameters on radial positioning of Bézier control points

	parameters on radial positioning	no. individuals in POF	$\mathbf{M}_2$	$\mathbf{M}_3$
twist	with	50	13.55	0.7066
	without	34	12.303	0.6943
chord	with	48	1.702	0.5698
	without	80	20.962	0.7760
twist & chord	with	36	20.859	1.1150
	without	7	5.667	2.1551

This implies that any blade geometry can be generated with either parameterization and observed differences are only due to altered evolutions of genetic optimizations.

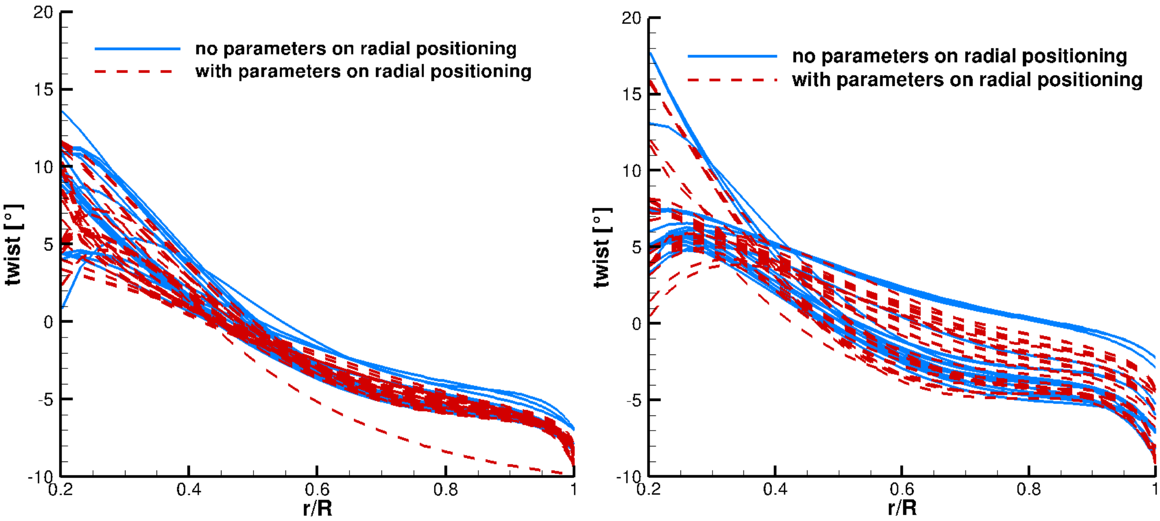

Figure 4.19: Pareto Set comparison of twist laws with and without parameters on radial positioning of inner Bézier control points of F.M.-L/D twist optimizations (left) and twist & chord optimizations (right)

In conclusion, minor differences are observed in the objective and parameter space for parameterizations using or not design variables on radial positioning of Bézier control points. These differences are not expected to be due to the parameterization but instead probably come from different advances towards the Pareto Optimal Front. As reducing the number of parameters is interesting for genetic algorithm optimizations to increase optimization convergence and even more when using surrogate models, the reduced parameterization will be used from this point onwards.

Single- and two-objective optimizations

Both single- and multi-objective optimizations are performed using F.M. and L/D as objective functions and by fixing the radial positions of Bézier control points, which leaves 6 parameters on twist and chord only and 12 parameters for the simultaneous twist and chord optimization. Hereafter, we investigate the number of generations typically required to achieve satisfactory convergence for the problem of interest, as well as the role of the number of individuals taken into account by the genetic algorithm at a given generation. Ref. [136] points out that a too small population may lead to premature convergence to suboptimal solutions, due to a

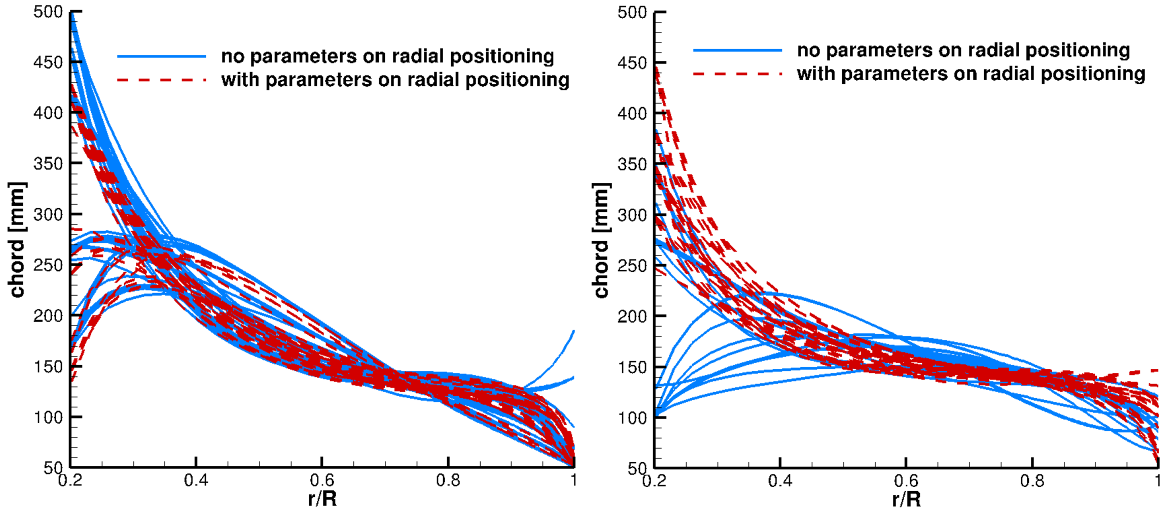

Figure 4.20: Pareto Set comparison of chord laws with and without parameters on radial positioning of inner Bézier control points of F.M.-L/D chord optimizations (left) and twist & chord optimizations (right)

lack of diversity. On the other hand, for a given number of function evaluations, too large populations lead to slow convergence to optimal solutions. Single-objective optimizations are performed using 40 individuals and 20 generations. First, we optimize for twist and chord laws separately. Then, a combined twist & chord optimization is carried out.

Twist optimization Pareto Optimal Fronts of multi-objective twist optimizations are illustrated in Figure 4.21. In the same figure, the results of single-objective optimizations in hover and in forward flight only are also reported for comparison, as well as the performance of the baseline 7A blade. Only hover performance is shown for the hover optimized blade as HOST failed to compute forward flight performance: no rotor equilibrium is found for this blade with high twist gradient.

Convergence of each of the multi-objective optimizations is demonstrated by inspection of Figures 4.22 to 4.24. For all optimizations, blade geometries improving rotor performance over the reference blade are found from the 3$^{\text{rd}}$ or 4$^{\text{th}}$ generation on. The numerical POF is almost converged starting from the 15$^{\text{th}}$ generation. The optimization with 40 generations of 40 individuals is completely converged in the 30$^{\text{th}}$ generation. Given the statistical dispersion inherent to genetic algorithms, it is difficult to conclude on requirements on numbers of individuals and generations needed for optimization convergence. Still, increasing the number of generations or individuals increases spread and distribution.

Figure 4.25 presents blade geometries of optimized blades. Even if slight differences may be observed for two-objective optimizations, Pareto Set twist laws are alike, especially in the outboard part of the blade. Especially the hover optimized blade has a high twist gradient, and its radial distribution closely approaches the theoretically optimal solution that was described in Section 1.2.2, namely a hyperbolic twist law. This is an important validation of the optimization loop.

Analyzing how the flow field changes after optimization is difficult for multi-objective optimizations, due to the large amount of POF solutions, but single-objective optimizations can be easily compared to the reference blade. F.M. is directly related to the rotor power consumption, which consists of profile and induced power [83]. Profile power may be assessed by the F.M.$_{\text{airfoil}}$, computed as $\sqrt{(C_l^3)/(C_d^2)}$ (see Section 1.2.1), which gives a measure of aerodynamic performance of local blade sections. Induced power is related to the induced

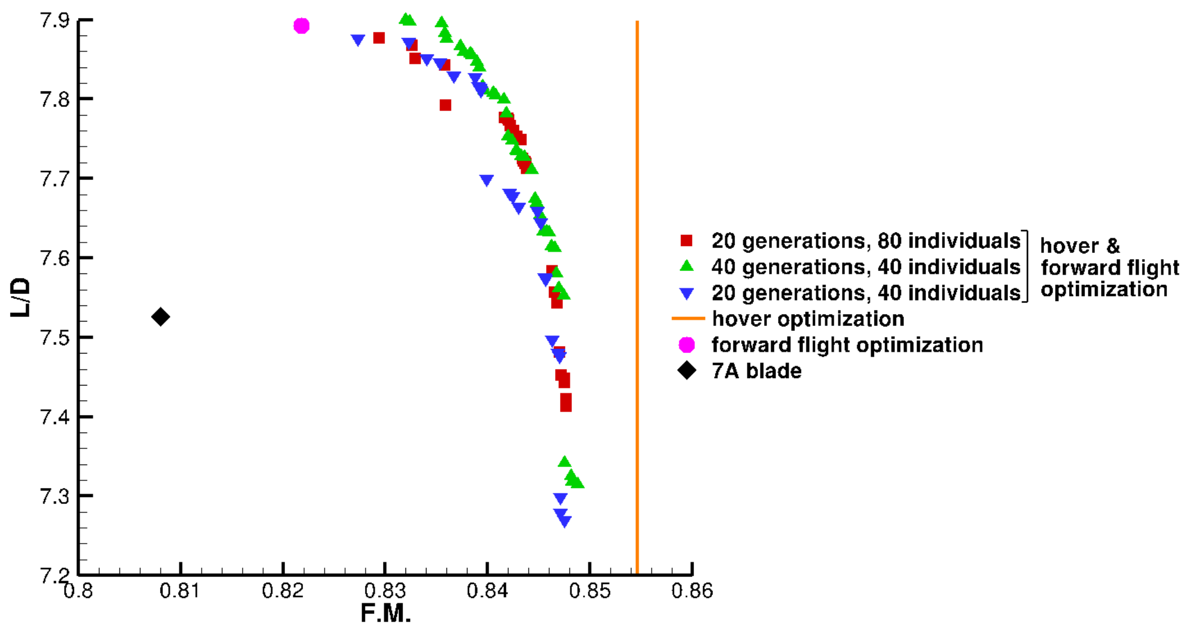

Figure 4.21: Pareto Optimal Front of twist law multi-objective optimizations with different combinations of generation and individual numbers, compared to single-objective optimizations and the 7A blade

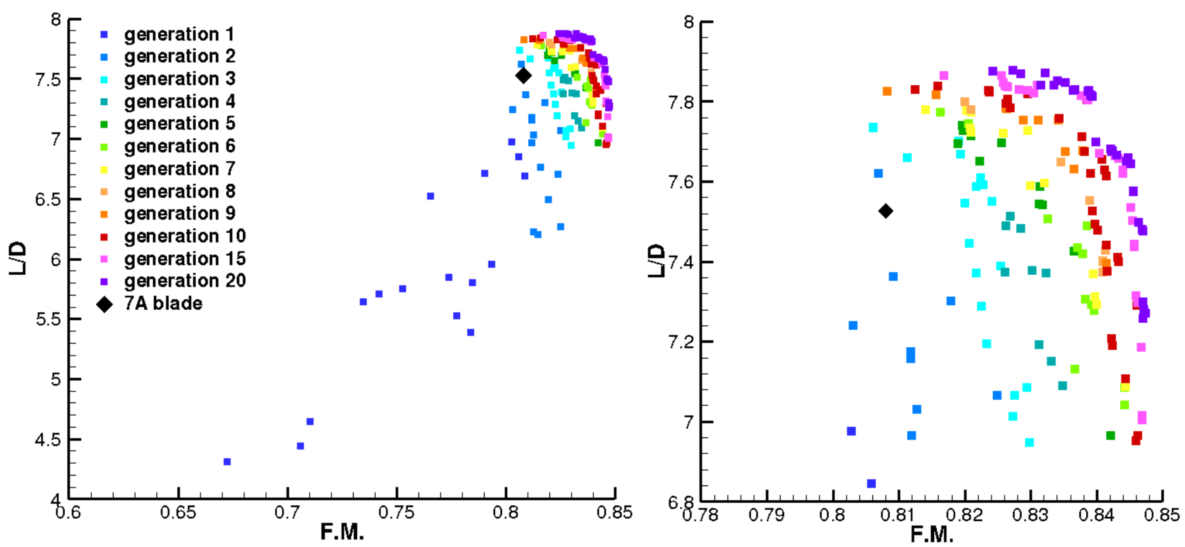

Figure 4.22: Optimization convergence of twist optimization with 20 generations of 40 individuals, overview (left) and zoom (right)

velocity distribution along the blade. Figure 4.26 illustrates that F.M.$_{\mathrm{airfoil}}$ distribution alters only slightly by optimization. No significant difference in profile power is expected since airfoil shape is unchanged. However, lower induced power is expected for the optimized blade: its induced velocity distribution better approaches the theoretically optimal constant distribution [145].

In forward flight, the L/D$_{\mathrm{airfoil}}$ may be analyzed for assessing local airfoil performance. Rotor performance improvement may also be seen in terms of an increase in lift force (expressed locally over a rotor disk by $C_l M^2$), a decrease of rotor power consumption (expressed in terms of $C_d M^3$) and an increase of the ratio of these two ($C_l M^2/C_d M^3$). Local Mach numbers are used in these variables. Improvements in these parameters achieved for the twist-optimized

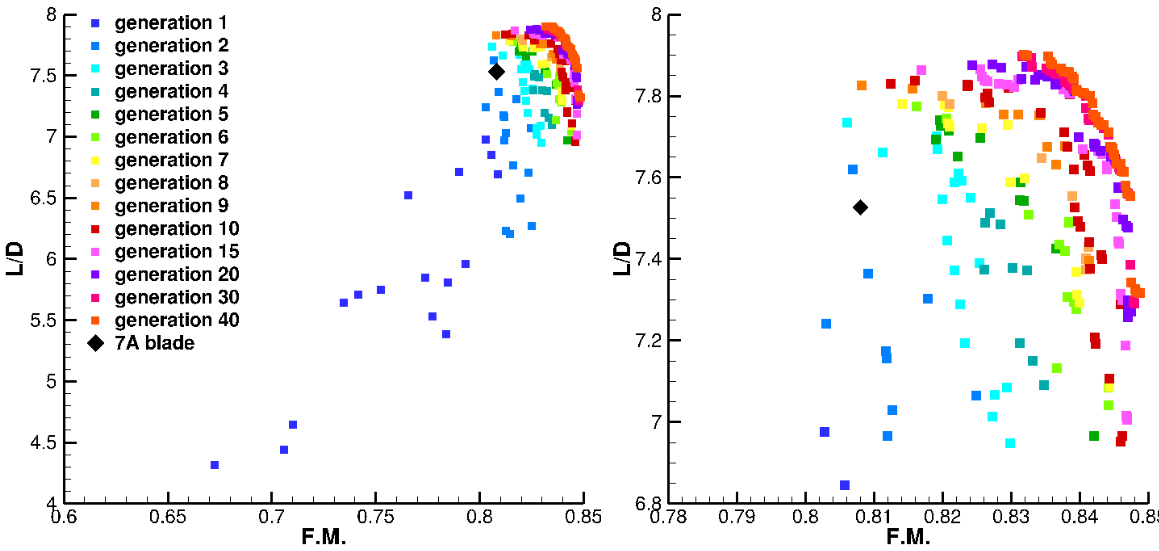

Figure 4.23: Optimization convergence of twist optimization with 40 generations of 40 individuals, overview (left) and zoom (right)

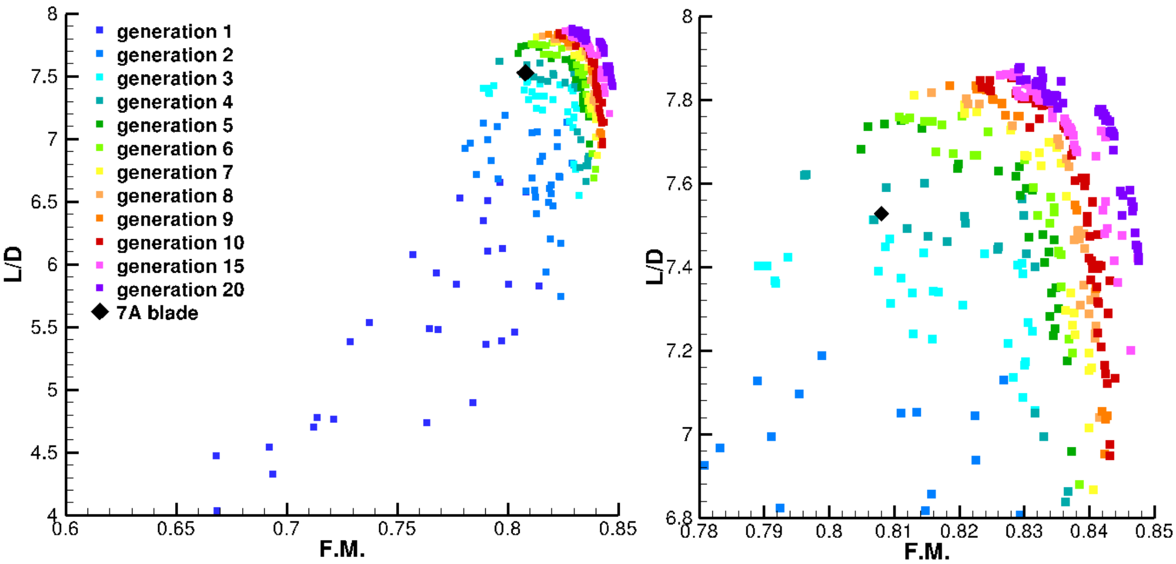

Figure 4.24: Optimization convergence of twist optimization with 20 generations of 80 individuals, overview (left) and zoom (right)

blade in forward flight over the baseline 7A blade are shown in Figure 4.27. Positive values reflect rotor performance improvement for L/D$_{\mathrm{airfoil}}$, $C_l M^2$ and $C_d M^3$. Note however that a positive value of $C_d M^3$ means that the optimized blade has a locally higher rotor power consumption than the reference blade. In this case, inspection of the $C_d M^3$ figure indicates that no significant difference in rotor power consumption is expected. Indeed, rotor power computed by HOST is equal to 69 kW for the optimized blade and to 71 kW for the reference blade. On the optimized blade, extra lift is generated over the inboard part of the advancing blade, where twist of the optimized blade is greater than that of the baseline. This is also the zone where the ratio of rotor lift over rotor power consumption shows a significant improvement of rotor performance.

In conclusion, improved rotor performance by forward flight twist law optimization is

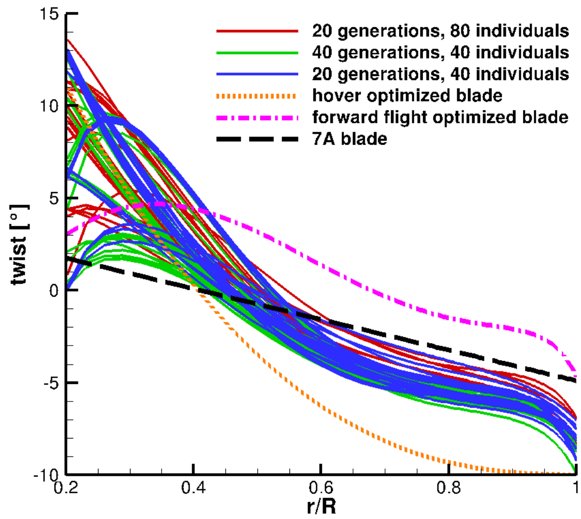

Figure 4.25: Blade geometries of various twist optimizations

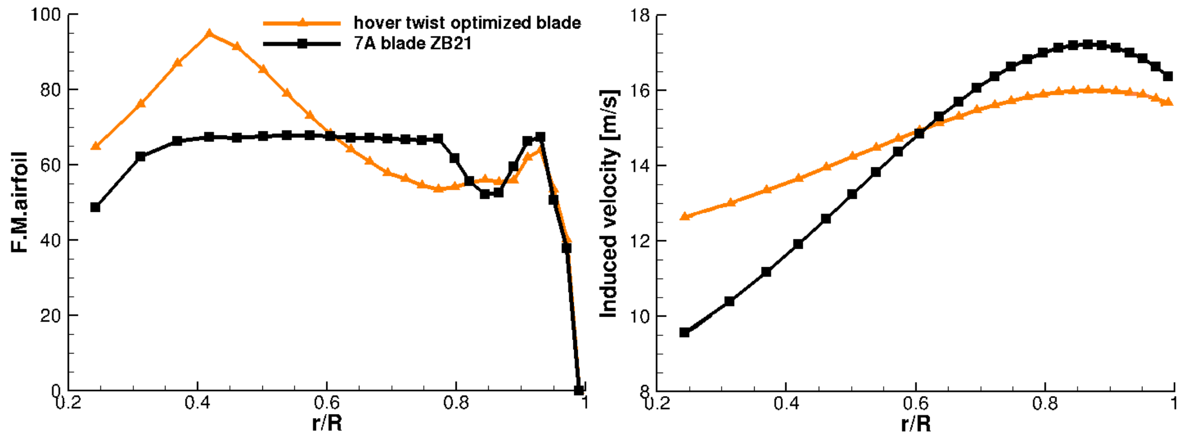

Figure 4.26: Comparison of local F.M.$_{\text{airfoil}}$ and induced velocity along the blade for the hover twist optimized and 7A blades (HOST computations)

related to an increase in twist angle in the inboard part of the blade leading to increased lift in this zone of advancing blades. Local consumed rotor power is not significantly affected by optimization.

Chord optimization Figure 4.28 shows Pareto Optimal Fronts of three multi-objective and two single-objective optimizations. No visual difference in spread or distribution is observed between the three multi-objective optimizations, only convergence is not completely achieved when the optimization is stopped at 20 generations for the population of 40 individuals. As these optimizations are constrained on upper and lower bounds of Mean Aerodynamic Chord (MAC), the optimization algorithm needs to understand relations between parameters and constraint violation. In all optimizations, the first generation contains only 5 to 10 individuals that do not violate the constraints. In total 60 to 70% of all tested blade geometries obey the MAC constraints, making them viable for the optimization. Exact numbers are given in Table 4.4. Including constraints in an optimization thus means that a significant number of generated blade geometries are not considered in the optimization.

Pareto Set chord laws are illustrated in Figure 4.29. Since POF solutions are similar for all

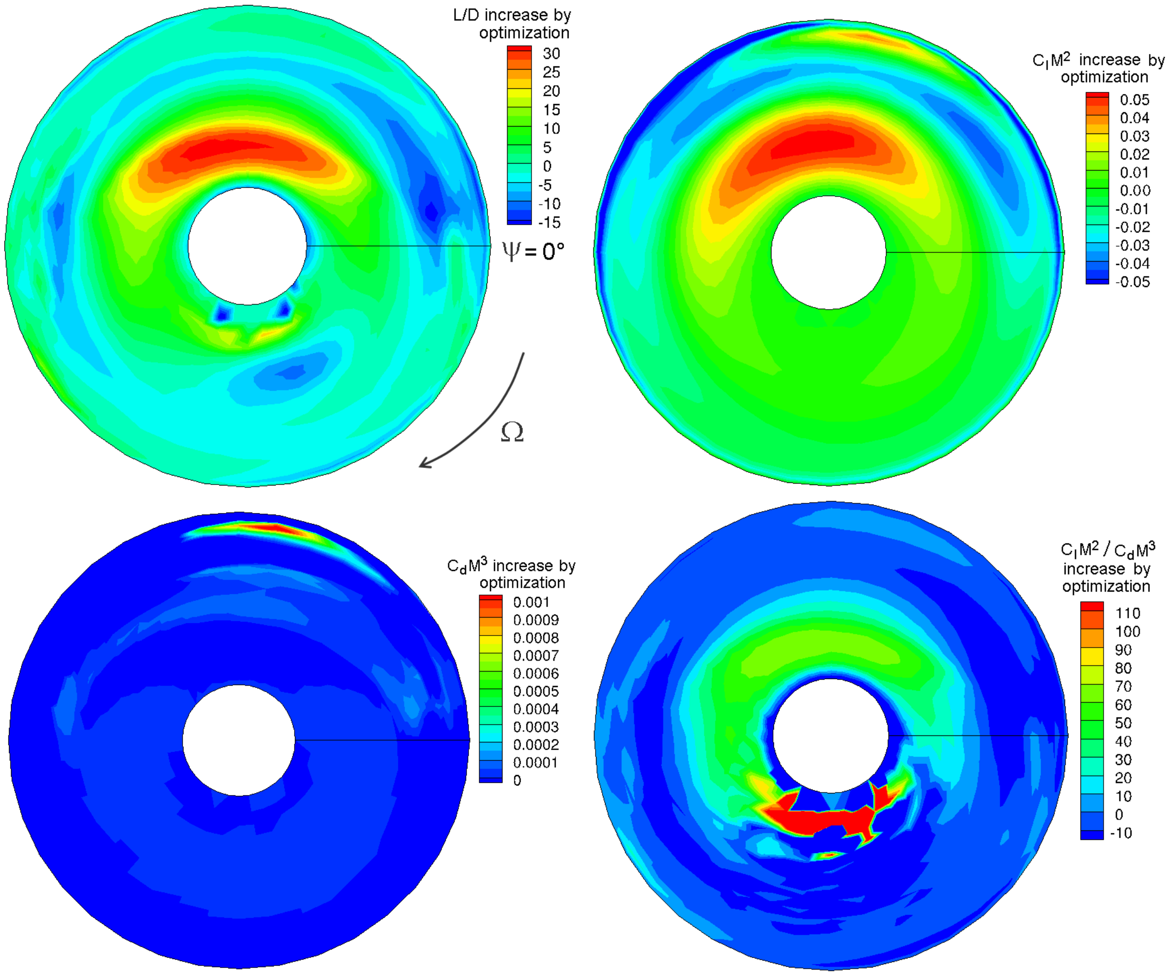

Figure 4.27: Gain of forward flight twist optimized blade with respect to 7A blade in terms of local rotor performance quantities over the rotor disk (HOST computations)

multi-objective optimizations, only the results obtained by using a population of 80 individuals over 20 generations is displayed here. Solutions that tend to maximize rotor performance in hover have a chord law that is close to the theoretically optimal solution having a hyperbolic shape, as described in Section 1.2.3 and [83]. The validity of the optimization loop is supported by correspondence of optimized chord law and theoretically expected solution, just as for the twist optimization. For improving forward flight performance, chord at the blade tip is reduced as much as possible. Indeed, this solution could have been expected from Figure 1.18, which shows that in forward flight the largest power consumption is due to outer blade sections. Thus, optimization tends to reduce chord in the outer part of the blade, even if a chord increase in the inboard part is required to obey the MAC constraint.

Combined twist and chord optimizations Combining parameterizations for twist and chord laws into one optimization allows generating a larger variety of blade geometries. Figure 4.30 shows POFs for this series of optimizations. As for the hover twist optimization, HOST simulation in forward flight conditions of the hover optimized blade did not succeed due to its high twist gradient. Again, both single-objective optimizations are located at opposite extremes of the two-objective Pareto Optimal Fronts. As before, the effect of different choices for the number of individuals and the total number of generations is investigated. Increasing the number of individuals helps finding a larger range of blade geometries. Figure 4.31 confirms

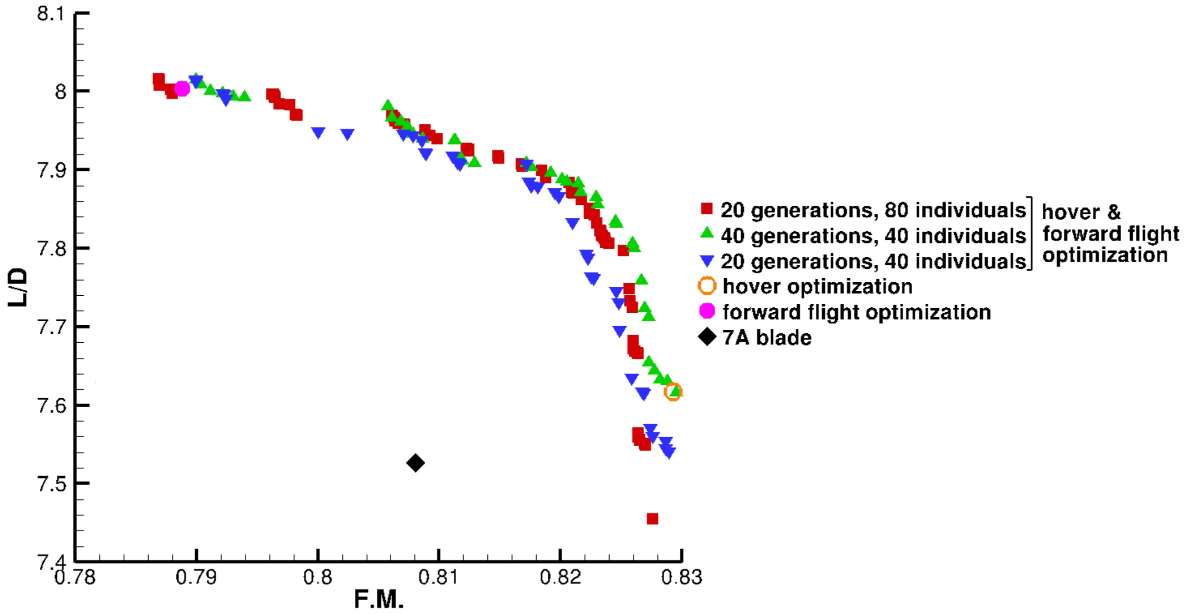

Figure 4.28: Pareto Optimal Front of chord law multi-objective optimizations with different combinations of generation and individual numbers, compared to single-objective optimizations and the 7A blade

Table 4.4: Number of generated blade geometries not violating the MAC constraint

		chord optimization	twist & chord optimization
2 objectives	80 ind, 20 gen	964	1014
	40 ind, 40 gen	1015	1014
	40 ind, 20 gen	479	501
1 objective	hover	559	573
	forward flight	558	537

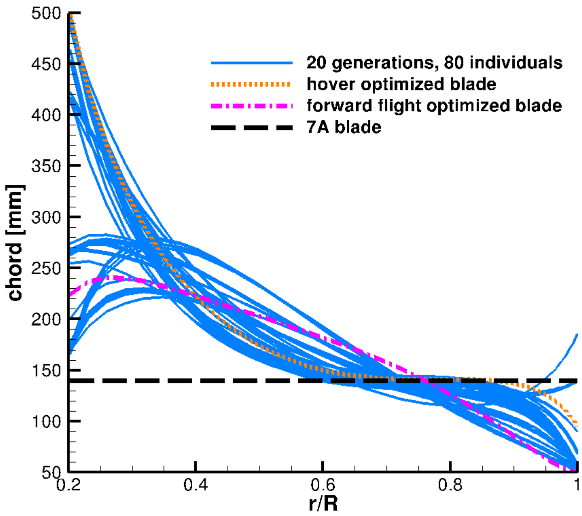

Figure 4.29: Blade geometries of various chord optimizations

this as the optimization of 80 individuals exhibits a large variety of geometry laws, whereas the optimization of 40 generations has converged to a limited set of solutions.

Nearly identical geometry laws are found for single-objective optimizations for a single-geometry law and the combined twist & chord optimization. Chord is always reduced at the blade tip, and often increased in the inboard part of the blade, especially for hover preferred solutions. Twist laws obtained from the combined twist & chord optimization differ from those found by the twist optimization. Whereas the twist gradient of most optimized blades is between 15 and 20°/R for twist optimizations, for the combined twist and chord optimization this gradient is close to 10°/R. Interaction effects between twist and chord appear to be non-negligible in terms of obtained blade geometries.

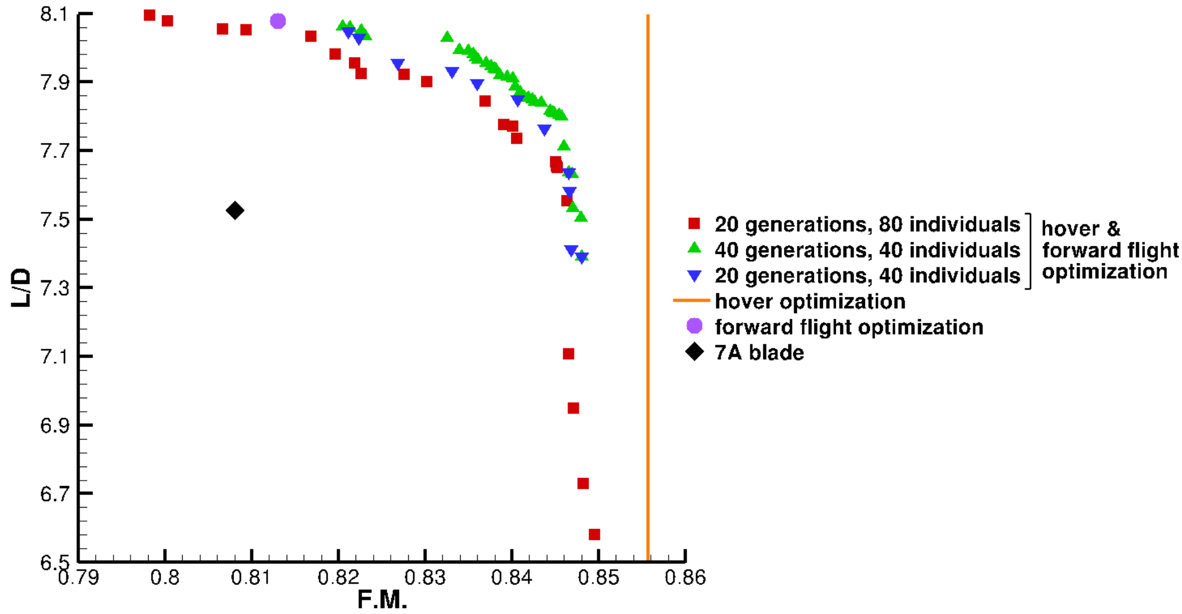

Figure 4.30: Pareto Optimal Front of combined twist & chord laws multi-objective optimizations with different combinations of generation and individual numbers, compared to single-objective optimizations and the 7A blade

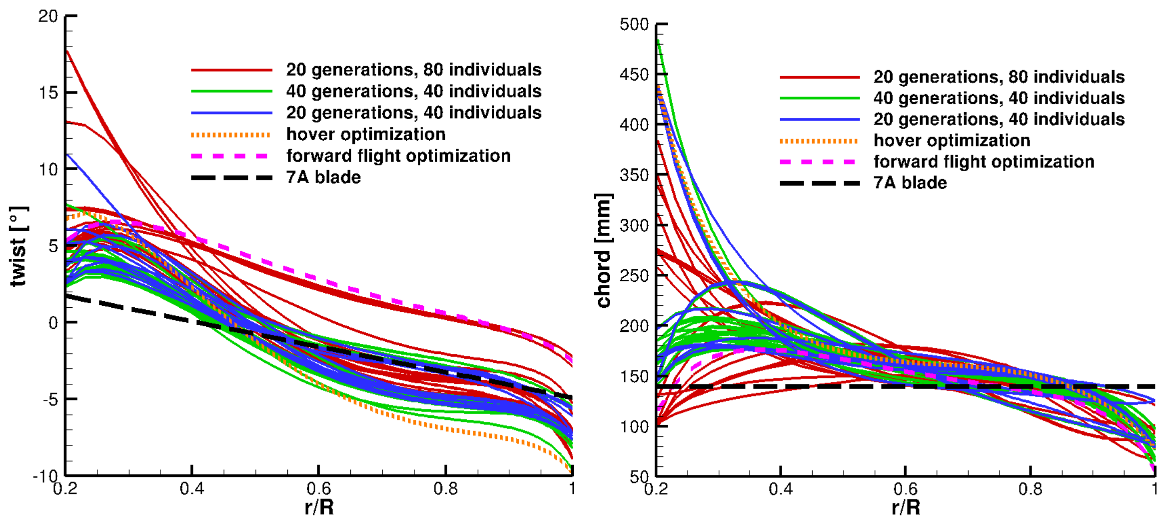

Figure 4.31: Blade geometries of various twist & chord optimizations: twist laws (left) and chord laws (right)

F.M.$_{\text{airfoil}}$ and induced velocity distributions of the hover optimized blade are compared to the 7A blade in Figure 4.32. It seems that the increase in F.M. is related to reductions of both profile power and induced power. The small reduction of F.M.$_{\text{airfoil}}$ near 0.7R is not expected to counter the beneficial effects of the inboard part, so that profile power is reduced by optimization. Induced power is lowest for a constant induced velocity distribution [83], which is better approached by the optimized blade than the 7A blade.

Compared to the local analysis of the twist optimized blade, the F.M.$_{\text{airfoil}}$ distribution does not change significantly when combining twist and chord parameters, indicating that a reduction of profile power is mainly related to twist optimization. The induced velocity distribution better approaches a constant curve for the combined twist and chord optimization, leading to lower induced power. Apparently, both design variables may influence induced power.

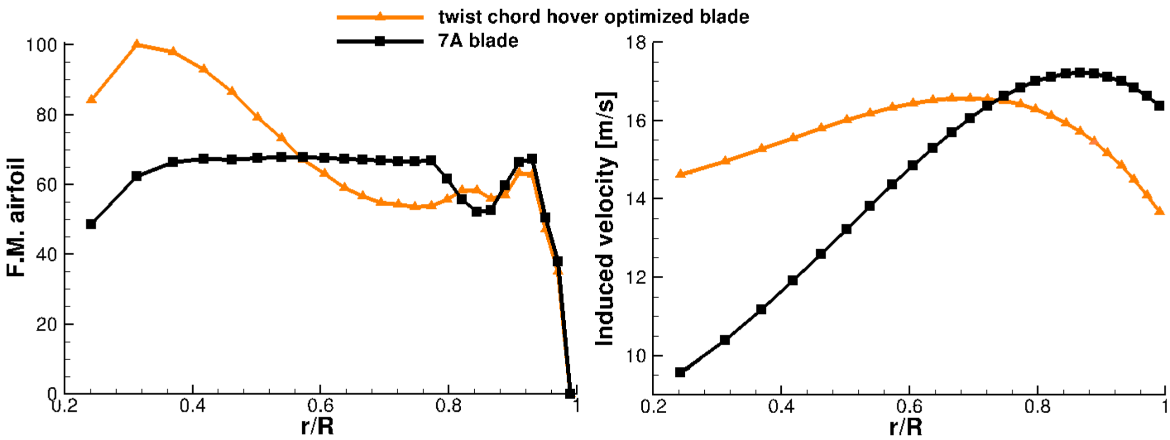

Figure 4.32: Comparison of local F.M.$_{\text{airfoil}}$ and induced velocity along the blade for the hover twist optimized and 7A blades (HOST computations)

Optimization in forward flight increases lift and L/D in the inboard part of the advancing blade, see Figure 4.33, just as for the twist optimization. Yet, lower lift is seen over a large part of blade tip sections. Differences in power consumption to overcome local airfoil drag are small. The ratio of local lift over local power consumption ($C_l M^2/C_d M^3$) is close to zero over the largest part of the rotor disk, but a rotor performance gain is observed in particular in the inboard part of the advancing blade. It seems that mainly optimized design of the inner part of the blade leads to rotor performance improvements.

It is interesting to see how results of separate twist and chord optimizations are positioned with respect to an optimization combining both geometry laws. Pareto Optimal Fronts of multi-objective optimizations with 80 individuals and 20 generations of all three parameterizations are shown in Figure 4.34. The chord law optimization improves mostly forward flight performance, whereas improvement of hover performance is mainly due to twist optimization. Combining both parameters indeed leads to even better rotor performance, simultaneously in hover and forward flight. These POFs confirm the local analyses of rotor performance, which already showed that hover performance increase is mainly due to twist law optimization.

The figure also shows rotor performance of two reconstituted blades that combine chord and twist laws of separate geometry law single-objective optimizations (hover twist and hover chord law optimizations are combined into the hover reconstituted blade, and the same for forward flight). The hover-reconstituted blade could not be recomputed in forward flight due to the high twist gradient. The forward flight reconstituted blade is positioned on the POF of the combined parameterization optimization, meaning combining separate twist and chord optimizations will lead to similar results as the combined twist and chord optimization.

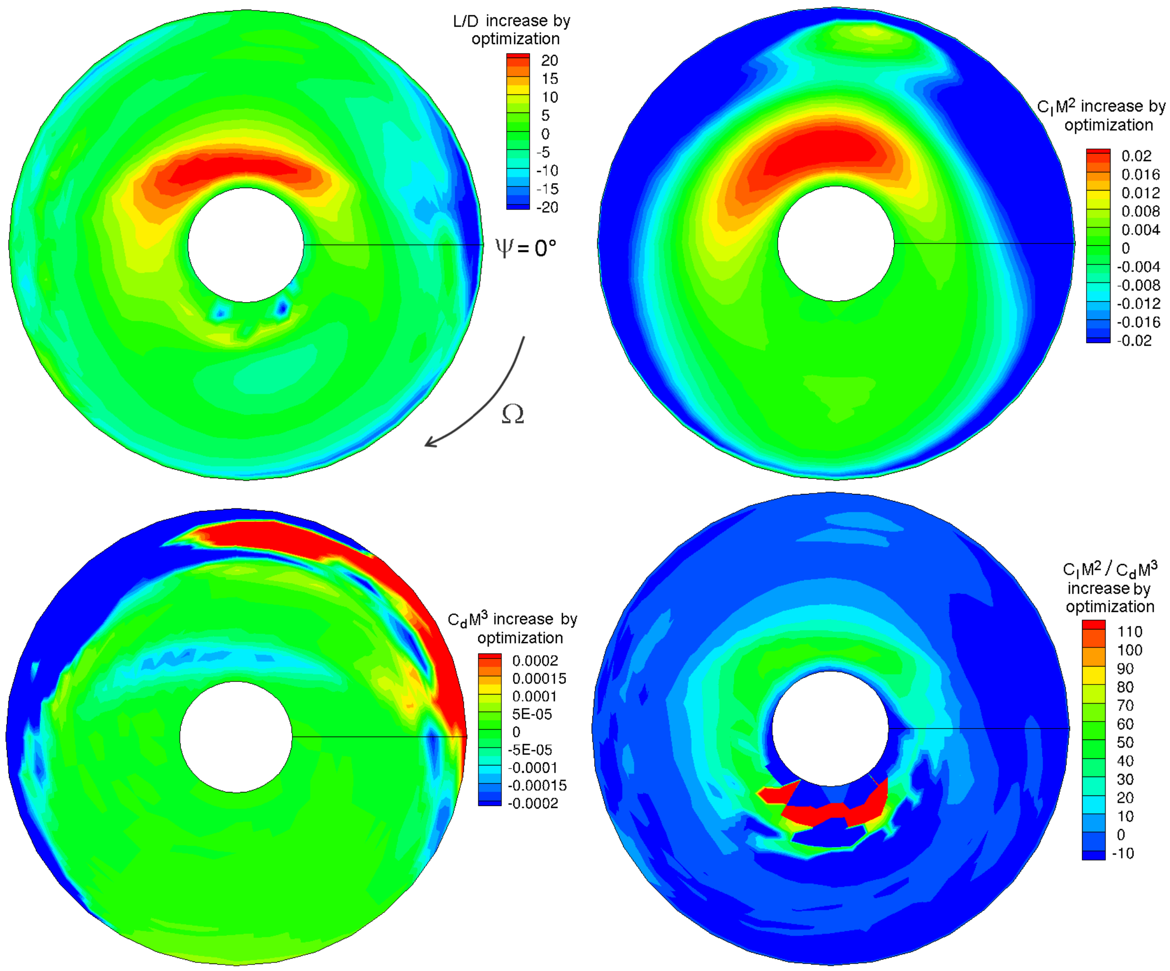

Figure 4.33: Gain of forward flight twist & chord optimized blade with respect to 7A blade in terms of local rotor performance quantities over the rotor disk (HOST computations)

Conclusions on genetic optimizations

A difficulty in the analysis of genetic algorithm optimization results is the non-deterministic nature of this method. This causes differences in terms of convergence, spread and distribution along Pareto Optimal Fronts of identical optimization problems. As this problem is inherent to the selected optimization method, and as this stochastic contribution will be present in all applied rotor optimizations, no systematic statistical analysis is made. Still, this feature should be kept in mind in all evaluations.

A first conclusion that can be drawn from this first series of optimizations is that theoretically expected solutions are reproduced for twist and chord optimizations. This is an important validation of optimizations, not only in terms of optimization methods, but also of selected objectives and parameterizations.

Different choices of objective functions always lead to improved rotor performance, but may result in different chord laws. This is due to a difference in evaluation of rotor drag and rotor consumed power in the reversed flow circle. Either of both may be used in applied optimizations, keeping in mind this difference.

A parameterization based on Bézier laws of 6 control points allows for a large flexibility for the optimizer to select best adapted geometry laws. Optimization results are only weakly sensitive to radial positioning of inner control points so that these can be fixed throughout the optimization. Reducing the number of design variables not only leads to faster convergence

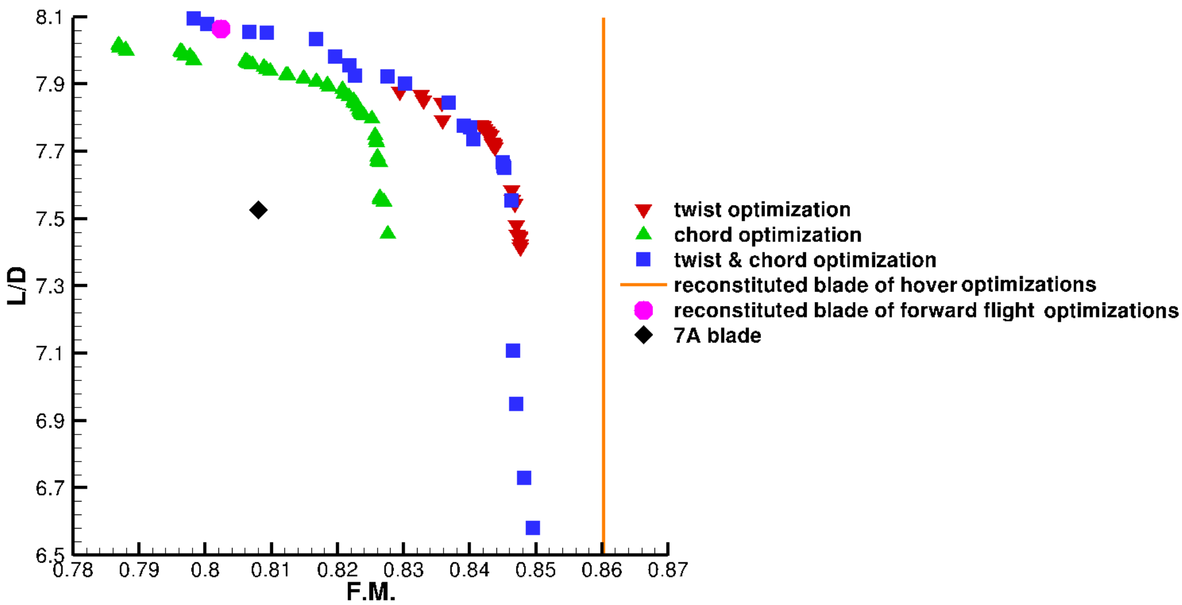

Figure 4.34: Pareto Optimal Front of separate and combined twist and chord optimizations, compared to reconstituted blades of hover and forward flight optimizations and the 7A blade

of the genetic algorithm optimization, but also eases response surface model construction.

Finally, 3 different combinations of generation and individual numbers were used, and it was seen that, in general, using a higher number of individuals leads to a more extended Pareto Optimal Front. Therefore, the combination of 20 generations of 80 individuals is selected.

4.2.3 Surrogate Based Optimization

The high computational cost associated with CFD-simulations makes direct coupling with genetic algorithms impractical. Therefore, a surrogate model is introduced in order to reduce the number of CFD simulations required by an optimization run. To investigate how the use of a surrogate model affects optimization results, preliminary validations are carried out for HOST-based optimizations: in this case, SBO results can be compared to full genetic algorithm optimizations. Several parameters of this SBO are tested: size of the initial Design of Experiment on which the first response surface is based, number of response surface updates and the number of simulated points added at each metamodel update. In addition, two different surrogate models are considered. By default, 80 points are used in the Design of Experiments used to build the first response surface. After each surrogate-based optimization, 20 blades are selected out of the non-dominated individuals to update the surrogate model. The default SBO uses five RSM update cycles.

Latin Hypercube Sampling (LHS) is used for design space exploration from which the first response surface is created. As this method depends on an initialization by a random seed, a certain LHS design may be more or less adapted for the current optimization problem [48]. To estimate the probability of initializing the SBO on a high or low quality response surface, 200 different seed values are tested and some statistical conclusions are obtained from this large data set. Pareto Optimal blade geometries obtained from all these SBO optimizations are recomputed with HOST to obtain the objective values that are used in the analyses.

All tests are performed on the combined twist and chord optimization using 12 design variables, 2 objective functions and 2 constraints. This test case is considered representative of industrial rotor blade optimizations.

Surrogate model

Gaussian process (GP) modelling was selected in Chapter 3 as an efficient and well-behaved response surface method. Hereafter, GP modelling is assessed against quadratic polynomial modelling. The latter requires a minimum of 91 cost function evaluations in the data set. As HOST simulations may fail due to too high gradients in blade geometry laws, 120 points are used in the Design of Experiment for both surrogate model constructions.

To test the quality of response surfaces, Pareto Set solutions obtained by SBO are recomputed with HOST so that the difference in F.M. and L/D between the response surface and HOST simulation is calculated as:

$$\text{difference objective} = \text{objective}_{\text{RSM}} - \text{objective}_{\text{HOST}} \tag{4.5}$$

Figure 4.35 shows differences of F.M. and L/D objectives for Gaussian Process and quadratic polynomial metamodels. It is clear that GP modelling allows a far more accurate prediction of simulation objective values than response surfaces based on Quadratic Polynomials for the same number of samples. This is confirmed by statistical analysis of all 200 seed values, as presented in Table 4.5. These numbers show that response surface quality in the region of interest is far lower for Quadratic Polynomials. Based on this, we retain Gaussian Processes for further studies.

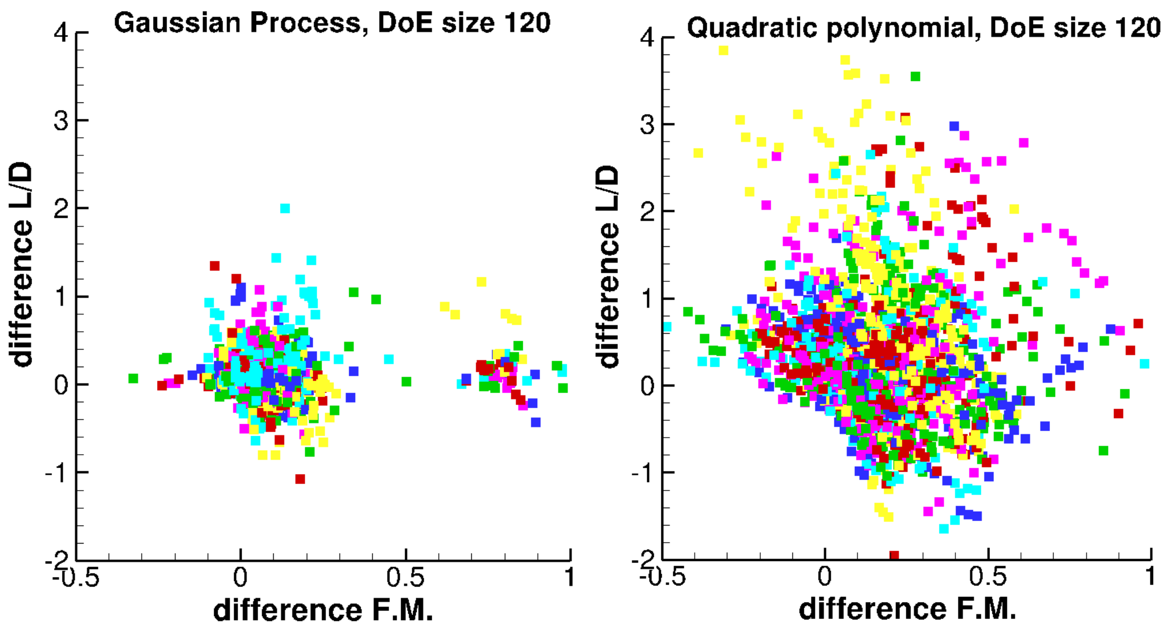

Figure 4.35: Difference in objective values of POF solutions as obtained on RSM and by HOST simulation, comparison of 200 tests with 120 points in DoE by metamodelling via Gaussian Processes (left) and Quadratic polynomials (right)

Table 4.5: Statistical information on differences of objective values of optimized blade geometries as computed on RSM and by HOST, by metamodelling via Gaussian Processes and Quadratic Polynomials

	difference F.M.		difference L/D	
	average	variance	average	variance
Gaussian Process	0.0725	0.0201	0.0742	0.0696
Quadratic Polynomial	0.1661	0.0361	0.3101	0.7651

Size of Design of Experiment

Using GP modelling, influence of the size of initial Design of Experiment is tested. It may be expected that interesting zones are found more easily for larger initial data sets as they better cover the design space. Initial data sets containing 40, 80 and 120 individuals are used, again for 200 different seed values to overcome the LHS-positioning probability problem. Pareto Optimal Fronts obtained from all these SBO optimizations are presented in Figure 4.36. The figure shows that best solutions obtained on a metamodel not always correspond to a performance improvement compared to the 7A blade. The number of blade geometries of improved rotor performance seems to increase with the size of DoE.

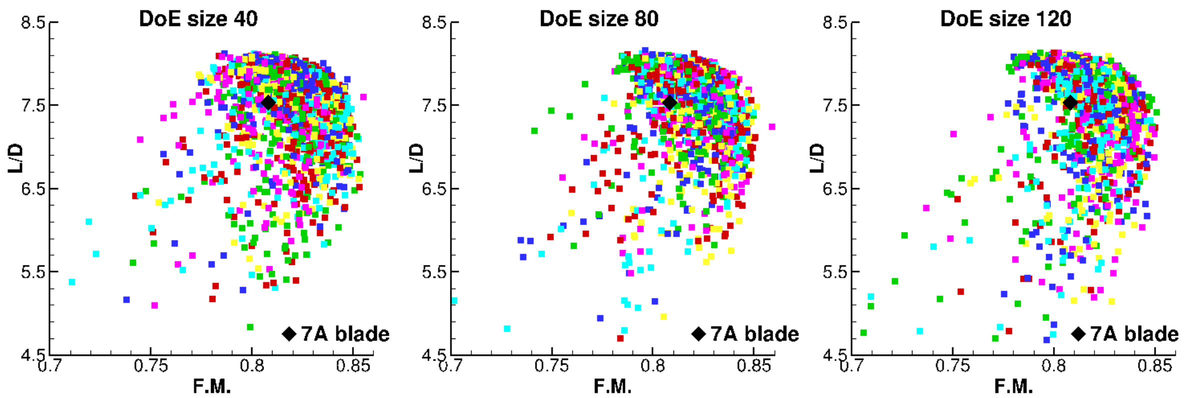

Figure 4.36: HOST recomputed optimal solutions obtained from SBO optimizations with different DoE sizes

In the same way as presented for the comparison of GP and Quadratic Polynomial metamodels, precision of response surfaces is evaluated by calculating differences of RSM and HOST computed objective values of Pareto Set solutions, see Figure 4.37, but does not allow for clear conclusions. To investigate this large data set, some statistical information is given in Table 4.6. Forward flight performance estimation by metamodel improves when increasing the size of initial DoE. However, metamodel quality seems to decrease for larger DoE sets in hover.

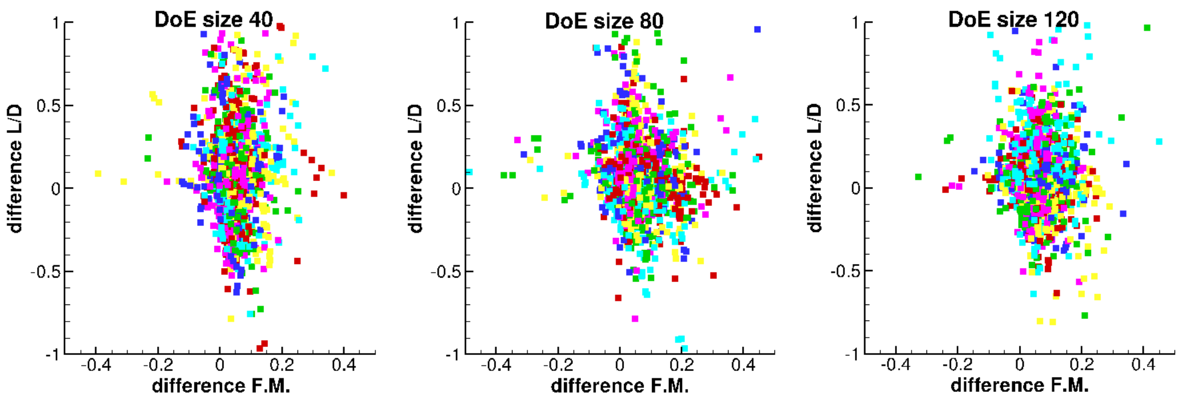

Figure 4.37: Comparison of difference between HOST computed and RSM objective values of Optimal blades found from SBOs with different initial DoE sizes

As opposite trends for hover and forward flight prediction by RSM are observed, a compromise DoE size of 80 is retained in the following.

Table 4.6: Statistical information on differences of objective values as computed on RSM and by HOST, using 40, 80 and 120 points in the initial DoE

	difference F.M.		difference L/D	
	average	variance	average	variance
40 points in DoE	0.0578	0.0159	0.1074	0.1528
80 points in DoE	0.0709	0.0265	0.0749	0.1151
120 points in DoE	0.0725	0.0201	0.0742	0.0696

Number of response surface update cycles

In this section, we investigate the effect of the number of RSM updates during an optimization. For these tests, 5 different numbers of RSM update cycles are evaluated: 1, 2, 5, 7 and 10. All SBO are initialized on the same DoE database. Figure 4.38 presents Pareto Optimal Fronts based on the last metamodel update (left), as recomputed by HOST (middle) and the difference in objective values of Pareto Optimal points between the response surface and HOST computations (right). When recomputing SBO results with HOST, Pareto Optimal solutions are found for all SBO. Convergence towards the genetic algorithm POF seems better when performing more RSM update cycles. In general terms, for forward flight performance, SBO solutions are close to those obtained from the full genetic algorithm optimization. In hover, it is challenging for response surface-based optimizations to find optimal solutions. The right image of Figure 4.38 shows that hover performance is systematically overpredicted on the response surface compared to HOST simulations. Forward flight metamodel prediction improves quickly; 2 RSM updates are sufficient to insure accurate predictions. No logical relation between number of RSM updates and response surface precision is seen for hover performance.

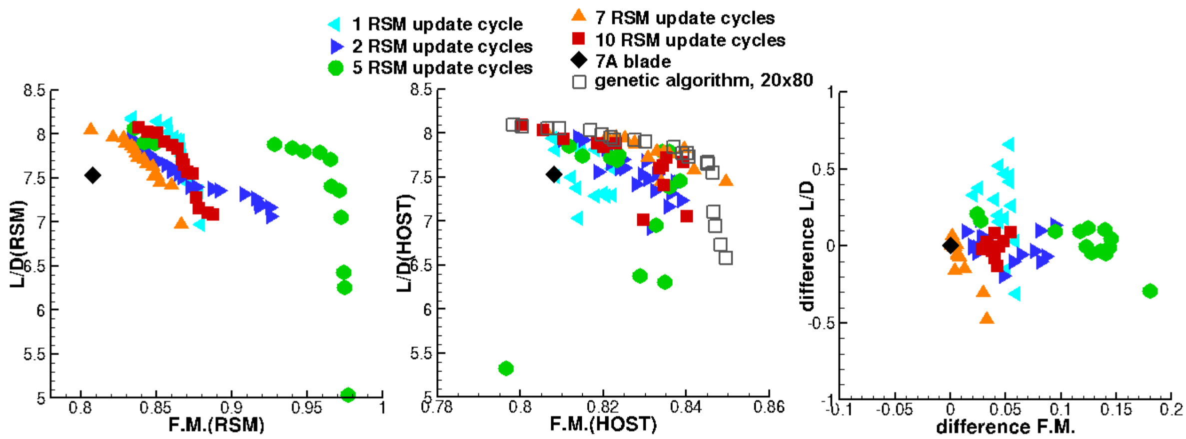

Figure 4.38: Comparison of Pareto Optimal Front obtained from SBO with different numbers of RSM update cycles

Blade geometries of SBO-obtained Pareto Optimal solutions are shown in Figure 4.41 for 1, 5 and 10 RSM updates. In general terms, obtained twist laws are alike, and are also comparable to genetic algorithm Pareto solutions. Some difference with the number RSM update cycles is seen for obtained chord laws. Whereas SBO with 5 update cycles find solutions with large chord sections at the inboard part, this is not the case for 1 and 10 RSM updates. The large variety of blade geometries found by genetic optimization is only found for the SBO with 5 updates.

From the above tests it remains difficult to conclude on convergence of response surface

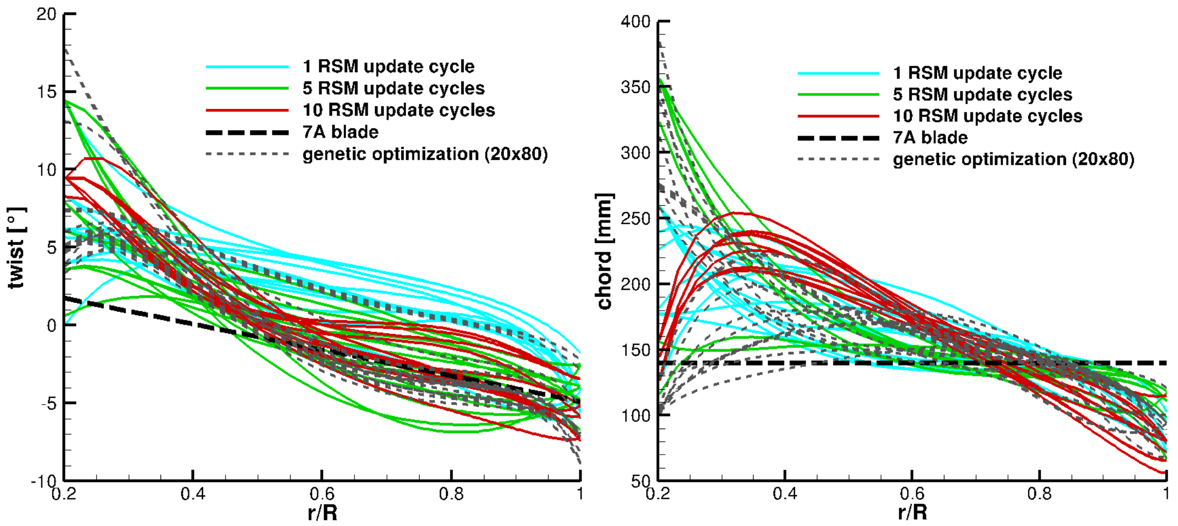

Figure 4.39: Comparison of blade geometries obtained from SBO with different numbers of RSM update cycles

and the surrogate based optimization in general. It is thus decided to continue using 5 update cycles, as 1 or 2 did not seem sufficient to the complete design exploration phase and 7 or 10 update cycles did not have a sufficient added value compared to the increased computational cost.

Size of response surface update cycles

Before comparing SBO to genetic algorithm optimization, a final test is done to evaluate the maximum number of points added at each RSM update cycle. These points are selected out of the sets of best-so-far solutions obtained from metamodel-based optimization. All solutions are added if the non-dominated set is smaller than the requested number of added points. In this study, different numbers of added points are tested: 5, 10, 20 and 40.

Figure 4.40 shows Pareto Optimal Fronts on the response surface (left), as computed by HOST (middle) and differences between these two (right). Again, metamodels overestimate hover performance, but a significant disparity between RSM and HOST simulation of L/D values is observed as well. Changing the number of individuals within a RSM update modifies optimization results, but no clear relation between update size and final POF quality can be found.

In the parameter space, see Figure 4.41, general tendencies of blade geometry modifications that lead to performance improvement are found in all SBO. Just as in the objective space, the number of individuals used for RSM updating does not seem to modify optimization quality.

Comparison of SBO to genetic algorithm optimization

To conclude on all performed tests and validate surrogate based optimizations, twist, chord and combined twist & chord optimizations are compared to genetic algorithm optimization. In these SBO, we use settings that were obtained previously: 80 individuals are contained in the Design of Experiments, on which a Gaussian Process metamodel is created. From optimization on this response surface, 20 best-so-far points are selected and computed by HOST to be added to the surrogate database. This update cycle will be performed 5 times to improve response surface quality in interesting zones.

Figure 4.42 to 4.44 illustrate progress of the SBO during update cycles by showing HOST computed objective values that are added to the RSM. In optimizations of chord laws individ-

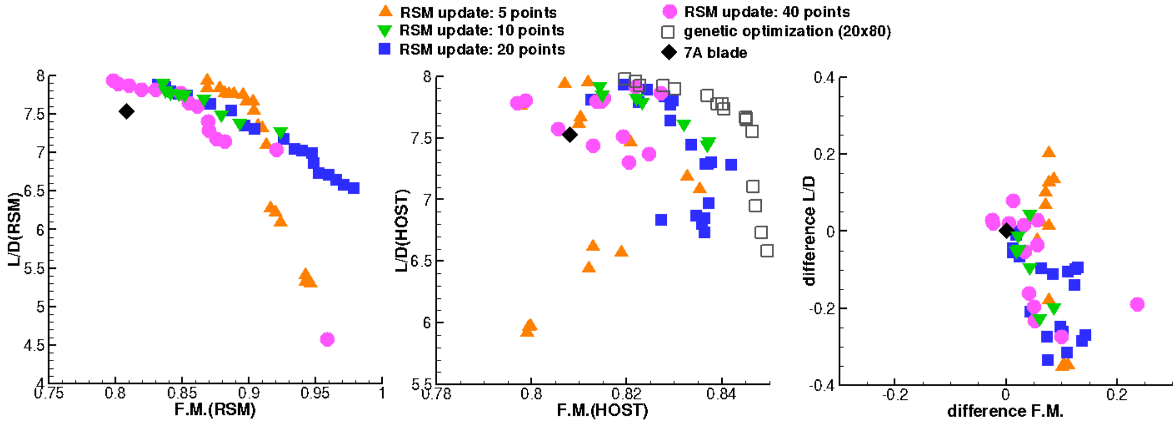

Figure 4.40: Comparison of Pareto Optimal Front obtained from SBO with different numbers of individuals added at RSM updates

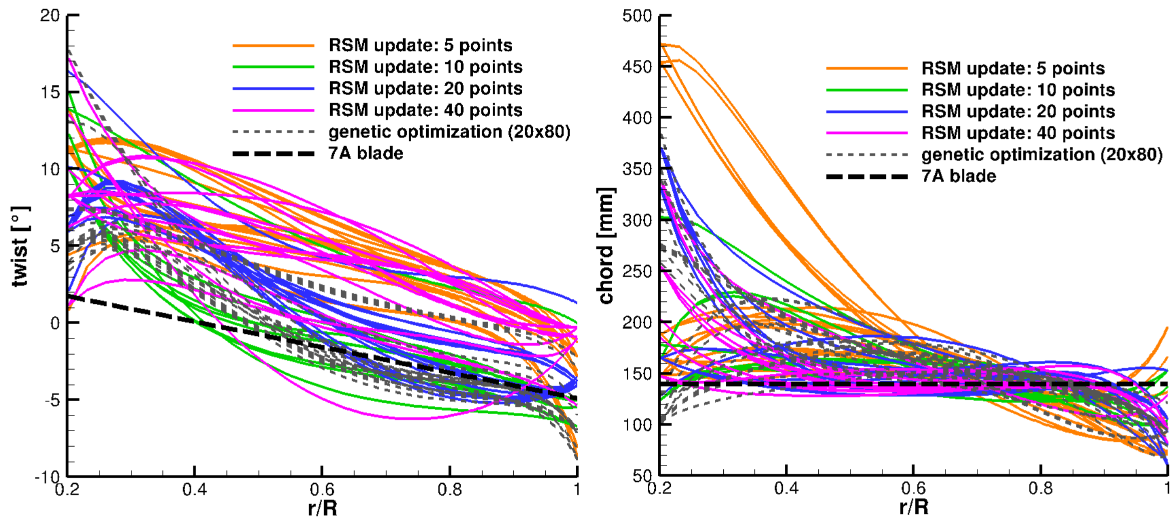

Figure 4.41: Comparison of blade geometries obtained from SBO with different sizes of RSM update cycles

uals with violated constraints are removed, so that only very few points of the DoE are shown. In the twist optimization, points having good forward flight performance are found from the 1^{st} RSM update step on. For hover flight performance, the RSM seems to have difficulty in correctly predicting relations between twist law parameters and performance objectives.

Concerning the chord optimization, Pareto Optimal solutions are found immediately and not much improvement is seen along subsequent RSM update steps. Yet, the initial DoE did not provide a valuable data set for response surface construction of objectives, as 68 out of 80 points had violated constraint values. Apparently, relations between parameters and objectives are easily found.

The combined twist & chord optimization has similar behaviour as the separate twist optimization, showing rapid forward flight performance improvement. Again hover performance seems to be difficult to understand and only limited performance improvement over subsequent steps is observed. Finally proposed solutions are performance improvement with respect to the reference blade, but are not as good as genetic algorithm optimization results.

Pareto Optimal Fronts of genetic and surrogate based optimizations of all three parameterizations are presented in Figure 4.45. All optimizations lead to significant performance increases in hover and forward flight. Surrogate based optimizations lead to optimized sets

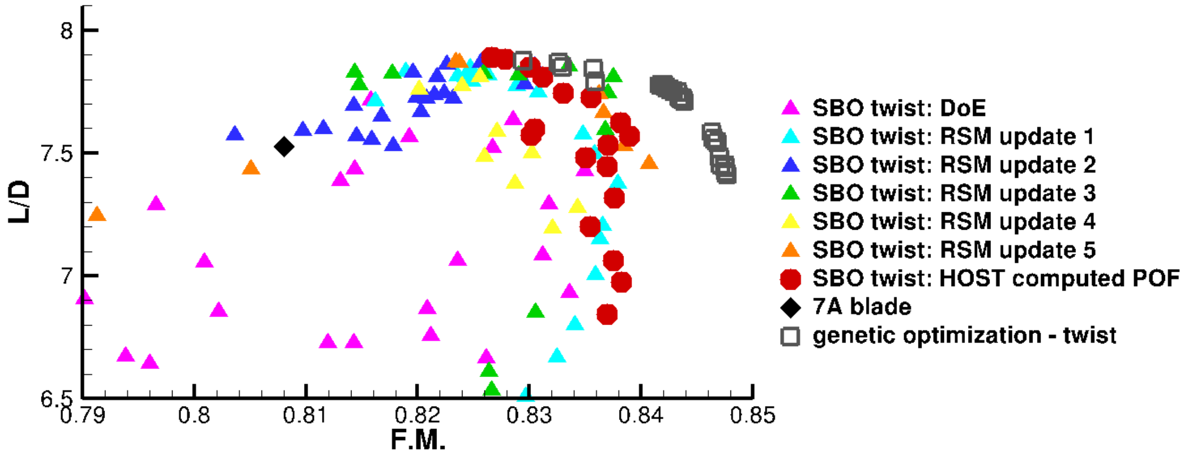

Figure 4.42: Comparison of SBO progression to Pareto Optimal Front of genetic optimization of twist optimization

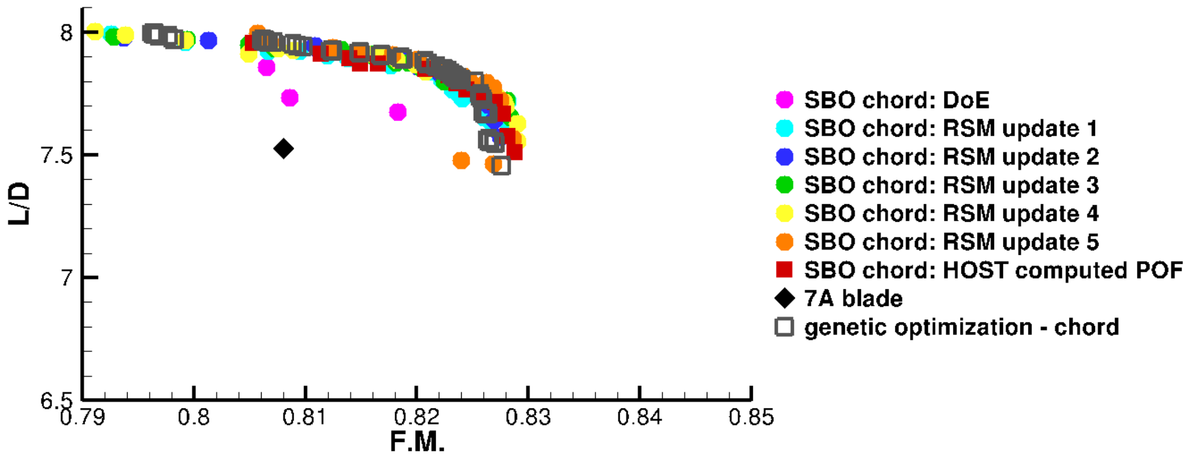

Figure 4.43: Comparison of SBO progression to Pareto Optimal Front of genetic optimization of GA of chord optimization

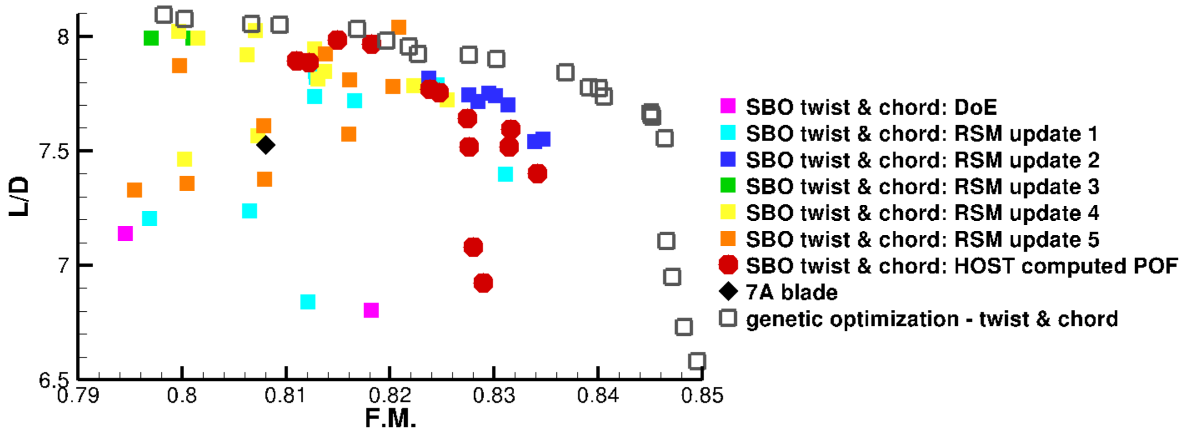

Figure 4.44: Comparison of SBO progression to Pareto Optimal Front of genetic optimization of combined twist & chord optimization

with large spread and a nice distribution. Yet, only the chord law metamodel optimization finds comparable performance as the full genetic optimization. In both twist optimizations, the response surface does not predict correctly relations between twist parameters and Figure of Merit. This may be due to the large extent of the twist law parameterization, leading to widely spaced DoE points for these parameters so that relations are not directly found.

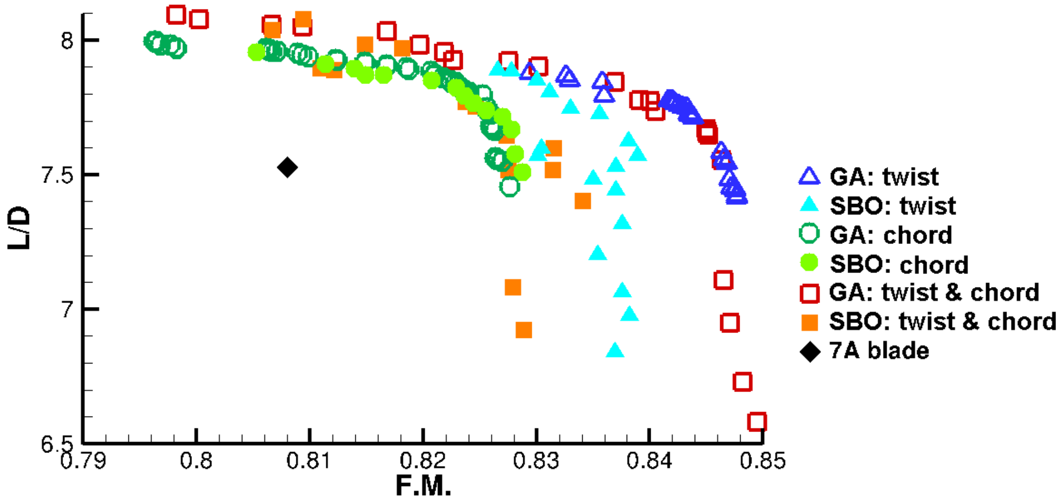

Figure 4.45: Comparison of Pareto Optimal Fronts obtained from genetic and surrogate based optimizations

As expected from earlier results, highest metamodel quality in the POF zone is found for the chord optimization, as illustrated in Figure 4.46. For this optimization, the surrogate model update cycles have led to a very accurate metamodel in the POF-zone. For twist and combined twist & chord optimizations, this accuracy level is clearly not achieved.

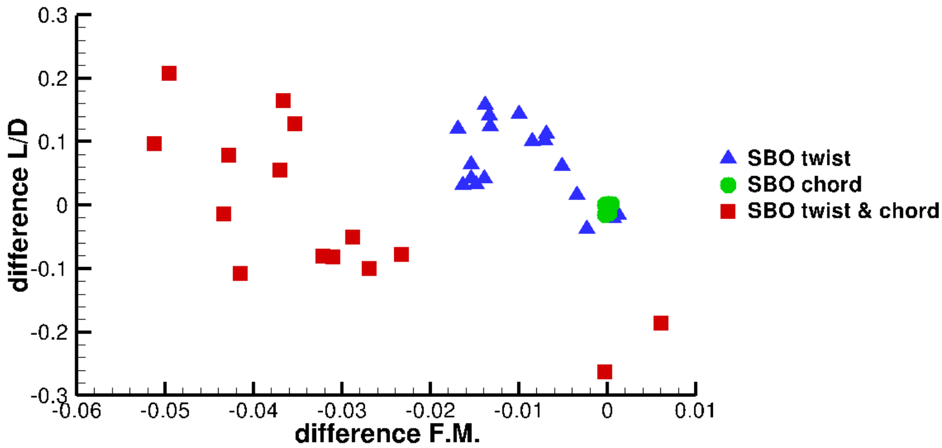

Figure 4.46: Difference in objective values between response surface model and HOST computations of Pareto Optimal points

Figures 4.47 and 4.48 compare twist and chord laws obtained with genetic algorithm and surrogate based optimizations. The images illustrate large similarities of obtained blade geometries, especially for the combined twist & chord optimization. In separate twist and chord optimizations, SBO leads to a larger spread of solutions compared to genetic algorithm optimization.

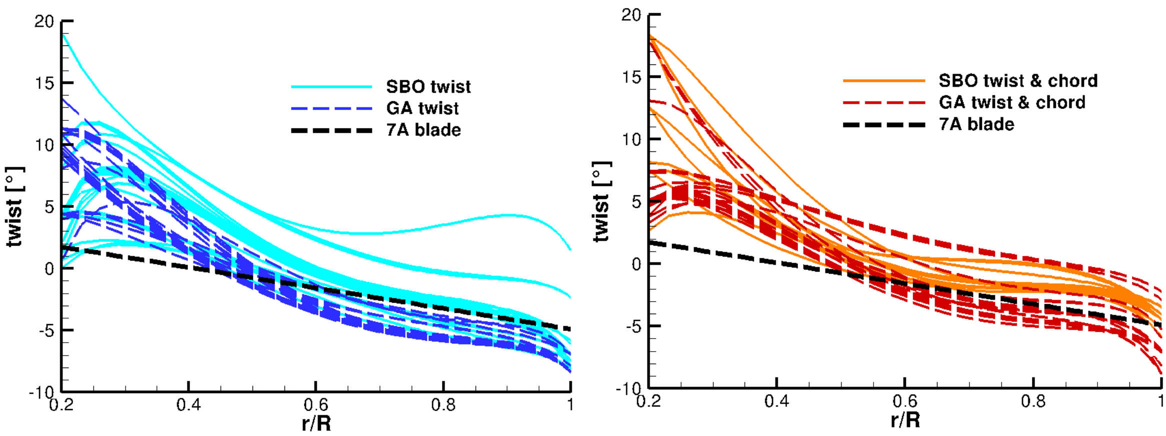

Figure 4.47: Twist laws obtained from separate twist (left) and combined twist & chord (right) surrogate based optimizatons, compared to GA-obtained twist laws

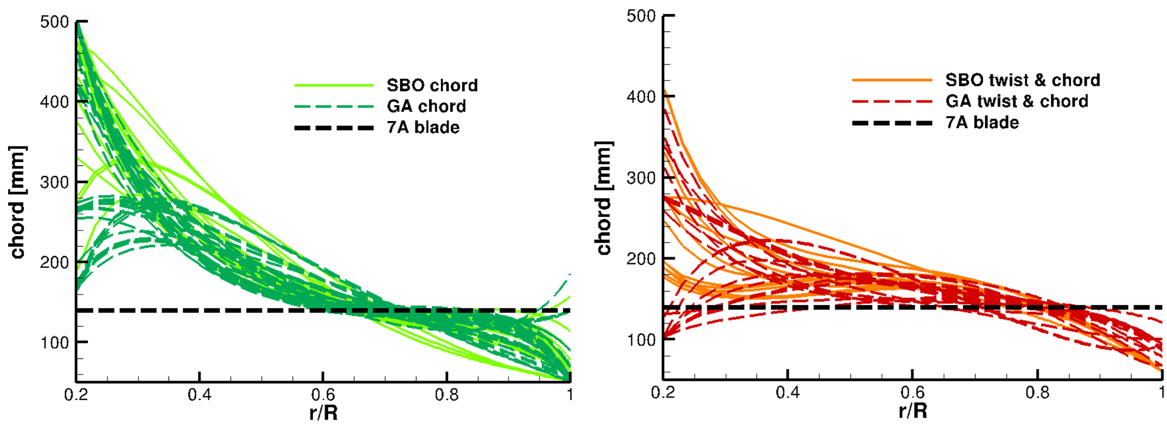

Figure 4.48: Chord laws obtained from separate chord (left) and combined twist & chord (right) surrogate based optimizatons, compared to GA-obtained chord laws

Conclusions on SBO optimizations

Surrogate Based Optimization is a promising technique that drastically reduces the number of simulations required in a genetic algorithm optimization. This is essential to include CPU- and time-costly CFD simulations in an industrial rotor blade design optimization.

Various tests on exact implementation of SBO have been carried out using low-cost HOST simulations. Based on this, we retain Gaussian Process modelling with 80 points in the initial dataset, followed by 5 RSM updates of 20 added points for the rest of this work. Yet, various ideas for potential improvements are given:

- Investigate other response surface models. From Figure 3.7, it was expected that relations between parameters and objectives in currently investigated optimization problems are smooth and continuous. This assumption may not be correct and more local metamodels may be used to better predict simulation results. In particular advanced response surface methods as artificial neural networks (ANN) and radial basis functions (RBF) are interesting for their relatively low requirements on the number of data points [2]. The Multivariate Adaptive Regression Spline (MARS) method might require a larger dataset, but generates local response surfaces in subregions, so that local variations of objective functions with design parameters can be predicted [2].

- Consider larger Design of Experiment sets and other methods of DoE positioning. Along with RSM-model, this was the only demonstrated way of final result improvement. It appears that the quality of the initial metamodel has a large influence in finding zones with good rotor performance. Improvement might come from switching to another DoE method, or simply by adding more points. Keeping total number of simulations constant, it might be more interesting to use more points in the initial DoE and less for local RSM quality updates.

- It is expected that updating the metamodel with new data points improves the response surface locally, in zones of interest. Yet, no clear conclusions are drawn on the way this update is done, either in terms of number of added simulation points or by the number of RSM update cycles. These uncertainties may be due to various reasons: genetic optimization on the response surface may not be sufficiently converged to decide on data points to be added and random selection within Pareto Optimal solutions may not lead to best update choices. Another potential problem is local overfitting of the surrogate model due to closely positioned data points. This may be resolved by treatment of the data set: points with comparable parameter sets should be removed from the database, as are point far away from Pareto solutions, so that the response model only considers a specific data set around the Pareto Optimal Front. This may lead to significant improvements of response surface quality.

4.2.4 Multi-fidelity optimization

A final goal of all previously performed tests is to prepare a Multi-Fidelity Optimization (MFO). This optimization type is considered as more suitable for industrial employment in rotor blade design. In fact, this optimization combines best features of both simulation tools and optimization methods: low-cost HOST simulations are used to explore the design space and eliminate design variable combinations leading to low rotor performance. This optimization is performed by a genetic algorithm as optimization requirements on the number of simulations is of less importance here. It is also used to select a set of blade geometries on which the CFD-based SBO will be initialized. Both steps of design space reduction and blade geometry selection require understanding of relations between objectives and parameters, so that the switch from low- to high-fidelity is not automated.

In a second stage, low-fidelity results are used to initialize a SBO with CFD simulations. A reduced SBO can be performed here, as start conditions are better chosen than design of experiment initialization of parameter combinations with a random seed.

In CFD-based optimization tests, Autogrid failed to create meshes of blades with large chord values and chord gradients. In general, meshes for blades with inboard chord sections larger than 0.20m were not feasible. As a solution, optimization parameter bounds are limited to 0.20m for CFD-based optimizations, as shown in Figure 4.49. The complete multi-fidelity optimization is performed with the reduced parameter set and HOST-based optimization results of the low-fidelity phase are different than results earlier obtained.

Low-fidelity stage

The HOST-based genetic optimization is meant to explore the design space. This exploration should, on the one hand, lead to a reduced parameter space used in the CFD-phase. At the same time, design variables corresponding to interesting blade geometries are inserted in the second stage to initialize the first response surface generation.

Figure 4.50 shows the optimization evolution in the objective space. This optimization evolution shows objective results of computed individuals of each generation. The optimization follows the steps described hereafter: in the first 4 generations the complete design space is

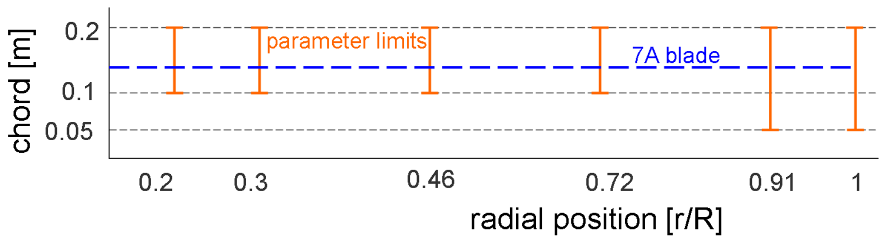

Figure 4.49: Modified chord law parameter bounds for CFD-based optimizations

explored. From the 6th generation on, the correct direction for maximizing both objectives simultaneously is found. From this point on, the Pareto Front is approached and solutions are refined.

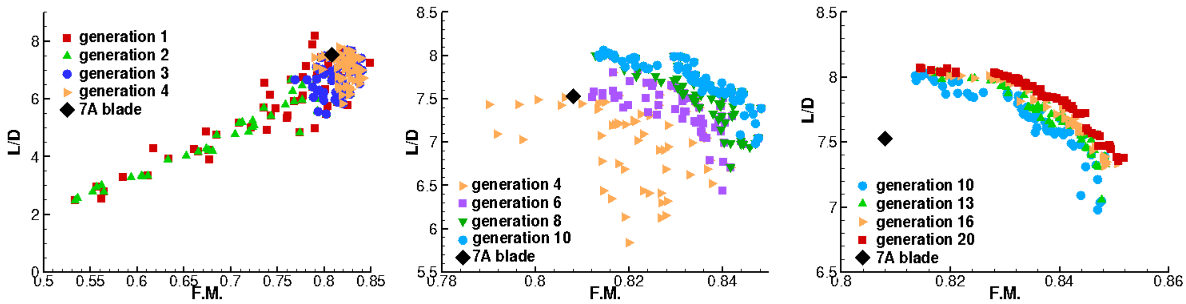

Figure 4.50: Objective values of tested blade geometries during an optimization (twist & chord optimization, 20 generations, 80 individuals)

Selected blade geometries for initialization of the CFD-based response surface should, on the one hand, correspond to optimal blade geometries for the HOST-based optimization, and, on the other hand, be sufficiently diversified to ensure a good exploration of the design space in the CFD-based step. As seen earlier, best geometries obtained from a HOST-based optimization may not completely correspond to best geometries in a CFD-based optimization. Selected geometries from the low-fidelity stage should thus allow the high-fidelity optimization to continue exploring design options. To fulfil both criteria simultaneously, individuals of generation 6 seem to be suitable for continued design exploration. Individuals of generation 10 are added to this data set, as they all have found improved solutions compared to the reference blade and they approach the HOST-based POF.

Individuals that violate constraints (13 individuals for generation 6 and 16 of generation 10) are removed from the data set. Additionally, forward flight simulation by HOST fails for respectively 13 and 12 individuals in generation 6 and 10, so that these individuals are removed as well from the set (required rotor harmonics could not be obtained for these individuals). This leaves thus (54+52=) 106 individuals to construct the first response surface.

Figure 4.51 illustrates twist and chord laws of blades created for generations 6 and 10 as well as final optimization results. It shows that blades of generations 6 and 10 contain a larger design space than Pareto Optimal blades. At the same time, this blade set is expected to generally provide better performance than randomly generated blades.

Presently, parameter space reduction is done by hand as engineering judgement plays an important role in this choice. Figures 4.52 to 4.55 present progress of subsequent generations in the search for relations between parameters and objective values. The images show how each parameter evolves during the optimization and to which value it tends for optimizing rotor performance.

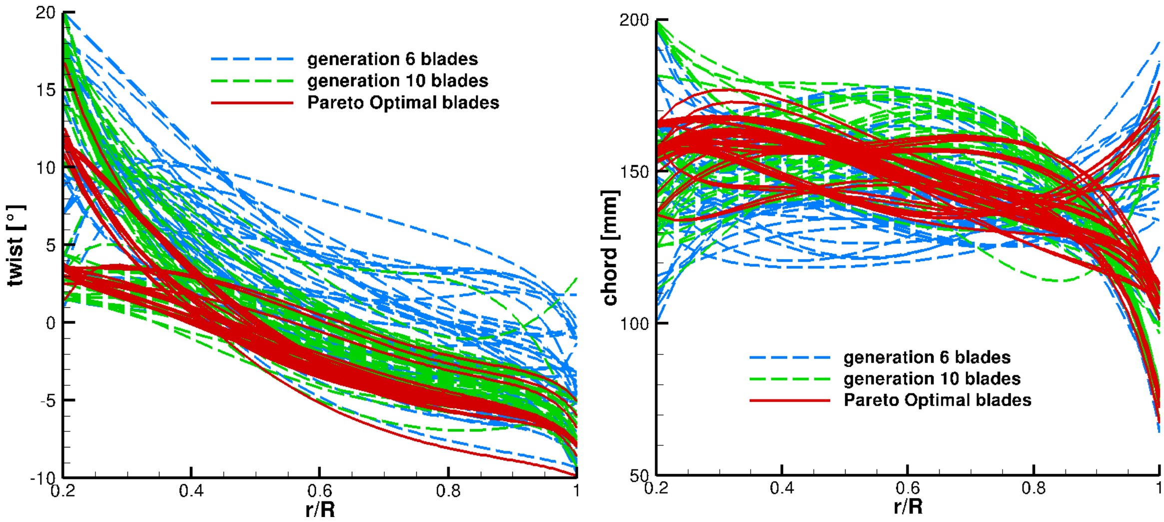

Figure 4.51: Comparison of blade geometry laws of individuals of 6$^{\text{th}}$ and 10$^{\text{th}}$ generations and HOST-based Pareto Optimal Front

Concerning twist parameters, it appears that mainly variables on the inboard part of the blade make the difference between Pareto Optimal blades. No specific relation between twist values and rotor performance in terms of F.M. and L/D is seen here, especially for the twist at radial positions of 0.2 and 0.46R. The design space should thus not be reduced too much here. Twist variables on the three outer blade sections (0.76, 0.91 and 1R) all converge towards specific values. In addition, these optimal twist values are similar for maximizing hover and forward flight performance. This implies that these parameter bounds may be reduced drastically.

For chord design variables often two solution types are found, which is especially well demonstrated for optimal chord parameters at 0.72R (Figure 4.55). These two distinct solutions were already observed earlier, for example in Figure 4.29. Solutions preferred in hover have a parabolic-shaped chord distribution, whereas forward flight optimized blades have a double taper law. Due to these two separate solution types, reduction of parameter limits is not as easy as for twist.

In conclusion, Table 4.7 presents new parameter limits based on low-fidelity optimization results. On average, the total design space is reduced by approximately 35%.

High-fidelity stage

The low-fidelity phase has prepared the more costly CFD-based optimization phase. First, the 106 individuals are computed by hover and forward flight CFD simulations. The first surrogate model will be based on these results. This response surface will then serve for an optimization. Finally, SBO results are recomputed by full CFD simulation to assess the feasibility and quality of optimized blades.

Whereas the low-fidelity stage was executed using objectives on F.M. and L/D, the CFD-based optimization maximizes F.M. in hover and $\bar{Z}/\bar{C}$ in forward flight. The latter objective is expected to have similar effects as the rotor power consumption objective that was tested in Section 4.2.2. As shown before, small differences in chord design in the inboard part of the blade may be expected from this objective difference.

Figure 4.56 shows hover and forward flight performance results of the 106 low-fidelity selected blades as computed from CFD simulations (4 simulations failed to converge). It shows that most blades selected from the HOST optimization also provide increased rotor

Table 4.7: New parameter limits and parameter space reduction obtained from inspection of HOST-based genetic optimization

parameter	lower bound	upper bound	reduction [%]
twist (0.2 r/R)	0	15	25
twist (0.3 r/R)	0	10	50
twist (0.46 r/R)	-5	10	25
twist (0.72 r/R)	-10	0	50
twist (0.91 r/R)	-10	2	40
twist (r/R)	-10	0	50
chord (0.2 r/R)	0.12	0.18	40
chord (0.3 r/R)	0.12	0.18	40
chord (0.46 r/R)	0.12	0.20	20
chord (0.72 r/R)	0.10	0.20	0
chord (0.91 r/R)	0.10	0.18	47
chord (r/R)	0.05	0.18	13

performance as computed by CFD. Without optimization, a blade set with improved rotor performance is already found from CFD computations.

Figure 4.57 illustrates the influence of two geometrical parameters on CFD-computed hover and forward flight performance. It appears that individuals with lower performance in both flight conditions compared to the 7A blade typically have a high value for the outboard twist control point at 0.91R. Also, blades positioned on or near the optimal front of this set generally have a high value for the chord control point at 0.72R. This shows that a double taper law is beneficial, especially for improving forward flight performance, just as was illustrated by the patents in Section 1.2.5.

Based on these CFD-results, a Gaussian Process surrogate model is constructed for the optimization. Optimized blade geometries are presented in Figure 4.58. It shows that optimal blade designs have geometries that are contained within the initially tested set of blades. This may also be due to the restricted parameter set used in the high-fidelity stage, which was selected from low-fidelity tests. Anyway, this implies that we can have confidence on surrogate model quality as no extrapolations are required.

Most SBO-optimized twist laws have a similar shape near the blade tip, and blades differ principally in inboard twist laws. Laws are comparable to those found in earlier optimizations. Optimized chord laws all look alike and are double-taper laws. Compared to HOST-based optimization results, chord is smaller at the blade root. This effect has two possible explanations. First, there is a difference in simulation fidelity: *elsA* considers three-dimensional effects in this area, whereas HOST only accounts for two-dimensional flow. Lift reduction at the blade root is thus only computed by CFD. Additionally, as demonstrated earlier, the CFD-objective $\bar{Z}/\bar{C}$ is comparable to rotor power consumption and tends to reduce chord at the blade root.

Another interesting opportunity of the large data set obtained with CFD-computation of low-fidelity selected blades is the availability of computational results of both simulation tools for these 106 blade geometries. These performance results are compared by normalizing them with the maximum value within the data set:

$$\text{difference F.M.} = \frac{\text{F.M.}_{\text{HOST}}}{\text{F.M.}_{\text{HOST}_{\max}}} - \frac{\text{F.M.}_{elsA}}{\text{F.M.}_{elsA_{\max}}} \tag{4.6}$$

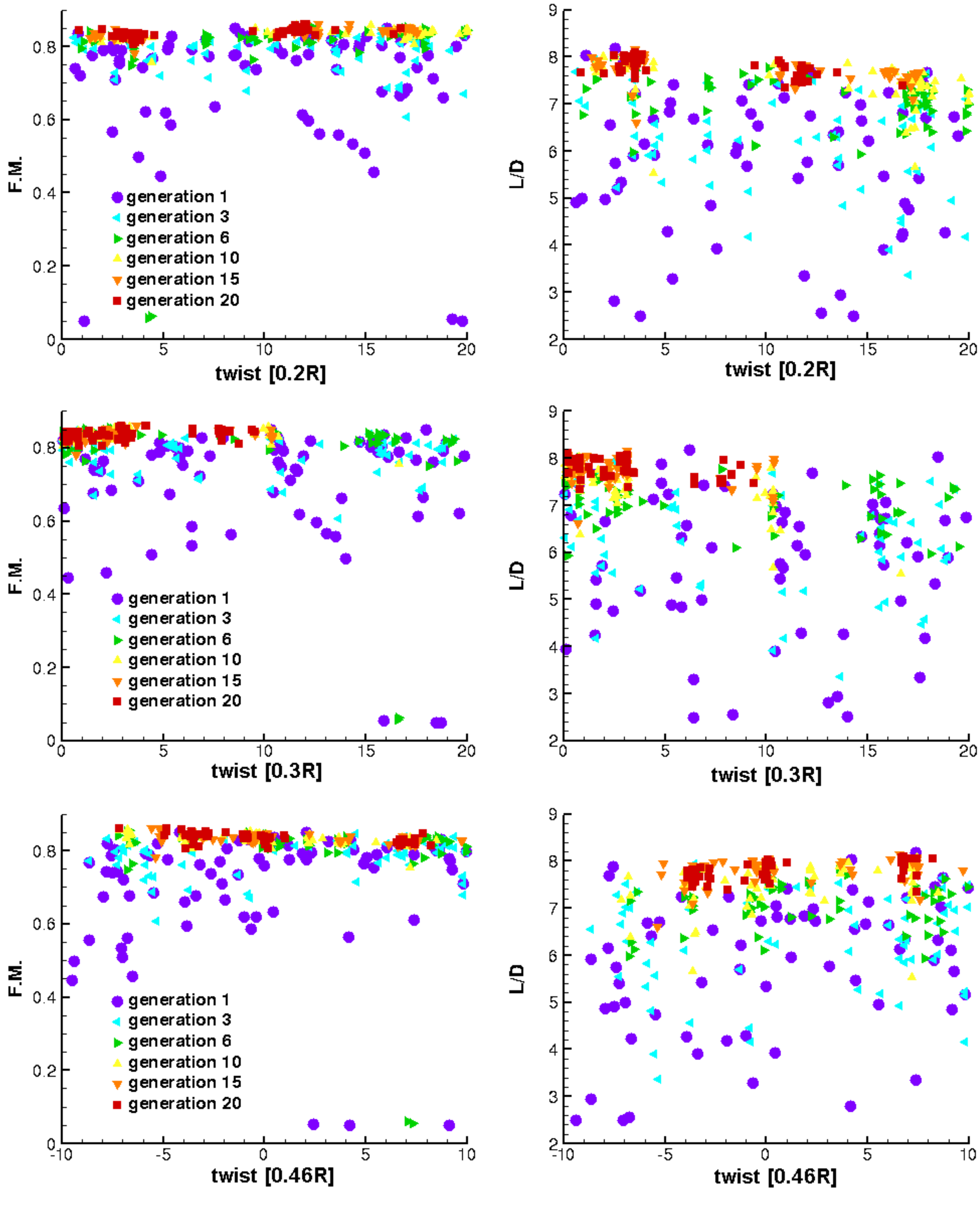

Figure 4.52: Optimization evolution in parameter space of 3 inboard twist design values

$$\text{difference FF performance} = \frac{\mathrm{L/D_{HOST}}}{\mathrm{L/D_{HOST_{max}}}} - \frac{\bar{Z}/\bar{C}_{elsA}}{\bar{Z}/\bar{C}_{elsA_{max}}} \tag{4.7}$$

Figure 4.59 plots performance differences in hover and forward flight of all blades. It shows that, for most blades, HOST overpredicts hover performance by 8 to 15% with respect to CFD. In forward flight, absolute performance values differ by ±20% between both simulation tools.

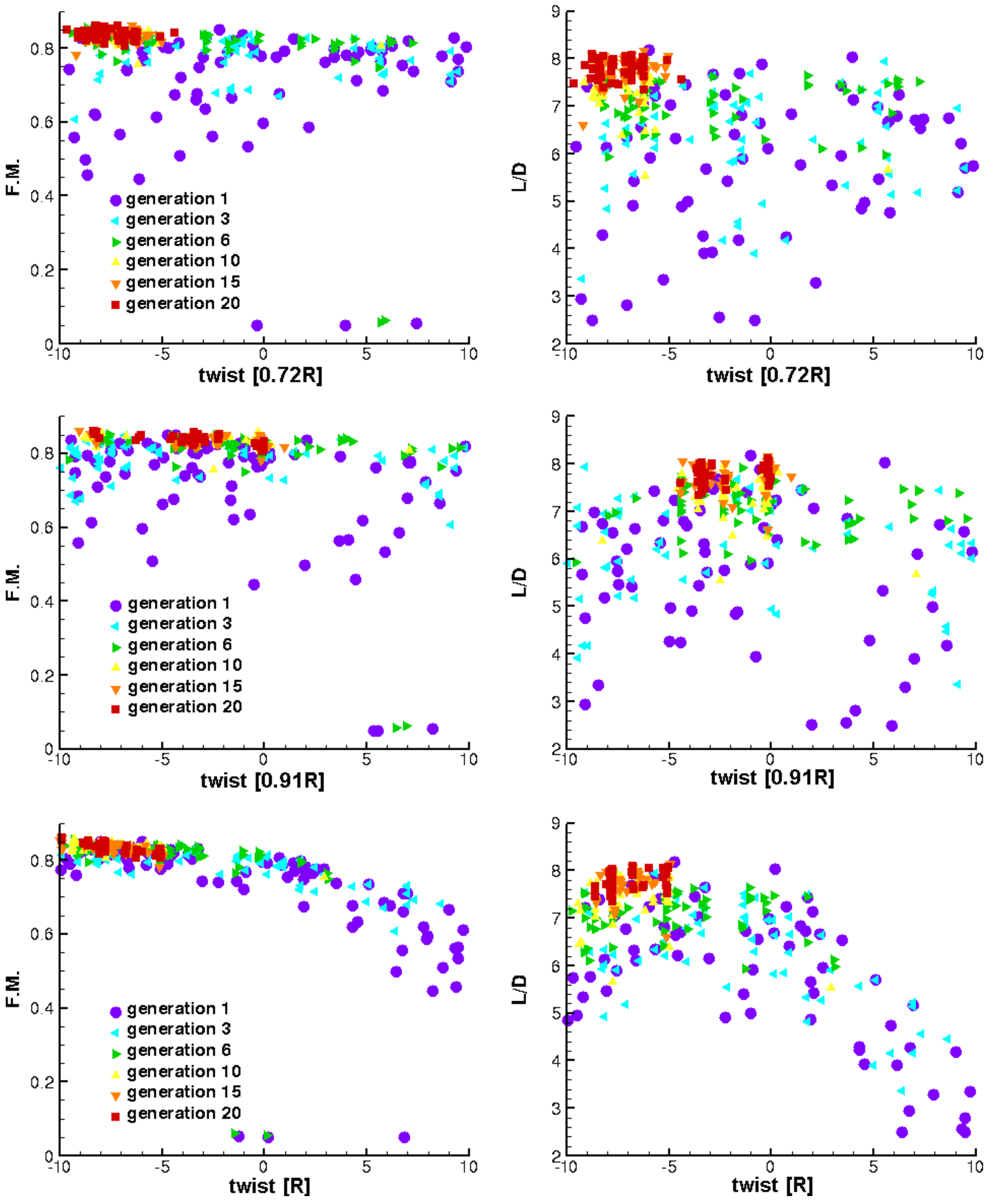

Figure 4.53: Optimization evolution in parameter space of 3 outboard twist design values

Blades in the left figure are coloured by their twist value at 0.72R showing that a high twist value at this radial position leads to large differences between HOST and *elsA*. In hover, this difference is about 25% and in forward flight even up to 60%. A similar figure given on the right hand side is coloured by the chord value at the blade root. It illustrates that for higher blade root values, large differences in hover performance predictions exist. Obtained performance values thus alter largely with simulation fidelity for this parameter. This may be explained by the three-dimensional effects that will occur in this blade zone, which are

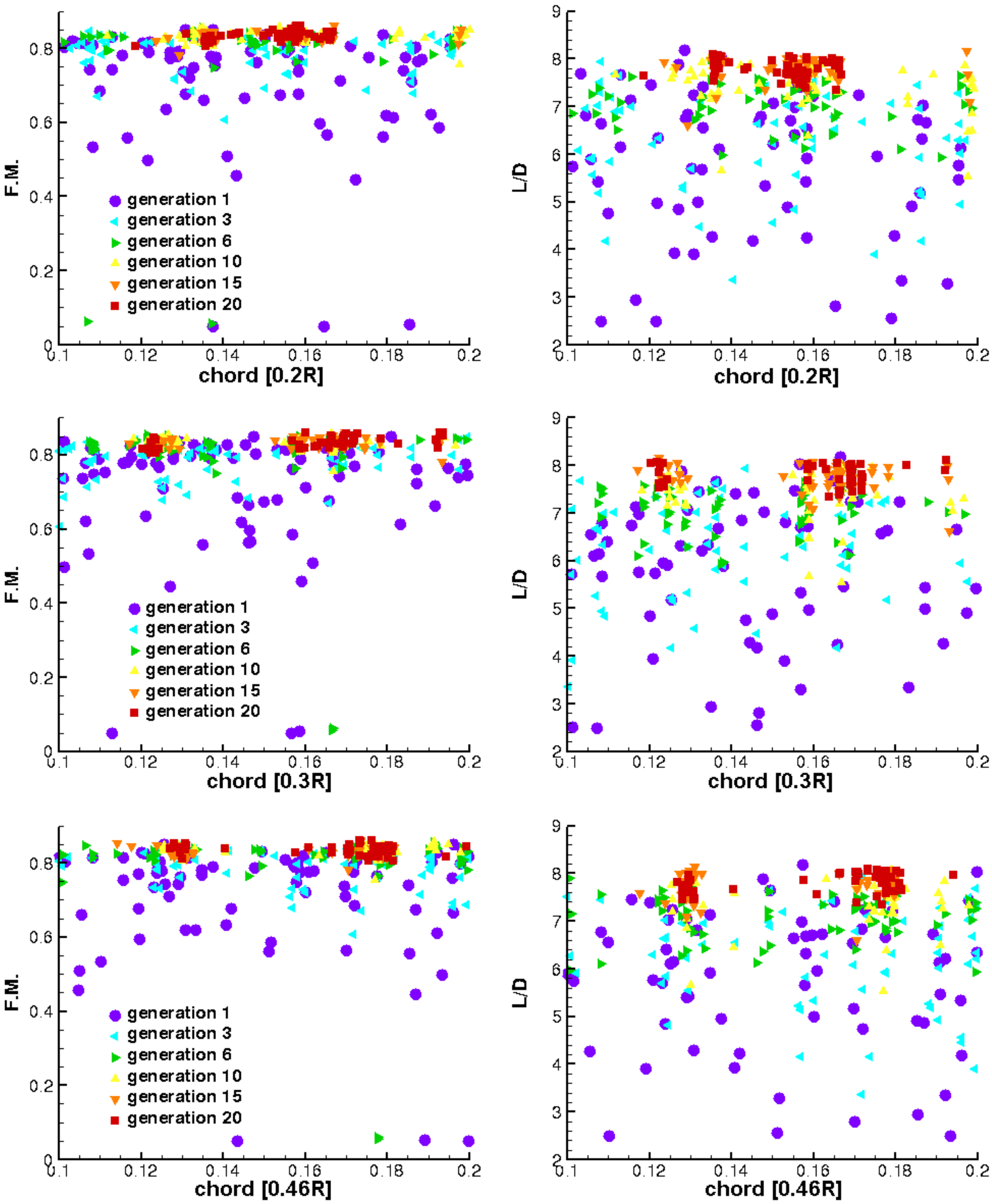

Figure 4.54: Optimization evolution in parameter space of 3 inboard chord design values

foreseen by CFD but not by HOST.

Multi-fidelity optimization results

The 23 blade geometries obtained from the CFD-based SBO are evaluated by CFD. Out of these 23, HOST forward flight computation failed for 3 blades and for another 3 blades the CFD simulation did not converge, leaving 17 blades within this 1st generation. CFD-computed performance results are shown in Figure 4.60. It shows that while some blades do

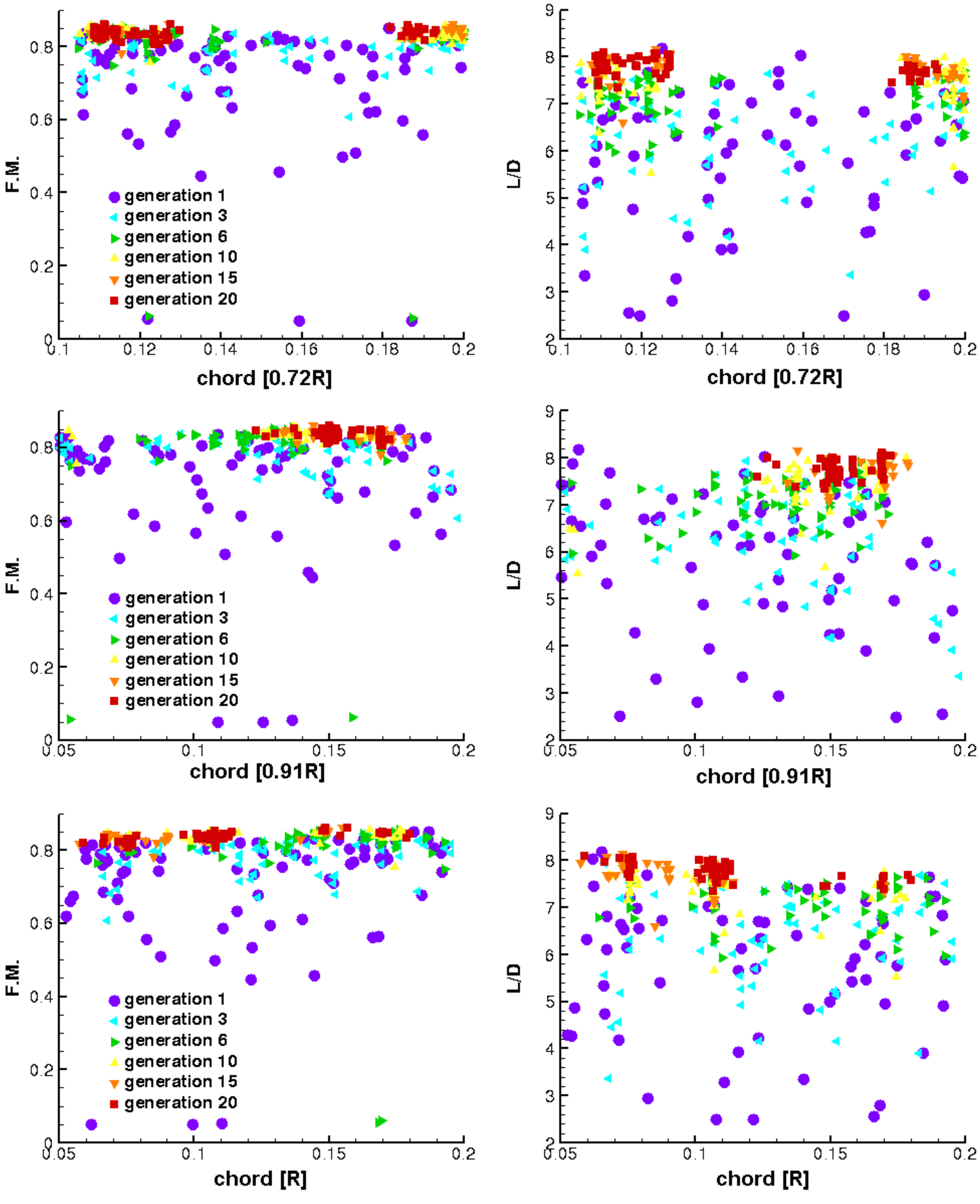

Figure 4.55: Optimization evolution in parameter space of 3 outboard chord design values

not outperform the low-fidelity selected blades, most SBO-optimized blades perform clearly better than these 106 initially tested blades: a new optimal front is found. In addition, a large performance gain of these blades with respect to the reference blade is observed.

Two optimized individuals are designated in Figure 4.60, individuals 2 and 15, which have particularly good performance in both flight conditions. Their twist and chord laws are shown in Figure 4.61. Double-taper chord laws are comparable but twist laws are different: individual 2 has a large twist gradient over the blade of nearly 25°. Distributions of dynamic

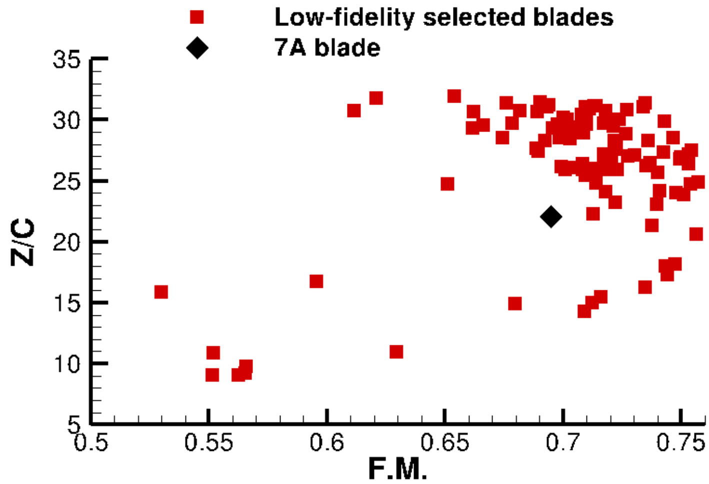

Figure 4.56: CFD simulated hover and forward flight performance of low-fidelity selected blades, compared to 7A blade performance

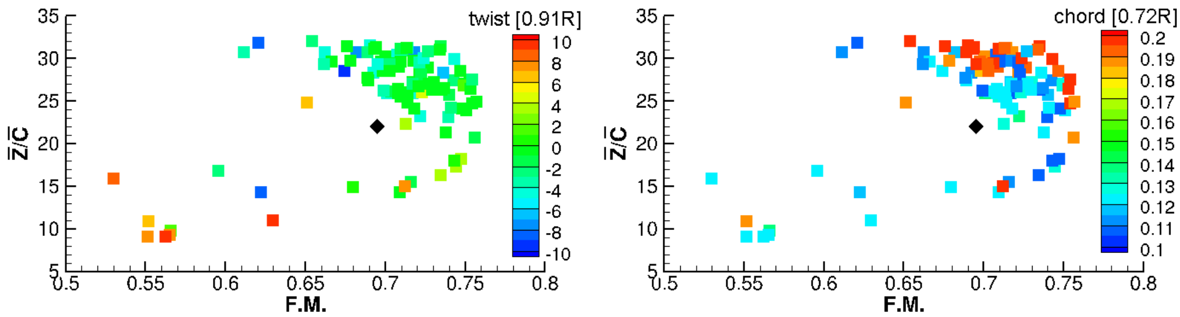

Figure 4.57: CFD simulated hover and forward flight performance of low-fidelity selected blades, coloured by values of twist at 0.91R (left) and chord at 0.72R (right)

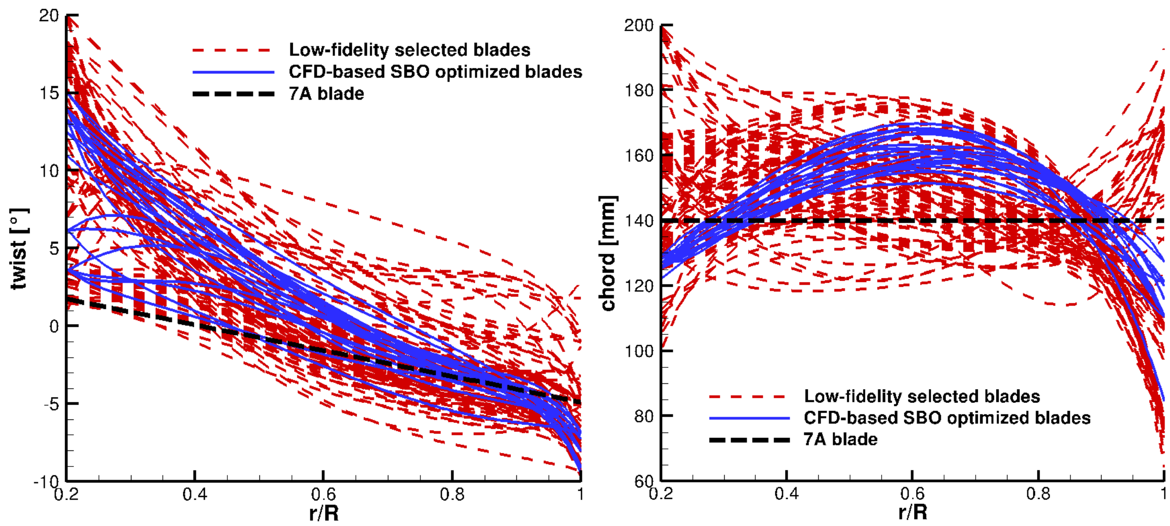

Figure 4.58: Twist (left) and chord (right) laws of CFD-based SBO optimal blades, compared to low-fidelity selected blades

pressure over the rotor disk of these individuals are compared to the 7A blade in Figure 4.62. The image shows that a significantly different dynamic pressure distributions are found

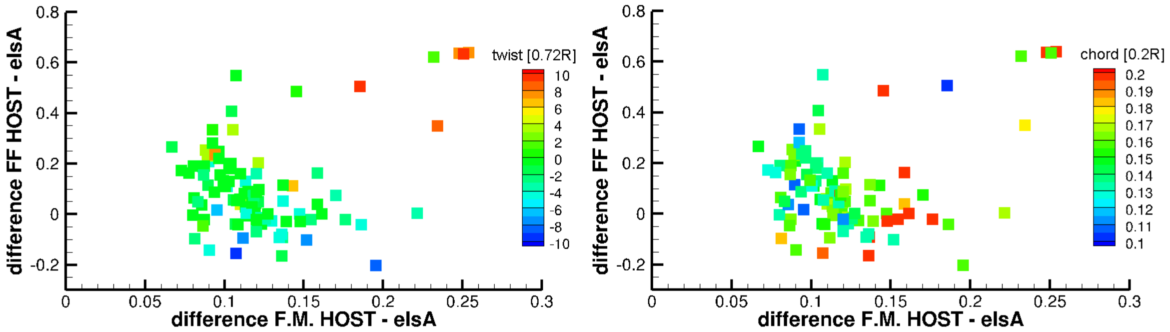

Figure 4.59: Comparison of HOST and *elsA* computed performance of 106 low-fidelity selected blades as coloured by twist value at 0.72R (left) and chord value at 0.2R (right)

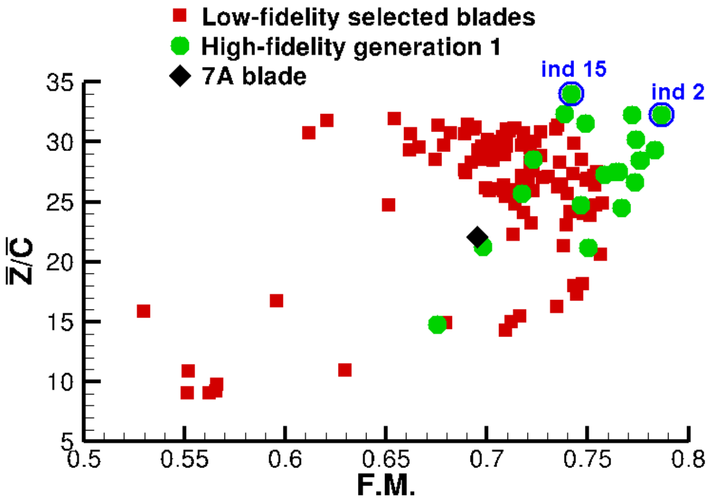

Figure 4.60: CFD performance results of low-fidelity selected blades, SBO-based optimized blades and 7A blade

for optimized and reference blades. The high positive dynamic pressure values at leading edges on advancing blade sides result from large negative pitching angles of blades. Indeed, rotor trims differ largely between optimized and 7A blades. Again, as for the local flow comparison of ORPHEE blades, rotor trim differences complicate local analysis of forward flight performance. This is also illustrated in Figure 4.63, which shows pressure distributions of the two selected individuals and the 7A blade at 0.85R of the advancing blade. Whereas the 7A blade generates a significant amount of lift at this section, optimized blades do not seem to generate much lift.

4.3 Conclusions on rotor blade optimizations

In this chapter, several optimization strategies were investigated and assessed. All of them are based on the use of a multi-objective Genetic Algorithm (GA), coupled with different simulation tools (HOST and/or *elsA*) and, eventually, surrogate models. Blade geometry was parametrized by means of Bézier curves, allowing to get different twist and chord distributions along the blade span, whereas airfoil geometry was kept fixed.

The influence of several parameters used in the GA, as the number of individuals in a generation, the number of generations required for convergence, and design parameter settings leading to a good compromise between cost and accuracy was selected. Precisely, typical

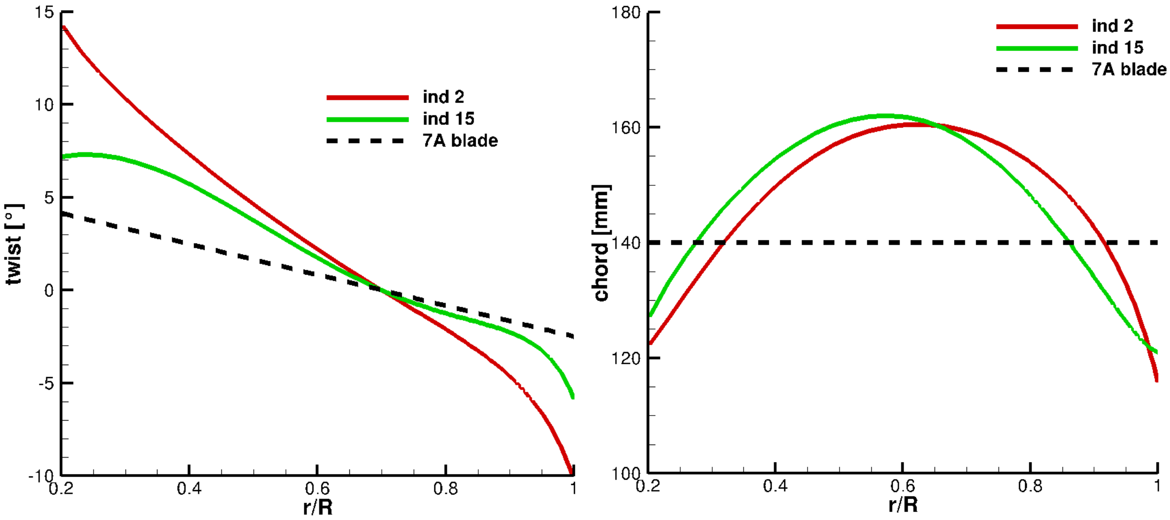

Figure 4.61: Twist and chord laws of selected individuals

population size and number of generations leading to a sufficiently converged and extended Pareto Front are identified (leading to a typical GA setting of 80 individuals evolving over 20 generations). Also, the effect of the mathematical form of response surface models (RSM) used for surrogate-based optimizations is investigated, allowing to select typical numbers of samples required in the initial Design of Experiments, the number and frequency of RSM update cycles, and the number of new sample points used for updating. The proposed settings are tested for HOST-based optimization runs, so that comparison with fully genetic optimizations (no RSM) is possible.

Knowledge acquired in these numerical experiments is finally used to set-up a multi-fidelity optimization strategy: initially, a HOST-based low-fidelity optimization is run to select interesting regions of the design space. Then, ranges of design parameters are restricted according to these preliminary findings, and a set of individuals representing a compromise between potentially optimal individuals according to the low-fidelity simulation tool and a good geometrical diversity for further investigations of the design space is selected. Such set is then simulated using the high-fidelity model (CFD), and a RSM is constructed. This RSM is used to further explore the design space and to refine the HOST-based Pareto Front using some high-fidelity information. The individuals of the resulting RSM Pareto Front are finally recomputed using CFD to get a finer estimate of their actual performance. The proposed procedure was shown to produce a set of blade designs possessing an improved performance (based on CFD estimates) with respect to HOST-optimized individuals, for a reduced turn-around time (less than 1 week), suitable for industrial applications.

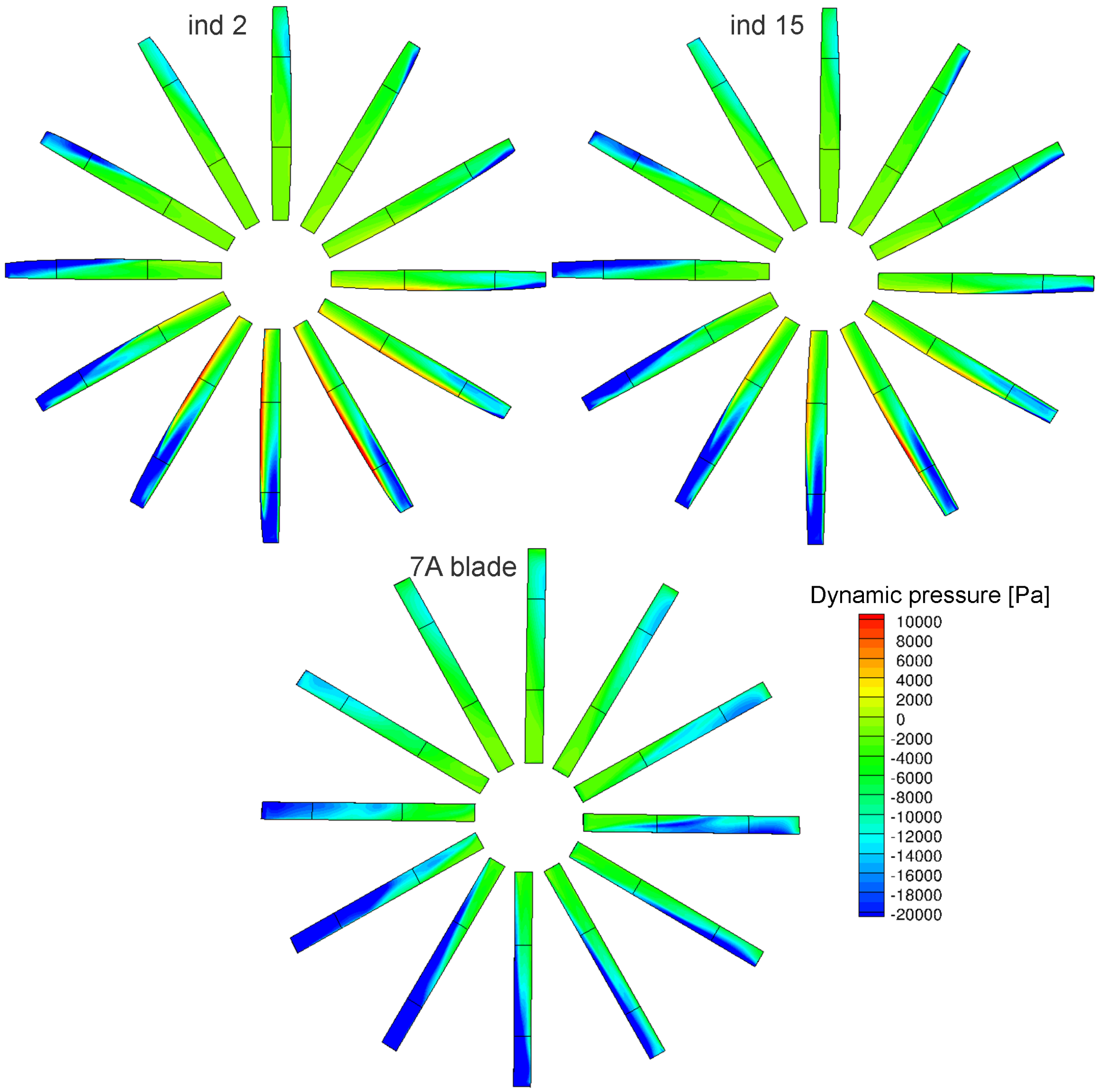

Figure 4.62: Dynamic pressure distributions over the rotor disk of 7A blade and individuals 2 and 15 of MFO generation 1

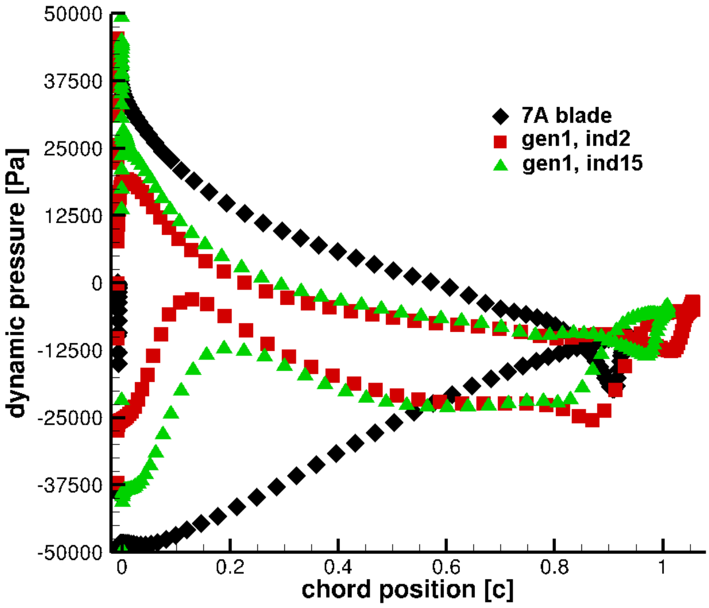

Figure 4.63: Dynamic pressure of 7A blade and individuals 2 and 15 of MFO generation 1, at 0.85R of advancing blade

Résumés en Français

Résumé chapitre 1

Le champ aérodynamique qui s'établit au voisinage des pales du rotor principal d'un hélicoptère diffère fondamentalement entre les deux principaux cas de vol habituellement rencontrés : le vol stationnaire et le vol d'avancement. En vol stationnaire, l'écoulement est axisymétrique autour de l'axe du mât rotor. En négligeant les vitesses induites dues aux sillages, la vitesse incidente localement perçue par les profils le long de l'envergure de la pale est fonction de la position radiale et de la vitesse de rotation. En vol d'avancement, cette vitesse locale devient aussi fonction de la vitesse propre de l'hélicoptère. Par conséquent, le vent incident localement perçu par les profils est dans ce cas fonction des positions radiale et azimutale, comme le montre la Figure 1.3. Les différences de vitesses locales entre la pale avançante et la pale reculante nécessitent des variations d'angle de pas sur un tour rotor afin d'équilibrer la portance rotor. De même, des variations d'angle de battement et de traînée existent afin d'alléger les efforts au niveau du mât rotor. Ces variations permettent d'équilibrer le rotor à tout instant lors d'une révolution.

La performance rotor en vol stationnaire est habituellement quantifiée par la Figure de Merit (F.M.), définies par l'équation 1.14. Ce paramètre représente l'efficacité du rotor à générer un effort de sustentation. En vol d'avancement, l'efficacité rotor est usuellement représentée par sa finesse, définie comme le rapport entre la portance générée par le rotor sur sa traînée (voir l'équation 1.18).

En complément des performances globales du rotor, divers phénomènes aérodynamiques peuvent être étudiés pour un aperçu plus local de l'écoulement. Il s'agit par exemple des tourbillons de saumon générés par les pales, qui modifient localement l'écoulement perçu par les pales suivantes, créant une structure complexe de sillage. Ce sillage interagit également avec le fuselage et les parties arrières. La vitesse induite est de l'ordre de 10 à 15 m/s en vol stationnaire, et de 0 à 8 m/s en vol d'avancement. En vol d'avancement, la vitesse locale du profil du saumon en pale avançante est transsonique, comme l'illustre la Figure 1.10. En pale reculante, la vitesse totale de la pale est égale à la vitesse locale due à la rotation à laquelle on retranche la vitesse d'avancement, ces deux vecteurs de vitesse étant de sens opposé. Près du mât rotor, la vitesse due à la rotation est plus faible que la vitesse d'avancement, et la vitesse totale de la pale est par conséquent localement négative. Dans ce cercle d'inversion, l'écoulement incident provient du bord de fuite.

Les pales du rotor principal des hélicoptères sont typiquement droites, présentent une envergure importante et un vrillage variant le long de l'envergure, comme le montre la Figure 1.13. Une pale est généralement définie géométriquement par le placement des profils et des lois de corde, vrillage, flèche et dièdre.

Différents critères peuvent être assignés aux profils, ce qui conditionnera la géométrie de la pale : un coefficient de portance maximal élevé, un nombre de Mach de divergence de traînée élevé, une finesse élevé pour une large plage de nombres de Mach, un faible coefficient de moment. Ces critères montrent les larges possibilités d'opérations sur les profils. Le placement des profils le long de la pale est mené habituellement afin d'augmenter l'épaisseur relative en partie interne, et de la diminuer vers le saumon.

Le vrillage permet d'orienter les profils en direction de l'écoulement. D'après la théorie de Froude, la puissance induite est minimale en vol stationnaire pour une loi de vrillage hyperbolique. En vol d'avancement, le vrillage est notamment adapté pour l'écoulement transsonique sur le saumon de la pale avançante. Aussi, les conditions de vol localement perçues par les sections de pale en vol d'avancement varient largement et le vrillage optimal varie donc autant sur le disque rotor. Combinant les deux cas de vol, une loi de vrillage de compromis doit être trouvée.

Comme pour le vrillage, la loi de corde optimale en vol stationnaire est une loi hyperbolique. En vol d'avancement, les extrémités de la pale ne génèrent pas beaucoup de portance et se placent dans des zones sensibles (cercle d'inversion et écoulement transsonique), ce qui implique la réduction de corde aux extrémités de la pale. A nouveau, un compromis entre le vol stationnaire et vol d'avancement doit être trouvé.

Un certain angle de dièdre peut être appliqué au saumon de pale afin d'écarter vers le bas le tourbillon de saumon. De même, un angle de flèche peut être imposé sur la partie extérieure de la pale dans le but de réduire le nombre de Mach effectif. Cependant, la conception du saumon est difficile car plusieurs phénomènes aérodynamiques apparaissent dans cette zone, rendant complexe l'anticipation de la performance rotor en fonction de variations locales de sa géométrie. Ceci rend également difficile la prédiction de l'influence du dièdre et de la flèche sur la performance globale. Pour ces raisons, la conception du saumon ne sera pas considérée dans le cadre de l'optimisation.

Dans les années 1990, le projet Optimisation d'un Rotor Principal d'Hélicoptère par l'Etude et l'Expérimentation (ORPHEE) a permis d'étudier quatre géométries de pale différentes. Ces pales diffèrent en loi de vrillage, loi de corde et forme en plan par rapport à une pale de référence. La Figure 1.26 montre les formes en plan de ces quatre pales. Des essais au banc balance pour le vol stationnaire et en soufflerie pour le vol d'avancement ont été effectué pour différentes conditions de vol. La pale EC4, avec loi de double flèche et double effilement, a la meilleure performance en vol stationnaire, comme l'illustre la Figure 1.28. La pale EC3, avec double effilement, présente la moins bonne performance pour ce cas de vol. Pour le vol d'avancement, l'inverse est observé, car l'EC3 donne les meilleures performances pour une large plage de conditions de vol en terme de charge rotor et vitesse d'avancement. L'EC4 est la moins bonne, mais ses performances s'améliorent avec l'augmentation de la charge rotor et de la vitesse d'avancement, par rapport aux autres pales. Les performances rotor en vol d'avancement sont présentées en Figures 1.29 et 1.30. Ces pales et les mesures correspondantes seront utilisées dans la suite pour l'évaluation des outils de simulation.

La conception des pales du rotor principal d'un hélicoptère requiert la recherche des solutions de compromis entre les deux cas de vol. Le jugement d'ingénieur ne permettant pas de trouver des solutions optimales pour ce problème multi-objectif, l'optimisation automatique semble par conséquent un outil adapté pour la conception des pales. Une optimisation de pale en vol stationnaire a déjà été réalisée dès 1987 [146], faisant appel à une méthode de gradient pour l'optimisation de corde et vrillage et utilisant un outil de simulation reposant sur la théorie de la ligne portante. Depuis, diverses optimisations ont été effectuées et publiées, utilisant ayant le plus souvent recours à des théories 2-D pour le calcul des performances rotor. La montée récente en puissance de calcul ouvre la voie au calcul de performance d'un grand nombre de géométrie de pales différents. Ceci s'accompagne d'une utilisation plus courante des algorithmes génétiques, qui demande un grand nombre d'évaluations de la fonction coût pour l'obtention du Front de Pareto, constitué de toutes les meilleures combinaisons de paramètres géométriques pour tous les objectifs. Ce nombre important d'évaluations est aujourd'hui un obstacle pour un couplage direct entre l'optimisation génétique et un code de calcul CFD permettant d'évaluer les objectifs. Des techniques d'optimisation comme les plans d'expérience et les surfaces de réponses ont cependant récemment ouvert la voie vers cette combinaison. La Figure 1.31 donne un aperçu des différents optimisations rotor publiées. En abscisse, la complexité de l'outil de simulation est croissante, des codes les plus simples reposant sur la théorie de la ligne portante jusqu'aux code de calcul CFD en vol d'avancement. En ordonnée, la complexité de l'optimiseur croît également, des méthodes fondées sur le calcul du gradient, en passant par les algorithmes génétiques qui recherche dans l'espace global, jusqu'aux techniques d'optimisation avancés.

Aujourd'hui les méthodes d'optimisation ainsi que les outils de simulation permettant l'évaluation des performances des géométries de pales existent, ce qui donne tous les ingrédients pour la création d'une boucle d'optimisation. Aussi, la montée en puissance de calcul permet d'entrevoir l'inclusion de la CFD dans une telle boucle. Néanmoins, divers défis doivent être relevés afin d'industrialiser cette boucle d'optimisation.

Tout d'abord, la validité des outils de simulation doit être évaluée, tout comme les avantages et limitations de chacun des outils. L'optimisation n'a seulement de sens que si les gains de performance des pales optimisées peuvent être reproduits en vol. Ceci implique que les outils de simulation doivent correctement prédire les performances rotor en fonction de la géométrie de pale. Ces vérifications sont à effectuer avant l'emploi de la boucle.

L'optimisation simultanée des géométries de pale en vol stationnaire et vol d'avancement est une obligation pour l'application industrielle de cette boucle d'optimisation. Même si l'optimisation mono-objectif est intéressante pour la compréhension des influences de géométrie sur la performance, les résultats ne peuvent pas être utilisés en industrie. L'optimisation multi-objectif est assurée par un algorithme génétique, ce qui demande un nombre important d'évaluations. Afin de réduire le coût de calcul, des techniques d'optimisation sont employés.

Enfin, la boucle d'optimisation est à valider par des optimisations des lois de vrillage et corde, séparément et simultanément. Deux outils de simulation sont utilisés, ainsi que divers méthodes et techniques d'optimisation. Aussi, la stratégie d'optimisation, proposée afin de répondre aux particularités de ce problème d'optimisation, est évaluée.

Résumé chapitre 2

à Eurocopter, deux outils de simulations sont employés pour la caractérisation des performances rotor. Dans le cadre de l'optimisation, la précision de prédiction est important, tout comme le temps de calcul. Le premier outil, HOST (Helicopter Overall Simulation Tool), est un code de simulation du mécanique de vol hélicoptère [29]. Le calcul des efforts aérodynamiques est traité par la théorie de la ligne portante. Le deuxième outil de simulation est le code de mécanique des fluides numérique *elsA* [35]. Ces outils diffèrent de par leur prise en compte des phénomènes physiques ainsi que le temps de calcul.

Plusieurs études sont effectuées afin d'évaluer la précision de calcul des deux outils de simulation. Aussi, divers paramètres de calcul sont testés afin de trouver les combinaisons menant à la meilleure prédiction de performances. Notamment le calcul des pales ORPHEE permet d'étudier l'effet des modifications géométriques sur les prédictions des performances. Par cette étude, plusieurs paramètres numériques sont évalués pour leur qualité de prévision. Ceci permet de trouver les paramètres donnant les meilleurs résultats de calcul. Aussi, la prédiction des différences de performance entre les quatre pales, conséquence des différences géométriques, est évaluée pour ces paramètres sélectionnés. En conclusion de cette étude, HOST permet d'estimer correctement l'effet de corde et flèche en vol stationnaire. La prédiction de l'influence de vrillage ne correspond pas aux mesures. Cependant, la précision de ces mesures est incertaine car les tendances ne correspondent pas aux attentes théoriques. En vol d'avancement, les différences de performance rotor sont correctement prédites pour les lois de vrillage et corde. L'effet de loi de flèche est systématiquement surévalué.

La prédiction du champ de vitesse induite est étudiée pour diverses vitesses d'avancement, par comparaison aux mesures de la NASA. Ces mesures sont effectuées légèrement au-dessus du disque rotor pour deux pales différentes et diverses vitesses d'avancement. Des modèles linéaires comme Meijer-Drees et Pitt & Peters permettent seulement de prédire des tendances globales du champ de vitesse induite. Les ordres grandeur sont mieux estimés par Pitt & Peters que par Meijer-Drees, mais les deux modèles manquent d'une description locale du champ. Les deux modèles basés sur sillage de forme fixe et libre, Metar et Mint, ne sont pas régulier en leur prédiction du champ de vitesse induite. Pour les cas test avec pale effilée, les prédictions sont relativement proches des mesures. Cependant, les mesures à hautes vitesses ne sont pas bien représentées par ces modèles sur une large zone du disque rotor. Enfin, le modèle FiSUW estime fidèlement les caractéristiques globales du champ de vitesse induite ; c'est pourquoi ce modèle est préféré dans la suite.

Le code de mécanique des fluides numérique *elsA* résout les équations de Navier-Stokes moyennées au sens de Reynolds (RANS) avec modèle de turbulence pour la fermeture du système. Dans cette étude, le modèle de turbulence $k-\omega$ de Menter avec correction SST et le modèle de seconde ordre de Speziale, Sarkar et Gatski (SSG) sont comparés. Pour la résolution du système, les schémas numériques de Jameson et AUSMp sont évalués. Le calcul d'un rotor en vol stationnaire repose sur la correspondance de l'écoulement pour chacune des pale, ce qui réduit le domaine de calcul à une seule pale et de conditions de périodicité, comme illustré en Figure 2.44. Pour le vol d'avancement, il faut prendre en compte le sillage du rotor complet, ce qui implique donc un maillage de toutes les pales. L'avancement en temps est assuré par un schéma de type Gear, suivant une séquence de trois calculs raffinant en pas de temps.

Afin d'étudier l'influence des certains paramètres de calcul, des mesures en soufflerie effectuées à la NASA du champ moyenné et turbulent autour d'une demi-aile sont comparées aux résultats des simulations. Cette étude montre que la dissipation numérique intrinsèque aux méthodes utilisées, ainsi qu'aux variations de taille des mailles, influence grandement les résultats. Cette dissipation peut être limitée par un raffinement du maillage, l'utilisation du schéma AUSMp plutôt que Jameson, et la modélisation de turbulence par modèle du second ordre. Cependant, même si le schéma AUSMp réduit le temps de calcul d'environ 10%, le raffinement de maillage et le passage du modèle de turbulence reposant sur l'hypothèse de Boussinesq vers un modèle du second ordre augmentent considérablement le temps de calcul.

à nouveau, des calculs sont effectuées sur les quatre pales ORPHEE afin d'évaluer l'influence des paramètres de calcul ainsi que la capacité de la CFD à reproduire la hiérarchie en performance des quatre pales. En vol stationnaire, les résultats issus du calcul de base, utilisant le mailleur VIS12, le schéma numérique AUSMp et le modèle de turbulence $k-\omega$, sont d'abord comparés aux mesures. Il apparaît que la hiérarchie en performance des quatre pales n'est pas complètement correctement prédite : l'EC4 reste au sommet de la hiérarchie pour le en vol stationnaire, mais la différence de performance entre l'EC1 et EC3 n'est pas correctement estimée.

Dans le but d'améliorer la prédiction des performances en vol stationnaire, des calculs avec modélisation du point de transition sont comparées aux calculs sans prise en compte de la position de transition d'un écoulement laminaire vers la turbulence. La prise en compte de la transition permet un accroissement des valeurs de performance rotor (F.M.) dû à la zone d'écoulement laminaire au bord d'attaque. En revanche, la hiérarchie des pales n'est pas modifiée par la prise en compte du point de transition.

L'effet de la densité de maillage est évalué en réalisant trois maillages de degré de raffinement différents. Le mailleur VIS12 présentant des difficultés à générer des maillages raffinés pour des pales non-rectangulaires (EC3 et EC4), le mailleur Autogrid est préferé pour cette étude et dans la suite pour les optimisations. Il apparaît que l'augmentation du raffinement du maillage résulte en une moins bonne convergence de calcul, due à la modélisation des phénomènes physiques instationnaires. Ceci implique que la convergence de maillage n'est pas atteinte et un maillage moins raffiné est préféré pour les calculs en vol stationnaire. Enfin, l'emploi d'un modèle du second ordre comme le modèle SSG offre des résultats de performance rotor très éloignés des mesures ou des résultats avec le modèle $k - \omega$.

En vol d'avancement, le paramètre $\bar{Z}/\bar{C}$ est utilisé comme représentation des performances rotor, car la traînée ne peut être calculé directement par la version d'*elsA* actuellement utilisée. La hiérarchie en performance rotor est seulement modifiée pour l'EC4 à forte vitesse d'avancement. Les calculs CFD sont effectués en partant d'une simulation HOST pour l'équilibre rotor correspondant aux conditions de vol. L'équilibre imposé pour HOST correspond à une charge moyenne pour un $\bar{Z}$ de 15, ce qui est approximativement ce que l'on retrouve par CFD pour les faibles vitesses d'avancement (230 et 280 km/h) mais pas pour les plus fortes vitesses d'avancement (315 et 350 km/h). Il semble que les champs aérodynamiques soient trop différents entre les simulations d'HOST et de la CFD, et qu'un rebouclage entre équilibre rotor et efforts calculés par CFD soit nécessaire pour les plus fortes vitesses d'avancement ($\mu \leq 0.37$). Ce rebouclage requiert au moins 2 calculs CFD en vol d'avancement, qui sont particulièrement coûteux, c'est pourquoi les fortes vitesses sont pour l'instant écartées pour l'optimisation. Pour les deux cas de vol à $\mu \leq 0.37$, l'influence du degré de raffinement du maillage de fond est mineure, ce qui fait que le maillage le plus grossier est préféré.

En résumé, HOST prédit correctement les performances rotor en vol stationnaire pour la loi de corde et de flèche. L'effet de loi de vrillage n'est pas correctement prédit, mais la qualité des mesures est mise en doute car les résultats de calcul correspondent aux attentes théoriques. Concernant les calculs CFD, l'influence de la forme en plan est prédite correctement, mais à nouveau la prévision de la loi de vrillage ne s'accorde pas aux mesures. Pour le vol d'avancement à faible vitesse d'avancement ($\mu \leq 0.37$), les outils HOST et CFD prédisent correctement l'influence des lois de corde et vrillage sur les performances rotor. L'effet de la loi de flèche n'est pas pris en compte par les deux outils de simulation. Même si aujourd'hui les capacités de prédiction sont égales pour les deux outils, les deux seront retenus dans la suite : HOST pour son faible coût de calcul, et la CFD pour les attentes d'amélioration de prédiction dans le futur.

Résumé chapitre 3

L'optimisation de pales du rotor principal d'un hélicoptère est un problème d'optimisation particulier et requiert une approche correspondant à ce problème précis. Afin de choisir la méthode d'optimisation la plus adaptée et de proposer une stratégie d'optimisation, les critères sont d'abord discutés. Premièrement, pour application industrielle, les géométries de pale doivent simultanément être optimisées pour les deux principaux cas de vol : vol stationnaire et vol d'avancement. Ceci implique la prise en compte de plusieurs objectives et contraintes dans la même optimisation. L'optimisation doit donc résulter en un ensemble de meilleures géométries de pales qui sont plus ou moins adaptées pour le vol stationnaire ou le vol d'avancement. Cet ensemble est généralement appelé Front de Pareto. Trouver le Front de Pareto permet à l'ingénieur d'ajouter d'autres objectifs ou contraintes dans le choix final d'une géométrie de pale. Si aujourd'hui seules les performances du rotor en vol stationnaire et vol d'avancement sont considérées, des objectifs et contraintes sur les efforts sur le rotor, la génération de bruit et la signature acoustique sont également à prendre en compte dans le choix d'une géométrie. La méthode d'optimisation doit donc être capable de prendre en compte au moins deux objectifs simultanément, voire plus dans le futur. Dans la boucle d'optimisation actuelle, deux outils sont implémentés pour l'évaluation des performances rotor. HOST est un code interne Eurocopter, mais *elsA* ne l'est pas. Dans le futur, d'autres outils peuvent être connectés à cette boucle afin d'évaluer d'autres objectifs et contraintes. Ceci nécessite cependant qu'aucune modification ne soit apportée aux outils de simulation pour leur connexion à la boucle d'optimisation. Un dernier critère concerne le nombre d'évaluations nécessaire pour trouver les optima. Ce nombre doit être limité afin de réduire le temps d'optimisation. Cependant, paralléliser des évaluations peut largement réduire ce temps total d'optimisation et ainsi permettre un nombre de simulations plus élevé. En total, l'optimisation doit être limitée à quelques heures pendant la phase de conception préliminaire, et d'ordre de quelques jours pendant la phase de conception détaillée. Avec un temps de restitution d'HOST de quelques minutes, et en faisant des simulations en parallèle, de nombreuses évaluations peuvent être effectués par cet outil de simulation. En revanche, la CFD demande quelques heures pour un calcul en vol stationnaire, et environ 60 heures pour un calcul en vol d'avancement, ce qui rend l'optimisation par calcul direct en série coûteuse en temps de calcul.

La méthode d'optimisation par algorithme génétique est retenue afin de répondre au mieux aux critères décrits. Les principaux avantages de cette méthode sont la prise en compte naturelle de plusieurs objectifs simultanément dans le but d'obtenir le Front de Pareto, et l'utilisation des outils de simulation comme une boîte noire, permettant ainsi de connecter n'importe quelle méthode de simulation à la boucle d'optimisation. L'inconvénient est le nombre d'évaluations plutôt élevé nécessaire pour obtenir les solutions optimales. Cependant, un certain nombre de simulations peut être lancés en parallèle, ce qui réduit le temps total d'optimisation.

Afin de réduire le nombre de simulations nécessaire pour trouver les optima, des techniques avancées d'optimisation sont employées. Il s'agit notamment des plans d'expérience et des surfaces de réponses. Un plan d'expérience est une manière de distribuer les points dans l'espace des paramètres qui permet de tirer le plus d'information possible en limitant le nombre de calculs. La technique d'échantillonnage hypercube Latin est choisie. Une surface de réponse est une modélisation mathématique des relations entre objectifs et paramètres. L'optimisation peut dès lors être effectuée utilisant ces fonctions, plutôt que les simulations complètes. Deux méthodes de surface de réponse seront testées : des fonctions polynômiales de deuxième ordre, ainsi que des Processus de Gauss qui reposent sur une fonction moyenne à laquelle sont ajoutées des fonctions de fluctuation. La libraire d'optimisation DAKOTA, développé par Laboratoire Sandia, est employée car elle contient toutes les méthodes et techniques d'optimisation recherchées.

Les différentes techniques d'optimisation présentées peuvent être combinées : un plan d'expérience initialise la première surface de réponse sur laquelle est effectuée l'optimisation. Des mises à jour de la surface de réponse dans les zones correspondant aux bonnes performances rotor permettent d'améliorer la qualité de prédiction dans la zone de solutions optimales. La Figure 3.8 schématise le principe d'une optimisation reposant sur une surface de réponse.

Une autre manière d'avancer vers les solutions optimales par calcul CFD tout en limitant le temps de calcul est l'optimisation multi-fidélité. Un exemple [46] regroupe des outils de faible et haute fidélité dans une surface de réponse combinée. Les performances calculées par les différents outils n'ont généralement pas la même valeur et les valeurs objectifs sont donc combiné dans une surface de réponse par une mise à l'échelle, comme le montre la Figure 3.9. Même si cette mise à l'échelle permet de rectifier les différences entre outils, une telle surface combinée ne peut être construite que si les gradients des performances rotor en fonction des variations géométriques sont comparables pour les deux outils. Cela est étudié par Wilke [151], qui calcule les performances rotor pour des modifications systématiques des paramètres géométriques. Ces calculs sont faits pour HOST avec diverses modèles de vitesse induite et des calculs CFD avec maillages plus ou moins raffinés. Les résultats montrent que les variations de corde, flèche et dièdre ont les mêmes tendances pour la plupart des calculs. En revanche, la prédiction des performances rotor en fonction des variations de vrillage au saumon diffère entre les calculs. Non seulement les ordres de grandeur changent largement avec l'outil de simulation, mais le vrillage de meilleure performance n'est également pas conservé. Cela veut dire que le gradient de la surface de réponse modifie avec l'outil de simulation, rendant impossible la construction d'une surface de réponse commune. L'idée d'une optimisation par surface de réponse multi-fidélité est ainsi écartée.

Une autre stratégie d'optimisation multi-fidélité est proposée : on commence par une optimisation par algorithme génétique avec l'outil de simulation de faible fidélité HOST. Les résultats de cette optimisation sont utilisées afin de réduire l'espace des paramètres et de sélectionner un série de géométrie de pales résultant en des bonnes performances rotor. Ces géométries seront utilisées dans la suite pour l'initialisation de la surface de réponse dans la phase haute-fidélité. L'optimisation repose sur cette surface de réponse, qui est améliorée par des mises à jour successives dans des zones de géométries intéressantes. Le processus de cette optimisation multi-fidélité est illustré par la Figure 3.11.

Résumé chapitre 4

Afin de valider la boucle d'optimisation, une validation pas à pas est effectuée. Ces optimisations ont pour but d'améliorer les performances de la pale 7A, qui est une pale droite et rectangulaire de référence, avec loi de vrillage aérodynamique linéaire. Une optimisation est d'abord effectuée à l'aide d'un algorithme génétique connecté à HOST. Ensuite, une nouvelle optimisation est réalisée en remplaçant l'algorithme génétique par une optimisation reposant sur des surfaces de réponse. Finalement, la stratégie d'optimisation est employée utilisant les deux méthodes d'optimisation et les deux outils de simulation. A chaque étape, divers tests sont menés afin de trouver les meilleures combinaisons de paramètres d'optimisation.

Une optimisation par algorithme génétique à l'aide de HOST est effectuée avec comme paramètres les lois de vrillage et corde séparément et simultanément. Les lois géométriques sont définies à l'aide de courbes de Bézier requérant 6 points de contrôle. Il apparaît que la position radiale des points de contrôle n'a pas d'influence significative sur le résultat de l'optimisation. Ces paramètres d'optimisation peuvent donc être enlevés, permettant ainsi une réduction du nombre de paramètres. Aussi, l'influence des objectifs est étudiée. On montre que considérer des objectifs sur la réduction de puissance rotor fournit les mêmes lois de corde optimales qu'en considérant des objectifs sur les performances rotor (F.M. en vol stationnaire et finesse en vol d'avancement). En revanche, ce n'est plus vrai quand on considère la loi de vrillage comme paramètre. Cette différence vient de la zone d'écoulement inversé côté pale reculante, où une traînée localement négative est générée, soulageant la traînée globale du rotor. Pourtant, la traînée s'oppose toujours à la rotation du rotor, augmentant le moment et donc la puissance nécessaire de passer cette partie du rotor. Cette opposition entre les directions de l'effort de traînée et le moment opposé à la rotation est illustrée à la Figure 4.15. De ce fait, une augmentation de la traînée dans le cercle d'inversion diminue la traînée rotor, mais ajoute de puissance rotor nécessaire, créant ainsi une différence entre les deux objectifs. C'est pourquoi les lois de vrillage obtenues sont différentes pour les deux objectifs. Dans la suite, des optimisations sont effectuées dans le but d'améliorer les performances rotor (donc F.M. et finesse rotor). Avec ces choix de paramètres et objectifs, des optimisations de vérification sont effectuées, séparément et simultanément pour les lois de vrillage et de corde. Des améliorations importantes sont obtenues, qui semblent provenir de modifications géométriques en partie intérieure de la pale. Aussi, des solutions optimales théoriquement attendues sont retrouvées avec fidélité par l'optimisation.

Ensuite, on compare les résultats issus de l'algorithme génétique à ceux obtenus par une optimisation reposant sur des surfaces de réponse. Deux modèles de surface de réponse sont proposés : des polynômes quadratiques et des Processus de Gauss. La précision de la surface de réponse faite avec des Processus de Gauss à la fin de l'optimisation s'avère meilleure que celle faite avec des polynômes. Une augmentation du nombre de points dans le plan d'expérience, du nombre de mises à jour de la surface de réponse pendant l'optimisation, et du nombre de point ajoutés à chaque mise à jour n'aboutit pas clairement à une amélioration des résultats de l'optimisation. La comparaison finale entre optimisation avec algorithme génétique et optimisation reposant sur des surfaces de réponse montre que l'optimisation de la corde résulte en les mêmes valeurs pour les objectifs et la géométrie optimale. Les optimisations de la loi de vrillage et simultanément vrillage et corde diffèrent, car l'optimisation faisant appel à des surfaces de réponse ne trouve pas de solutions notamment optimales pour le vol stationnaire. Ceci vient du fait que l'équilibre rotor en vol d'avancement est délicat à trouver pour des lois de vrillage à forts gradients, pourtant préférables pour les performances en vol stationnaire. L'algorithme génétique semble arriver à trouver des solutions en essayant plusieurs géométries. Par contre, le recours aux surfaces de réponse n'est seulement intéressant si un nombre réduit de géométries est testé par simulation. Certaines géométries peuvent donc être écartées si des moins bonnes performances sont trouvés pour des géométries proches. Pour cette raison, l'optimisation sur surface de réponse ne trouve pas les solutions optimales en vol stationnaire. Cependant, les gains en performance sont significatifs pour toutes les optimisations sur surface de réponse par rapport à la pale de référence. Aussi, pour l'optimisation sur surface de réponse, seulement 280 géométries de pale ont été testées, ce qui représente une diminution importante par rapport à l'optimisation par algorithme génétique, pour laquelle 1600 géométries ont été nécessaires.

Enfin, on effectue une validation de la stratégie d'optimisation. Cette optimisation est effectuée pour les lois de vrillage et corde simultanément, dans le but de maximiser les performances en vol stationnaire (F.M.) et vol d'avancement (finesse rotor). Pour la première étape, l'optimisation par algorithme génétique avec HOST est utilisée. Les résultats de cette optimisation montrent vers quels valeurs les paramètres tendent pour optimiser les deux objectifs (voir les Figures 4.52 à 4.55). La réduction de l'espace des paramètres est d'environ 35%. Aussi, la phase avec HOST permet de sélectionner des pales de géométrie intéressante pour l'initialisation de la surface de réponse à construire avec l'outil de simulation de haute fidélité. Cette sélection devrait fournir une large plage de géométries de pale afin de générer une surface de réponse de haute qualité. Il n'est pas attendu que les pales optimales vu par HOST soient aussi optimales pour la CFD. Les géométries définissant le Front de Pareto obtenues avec HOST ne sont donc pas sélectionnées pour l'initialisation de la phase haute-fidélité. En fait, les géométries des pales des générations 6 et 10 sont retenues, car elles montrent une amélioration de performance par rapport à la pale de référence, sans pour autant avoir convergé vers une sélection géométriquement restreint de l'optimum. Les performances de 106 géométries ainsi obtenues sont calculées par la CFD en vol stationnaire et en vol d'avancement. Il apparaît que ces pales présentent des meilleures performances que la pale de référence, ce qui est prédit autant avec HOST que par CFD. La correspondance de ces résultats augmente le niveau de confiance que l'on a en les résultats issus de l'optimisation. L'optimisation sur la surface de réponse créée à partir de ces résultats CFD permet de chercher des meilleures géométries de pale. Effectivement, l'optimisation aboutit à des géométries présentant de meilleures performances, autant en vol stationnaire qu'en vol d'avancement, par rapport à la pale de référence et par rapport aux pales sélectionnées à partir de l'optimisation avec HOST.

La validation de la boucle d'optimisation est faite pas à pas, commençant par une optimisation par algorithme générique avec HOST, puis en utilisant une surface de réponse, et finalement par la stratégie d'optimisation proposée dans ce mémoire. D'une part, la boucle d'optimisation est validée car elle permet de trouver de meilleures géométries de pale, mais aussi de trouver les résultats théoriquement attendus. D'autre part, ces études mettent en évidence les paramètres les plus adaptés pour l'utilisation de la boucle d'optimisation.

Conclusions and perspectives

Conclusions

The aerodynamic design of helicopter rotor blades is a particularly difficult problem due to the diversity of flight conditions that have to be taken into account, namely hover and forward flight. In forward flight, local variations of angle-of-attack and velocity as seen by airfoil sections lead to complicated relations between blade geometry and rotor performance. In addition, complex flow phenomena, such as transonic flow, dynamic stall, reversed flow and wake structure occur over the rotor disk. Differences in aerodynamic flow field between the two flight conditions lead to just as different optimal blade geometries.

An industrial blade design needs to account for both flight conditions simultaneously. As the design problem is too complicated to find a solution by expert judgement, automated optimization is a proficient tool for designing helicopter rotor blades. Simultaneous consideration of conflicting requirements for hover and forward flight is an important step forward in finding compromise solutions that comply with industrial demands. To this purpose, an optimization loop is built by coupling an optimization algorithm with rotor performance simulation tools. Even if these elements taken apart are not new, optimization loops have become feasible only recently thanks to improved simulation accuracy and increased computational power.

Simulation accuracy is a crucial issue in rotor blade design because the usefulness of optimization results strongly depends on the reliability of simulation models. Rotor performance predictions at Eurocopter are based on two simulation tools: comprehensive rotorcraft code HOST and Computational Fluid Dynamics (CFD) software *elsA*. The aerodynamics model in HOST [29] is based on lifting line theory in which loads over 2D blade elements are estimated using local flow characteristics and look-up tables of aerodynamic coefficients. CFD software *elsA* [35] solves the discrete RANS equations on multi-block structured computational meshes.

Recent increases in computational power allows testing large quantities of blade geometries with low-cost simulation methods, or a smaller number on costlier CFD simulations. Genetic algorithm optimization, accounting simultaneously for both flight conditions, can thus be used in combination with HOST simulations. For employment of CFD computations within the optimization loop other techniques are to be explored.

The current work presents major advances in industrial rotor blade optimization: first, simulation tools are assessed to acquire knowledge on their accuracy, limits and best computational settings. Secondly, an optimization strategy is developed to provide blade designs within the industrial limited return times. Finally, these simulation and optimization methods are combined into an optimization loop that is validated by various tests.

Validity of rotor performance simulation tools is investigated to qualify rotor performance prediction capabilities and limitations of both methods. To assess representation of the induced velocity field by various HOST models, comparisons to NASA measurements are performed. The induced velocity model FiSUW [25] turned out to provide the best estimation of this field. For CFD assessment, experimental data of wing tip vortex formation and transport are compared to numerical simulations. From this study, the numerical scheme AUSMp is selected for its reduced dissipation and lower computational effort. The ability of both simulation tools to capture hover and forward flight rotor performance as a function of blade geometry is evaluated by comparison to measurements for a set of rotor blades extensively investigated in the framework of the ORPHEE project. It appeared that HOST correctly predicts the effect of chord and sweep laws in hover, and of twist and chord laws in forward flight. Elastic blade deformations are found to have a moderate impact on the predicted performance, so that a rigid blade model was preferred for simplicity. *elsA* correctly foresees the effect of chord and sweep laws on hover performance and of twist and chord in forward flight. From this study, coarse meshes and $k - \omega$ turbulence modelling are recommended.

Another validation aspect of the optimization loop concerns optimization tools. Main requirements for this particular industrial design problem are simultaneous consideration of multiple objectives, the search for globally optimal solutions and non intrusiveness so that any simulation tool can be easily used within the optimization loop. These criteria lead to the choice of genetic algorithms. As such algorithms require a high number of function evaluations, only HOST-based optimizations are performed with genetic algorithms directly. For CFD simulations, we considered advanced optimization techniques to further reduce the number of cost function evaluations. Design of Experiments (DoE) provides an intelligent distribution in the design space to gather as much information on relations between parameters and objectives by running as few simulations as possible. Response Surface Modelling (RSM) is used to generate analytical functions that relate design parameters with optimization objectives and constraints. In a Surrogate Based Optimization (SBO), an initial response surface is created from simulations in points chosen by the DoE. The actual optimization is then performed on this surrogate model. Successive surrogate update steps are used to improve response surface quality in interesting zones when approaching the optimum. Gaussian Processes were selected as surrogate model of the present design problem. Comparison of full genetic algorithm optimizations to SBO shows that results may be similar while requiring up to 80% less cost function evaluations. But, random parameters used to construct the RSM, especially DoE distribution, appear to influence SBO results largely. Several questions on exact implementation of SBO remain as they depend on the precise design problem and should be further investigated in the future.

In spite of significant cost reductions enabled by SBO, the total computational cost still remained too high for forward flight CFD simulation. For this reason, we proposed a hierarchical optimization strategy, combining simulation methods within the same optimization. While being the most straightforward solution, a combined low- and high-fidelity simulation response surface was not possible in this particular design problem: not only absolute performance values differ between both simulation tools, but also trends of rotor performance as a function of blade geometry are not always similar. Therefore, a different Multi-Fidelity Optimization (MFO) strategy was proposed. First, a genetic algorithm optimization is performed based on low-fidelity, low-cost HOST simulations to explore the design space. This allows reducing the design space by analysis of low-fidelity optimal results and selecting an extended set of "interesting" blade geometries that are used to initialize the CFD-based surrogate model. This model is used in the subsequent CFD-based optimization step.

To validate the optimization loop, first HOST-based genetic algorithm optimizations are executed. Optimizations are performed using objectives on Figure of Merit (F.M.) and Lift-to-Drag ratio (L/D) and geometry laws based on Bézier curves with 6 control points at fixed spanwise positions. An extended set of 80 individuals is preferred for achieving large spread along the Pareto Optimal Front. Single- and two-objective optimizations of twist, chord and combined twist & chord laws are performed. Theoretically expected optimal solutions for twist and chord laws in hover are found, validating the optimization loop. Genetic algorithm optimizations are compared to Surrogate Based Optimizations. In general, SBO allows for a great reduction of the number of simulations required to find optimal blade geometries, even if these may be less optimal than for full genetic algorithm optimizations. Finally, the multi-fidelity optimization strategy is tested and provides consistent results compared to earlier optimizations. The MFO strategy reduces the number of required CFD simulations sufficiently to include CPU-costly forward flight CFD simulations in the optimization loop while respecting the industrial return time of a couple of days. The performance gains of blade geometries obtained from MFO can be trusted, as these are based on both simulation tools. For these two reasons, the MFO strategy is particularly interesting for including CPU-costly simulations in an industrial optimization loop.

In summary, this work provides a contribution to an industrial framework for aerodynamic optimization of helicopter rotor blades. Improved knowledge on rotor performance simulation accuracy, combined with employment of advanced optimization techniques provides Eurocopter with a feasible and efficient automated design technique.

Perspectives

The present work has provided answers to several questions about rotor optimization, but new questions are raised as well. Ideas for improvements of the current state of the art are given next.

A major research topic concerns simulation accuracy. As shown by NASA's Fundamental Aeronautics Program to improve rotor performance simulation prediction accuracy by 35% [164], these simulations are not yet as accurate as for fixed-wing aircraft. This large improvement margin implies that rotor computations are not yet mature enough to provide accurate performance predictions in all flight cases. HOST simulations may be improved by better induced velocity modelling in hover and at high-speed forward flight. Also modelling of blade elasticity of non-rectangular blades is expected to improve positioning of the blade with respect to the wake structure, and thereby its aerodynamic response.

For CFD simulations, various axes of improvement can be given as well: CFD computations accuracy has to be improved, mainly to better preserve the wake structure. To this end, mesh refinement is expected to be an important factor, but requires increased computational power. Automatic mesh refinement techniques may alleviate this aspect. Higher-order numerical schemes also help limiting numerical dissipation. And as seen, improved turbulence modelling also plays a major role. Even if transition modelling was neglected in the present work, it is expected that laminar flow exists over the leading edge, so that the present fully turbulent approximation causes a too high drag and alters stall characteristics. Once a better flow field accuracy level is achieved, transition computation is to be considered in rotor computations. As demonstrated in the ORPHEE study, rotor harmonics calculation by HOST as required for forward flight CFD simulations is inaccurate at high-speed forward flight. This may resolved by either improving HOST's simulation, or by coupling of HOST and CFD simulations. The latter solution implies performing at least two forward flight CFD simulations so that total simulation time increases significantly.

Concerning optimization tools, further work is required about surrogate modelling. Specific issues that have to be resolved concern the distribution of points within the DoE, the choice of a suitable surrogate model for irregular response surfaces and the best way of updating the response surface during the optimization.

The present optimization loop only considers aerodynamic performance design goals by optimization of the external blade shape. Industrial requirements on rotor loads, acoustics, vibrations and production are verified a posteriori to the optimization. To create a more industrial blade design framework, incorporation of additional objectives and constraints within the optimization is required. This implies that more simulation tools need to be included in the optimization loop. The generic architecture of the proposed loop allows for easy implementation of different cost function solvers, but validation studies, as performed here for HOST and *elsA*, are required. Furthermore, optimization parameters on the internal blade structure are to be added. This is not only required for evaluating objectives and constraints on blade production, but will also allow for improved prediction of all other industrial requirements. In fact, it is expected that incorporation of blade deformation modifies aerodynamic performance optimization results. The inclusion of objectives on rotor loads, vibrations and acoustics all involve aeroelastic coupling effects as well. A future industrial optimization framework is sketched in Figure C.1, comparing to today's available optimization loop.

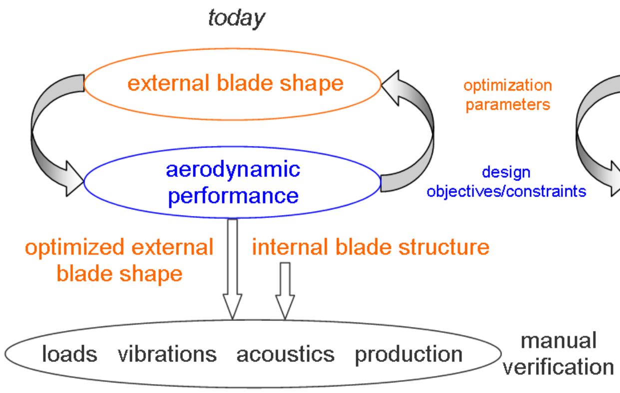

Figure C.1: Today's and future aspects within the optimization loop

Including objectives on robustness of blade geometries may also enhance confidence for industrial applications. Uncertainty quantification methods may also help in assuring robustness of selected blade geometries. The DAKOTA optimization library offers these capabilities.

A last idea for enhanced use of optimization results concern treatment of large data sets. Visualization of high-dimensional design problems is complicated, making it difficult to understand relations between design variables and optimization objectives. Statistical analysis of results may help finding these relations. Preferably, specific tools for this goal should be evaluated.

All these ideas show how vast the rotor optimization framework is, spanning various disciplines.

Conclusions et perspectives en Français

Conclusions

La conception aérodynamique des pales du rotor principal d'un hélicoptère est un problème particulièrement difficile du fait de la diversité des conditions de vol qui doivent être prises en compte, à savoir le vol stationnaire et le vol d'avancement. En vol d'avancement, des variations locales d'incidence et de vitesse vue par les profils résultent en des relations complexes entre la géométrie de pale et les performances rotor. De plus, des phénomènes complexes, comme l'apparition d'un écoulement transsonique au voisinage du saumon, le décrochage dynamique, d'écoulement inversé et la génération du sillage, apparaissent sur le disque rotor. Ces différences entre les deux conditions de vol résultent en des géométries de pale optimales aussi différentes.

La conception industrielle des pales doit prendre en compte les deux conditions de vol simultanément. Ce problème de conception est trop complexe pour trouver des solutions par jugement de spécialiste. De par ce fait, l'optimisation automatisée est un outil adapté pour la conception des pales d'hélicoptère. La considération simultanée des critères pour le vol d'avancement et le vol stationnaire est une avancée importante pour trouver des solutions de compromis qui satisfassent les exigences industrielles. Dans ce but, une boucle d'optimisation est construite en couplant un algorithme d'optimisation avec des outils de simulation des performances rotor. Même si chaque outil isolé n'est pas nouveau, la boucle d'optimisation est récemment devenue réalisable grâce à l'amélioration récente de la précision de simulation et l'augmentation de la puissance de calcul disponible.

La précision de simulation est un point crucial pour la conception des pales puisque l'utilité des résultats de l'optimisation dépend largement de la fiabilité des modèles de simulation. La prédiction des performances rotor à Eurocopter repose sur deux outils de simulation : le code de mécanique de vol des hélicoptères HOST et le code de mécanique des fluides numérique (Computational Fluid Dynamics ; CFD) *elsA*. Le modèle aérodynamique d'HOST est basé sur la théorie de ligne portante, pour laquelle les efforts sur des éléments 2D sont estimés par les caractéristiques locales de l'écoulement et des polaires tabulées des profiles pour les coefficients aérodynamiques [29]. Le code CFD *elsA* résout les équations RANS discrétisés sur des maillages structurés [35].

L'augmentation récente de la puissance de calcul permet de tester des grandes quantités de géométries de pale avec des outils de simulation à faible coût, ou un nombre plus faible avec des simulations de type CFD. L'optimisation par algorithme génétique, qui prend en compte les deux conditions de vol simultanément, est donc possible pour des simulations avec HOST. Pour l'emploi des calculs CFD dans la boucle d'optimisation, d'autres techniques d'optimisation sont à explorer.

Le mémoire présente des avancées majeures pour l'optimisation industrielle des pales du rotor : premièrement, les outils de simulation sont évalués afin de connaître leur précision de calcul, les limites et les paramètres numériques mieux adaptés. Ensuite, une stratégie d'optimisation est développée dans le but de fournir des conceptions de pale en une période de temps acceptable en industrie. Enfin, ces outils de simulation et d'optimisation sont combinés dans une boucle d'optimisation qui est validée par diverses tests.

La validité des outils de simulation des performances rotor est évalué afin de qualifier la capacité et les limitations des outils à prédire ces performances. La représentation du champ de vitesse induite par diverses modèles proposés dans HOST est évaluée par comparaison aux mesures effectuée à la NASA. Le modèle de vitesse induite FiSUW [25] s'avère fournir la meilleure estimation de ce champ. Pour l'évaluation de la CFD, des données expérimentales de la formation et du transport d'un tourbillon de saumon d'une aile sont comparées aux simulations numériques. À partir de cette étude, le schéma numérique AUSMp est sélectionné pour sa dissipation numérique limitée et le faible coût de calcul qu'il engendre. La capacité des deux outils de simulation à prédire les performances rotor en vol stationnaire et vol d'avancement est évaluée par comparaison aux mesures d'une série de pales étudiée en détail dans le cadre du projet ORPHEE. Il s'est avéré qu'HOST prédit correctement l'effet des lois de corde et flèche en vol stationnaire, et des lois de vrillage et de corde en vol d'avancement. La prise en compte des déformations élastiques de la pale paraît influencer seulement légèrement la prédiction des performances, ce qui fait qu'une modélisation de pale rigide est préférée pour sa simplicité. *elsA* prévoit correctement l'effet de corde et flèche en vol stationnaire, et de vrillage et corde en vol d'avancement. Cet étude résulte en la recommandation d'utiliser des maillages relativement grossier et un modèle de turbulence $k - \omega$.

Un autre aspect de validation de la boucle d'optimisation concerne les outils d'optimisation. Les principaux critères pour ce problème industriel sont la prise en compte simultanée de plusieurs objectifs, la recherche pour des solutions globalement optimales, sans aucune modification des outils de simulation ce qui permet de facilement incorporer des codes dans la boucle d'optimisation. Ces critères mènent à choisir pour des algorithmes génétiques. Le nombre d'évaluations de la fonction coût relativement élevé pour cet algorithme fait que seulement les optimisations fondées sur des calculs HOST peuvent être effectué avec des algorithmes génétiques directement. Pour des calculs CFD, on a considéré des techniques d'optimisation avancées afin de réduire au minimum le nombre d'évaluations de la fonction coût. Des plans d'expérience apportent une distribution intelligente dans l'espace des paramètres afin de récolter le plus d'information possible des relations entre paramètres et objectifs en utilisant le moins de simulations possible. Des surfaces de réponse sont utilisées afin de générer des fonctions analytiques qui relient les paramètres de conception et les objectifs et contraintes de l'optimisation. Dans une optimisation reposant sur des surfaces de réponse, une surface de réponse initiale est construite à partir des simulations en des points choisis par le plan d'expérience. L'optimisation réelle est effectuée ensuite sur la surface de réponse. Des mises à jour successives sont utilisées afin d'améliorer la qualité de la surface de réponse en les zones d'intérêt où des solutions optimales sont approchées. Une modélisation par "Gaussian Processus" a été sélectionnée comme modèle de surface de réponse pour le problème de conception actuel. Des optimisations complètes par algorithme génétique sont comparées aux optimisations basées sur surface de réponse. Ces comparaisons montrent que les résultats peuvent être similaires, alors que l'optimisation sur surface de réponse nécessite jusqu'à 80% moins d'évaluation de la fonction coût. Mais, des paramètres aléatoires utilisés pour la construction de la surface de réponse, en particulier la distribution du plan d'expérience, s'avèrent largement influencer les résultats de l'optimisation sur surface de réponse. Plusieurs questions concernant l'implémentation exacte des optimisations sur surface de réponse restent à resoudre, car elles dépendent du problème de conception exacte et doivent être investigué plus en détail dans le futur.

Malgré les réductions de coût significatives, le coût total de calcul reste toujours encore trop élevé pour des simulations CFD en vol d'avancement. Pour cette raison, on a proposé une stratégie d'optimisation hiérarchique, qui combine les deux outils de simulation dans la même optimisation. Alors que la solution directe serait de créer une surface de réponse qui combine les résultats des outils de simulation de faible et haute fidélité, ceci n'est pas possible pour ce particulier problème d'optimisation : pas seulement les valeurs absolus des performances rotor diffèrent entre les outils de simulation, aussi les tendances des performances rotor en fonction de la géométrie de pale ne sont pas toujours similaires. En conséquence, une autre stratégie d'optimisation multi-fidélité est proposée. Tout d'abord, une optimisation avec algorithme génétique est effectuée, utilisant les calculs sur le modèle de faible fidélité et faible coût HOST afin d'explorer l'espace des paramètres. Cette phase permet de réduire l'espace des paramètres par l'analyse des résultats optimaux et de sélectionner des géométries de pale "intéressantes" qui seront utilisées dans la suite pour l'initialisation de la surface de réponse créée à partir des calculs CFD. Ce modèle est utilisé pendant la phase haute-fidélité d'optimisation sur surface de réponse basée sur calculs CFD.

Afin de valider la boucle d'optimisation, on a d'abord réalisé des optimisations avec algorithme génétique et HOST. Des optimisations sont effectuées avec comme objectifs la maximisation de la Figure de Mérite (F.M.) et de la finesse, en utilisant des lois géométriques construites par courbes de Bézier avec 6 points de contrôle à des points radial fixes. Un ensemble étendu à 80 individus est préféré pour atteindre un Front de Pareto étalé. Des optimisations avec un et deux objectifs pour des lois de vrillages, de corde et de vrillage et corde combiné sont effectuées. Des solutions théoriquement attendues pour les lois de vrillage et de corde en vol stationnaire sont trouvées, ce qui valide la boucle d'optimisation. Des optimisations par algorithme génétique sont comparées aux optimisations basées sur surface de réponse. En général, l'optimisation sur surface de réponse permet une grande réduction du nombre de simulations nécessaires pour la recherche des géométries de pale optimales, même si ces pales peuvent être moins optimales que celles obtenues des optimisations par algorithme génétique. Au final, la stratégie d'optimisation multi-fidélité est testée et donne des résultats cohérents avec les optimisations effectuées précédemment. La stratégie multi-fidélité réduit le nombre de simulations CFD significativement, ce qui permet d'inclure les calculs coûteux de CFD en vol d'avancement dans la boucle d'optimisation, tout en assurant un temps de retour acceptable en industrie. On peut avoir confiance en les gains de performance rotor obtenus par la stratégie d'optimisation puisqu'ils sont basés sur les deux outils de simulation. Pour ces deux raisons, la stratégie d'optimisation multi-fidélité est particulièrement intéressante pour inclure des calculs coûteux en temps CPU dans une boucle d'optimisation industrielle.

En résumé, cette thèse fournit une contribution pour l'optimisation aérodynamique des pales du rotor des hélicoptères dans un cadre industriel. Des connaissances améliorées de la précision de calcul des performances rotor, combinées à l'emploi des techniques d'optimisation avancées apporte à Eurocopter une technique de conception automatisée efficace.

Perspectives

Cette thèse fournit des réponses à diverses questions concernant l'optimisation rotor, mais d'autres questions ont aussi été souslevées. Des idées pour des améliorations de l'état de l'art actuel sont données dans la suite.

Un sujet principal de recherche concerne la précision des simulations. Comme le démontre le projet de la NASA, Fundamental Aeronautics Program [164], qui cherche à augmenter la précision de prédiction des charges et performances rotor de 35%, ces simulations ne sont pas encore aussi précises que celles des avions à voilure fixe. Cette large marge d'amélioration implique que les calculs rotor ne sont pas encore suffisamment matures en vue de fournir des prédictions de performances en tous les cas de vol. Des simulations HOST peuvent être améliorées par une meilleure description des champs des vitesses induites en stationnaire et en vol d'avancement à forte vitesse. Aussi, la modélisation de la souplesse des pales non-rectangulaires est attendue d'améliorer le positionnement de la pale par rapport au champ de sillage, ce qui modifierait la réponse aérodynamique.

Pour les simulations CFD, divers axes d'amélioration peuvent être préparés : la précision des calculs CFD doit être améliorée, notamment pour une meilleure conservation du sillage. Dans ce but, le raffinement du maillage est considéré comme un facteur important, mais ceci demande une puissance de calcul accrue. Le raffinement du maillage automatique peut alléger cet aspect. Des schémas numériques d'ordre élevé peuvent également aider à limiter la dissipation numérique. Et, comme démontré dans ce mémoire, la modélisation de la turbulence joue également un rôle important. Même si la modélisation de la transition est négligée dans ce travail, il est attendu qu'un écoulement laminaire existe sur le bord d'attaque, ce qui fait que l'approche actuelle d'un écoulement tout turbulent résulte en une prédiction de traînée trop important et une modification des caractéristiques de décrochage. Une fois qu'une meilleure précision de la prédiction du champ d'écoulement est réalisée, le calcul du point de transition devrait être pris en compte dans les calculs rotor. Comme démontré lors de l'étude ORPHEE, le calcul des harmoniques rotor fait par HOST et nécessaire pour des calculs CFD en vol d'avancement, n'est pas précise à grande vitesse d'avancement. Ceci peut être résolu par une amélioration de la simulation d'HOST, ou par le couplage des simulations d'HOST et de la CFD. Néanmoins, cette dernière solution demande au moins deux calculs CFD en vol d'avancement, ce qui augmente considérablement le temps de calcul.

Concernant les outils d'optimisation, des études additionnelles sont nécessaires pour la modélisation par surface de réponse. Des questions spécifiques qui restent à résoudre concernent la distribution des points dans le plan d'expérience, le choix d'une modèle adéquat pour des surfaces de réponse irrégulières et la meilleure manière de mise à jour de la surface de réponse pendant l'optimisation.

La boucle d'optimisation actuelle considère seulement les performances aérodynamiques comme objectifs d'optimisation pour la forme extérieure de la pale. Des critères industriels pour les charges rotor, l'acoustique, les vibrations et de production sont seulement vérifié a posteriori. Afin de créer une boucle d'optimisation de conception de pale plus industrielle, l'inclusion d'objectifs et contraintes additionnelles est nécessaire. Ceci implique que d'autres outils de simulation doivent être inclus dans la boucle d'optimisation. L'architecture générique de la boucle d'optimisation proposée permet un implémentation facile des différents codes de calcul de la fonction coût, mais des études de validation, comme effectuées ici pour HOST et *elsA*, sont nécessaires. De plus, des paramètres d'optimisation de la structure interne de la pale sont à ajouter. Ceci n'est pas seulement demandé pour l'évaluation des objectifs et contraintes concernant la production de pale, mais aussi afin de permettre l'amélioration de prédiction d'autres critères industrielles. Au fait, il est attendu que l'incorporation des déformations de pale modifient les résultats de l'optimisation en termes de performances aérodynamiques. L'inclusion des objectifs de charges rotor, vibrations et acoustique tous également concernent le couplage aéro-élastique. Une future boucle d'optimisation industrielle est schématisée en Figure C.1, comparée à la boucle d'optimisation disponible aujourd'hui.

L'ajout des objectifs concernant la robustesse des géométries de pale peut également améliorer la confidence pour des applications industrielles. Des méthodes d'évaluation de l'incertitude peuvent aider à assurer la robustesse des géométries de pale sélectionnées. La librairie d'optimisation DAKOTA propose ces capacités.

Une dernière idée de l'utilisation améliorée des résultats d'optimisation concerne le traitement de grandes séries de données. La visualisation des problèmes de conception avec beaucoup

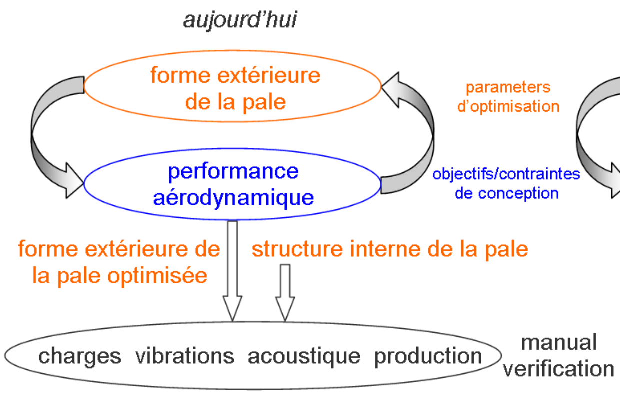

Fig. C.1: Boucle d'optimisation disponible aujourd'hui et dans le futur

de dégrés de liberté est complexes, ce qui rend difficile la compréhension des relations entre paramètres de conception et objectifs d'optimisation. L'analyse statistique des résultats peut aider à trouver ces relations. De préférence, des outils dédiés à cette tâche sont à employer.

Toutes ces idées montrent l'envergure de l'optimisation rotor, couvrant diverses disciplines.

Bibliography

[1] B.M. Adams, K.R. Dalbey, M.S. Eldred, D.M. Gay, L.P. Swiler, W. J. Bohnhoff, J.P. Eddy, K. Haskell, and P.D. Hough. DAKOTA, A Multilevel Parallel Object-Oriented Framework for Design Optimization, Parameter Estimation, Uncertainty Quantification, and Sensitivity Analysis Version 5.0 Reference Manual. 2009.

[2] B.M. Adams, K.R. Dalbey, M.S. Eldred, D.M. Gay, L.P. Swiler, W.J. Bohnhoff, J.P. Eddy, K. Haskell, and P.D. Hough. DAKOTA, A Multilevel Parallel Object-Oriented Framework for Design Optimization, Parameter Estimation, Uncertainty Quantification, and Sensitivity Analysis. Version 5.0 User's Manual. 2009.

[3] C.B. Allen, A.M. Morris, and T.C.S. Rendall. Development of Generic CFD-Based Aerodynamic Optimisation Tools for Helicopter Rotor Blades. In *25th AIAA Applied Aerodynamics Conference*, 2007.

[4] C.B. Allen, A.M. Morris, and T.C.S. Rendall. CFD-Based Aerodynamic Shape Optimization of Hovering Rotors. In *27th AIAA Applied Aerodynamics Conference*, 2009.

[5] C.B. Allen, A.M. Morris, and T.C.S. Rendall. Aerodynamic Optimisation of Hovering Helicopter Rotors using Efficient and Flexible Shape Parameterisation. In *26th AIAA Applied Aerodynamics Conference*, 2008.

[6] C.B. Allen and T.C.S. Rendall. CFD-Based Shape Optimization of Hovering Rotors Using Global and Local Parameters. In *28th AIAA Applied Aerodynamics Conference*, number July, 2010.

[7] M. Allongue and J.P. Drevet. New rotor test rig in the large Modane wind tunnel. In *15th European Rotorcraft Forum*, 1989.

[8] S.L. Althoff, J.W. Elliott, D.R. Hoad, and R.H. Sailey. Inflow measurements made with a laser velocimeter on a helicopter model in forward flight, volume 10, 1990.

[9] S.L. Althoff, J.W. Elliott, D.R. Hoad, and R.H. Sailey. Inflow measurements made with a laser velocimeter on a helicopter model in forward flight, volume 11, 1990.

[10] S.L. Althoff, J.W. Elliott, D.R. Hoad, and R.H. Sailey. Inflow measurements made with a laser velocimeter on a helicopter model in forward flight, volume 9, 1990.

[11] S.L. Althoff, J.W. Elliott, and R.. Sailey. Inflow measurements made with a laser velocimeter on a helicopter model in forward flight, volume 3, 1988.

[12] S.L. Althoff, J.W. Elliott, and R.H. Sailey. Inflow measurements made with a laser velocimeter on a helicopter model in forward flight, volume 5, 1988.

[13] S.L. Althoff, J.W. Elliott, and R.H. Sailey. Inflow measurements made with a laser velocimeter on a helicopter model in forward flight, volume 2, 1988.

[14] S.L. Althoff, J.W. Elliott, and R.H. Sailey. Inflow measurements made with a laser velocimeter on a helicopter model in forward flight, volume 1, 1988.

[15] S.L. Althoff, Joe W. Elliott, R. Hoad, and R.H. Sailey. Inflow measurements made with a laser velocimeter on a helicopter model in forward flight, volume 8, 1990.

[16] S.L. Althoff, Joe W. Elliott, and R.H. Sailey. Inflow measurements made with a laser velocimeter on a helicopter model in forward flight, volume 4, 1988.

[17] S.L. Althoff, D.R. Hoad, J.W. Elliott, and R.H. Sailey. Inflow measurements made with a laser velocimeter on a helicopter model in forward flight, volume 6, 1989.

[18] S.L. Althoff, D.R. Hoad, J.W. Elliott, and R.H. Sailey. Inflow measurements made with a laser velocimeter on a helicopter model in forward flight, volume 7, 1989.

[19] G. Arnaud, B. Benoit, and F. Toulmay. Improvements to the Aerodynamic Model of the R85 Helicopter Rotor Code Validation and Applications. In *28th ISL Applied Aerodynamics Symposium*, 1991.

[20] B. Aupoix, D. Arnal, B. Chaouat, F. Chedevergne, S. Deck, V. Gleize, P. Grenard, and E. Laroche. Transition and Turbulence Modeling. *AerospaceLab - the ONERA journal*, (2), 2011.

[21] A. Bagai, R.C. Moffitt, R.H. Blackwell Jr., and T.A. Krauss. Rotor blade for a high speed rotary-wing aircraft, 2005. Patent application number US2006/0265418A1.

[22] T.J. Baker. Three Decades of Meshing; a Retrospective View. In *16th AIAA Computational Fluid Dynamics Conference*, 2003.

[23] G. Barakos and C.S. Johnson. Development of a Framework for Optimising Aspects of Rotor Blades. In *66th Annual Forum of the American Helicopter Society*, 2010.

[24] P.-M. Basset, O. Heuze, J.V.R. Prasad, and M. Hamers. Finite State Rotor Induced Flow Model For Interferences and Ground Effect. In *57th Annual Forum of the AHS*, 2001.

[25] P.-M. Basset and R.A. Ormiston. Comparison and validation of the France/USA finite state rotor dynamic inflow models. In *36th European Rotorcraft Forum*, 2010.

[26] C. Bailly and G. Comte-Bellot. *Turbulence*. CNRS Editions, 2002.

[27] P. Beaumier, M. Costes, B. Rodriguez, M. Poinot, and B. Cantaloube. Weak and strong coupling between the elsA CFD solver and the HOST helicopter comprehensive analysis. In *31th European Rotorcraft Forum*, 2005.

[28] M. Bebesel, G. Polz, and E. Schöll. Aerodynamic and aeroacoustic layout of the ATR (Advanced Technology Rotor). In *55th Annual Forum of the American Helicopter Society*, 1999.

[29] B. Benoit, A.-M. Dequin, K. Kampa, W. Von Grünhagen, P.-M. Basset, and Bernard Gimonet. HOST, a General Helicopter Simulation Tool for Germany and France. In *56th Annual Forum of the American Helicopter Society*, 2000.

[30] M.J. Bhagwat and J.G. Leishman. On the Relationship Between Blade Circulation and Tip Vortex Characteristics. In *54th Annual Forum of the American Helicopter Society*, 1998.

[31] M. Bompard and J. Peter. Local Search Methods for Design in Aeronautics. *NATO, RTO-EN-AVT-167*.

[32] G. Le Bouar, M. Costes, and P. Devinant. Numerical simulations of unsteady aerodynamics of helicopter rotor in manoeuvring flight conditions. *Aerospace Science and Technology*, 8:11–25, 2004.

[33] W.G. Bousman. Airfoil Design and Rotorcraft Performance. In *58th Annual Forum of the American Helicopter Society*, 2002.

[34] A. Brocklehurst, J. Beedy, G. Barakos, K. Badcock, and B. Richards. Experimental and CFD investigation of helicopter BERP tip aerodynamics. In *Conference on Computational and Experimental Methods*, 2003.

[35] L. Cambier, S. Heib, and S. Plot. The ONERA elsA CFD software: input from research and feedback from industry. In *28th International Congress of the Aeronautical Sciences*, 2012.

[36] L. Cambier and J.-P. Veuillot. Status of the elsA CFD Software for Flow Simulation and Multidisciplinary Applications. In *46th AIAA Aerospace Sciences Meeting and Exhibit*, 2008.

[37] F.X. Caradonna and C. Tung. Experimental and Analytical Studies of a model helicopter rotor in hover. *NASA Technical Memorandum 81232*, 1981.

[38] J.W. Carter Jr. and J.G. Roncz. Airfoil suitable for forward and reverse flow, 2001. Patent application number US2002/0005458A1.

[39] P. Chassaing. *Turbulence en mécanique des fluides*. Cépaduès-éditions, 2000.

[40] R.T.N. Chen. A Survey of Nonuniform Inflow Models for Rotorcraft Flight Dynamics and Control Applications. *NASA Technical Memorandum 102219*, 1989.

[41] S. Choi and A. Datta. CFD Prediction of Rotor Loads using Time-Spectral Method and Exact Fluid-Structure Interface. In *26th AIAA Applied Aerodynamics Conference*, 2008.

[42] Seongim Choi, Ki H Lee, Juan J. Alonso, and Anubhav Datta. Preliminary Study on Time-Spectral and Adjoint-Based Design Optimization of Helicopter Rotors. In *AHS Specialist's Conference on Aerodynamics*, 2008.

[43] J. Chow, G. Zilliac, and P. Bradshaw. Turbulence Measurements in the Near Field of a Wingtip Vortex. *NASA Technical Memorandum 110418*, 1997.

[44] Y. Collette and P. Siarry. Three new metrics to measure the convergence of metaheuristics towards the Pareto frontier and the aesthetic of a set of solutions in biobjective optimization. *Computers & Operations Research*, 32:773 – 792, 2005.

[45] K. Collins, J. Bain, N. Rajmohan, L. Sankar, T.A. Egolf, R.D. Janakiram, K. Brentner, and L. Lopes. Toward a High-Fidelity Helicopter Rotor Redesign Framework. In *64th Annual Forum of the American Helicopter Society*, 2008.

[46] K. Collins and L. Sankar. Application of Low and High Fidelity Simulation Tools to Helicopter Rotor Blade Optimization. In *65th Annual Forum of the American Helicopter Society*, 2009.

[47] T.J. Craft, A.V. Gerasimov, and B.E. Launder. A computational study of the near-field generation and decay of wingtip vortices. *International Journal of Heat and Fluid Flow*, 27:684–695, 2006.

[48] S.B. Crary. Design of Computer Experiments for Metamodel Generation. *Analog Integrated Circuits and Signal Processing*, 32(1):7–16, 2002.

[49] R. Cucitore, M. Quadrio, and A. Baron. On the effectiveness and limitations of local criteria for the identification of a vortex. *Journal Of Mechanics*, 18(2):261–282, 1999.

[50] K. Deb, A. Pratap, S. Agarwal, and T. Meyarivan. A Fast and Elitist Multiobjective Genetic Algorithm: NSGA-II. *IEEE Transactions on Evolutionary Computation*, 6(2):182–197, 2002.

[51] G. Depommier, D. Alfano, D. Leusink, and G. Leymary. Computation of transition to turbulence on rotor blades. In *37th European Rotorcraft Forum*, 2011.

[52] A. Dumont, A. Le Pape, J. Peter, and S. Huberson. Aerodynamic Shape Optimization of Hovering Rotors Using a Discrete Adjoint of the RANS equations. In *65th Annual Forum of the American Helicopter Society*, 2009.

[53] A. Dumont, A. Le Pape, J. Peter, and S. Huberson. Sensitivity Analysis Using Direct Differentiation and Adjoint Vector Methods for Helicopter Rotor Flow In Hover. In *12th AIAA/ISSMO Multidisciplinary Analysis and Optimization Conference*, 2008.

[54] K. Duraisamy. *Studies in Tip Vortex Formation, Evolution and Control*. PhD thesis, University of Maryland, 2005.

[55] R. Duvigneau and M. Visonneau. Hybrid Genetic Algorithms and Artificial Neural Networks for Complex Design Optimization in CFD. *International Journal for Numerical Methods in Fluids*, 44(11):1257–1278, 2002.

[56] M.S. Eldred, A.A. Giunta, S.F. Wojtkiewicz, and T.G. Trucano. Formulations for surrogate-based optimization under uncertainty. In *9th AIAA/ISSMO Symposium on Multidisciplinary Analysis and Optimization*, 2002.

[57] D. Falchero, G. Arnaud, F. Beroul, J. Bailly, P. Beaumier, and Y. Delrieux. Two-sweep rotary wing blade with limited taper ratio, 2004. Patent number US7331765B2.

[58] J. Fan, W. Yuan, H. Kang, and C. Yan. Performance Analysis of Upwind Scheme for Entropy Condition and Discontinuities. In *46th AIAA Aeospace Sciences Meeting and Exhibit*, 2008.

[59] K.-T. Fang, R. Li, and A. Sudjianto. *Design and Modelling for Computer Experiments*. Chapman & Hall/CRC Computer Science and Data Analysis Series, 2006.

[60] A.I.J. Forrester and A.J. Keane. Recent advances in surrogate-based optimization. *Progress in Aerospace Sciences*, 45:50–79, 2009.

[61] T.B. Gatski, S. Sarkar, and C.G. Speziale. Modeling the pressure-strain correlation of turbulence - an invariant dynamical systems approach. *NASA Contractor Report 181979*, 1990.

[62] H. Glauert. A General Theory of the Autogyro. *British ARC RM*, 1111, 1926.

[63] B. Gmelin, Y.H. Yu, W.R. Splettstoesser, J.J. Philippe, J. Prieur, and T.F. Brooks. Reduction of helicopter blade-vortex interaction noise by active rotor control technology. *Progress in Aerospace Sciences*, 33(97):647–687, 1997.

[64] M. Hamers and P.-M. Basset. Application of the Finite State Unsteady Wake Model in Helicopter Flight Dynamic Simulation. In *26th European Rotorcraft Forum*, number September, 2000.

[65] Y.O. Han, J.G. Leishman, and A.J. Coynet. On the turbulent structure of a tip vortex generated by a rotor. In *52nd American Helicopter Society Annual Forum*, 1996.

[66] B. Hansford, S. Stacey, and R. Harrison. BERP IV the design, development and testing of an advanced rotor blade. In *65th Annual Forum of the American Helicopter Society*, 2009.

[67] J.L. Hill, S.T. Shaw, and N. Qin. Engineering Prediction of laminar/turbulent transition for isolated helicopter rotors in hover. In *30th European Rotorcraft Forum*, 2004.

[68] G. Iaccarino and K. Duraisamy. Curvature correction and application of the v2-f turbulence model to tip vortex flows. *Center for Turbulence Research, Annual Research Briefs*, 2005.

[69] M. Imiela. High-fidelity optimization framework for helicopter rotors. In *35th European Rotorcraft Forum*, 2009.

[70] M. Imiela. Investigation of Aeroelastic Effects for a Helicopter Main Rotor in Hover. In *36th European Rotorcraft Forum*, 2010.

[71] M. Imiela. High-fidelity optimization framework for helicopter rotors. *Aerospace Science and Technology*, 1:1–15, 2011.

[72] A. Jameson, W. Schmidt, and E. Turkel. Numerical solution of the Euler equations by Finite Volume Methods Using Runge-Kutta Time-Stepping Schemes. In *AIAA 14th Fluid and Plasma Dynamic Conference*, 1981.

[73] C.S. Johnson and G.N. Barakos. Development of a Framework for Optimising Rotor Blade Designs. In *46th Symposium of Applied Aerodynamics*, 2011.

[74] W. P. Jones and B. E. Launder. The calculation of low-reynolds-number phenomena with a two-equation model of turbulence. *International Journal of Heat Mass Transfer*, 16:1119–1130, 1973.

[75] S. Krishnamurty and G.C. Wilmes. Preference-Based Updating of Kriging Surrogate Models. In *10th AIAA/ISSMO Multidisciplinary Analysis and Optimization Conference*, 2004.

[76] M. Lazareff, A.-M. Vuillot, and L. Cambier. elsA Theoretical Manual. ONERA-DSNA, 2.0 edition, April 2008.

[77] J. Laurenceau, M. Montagnac, M. Meaux, and P. Sagaut. Comparison of Gradient Based and Gradient Enhanced Response Surface Based Optimizers. *AIAA Journal*, 48(5):981–994, 2010.

[78] G. Legras. *Analyse des mécanismes d'action des traitements de carter dans les compresseurs axiaux*. PhD thesis, Ecole Centrale de Lyon, 2011.

[79] A. Le Pape. Numerical aerodynamic optimization of helicopter rotors: multi-objective optimization in hover and forward flight conditions. In *31th European Rotorcraft Forum*, 2005.

[80] A. Le Pape and P. Beaumier. Numerical optimization of helicopter rotor aerodynamic performance in hover. *Aerospace Science and Technology*, 9:191–201, 2005.

[81] S.W. Lee and O.J. Kwon. Multi-point aerodynamic shape optimization of rotor blades using unstructured meshes. In *30th European Rotorcraft Forum*, 2004.

[82] S.W. Lee and O.J. Kwon. Aerodynamic Shape Optimization of Rotor Blades in Hover Using Unstructured Meshes. In *60th Annual Forum of the American Helicopter Society*, 2004.

[83] J. Gordon Leishman. *Principles of Helicopter Aerodynamics*. Cambridge University Press, second edition, 2006.

[84] A. Lerat, F. Falissard, and J. Sidès. Vorticity preserving schemes for the compressible Euler equations. *Journal of Computational Physics*, 225:635–651, 2007.

[85] H. Li and Q. Zhang. Multiobjective Optimization Problems With Complicated Pareto Sets, MOEA/D and NSGA-II. *IEEE Transactions on Evaluationary Computation*, 13(2):284–302, 2009.

[86] M.-S. Liou. A Sequel to AUSM: AUSM+. *Journal of Computational Physics*, 129:364–382, 1996.

[87] M.-S. Liou and C.J. Steffen Jr. A New Flux Splitting Scheme. *NASA Technical Memorandum 104404*, 1991.

[88] E. Lutton. Algorithmes génétiques et algorithmes évolutionnaires. *Techniques de l'ingénieur*.

[89] R. T. Marler and J. S. Arora. Survey of multi-objective optimization methods for engineering. *Structural and Multidisciplinary Optimization*, 26(6):369–395, 2004.

[90] P.B. Martin and J.G. Leishman. Trailing votrex measurements in the wake of a hovering rotor blade with various tip shapes. In *58th Annual Forum of the AHS International*, 2002.

[91] I. Mary. *Méthode de Newton approchée pour le calcul d'écoulements instationnaires comportant des zones à très faibles nombres de Mach*. PhD thesis, Université de Paris XI-Orsay, 1999.

[92] A. Massaro, A. D'Andrea, and E. Benini. Multiobjective-Multipoint Rotor Blade Optimization in Forward Flight Conditions Using Surrogate-Assisted Memetic Algorithms. In *37th European Rotorcraft Forum*, 2011.

[93] W.J. McCroskey. Measurements of boundary layer transition, separation and streamline direction on rotating blades, 1971.

[94] F. R. Menter. Improved Two-Equation k-omega Turbulence Models for Aerodynamic Flows. *NASA Technical Memorandum 103975*, 1992.

[95] F. R. Menter, M. Kuntz, and R. Langtry. Ten Years of Industrial Experience with the SST Turbulence Model.

[96] B. Michéa, A. Desopper, and M. Costes. Aerodynamic rotor loads prediction method with free wake for low speed descent flights. In *18th European Rotorcraft Forum*, 1992.

[97] B. Michel. *Contribution à la simulation numérique efficace des écoulements dans les prises d'air supersoniques*. PhD thesis, Ecole Nationale Supérieure d'Arts et Métiers, 2004.

[98] A.M. Morris, C.B. Allen, and T.C.S. Rendall. An Efficient Shape Parameterisation Method Applied to Aerodynamic Optimisation of Helicopter Rotors. In *47th AIAA Aerospace Sciences Meeting Including the New Horizons Forum and Aerospace Exposition*, 2009.

[99] Siva K. Nadarajah and Charles A. Tatossian. Multi-objective aerodynamic shape optimization for unsteady viscous flows. *Optimization and Engineering*, 11(1):67–106, 2010.

[100] E.J. Nielsen, E.M. Lee-Rausch, and W.T. Jones. Adjoint-Based Design of Rotors Using the Navier-Stokes Equations in a Noninertial Reference Frame. In *65th Annual Forum of the American Helicopter Society*, 2009.

[101] T. Okabe, Y. Jin, and B. Sendhoff. A Critical Survey of Performance Indices for Multi-Objective Optimisation. In *Congress on Evolutionary Computation*, 2003.

[102] K. Pahlke, F. Le Chuiton, and A. D'Alascio. Application of a structured and an unstructured CFD-method to the fuselage aerodynamics of the EC145 helicopter. Prediction of the time averaged influence of the main rotor. In *European Congress on Computational Methods in Applied Sciences and Engineering (ECCOMAS)*, 2004.

[103] S. Pal and S.K. Gauri. Assessing effectiveness of the various performance metrics for multi-response optimization using multiple regression. *Computers & Industrial Engineering*, 59(4):976–985, 2010.

[104] F.J. Perry. Helicopter rotor blades, 1989. Patent number EP0351104B1.

[105] D.A. Peters. Integration of dynamic, aerodynamic, and structural optimization of helicopter rotor blades. *NASA-CR 189018*, 1991.

[106] D.M. Pitt and D.A. Peters. Rotor dynamic inflow derivatives and time constants from various inflow models. In *9th European Rotorcraft Forum*, 1983.

[107] C. Poloni, A. Giurgevich, L. Onesti, and V. Pediroda. Hybridization of a multi-objective genetic algorithm, a neural network and a classical optimizer for a complex design problem in fluid dynamics. *Computer methods in applied mechanics and engineering*, 186:403–420, 2000.

[108] G. Puigt and H. Deniau. CFD e-Learning Mesh and discretization. 2011.

[109] N.V. Queipo, R.T. Haftka, W. Shyy, T. Goel, R. Vaidyanathan, and P.K. Tucker. Surrogate-based analysis and optimization. *Progress in Aerospace Sciences*, 41:1–28, 2005.

[110] N.V. Queipo, S. Pintos, E. Nava, and A. Verde. Setting Targets for Surrogate-based Optimization. In *51st AIAA/ASME/ASCE/AHS/ASC Structures, Structural Dynamics and Materials Conference*, 2010.

[111] N.V. Queipo, A. Verde, S. Pintos, and R.T. Haftka. Assessing the Value of Another Cycle in Surrogate-Based Optimization. In *11th AIAA/ISSMO Mutlidisciplinary Analysis and Optimization Conference*, 2006.

[112] M. Ramasamy. *Contributions to the Measurement and Analysis of Helicopter Blade Tip Vortices*. PhD thesis, University of Maryland, 2004.

[113] M. Ramasamy, B. Johnson, and J.G. Leishman. Turbulent Tip Vortex Measurements Using Dual-Plane Digital Particle Image Velocimetry. In *64th Annual Forum of the American Helicopter Society*, 2008.

[114] R.G. Regis and C.A. Shoemaker. Improved strategies for radial basis function methods for global optimization. *Journal of Global Optimization*, 37:113–135, 2007.

[115] T. Renaud, M. Costes, and S. Péron. Computation of GOAHEAD configuration with Chimera assembly. *Aerospace Science and Technology*, 19(1):50–57, 2012.

[116] K. Richter, S. Koch, A.D. Gardner, H. Mai, and A. Klein. Experimental investigation of unsteady transition on a pitching rotor blade airfoil. In *38th European Rotorcraft Forum*, 2012.

[117] T.D. Robinson, M.S. Eldred, K.E. Willcox, and R. Haimes. Strategies for Multifidelity Optimization with Variable Dimensional Hierarchical Models. In *47th AIAA/ASME/ASCE/AHS/ASC Structures, Strucutral Dynamics and Materials Conference*, 2006.

[118] B. Rodriguez. Numerical simulation of Blade Vortex Interaction and Vortex Ring State aerodynamics using a fully time marching unsteady wake model. In *33rd European Rotorcraft Forum*, 2007.

[119] M. Sasena, P. Papalambros, and P. Goovaerts. Global optimization of problems with disconnected feasible regions via surrogate modeling. In *9th AIAA Symposium on Multidisciplinary Analysis and Optimization*, 2002.

[120] O. Saunier, C. Benoit, G. Jeanfaivre, and A. Lerat. Third-order Cartesian overset mesh adaptation method for solving steady compressible flows. *International Journal for Numerical Methods in Fluids*, (57):811–838, 2008.

[121] J. Seddon. *Basic Helicopter Aerodynamics*. American Institute of Aeronautics and Astronautics Education Series, 1990.

[122] S. Shan and G.G. Wang. Survey of Modeling and Optimization Strategies for High-Dimensional Design Problems. In *12th AIAA/ISSMO Multidisciplinary Analysis and Optimization Conference*, 2008.

[123] T.W. Simpson, T.M. Mauery, J.J. Korte, and F. Mistree. Kriging Models for Global Approximation in Simulation-Based Multidisciplinary Design Optimization. *AIAA Journal*, 39(12), 2001.

[124] T.W. Simpson, V. Toropov, V. Balabanov, and F.A.C. Viana. Design and Analysis of Computer Experiments in Multidisciplinary Design Optimization: A Review of How Far We Have Come - or Not. In *12th AIAA/ISSMO Multidisciplinary Analysis and Optimization Conference*, 2008.

[125] R. Steijl, G. Barakos, and K. Badcock. A framework for CFD analysis of helicopter rotors in hover and forward flight. *International Journal for Numerical Methods in Fluids*, (51):819–847, 2006.

[126] H. Sun, Y. Kim, S. Lee, and D. Lee. Aerodynamic Design of Helicopter Rotor Blade in Forward Flight Using Response Surface Methodology. In *58th Annual Forum of the American Helicopter Society*, 2002.

[127] H. Sun and S. Lee. Response surface approach to aerodynamic optimization design of helicopter rotor blade. *International Journal for Numerical Methods in Fluids*, (64):125–142, 2005.

[128] L.P. Swiler. Gaussian Processes in Response Surface Modeling. In *IMAC-XXIV: Conference & Exposition on Structural Dynamics*, 2006.

[129] C.A. Tatossian and S.K. Nadarajah. Multi-objective Constrained Optimization using a Non-Linear Frequency Domain based Adjoint Approach. In *63rd Annual Forum of the American Helicopter Society*, 2007.

[130] C.A. Tatossian and S.K. Nadarajah. Optimum Shape Design of Helicopter Rotors in Forward Flight via Control Theory. In *18th AIAA Computational Fluid Dynamics Conference*, 2007.

[131] C.A. Tatossian and S.K. Nadarajah. Aerodynamic shape optimization of hovering rotor blades using a non-linear frequency domain approach. In *Aerospace Sciences Meething and Exhibit*, 2008.

[132] M.E. Tauber and R.G. Langhi. Transonic Rotor Tip Design Using Numerical Optimization. *NASA Technical Memorandum 86771*, 1985.

[133] J.J. Thibert, A.-M. Rodde, and J.-M.E. Pouradier. Profil de pale pour voilure tournante d'aéronef, 1980. Patent application number FR2490586A1.

[134] A. DeHondt and F. Toulmay. Influence of fuselage on the inflow performance and trim. *Vertica*, 14/4:573–585, 1990.

[135] F. Toulmay and J.M. Zibi. Pale à extrémité en flèche pour voilure tournante d'aéronef, 1996. Patent number EP0842846B1.

[136] R.A. Van Den Braembussche. Tuning of Optimization Strategies. *NATO, RTO-EN-AVT-167*, 2010.

[137] R.A. Van Den Braembussche. Global Optimization Methods: Theoretical Aspects & Definitions. *NATO, RTO-EN-AVT-167*, 2010.

[138] H. Van Der Ven. An adaptive multitime multigrid algorithm for time-periodic flow simulations. *Journal of Computational Physics*, 227/10:5286–5303, 2008.

[139] F. Viana, R. Haftka, and L. Watson. Why Not Run the Efficient Global Optimization Algorithm with Multiple Surrogates? In *51st AIAA/ASME/ASCE/AHS/ASC Structures, Structural Dynamics and Materials Conference*, 2010.

[140] M. Visonneau and R. Duvigneau. Hybrid genetic algorithms and neural networks for fast CFD-based design. In *9th AIAA symposium on multidisciplinary analysis and optimization*, 2002.

[141] N.A. Vu, H.-J. Kang, A. I. Azamatov, J.-W. Lee, and Y.-H. Byun. Aerodynamic design optimization of helicopter rotor blades in hover performance using advanced configuration generation method. In *35th European Rotorcraft Forum*, 2009.

[142] N.A. Vu, J.-W. Lee, Y.-H. Byun, and S. Kim. Aerodynamic Design Optimization of Helicopter Rotor Blades including Airfoil Shape. In *66th Annual Forum of the American Helicopter Society*, 2010.

[143] A. Vuillet. Rotor and blade aerodynamic design. *AGARD - FDP Special course on Aerodynamics of Rotorcraft*, 1990.

[144] D.A. Wachspress and T.R. Quackenbush. Rotor blade with optimized twist distribution, 2001. Patent number US6497385B1.

[145] D.A. Wachspress, T.R. Quackenbush, and C.L. Solomon. On minimum induced power of the helicopter rotor. In *61st Annual Forum of the American Helicopter Society*, 2005.

[146] J.L. Walsh, G.J. Bingham, and M.F. Riley. Optimization methods applied to the aerodynamic design of helicopter blades. *NASA Technical Memorandum 89155*, 1987.

[147] L. Wang. A hybrid genetic algorithm-neural network strategy for simulation optimization. *Applied Mathematics and Computation*, 170(2):1329–1343, 2005.

[148] F.-S. Wei and C. Gunsallus. A new approach to rotor blade performance design improvement. In *48th AIAA Structures, Structural Dynamics and Materials Conference*, 2007.

[149] P. Wernert, G. Koerber, F. Wietrich, M. Raffel, and J. Kompenhans. Demonstration by PIV of the non-reproducibility of the flow field around an airfoil pitching under deep dynamical stall conditions and consequences thereof. *Aerospace Science and Technology*, (2):125–135, 1997.

[150] D.C. Wilcox. *Turbulence Modeling for CFD*. DCW Industries, third edition, 2006.

[151] G. Wilke. Variable Fidelity Optimization of Required Power of Rotor Blades: Investigation of Aerodynamic Models and their Application. In *38th European Rotorcraft Forum*, 2012.

[152] J. Wu and S. Azarm. Metrics for Quality Assessment of a Multiobjective Design Optimization Solution Set. *Journal of Mechanical Design*, 123, 2001.

[153] S. Xue, B. Docker, J. Narramore, and Z.-X. Han. Integrated Aero-Acoustics Rotor Simulation and Design Optimization. In *12th AIAA/CEAS Aeroacoustics Conference*, 2006.

[154] C. Yang, T. Aoyama, S. Chae, K. Yee, S. Jeong, and S. Obayashi. Blade Planform Optimization to Reduce HSI Noise of Helicopter in Hover. In *64th AHS Forum*, 2008.

[155] W.T. Yeager, P.H. Mirick, K.W. Noonan, J.D. Singleton, and M.L. Wilbur. Performance Wind-Tunnel Rotor Blade. *NASA Technical Memorandum 4754*, (May 1997), 1997.

[156] S. Yoon and A. Jameson. An LU-SSOR Scheme for the Euler and Navier-Stokes Equations. *NASA Contractor Report 179556*, 1986.

[157] A. Younis, Z. Dong, J. Gu, and G. Li. Trends, Features, and Tests of Common and Recently Introduced Global Optimization Methods. In *12th AIAA/ISSMO Multidisciplinary Analysis and Optimization Conference*, 2008.

[158] Q. Zhang, W. Liu, E. Tsang, and B. Virginas. Expensive Multiobjective Optimization by MOEA/D with Gaussian Process Model. *IEEE Transactions on Evolutionary Computation*, 14(3):456–474, 2010.

[159] A. Zhou, B.-Y. Qu, H. Li, S.-Z. Zhao, P.N. Suganthan, and Qingfu Zhang. Multiobjective evolutionary algorithms: A survey of the state of the art. *Swarm and Evolutionary Computation*, 1:32–49, 2011.

[160] E. Zitzler. *Evolutionary Algorithms for Multiobjective Optimization: Methods and Applications*. PhD thesis, Swiss Federal Institute of Technology Zurich, 1999.

[161] E. Zitzler, K. Deb, and L. Thiele. Comparison of Multiobjective Evolutionary Algorithms: Empirical Results. *Evolutionary Computation*, 8(2):173–195, 2000.

[162] E. Zitzler, L. Thiele, M. Laumanns, and C.M. Fonseca. Performance Assessment of Multiobjective Optimizers: An Analysis and Review. *IEEE Transactions on Evolutionary Computation*, 7(2):117–132, 2002.

[163] Definition optimization method, november 2012. `http://www.merriam-webster.com/`.

[164] Nasa's fundamental aeronautics program, january 2013. `http://www.aeronautics.nasa.gov/fap/rotary_wing.html`.

OUTILS NUMERIQUES AVANCES POUR L'OPTIMISATION AERODYNAMIQUE DES ROTOR D'HELICOPTERE

RESUME : La conception aérodynamique des pales du rotor principal d'un hélicoptère doit simultanément prendre en compte plusieurs objectifs relatifs aux critères du vol stationnaire et vol d'avancement. Cette thèse vise à développer une boucle d'optimisation automatisée combinant des algorithmes d'optimisation avancés et des outils de simulation. Deux outils de simulation sont employés pour la prédiction des performances rotor : le code de mécanique de vol HOST, ainsi que le code de Mécanique des Fluides Numérique (MFN) *elsA*. Une analyse de ces outils est effectuée pour des cas test bien documentés afin d'estimer leur capacité à prédire des tendances de performances rotor en fonction de la géométrie de pale. L'influence des paramètres numériques est également caractérisée. Aussi, une stratégie d'optimisation est développée, permettant la prise en compte de plusieurs objectifs et de contraintes complexes, ainsi que la détermination d'optima globaux pour ce problème multimodale. Suivant ces critères, un algorithme génétique (AG) est sélectionné. Afin de réduire le nombre d'évaluations nécessaires, une stratégie d'optimisation multi-fidélité est proposée : une optimisation préliminaire utilisant l'AG et HOST est utilisée pour la réduction de l'espace des paramètres en sélectionnant la zone de haute performance. Ensuite, une surface de réponse est construite avec des calculs haute-fidélité des pales de haute performance comme vu par l'étape préliminaire. L'optimisation est finalement effectuée sur cette surface de réponse haute-fidélité. L'approche proposée résulte en une augmentation significative des performances rotor, tout en respectant le critère industriel relatif au nombre de calculs coûteux comme MFN. L'approche proposée se révèle être un outil efficace pour la conception de pales du rotor principal d'hélicoptère.

Mots clés : optimisation multi-objectif, hélicoptère, aérodynamique, pales du rotor, conception

ADVANCED NUMERICAL TOOLS FOR AERODYNAMIC OPTIMIZATION OF HELICOPTER ROTOR BLADES

ABSTRACT : The aerodynamic design of helicopter rotor blades requires taking into accounted multiple objectives simultaneously, to provide a compromise solution for the conflicting requirements associated to hover and forward flight conditions. The present work aims at developing an automated optimization based on the combination of advanced optimization algorithms and simulation tools. As a preliminary step, candidate simulation methods and optimization algorithms are assessed in detail. Two simulation methods are employed for the computation of rotor performance: the in-house Helicopter Overall Simulation Tool (HOST), based on the blade element method, and ONERA's Computation Fluid Dynamics (CFD) code *elsA*. An in-detail analysis of both simulation tools for well documented test cases is carried out, with focus on their capability of predicting trends of the global rotor performance as a function of blade geometry. The impact of computation settings is also characterized. Then, an optimization strategy is developed, allowing the incorporation of multiple objectives and complex constraints, and the detection of global optima for multi-modal problems. Based on these criteria, a genetic algorithm (GA) is selected. To reduce the number of simulations required to find optimal solutions, a Multi-Fidelity Optimization (MFO) strategy is proposed: a preliminary low-fidelity GA optimization stage based on HOST simulations is used to reduce the design space by selecting a high-performance subspace. Then, a CFD-based surrogate model is constructed on the reduced design space by using a sample of high-performance blade from the low-fidelity step. The final optimization step is run on the high-fidelity surrogate. The proposed MFO approach results in significant rotor performance improvements while using a far lower number of costly CFD evaluations of the objective functions with respect to a full GA optimization. The proposed approach is shown to represent an efficient design tool for industrial helicopter rotor blade design.

Keywords : multi-objective optimization, helicopter, aerodynamics, rotor blades, design